Stability of compacted bentonite for radionuclide retardation – Experiments and modelling

(Project KOLLORADO-e; Final Report)

Florian Huber[1], Ulrich Noseck[2] & Thorsten Schäfer[1] (Eds.)

[1]Karlsruhe Institut für Technologie (KIT), Institut für Nukleare Entsorgung (INE)

[2]Gesellschaft für Anlagen- und Reaktorsicherheit (GRS) gGmbH

(September 2016)

List of content

List of figures

List of tables

1 Introduction

1.1 Scope of the work

In order to assess the relevance of colloidal influences on radionuclide transport for the long-term safety of a radioactive waste repository, the KOLLORADO-e project integrates the results of in-vitro (geochemical), in-situ and in-silico (hydrogeological) studies. From the commonly considered set of necessary conditions (colloid presence/generation, their mobility and stability as well as the uptake of radionuclides and the irreversibility of this sorption process) required for a non-negligible impact of colloids on the pollutant propagation *(Smith et al., 2008)* the project focuses on the questions of

- colloid generation from compacted bentonite under low saline groundwater conditions (reference repository evolution in *(SKB, 2006a; SKB, 2006b)*),

- nanoparticle mobility and

- radionuclide uptake/sorption mechanisms and the appropriate implementation of relevant data into a transport code.

Our results provide feedback for the design of future experiments. In particular the Grimsel Test Site Phase VI Project CFM (**C**olloid **F**ormation and **M**igration) realizes low flow rates similar to repository post-closure conditions in order to capture the slow desorption dynamics of tri- and tetravalent actinides from bentonite colloids and to better simulate repository relevant conditions of low ionic strength groundwater contact to the geo-engineered barrier (http://www.Grimsel.com/gts-phase-vi/cfm-section/cfm-introduction). The concomitant extended durations and the higher overhead in general necessitate a careful choice of parameters. Reactive transport modelling allows assessing the impact of various scenarios, which are difficult or too expensive to realize under in-situ conditions.

Finally, yet importantly our results may serve as a basis for an appraisal of the implications of colloid presence in the vicinity of radioactive waste repositories in different deep geological host-rock formations.

1.2 State of the art

Generation of energy by nuclear fission leads to the production of radioactive waste, which contains uranium, plutonium, fission products and the so-called "minor actinides" such as neptunium, americium and curium. The safe disposal of this highly toxic and radioactive waste demands its isolation from the biosphere for several hundred thousand years. In the German Safety requirements for the disposal of heat generating radioactive waste a site-specific safety

case covering a compliance period of one million years must be made to show the safety of the system (BMU, 2009). In this respect one of the most important aspects is the issue of radionuclide behavior (mobilization, release and transport) in the repository system. It is the primary aim of nuclear waste disposal to immobilize and contain long-lived radionuclides (actinides, activation and fission products) over a geological timescale in the repository. It is an internationally agreed concept to dispose of high-level radioactive waste in deep geological repositories using a multi-barrier system *(Alonso et al., 2006b; Yoshida and Takeuchi, 2005)*. The multi-barrier system is composed of the following:

- the waste matrix itself consisting of the spent fuel and its container (technical barrier)

- the geotechnical barrier consisting of the backfill material; this report focuses solely on compacted bentonite, and

- the geological barrier (e.g., salt, granite, clay; this report focuses on crystalline host rocks).

For each of these barriers those processes have to be examined and described which potentially lead to the mobilization or immobilization of radionuclides. Beside transport a variety of geochemical processes can take place in the individual barriers (e.g., redox reactions, hydrolysis, sorption/desorption, dissolution/precipitation, colloid formation) and each has to be evaluated. The aim is to determine rates for the immobilization and/or mobilization of the radionuclides during transport through the individual barriers and from this it is possible to derive source terms for radionuclide release out of the barriers considering various scenarios. The combined source terms allow quantification of the potential release of long-lived radionuclides into the biosphere and hence provide a basis for a geochemically well-founded long-term safety analysis.

The engineered barrier system (EBS) of a deep geological repository for high-level nuclear waste foresees in most concepts *(POSIVA, 2012; SKB, 2011)* the use of bentonite as buffer and backfill material. Bentonite clay has been found to be an appropriate material for the geotechnical barrier of the multi-barrier system due to its swelling properties *(Pusch, 1983; Push, 1983) (Sellin and Leupin, 2013)* inhibiting groundwater access to the waste canister and retarding radionuclide transport in form of dissolved and colloidal phases (safety functions "sorb radionuclides" and "filter colloids", as defined by SKB *(SKB, 2011)*) away from the repository near field *(Liu and Neretnieks, 2006)*. However, depending on the physico-chemical conditions (e.g., gas and water pressure, groundwater flow velocity) the bentonite barrier may also be eroded by colloid formation *(Alonso et al., 2006b; Apted et al., 2010; Birgersson et al., 2009; Gallé, 2000; Jansson, 2009; Moreno et al., 2010; Robinson and Bath, 2011; Schäfer et al., 2012; Yoshida and Takeuchi, 2005)*. Bentonite colloid erosion has been reported to take place at the interface between the compacted bentonite buffer and granite *(Baik et al., 2007; Missana et al., 2003)*. These results as well as laboratory bentonite erosion experiments *(Alonso et al., 2007a)* show a dependency of the colloid source term on ionic strength, pH, bentonite compaction and flow velocity. Under certain conditions, as e.g. imperfect backfilling and defects in plugs or fracturing radionuclide transport through the bentonite barrier may be rather quick. Speciation of radionuclides in the groundwater/pore water mixing zone might control in such

worst case scenarios the radionuclide mobility in the far-field *(Kunze et al., 2008)*. The heavily discussed scenario of glacial water intrusion *(Liu and Neretnieks, 2006)* estimates a high erosion of bentonite buffer due to the contact with glacial water of high pH and low salinity favouring the release of bentonite colloids/particles. In the framework of the Grimsel Test Site (GTS) Phase VI the international Colloid Formation and Migration (CFM) project with partners from Japan (JAEA, AIST and CRIEPI), Switzerland (NAGRA), Sweden (SKB), Finland (POSIVA), South Korea (KAERI), United States of America (US DOE), United Kingdom (RWM) and Germany (BMWi, KIT-INE) investigate processes related to this bentonite erosion and the possible formation of colloids. The migration of bentonite colloids and associated radionuclides in the shear zone under investigation in CFM has been demonstrated in earlier studies *(Geckeis et al., 2004; Kretzschmar and Schäfer, 2005; Möri et al., 2003)*.

Beside the formation/erosion of colloidal material of smectite origin also the neo-formation of colloids due to the geochemical gradients and oversaturation of mixing waters has to be considered. Colloid formation in chemically disturbed environments has been documented in a couple of cases. Acid mine drainage waters show the formation of colloids and the mobility of heavy metals is strongly associated with this colloidal phases *(Zänker et al., 2002; Zänker et al., 2003)*. Studies with simulated tank waste solution (TWS) from the U.S. Department of Energy (DOE) Hanford Site (Washington State) showed that the maximum formation of mobile colloids occurred at the plume fronts with calcium carbonate as one of the dominant phases of the plume front colloids *(Wan et al., 2004)*. The authors identified the cation exchange process during infiltration of the high-Na^+ TWS solution, with complete replacement of exchangeable Ca^{2+}/Mg^{2+} from the sediment caused accumulation of these divalent cations at the moving plume front. Precipitation of supersaturated Ca^{2+}/Mg^{2+}- bearing minerals caused dramatic pH reduction at the plume front which triggered, in turn, precipitation of other minerals. Concerning the formation of aluminosilicate colloids laboratory studies have already demonstrated that these newly formed phases can have a significantly influence on the speciation of trivalent actinides *(Kim et al., 2005)*.

Colloids are known to be ubiquitous in natural groundwater and have been frequently discussed as potential carriers for radionuclides. Colloids show, in comparison with ionic species, a different migration behaviour due to their comparatively larger size, charge and low diffusion coefficient the probability to penetrate into matrix pores of the host rock is lower and therefore they may be transported unretarded or in the fastest streamlines of the laminar flow field being faster than the average groundwater velocity monitored by dissolved conservative tracers. Thus, colloid bound contaminants such as radionuclides may interact to a lesser degree with the surface of the host rock minerals and can be transported over considerable distances. Transport of man-made nanoparticles as well as natural occurring radionuclides by colloids has been reported e.g. for the Nevada Test Site, USA *(Buddemeier and Hunt, 1988; Kersting et al., 1999)* and the Whiteshell Research Area, Canada *(Vilks et al., 1991)*.

However, colloids can also be retained by interaction with mineral surfaces or by agglomeration, sedimentation and filtration. All processes strongly depend on geochemical parameters, e.g., pH, ionic strength or colloid concentration. Therefore, the colloid stability is a key parameter for colloid facilitated transport. Dynamic light scattering (photon correlation spectroscopy;

PCS) is frequently used to determine the coagulation rate and critical coagulation concentration (CCC) of various clay colloid suspensions *(Kretzschmar et al., 1998; Missana and Adell, 2000; Novich and Ring, 1984)*. Montmorillonite platelets are the major colloidal particles found to be mobilized from Febex bentonite. Due to their permanent negative face charge originating from isomorphous substitution and their pH dependent edge charge caused by broken tetrahedral and octahedral sheets exposing silanol and aluminol groups *(Jasmund and Lagaly, 1993; Meunier, 2005)* three different modes of interactions can be distinguished: edge-face (EF), edge-edge (EE) and face-face (FF). In order to be able to predict montmorillonite colloid stability based on extended DLVO-theory *(Derjaguin and Landau, 1941; Verwey and Overbeek, 1948)* the overall surface potential has to be separated into potentials and interaction modes associated with the edge and face geometry of the montmorillonite platelets and summing up hydration forces, born repulsion, electric double layer repulsion and London - van der Waals attraction. One suitable approach is the geometrical assumption made by Mahmood et al. *(2001)* to calculate the total interaction energy by using a half-cylinder with the radius equal to half the thickness of the montmorillonite platelet.

In the Colloid and Radionuclide Retardation (CRR) experiment carried out at the Grimsel Test Site (GTS), Phase V, the in situ migration behaviour of selected radionuclides and chemical radionuclide homologues in the presence and absence of bentonite colloids in a water-conducting shear zone was studied *(Geckeis et al., 2004; Möri et al., 2003)*. Under fast flow conditions (~36 m/d) recovery of injected bentonite colloids was in the range of 50-100 %. Related laboratory experiments in granodiorite bore cores from the same site using carboxylated polystyrene (latex) colloids showed colloid recoveries ranging from 10 to nearly 50 % *(Schäfer et al., 2004)* under longer fracture residence times. Similarly low colloid recoveries with increasing residence time were found by other investigators *(Missana et al., 2008)*. The authors conclude that even under geochemical conditions where colloids are highly stabilized (low salinity, high pH) adsorption/filtration onto mineral surfaces may occur. In the Colloid Formation and Migration (CFM) project the fluid travel times are enhanced by up to two orders of magnitude compared to CRR, enabling a further study of the colloid filtration process. Colloid recoveries are found in the range of 99 to 40 % showing a slight trend of decreasing filtration rates with increasing travel time *(Huber et al., 2014)*. The extent of colloid adsorption on natural mineral surfaces may be influenced by, e.g., the chemical heterogeneity of the mineral surfaces, surface roughness, surface coatings, discrete surface charges (mineral edges and planes), mineral dissolution, the presence of dissolved ions or by matrix diffusion *(Alonso et al., 2007c; Bowen and Doneva, 2000; Johnson et al., 1996; Patelli et al., 2006; Stumpf et al., 2008; Vakarelski et al., 2000)*. Degueldre et al. *(Degueldre et al., 1996)* carried out sorption experiments at pH 8 (I = 10-2 M NaClO4) with clay colloids and several single minerals (muscovite, biotite, quartz, feldspar) comprising the Grimsel granodiorite and observed considerable colloid adsorption. *(Alonso et al., 2004)* studied the interactions between gold colloids and a granite surface by μ-Particle Induced X-Ray Emission (μPIXE) to determine the amount of adsorbed colloids on different minerals under varying chemical conditions. These authors concluded that adsorption of colloids on rock surfaces is generally determined by electrostatic interactions. However, colloid adsorption was also detected under unfavourable (repulsive)

colloid-fracture surface attachment conditions (e.g., alkaline pH). It was suggested that chemical effects may enhance colloid/rock interaction when favourable (attractive) electrostatic interaction does not exist. Furthermore, theoretical studies have been performed to calculate surface charge heterogeneity effects (e.g., *(Velegol and Thwar, 2001)*). These effects have also been experimentally evaluated, e.g. for Cu ion adsorption onto silica *(Taboada-Serrano et al., 2005)*.

The issues mentioned above have been investigated in detail within the KOLLORADO-1 and KOLLORADO-2 reports *(Huber et al., 2014; Schäfer, 2010)* which give a good overview of the state-of-the-art as basis of the project for the partners KIT-INE and GRS.

1.3   Aims and Approach

Laboratory program. The laboratory program conducted within the project KOLLORADO-e aimed on deriving further knowledge and data on (i) mechanisms of the interaction between colloids, radionuclides and fracture filling material[1] and (ii) on the colloid-facilitated radionuclide migration This will be elaborated in detail below:

Concerning the interaction mechanisms between colloids, radionuclides and fracture filling material the following aspects are investigated in detail within the KOLLORADO-e project:

- Evaluation of radionuclide speciation in groundwater and porewater: The selection of radionuclide tracers in the field experiments is extended. Beside conservative tracers the cocktail should contain weakly sorbing trace like ^{22}Na, ^{45}Ca, ^{85}Sr, ^{133}Ba,^{137}Cs and dependent on the oxidation state strongly sorbing tracers of the radionuclides ^{232}Th, ^{233}U, ^{237}Np, $^{238/242/244}$Pu, $^{241/243}$Am. In order to evaluate their migration behaviour in the field experiments, it is necessary to know their speciation and solubility in bentonite porewater, Grimsel groundwater and in the mixing zone of both.

- Bentonite erosion and colloid formation at the bentonite porewater interface: In order to better understand the erosion behaviour – especially of the FEBEX Bentonite – a systematic variation of the parameters compaction density, chemistry of contact water (ionic strength, pH-value, cation composition), contact surface and angle and type of bentonite (raw material or homo-ionic Na/Ca form) is performed. Static and dynamic experiments are carried out and results are compared with modelling approaches. An important aspect regards the modification of the bentonite. Synthetic montmorillonite with structural incorporated Ni and Zn is fabricated and a defined fraction is mixed to the bentonite colloids to distinguish them from natural colloids in the Grimsel groundwater. It is important to know, whether the erosion behaviour of this type of bentonite differs from the conventional bentonite.

---

[1] The fracture filling material mainly consists of fault gouge.

- Colloid stability and interaction with fracture filling material: The work within the KOL-LORADO-e project is focused on the characterization of the mineral surfaces with respect to their roughness and its impact on the interaction mechanisms between colloid phases and the mineral / fracture surface. Particularly, under the glacial meltwater conditions of the Grimsel rock laboratory the interaction forces are low and surface topography in the sub µm range can play an important role for the attachment of colloid phases. As methods Atomic Force Microscopy (AFM) and Vertical Scanning Interferometry (VSI) are applied.

- Interaction of radionuclides, colloids and fracture filling material: A focus of the investigations in the KOLLORADO-e project is brought to the determination of data for the radionuclide reversibility kinetics, which are necessary to simulate the field and laboratory experiments and are directly used in the transport codes. This includes analysis of the interaction reversibility and kinetics of radionuclides with the clay colloids as well as interaction between radionuclides and the fracture filling material. The latter became of particular interest, when the long-term tailing of the breakthrough was analysed and the sorption coefficient of radionuclides on the fracture filling material turned out to be a parameter of high influence on the form and location of the curve in the long term.

Concerning the colloid-facilitated radionuclide migration specific field experiments are performed. These are accompanied by selected laboratory experiments. In particular, the following aspects are highlighted:

- Mock-up tests: The mock-up test for the long-term in situ test (LIT) at KIT-INE has been continued until source emplacement in the field (s. below). It aims at studying the feasibility of the long-term in situ test (emplacement of the packer system with compacted bentonite rings in the MI shear zone at the GTS) concerning the radionuclide labelling and addition of structural substituted montmorillonite.

- In-situ experiments at GTS: The long-term in-situ test (LIT) intends to investigate in situ colloid formation and mobilisation of radionuclides from a radionuclide-labelled bentonite plug. The bentonite buffer material and the radionuclide source were emplaced in the shear zone in May 2014. The LIT is described in detail by *(NAGRA, 2016)*.

- Field tracer test: One additional field tracer migration test, CFM RUN 13-05, is performed. The test was performed at a dipole, which was already used in the CRR project (Run #32), but the travel time was increased from about 1.5 hours to 50 hours. It targeted to investigate the transferability of the results obtained at the CFM dipole to another dipole in the shear zone and to compare results obtained during the CRR project at the same dipole under significantly increased travel times.

- The application and further development of Accelerator Mass Spectroscopy (AMS, Quinto et al., 2015) offered the opportunity to study the long-term mobility of radionuclides by sampling the tailing of the breakthrough curve over a period of six months and

will provide additional details on the sorption/desorption processes/kinetics of the fracture filling material.

The analysis of samples by HR-ICP-MS, LIBD/ s-curve LIBD, LSC, γ-spectrometry and AMS of the migration experiments and the LIT performed at GTS in the framework of the CFM project was almost exclusively performed by KIT-INE. This included analysis of several homologues (Tb, Eu, Hf, Th) or radionuclides (Cs, Na, Ba, Am, Th, Pu, Np) and bentonite colloids. In addition, for the radionuclide migration test (CFM Run 13-05) the mobile LIBD system was transferred to the GTS for on-site colloid detection.

Modelling. One goal is to shed light on the multitude of different interaction forms and paths between radionuclides, colloids and the sediment matrix. Special interest was on (i) the consequences of kinetically controlled adsorption and desorption processes and (ii) on the effect of fracture heterogeneity on bentonite erosion. The following two approaches were used:

(a) Extend an available 2D model on bentonite erosion to include heterogeneous flow fields based on random aperture distributions.

(b) macroscopic 1D/2D models using simplified geometry implementing sorption/desorption kinetics of colloids/radionuclides.

The RN colloid sorption/desorption and filtration parameters derived in the laboratory program by KIT-INE provide necessary input for transport calculations. Having calibrated the hydrogeological parameters with tracer data, the thus configured problem is then employed to make predictions for the migration of radionuclides and colloids, which are in turn compared to respective experiments in order to validate the models. During this project phase, an additional field dipole conservative tracer, colloids and radionuclides experiment was performed. Therewith, altogether five field migration experiments are available covering a range of two orders of magnitude number with respect to the travel time. This enabled the investigation of the time dependent desorption process of radionuclides from the colloids with regard to a two-site model (desorption with two different kinetic rates).

The application of the AMS (see above) provided data on the long-term tailing of the breakthrough curves of ^{243}Am, ^{242}Pu and ^{236}Np. Within this project data for CFM Run 12-02 became available so that model calculations including parameter variations could be performed to simulate the experimental data and to identify the most relevant processes with impact on the long-term behaviour of the trivalent ^{243}Am and the tetravalent radionuclide ^{242}Pu.

For the computer simulations in the project KOLLORADO-e emphasis was put on the application of the 1D-transport COFRAME *(Reiche et al., 2016)* which considers colloid facilitated radionuclide transport in fractured media by a double porosity approach. The field tests already finalized before start of the project are simulated in order to test the code and to derive parameters, which can then be used for predictive calculations of the new radionuclide migration experiment CFM RUN 13-05.

The computer code COFRAME is developed for its application in long-term safety assessment and can be applied to large model areas and long periods considered there *(Reiche et al.,*

2016). In order to estimate the impact of colloid-facilitated transport for the long-term safety of a repository under more realistic conditions, calculations with the code COFRAME are carried out for the conditions of the Finnish repository site considered in *(POSIVA, 2012)*. The interaction parameters for the colloid facilitated radionuclide transport are derived from all available CFM field tests and therewith allow evaluating the long-term colloid-facilitated radionuclide transport on the state of the art.

Simulation of bentonite erosion in a 2D fracture is accomplished by extending a model provided by I. Neretnieks from KTH Stockholm, Sweden *(Moreno et al., 2011)*. Extension of the model comprised the use of random aperture distributions instead of constant apertures as considered up to now. First simulations have been carried out in the end phase of the Kollorado-e project and will be continued in more detail within the Kollorado-e^2 project. The aim of the work is the assessment of the impact of fracture heterogeneity on the extent of bentonite erosion behaviour and erosion rates as function of flow velocity and fracture aperture correlation length.

1.4   List of publications within KOLLORADO-e

PhD thesis:

- Rinderknecht, Franz. *Bentonite erosion and colloid mediated transport of radionuclides in advection controlled systems*. (in Vorbereitung) Doktorarbeit, Karlsruhe Institut für Technologie (KIT).

Peer reviewed publications of INE in the framework of KOLLORADO-2:

- Delavernhe, L.; Steudel, A.; Darbha, G. K.; Schäfer, T.; Schuhmann, R.; Wöll, C.; Geckeis, H.; Emmerich, K. *Influence of mineralogical and morphological properties on the cation exchange behaviour of dioctahedral smectites*. Colloids and Surfaces A: Physicochemical and Engineering Aspects 2015, 481, 591-599.

- Norrfors, K. K.; Bouby, M.; Heck, S.; Finck, N.; Marsac, R.; Schäfer, T.; Geckeis, H.; Wold, S. *Montmorillonite colloids: I. Characterization and stability of dispersions with different size fractions*. Appl. Clay Sci. 2015, 114, (0), 179-189.

- Norrfors, K. K.; Marsac, R.; Bouby, M.; Heck, S.; Wold, S., Lützenkirchen, J.; Schäfer. *Montmorillonite colloids: II. Colloidal size dependency on radionuclide adsorption*. Appl. Clay Sci. 2016, 123, 292-303.

- Quinto, F.; Golser, R.; Lagos, M.; Plaschke, M.; Schäfer, T.; Steier, P.; Geckeis, H. *Accelerator Mass Spectrometry of Actinides in Ground- and Seawater: An Innovative Method Allowing for the Simultaneous Analysis of U, Np, Pu, Am, and Cm Isotopes below ppq Levels*. Anal. Chem. 2015, 87, (11), 5766-5773.

- Friedrich F., Schild D., Weidler P.G., Schäfer T. *Hydration of FEBEX bentonite observed by environmental scanning electron microscopy (ESEM)*. CMS Lecture Series 2016, Vol. 21, 199-210.

- Reiche, T., Noseck, U., Schäfer, T. *Migration of Contaminants in Fractured-Porous Media in the Presence of Colloids: Effects of Kinetic Interactions*.Transport Porous Med. 2015, 1-28.

- Stoll, M., Huber, F. M., Darbha, G. K., Schill, E., Schäfer, T. *Impact of gravity, collector surface roughness and fracture orientation on colloid retention kinetics in an artificial fracture*. J. of Colloid Interface Sci. 2016, 475, 171-183.

2 Experimental Program

2.1 Laboratory program

2.1.1 Bentonite derived colloid characterization

2.1.1.1 Influence of mineralogical and morphological properties on the cation exchange behaviour of dioctahedral smectites

Reprinted with permission from Elsevier Ltd: "*Montmorillonite colloids: I. Influence of mineralogical and morphological properties on the cation exchange behavior of smectites*" by L. Delavernhe, A. Steudel, G.K. Darbha, T. Schäfer, R. Schuhmann, C. Wöll, H. Geckeis and K. Emmerich. Colloid and Surfaces A: Physicochemical and Engineering Aspects 481 (2015) 591-599.

Introduction

Smectite interfacial interactions with the environment, involving water binding and/or trace element sorption capacity, are mainly responsible for the bentonite properties in widespread applications, such as absorbents, binders in molding sands, or geotechnical barriers in waste repositories *(Harvey and Lagaly, 2006)*. Chemical, mineralogical, and morphological properties of smectites associated with process parameters, such as pH and ionic strength of medium or temperature and pressure, determine their behaviour *(Bergaya and Lagaly, 2006)*. The most common di-octahedral smectites belong to the montmorillonite - beidellite series with a general formula of $M^{v+}_{(x+y)/v}((Al, Fe(III))_{2-y}(Mg, Fe(II)_y))(Si_{4-x}Al_x)O_{10}(OH)_2$. Here, x+y is the layer charge resulting from the substitutions within the tetrahedral and octahedral sheets ranging from 0.2 to 0.6 mol/formula unit (f.u.) and M^{v+} denotes the interlayer monovalent or divalent cations *(Brigatti et al., 2006)*. Montmorillonites and beidellites are defined by a main layer charge located in the octahedral sheets (x << y) and in the tetrahedral sheets (x >> y), respectively, with a low iron content. Permanent charge, independent of the pH induced by the layer charge, and variable charges induced by the amphoteric sites (silanol/aluminol) at the edges of the clay particle govern the charge's heterogeneity distribution *(Sposito, 1989)*. It determines the stability and rheological properties of suspensions in particular *(Tombacz and Szekeres, 2004)*. The cation exchange capacity (CEC), one of the most important properties of smectite, originates mainly from the layer charge. However, about 10-20% of CEC are due to variable charges depending on the pH and ionic strength of the background electrolyte *(Kaufhold and Dohrmann, 2013; Vogt and Köster, 1978)*. Distinction of the influence of smectite properties (layer charge, particle size, etc.) and medium parameters (pH, ionic strength, etc.) on the behaviour is a challenge. An extensive database on acid-base potentiometric titration is available to characterize the acid/base properties of clays *(Bourg et al., 2007; Bradbury and Baeyens, 1999; Duc et al., 2006; Rozalén et al., 2009; Tournassat et al., 2004b; Zarzycki and Thomas,*

2006). However, correlation with chemical and/or morphological parameters was restricted to a few samples *(Tournassat et al., 2003)*. Consequently, application of the data obtained to a few reference smectites for e.g. predictive reactive transport modelling might imply unnecessary uncertainties. In order to assess bentonite performance and predict/control the long-term behaviour of bentonites, a fundamental understanding of montmorillonite properties is required and their structure / functionality relation has to be identified.

Therefore, the aim of our study is to provide a sound characterization of the mineralogical properties in conjunction with morphological parameters as a basis for further research into the structure functionality of montmorillonite, including the trace element sorption properties, colloidal stability, and hydration behaviour of technical bentonites.

Materials and Methods

Materials Origin. Four blended bentonites with a high di-octahedral smectite content *(Kaden et al., 2013; Steudel and Emmerich, 2013; Wolters et al., 2009)* were selected: Calcigel® (Bavaria, Germany) *(Abdul Aziz et al., 2010; Ulbig, 1994)* and Volclay® (Wyoming, USA) *(Heathman, 1939; Moll, 2001)* formed by diagenetic alteration of volcanic ash, together with the Cabo de Gata bentonite (Almería, Spain) kindly supplied by ENRESA *(Caballero et al., 2005; Caballero et al., 1985; Leone et al., 1983)* and the bentonite P provided by Süd-Chemie AG (Germany) which were formed by hydrothermal alteration of pyroclastic rocks. The first three bentonites were characterized extensively as potential reference buffer/backfill materials in the context of a geotechnical barrier reported as Calcigel or Montigel *(Müller-Vonmoos and Kahr, 1982; Svensson et al., 2011; Vogt and Köster, 1978)*, MX-80 *(Müller-Vonmoos and Kahr, 1982; Pusch, 2006; Svensson et al., 2011)*, and Febex *(Huertas et al., 2000; Rozalén et al., 2009)*, respectively, just to mention a few references.

Material Pre-treatment. Chemical treatments to separate the fraction < 0.2 µm from the bulk bentonite were applied to reduce the cementing interactions of carbonates, iron (hydr)oxides, and organic materials *(Carrado et al., 2006; Tributh and Lagaly, 1986)*. Sets of 100 g or 200 g of raw bentonite were purified according to the procedure detailed in Wolters et al. *(Wolters et al., 2009)*: Carbonates were decomposed by an acetic acid-acetate buffer treatment *(Tributh and Lagaly, 1986)*; iron (hydr)oxides as well as aluminium and manganese (hydr)oxides were dissolved by a buffered dithionite-citrate solution *(Mehra and Jackson, 1960)*; organic matters were decomposed by the addition of hydrogen peroxide *(Tributh and Lagaly, 1986)*; and a 1 M sodium chloride solution for repeated washing to remove excess reactants was used. The Na-exchanged dispersions of the purified bentonites were dialyzed to remove chloride and surplus cations until the solutions reached a conductivity of 5 µS/cm. For this purpose, a cellulose hydrate Nadir®-dialysis tubing of average pore size of 25-30 Å was used. Then, a sequential fractionation was carried out according to Stokes' equivalent sphere diameter *(Lagaly, 2006; Tributh and Lagaly, 1986)*. First, dispersions were passed through a 63 µm sieve to collect the sand fraction. Then, the clay fraction < 2 µm was separated from the silt fraction 2-

63 µm by successive gravitational sedimentation. The silt fractions 2-6.3 µm, 6.3-20 µm, and then the remaining fraction 20-63 µm were obtained by several successive gravitational sedimentations. The clay fractions < 0.2 µm, 0.2-0.6 µm, and then the remaining fraction 0.6-2 µm were obtained by several successive centrifugal sedimentations from the < 2 µm dispersion after 25 min at 4347 g-force and 10 min at 1206 g-force, respectively, at 20 °C (Heraeus Multifuge 3SR). All fractions were oven-dried at 60 °C and were gently ground in an agate mortar. The < 0.2 µm fractions were stored at a relative humidity of 53% over $Mg(NO_3)_2$, the other fractions were stored in sealed containers for further investigations. Subsamples < 0.2 µm were Li-saturated by three exchanges with LiCl solution equivalent to 20-fold the CEC of the samples according to the homo-ionic exchange process described in *(Steudel and Emmerich, 2013)*. Then, Li-saturated samples were heated at 300 °C for 24 h to obtain reduced-charge montmorillonites (RCM) according to the Hofmann-Klemen effect *(Greene-Kelly, 1953; Hofmann and Klemen, 1950)*.

In the following sections, the notations B*X*-M0.2Na and B*X*-M0.2Li-300 are used for Na-saturated materials < 0.2 µm and for RCM materials, respectively, with *X* = C, V, S, or P for Calcigel®, Volclay®, the Cabo de Gata, and the P bentonites.

Table 2-1: Peak positions, basal reflection rationality descriptors of XRD patterns, and non-exchangeable potassium content.

Sample	d_{001} [Å]			d_{060} [Å]	Basal reflection rationality EG			Non-exchangeable K_2O [%]	Greene-Kelly test		
	AD	EG	550°C	Powder	CV	Δ2θ	I(%)-Sm		d_{001} [Å] AD	Δ2θ 002/004	$ξ_T$ [%]
BC-M0.2Na	12.4	17.1	9.7	1.500	0.59 ± 0.00	5.44 ± 0.01	< 10	0.59 ± 0.03	9.8	0.06	25
BV-M0.2Na	12.2	16.9	9.6	1.498	0.24 ± 0.00	5.34 ± 0.01	< 10	0.03 ± 0.01	9.5	0.08	30
BS-M0.2Na	12.4	16.8	9.8	1.499	0.81 ± 0.04	5.55 ± 0.01	10-20	0.73 ± 0.03	9.8	0.03	19
BP-M0.2Na	12.6	16.9	9.6	1.499	0.57 ± 0.04	5.47 ± 0.01	< 10	0.05 ± 0.01	9.6	0.04	22

Mineralogical and Chemical Characterization. Mineralogical identification was accomplished by X-ray diffraction (XRD) (Siemens D5000 diffractometer, CuKα radiation, scintillation detector, detector slits of 0.1 mm, divergence and anti-scatter slits of 0.6 mm) using randomly oriented powders and oriented preparations. Oriented samples, 10 mg clay/cm² on glass slides, were measured after drying at room temperature (AD), solvation with ethylene glycol (EG) and glycerol (GLY), and heating at 375 °C and 550 °C with 0.02° 2θ step intervals from 2 to 35° 2θ with 5 s per step. The presence of interstratified illite-smectite (I-Sm) layers was obvious form the XRD patterns after EG solvation and by calculation of the coefficient of variation (CV) to estimate the regularity of the interstratified phases *(Bailey, 1982; Moore and Reynolds, 1997)*. The layer charge density distribution was determined according to the alkylammonium method *(Lagaly and Weiss, 1969; Lagaly and Weiss, 1971)* following two exchange procedures of 100 mg of powder with 3 ml of n-alkylammonium formate solutions with alkylammonium molecules of chain lengths (nc) ranging from 4 to 18, except 17, for 72 h at 60 °C with subsequent 16 washings with 3 mL of ethanol. Then, oriented samples were prepared on glass slides, dried

at room temperature with muscovite as internal standard, and stored overnight in a desiccator above P_2O_5 until XRD measurement. The layer charge distribution was calculated considering the optimized particle size correction for particles < 0.2 μm adjusted from Lagaly *(Lagaly, 1994)* with the area occupied by a flat-lying alkyl ammonium (A_c) calculated as $A_c = 1.27 * 4.5 * n_c + 12$ for $n_c \leq 11$ and $A_c = 1.27 * 4.5 * n_c + 8$ for $n_c \geq 12$. The mean layer charge density ( ) increased by about 0.02 eq./f.u. after the particle size correction.

Table 2-2: Classification of dioctahedral smectites.

Sample	Layer charge [eq/f.u.]		Octahedral distribution $w_{tv/cv}$ [%]		Fe [%] of octahedral cations		Tetrahedral charge [%] of total charge		Mineral
BC-M0.2Na	Low	0.30	*cv/tv*	44/56	Ferrian	16	Beidellitic	30	Montmorillonite
BV-M0.2Na	Low	0.26	*cv*	0/100	-	9	Beidellitic	36	Montmorillonite
BS-M0.2Na	Low	0.37	*cv/tv*	41/59	-	12	Beidellitic	12	Montmorillonite
BP-M0.2Na	Low	0.32	*cv/tv*	39/61	-	8	-	4	Montmorillonite

The major elements were quantified chemically by X-ray fluorescence analyses (XRF) (Philips MagiX PRO spectrometer, Rhodium X-ray tube, 3.2 kW) using air-dry powder samples fused with $Li_2B_4O_7$ (mixing ratio 1:7). Quantification of the Fe(II) content was carried out by potentiometric titration of Ce(IV) after HF/H_2SO_4 digestion. The loss on ignition was determined separately at 1000 ºC. Stoichiometric composition of the montmorillonites was calculated based on the assumption of 22 negative charges and the measured mean layer charge according to Köster *(Köster, 1977)* using XRF analysis after impurities correction as detailed in Wolters et al. *(Wolters et al., 2009)*. Titanium was considered to be discrete titanium oxide. The equivalent permanent inter-lamellar cation exchange capacity (CEC_P) was calculated from the mean layer charge (ξ in eq./f.u.) and the molar mass of the formula unit (M in g/mol) according to $CEC_P = \xi / M * 10^5$ in cmol(+)/kg. The occupancy of *cis-* and *trans*-positions within the octahedral sheet was quantified by simultaneous thermal analysis (STA) (STA 449C Jupiter connected to a quadrupole mass spectrometer 403 C Aëlos, Netzsch, IPI) at the dehydroxylation temperature of 600 °C *(Wolters and Emmerich, 2007)*.

Particle Size Characterization. Morphological characteristics of the fundamental particles were determined by atomic force microscopy (AFM) (Bruker dimension 3100 equipped with a Nanoscope IV controller in the contact mode under ambient conditions). Dispersions of 50 mg/L in ultrapure water after 15 min of ultra-sonication (37 KHz) were deposited by spin coating onto a freshly cleaved muscovite to ensure a good dispersion onto the surface. AFM images were processed with the Scanning Probe Image Processing software (SPIP, Image Metrology) to extract the thickness (h), the basal area (A), and the perimeter (P) of each particle. Measurement uncertainties of perimeter and basal area due to tip artefacts were estimated to amount to 9-17% and 5-9% for a ~ 1 mm thick disk of 100 nm and 200 nm in diameter, respectively *(Plaschke et al., 2001)*. The weighted mean values were calculated to take into account the particle size distribution influence as follows: $\bar{x} = \Sigma x_i * m_i / m_t$, with x_i being the recorded parameter of the particle i, m_i the mass of the particle i ($m_i = \rho_s * h_i * A_i$), and m_t the sum of the masses of all analysed particles ($m_t = \rho_s \Sigma h_i * A_i$), where ρ_s is the specific density of the

particles *(Bickmore et al., 2002; Tournassat et al., 2003)*. For single particles of identical thickness, the formula was simplified as $\overline{x} = \Sigma\, x_i * A_i / A_t$, with A_i being the basal area of the particle i and A_t the sum of the basal areas of all analysed particles. Therefore, the specific edge surface area ($a_{s,edge}$) and the specific basal surface area ($a_{s,basal}$) of single particles were calculated based on the perimeter/basal area ratio ($R_{P/A}$ in nm^{-1}) and the thickness as follows: $a_{s,edge}$ = $\overline{R}_{P/A} / \rho_s * 10^6$ [m^2/g] and $a_{s,basal} = 2/ (\rho_s * h)\, 10^6$ [m^2/g] with h = 0.96 nm and ρ_s = 2700 kg/m^3.
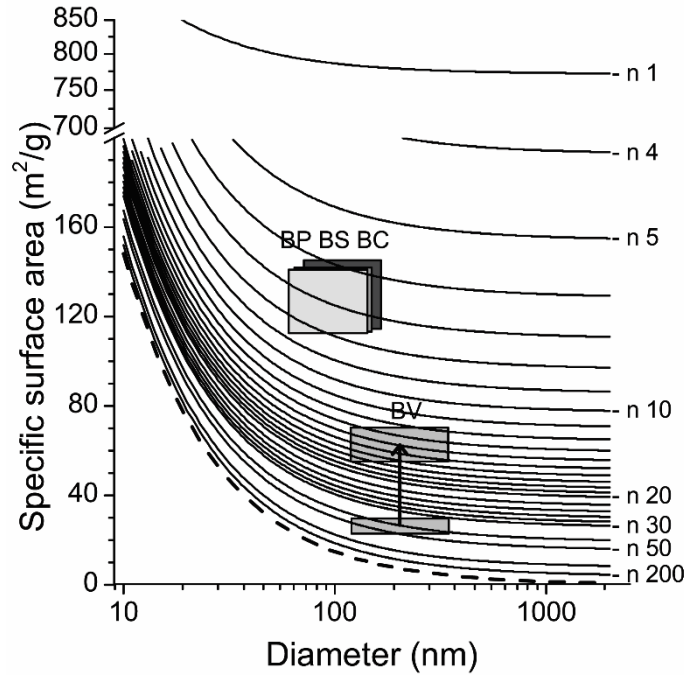
Figure 2-1: Specific surface area of quasi-crystalline layer stacks as a function of diameter, layers stacked, and as,edge (dashed line). Boxes of the reduced-charge materials and BV Na-saturated materials based on as,edge (20% of uncertainties) and d (40% of dispersion).

The argon adsorption isotherm at 87 K on powder of oven-dried samples and RCM previously outgassed at 95 °C for 12 h (Autosorb-1-MP, Quantachrome Instrument) were measured. The specific surface area was calculated according to the BET method *(Brunauer et al., 1938)* ($a_{s,BET}$) in the adsorption range of 0.02-0.2 p/p$_0$. The gas sorption in this pressure range is well-known to take place concurrently at the external surface of the particles and at the micro-pores by condensation resulting from the turbostratic arrangement of the clay *(Michot and Villiéras, 2006)*. The micro-pore volume, i.e. equivalent volume of pores of diameter < 2 nm, calculated by the non-local density functional theory (NLDFT) *(Tarazona et al., 1987)* (zeolite/silica model on the adsorption branch of the isotherm) may represent about 70% of the total pore volume (Table 2-6). Note that the contribution of micro-porosity due to the overlap of the layers to gas adsorption at low pressures is estimated to range from 7-20% for kaolinites *(Delon et al., 1986)* and from 10-40% for smectites *(Le Forestier et al., 2010)*. The contribution of micro-porosity is influenced by the particle size distribution and its broadness. As the diameter of Ar (0.336 nm) is larger than the interlayer dimension of collapsed Na-saturated montmorillonites (d_{001} ranging between 0.96 and 0.98 nm resulting in interlayer opening of 0.30 and 0.33 nm, respectively),

micro-porosity due to gas penetration into interlayer spaces *(Kaufhold et al., 2010; Rutherford et al., 1997)* was neglected. Considering a layer stacking model (n layers per stack of diameter d [nm]), the specific edge surface area and the specific basal surface were calculated as follows: $a_{s,edge} = 4 / (\rho_s * d)\ 10^6$ [m²/g] and $a_{s,basal} = 2 / (\rho_s * h * n)\ 10^6$ [m²/g], which is characteristic of dehydrated smectites. The edge surface area is independent of the layer stacking (dashed line in Figure 2-1). Then, the specific surface area measured by gas sorption ($a_{s,BET}$) was compared with the specific surface area of the model considering an over-estimation of about 20% of the layer stacking as a function of the mean weighted particle diameter measured by AFM with a diameter dispersion of 40%.

Cation Exchange Capacity. Cation exchange capacity (CEC) of the samples was measured following the Cu-trien method according to Meier and Kahr *(Meier and Kahr, 1999)*. The dispersion of 50 mg of Na-saturated materials or 100 mg of Li-saturated RCM in 10 mL of deionized water adjusted at different pH using HCl or NaOH solutions in 50 mL centrifuge tubes was allowed to equilibrate for 24 h by end-over-end shaking. Then, the pH values were controlled (FiveEasy® FE20 pH meter equipped with Inlab® Expert Pt1000 electrode, Mettler Toledo) after centrifugation (4347 g-force for 25 min at 20 °C). Samples were re-dispersed before addition of 5 mL of 0.01 M Cu-trien solution (total Cu-trien concentration of 0.003 mol/L) and cation exchanges were allowed to take place for 48 h under end-over-end shaking. Then, after centrifugation (4347 g-force for 10 min at 20 °C), a few mL of the supernatant was used for VIS measurements at 580 nm (Genesys 10 UV, Thermo Scientific). After this, the pH was controlled again. pH evolution is given in the supplementary data. In addition, the exchangeable cations were subsequently analysed by ICP-OES (Optima 8300 DV, Perkin Elmer) *(Steudel and Emmerich, 2013)*. The Cu-trien concentration in the supernatant was compared with Cu-trien calibration solutions in the pH range investigated, corrected by the extinction coefficient of Cu-trien that is known to be dependent on the pH *(Ammann et al., 2005; Kaufhold and Dohrmann, 2013)*. Additional correction at pH < 6 resulting from the speciation of the Cu-trien complex *(Golub et al., 1995; Nurchi et al., 2013)* was taken into account, e.g. Cu-trien charge was 2.30, 2.04, and 2 at pH 4, 5, and 6, respectively. Measurements were carried out at room temperature (21 ± 1 °C). The CEC values are given for a total anhydrous solid after water content determination by STA up to 250 °C.

Table 2-3: Chemical composition of the major elements [wt.%] (normalized to 100%).

Sample	SiO_2	Al_2O_3	Fe_2O_3	FeO	MgO	Na_2O	CaO	K_2O	TiO_2
BC-M0.2Na	64.44	21.33	6.45	0.30	3.45	3.09	0.06	0.67	0.21
BV-M0.2Na	66.13	23.68	3.72	0.49	2.48	3.23	0.07	0.05	0.15
BS-M0.2Na	64.74	19.80	5.00	0.10	5.60	3.70	0.07	0.84	0.15
BP-M0.2Na	66.33	19.80	3.59	0.26	5.62	3.96	0.11	0.07	0.25

Results and Discussion

Mineralogical and Chemical Heterogeneity of Smectites. Na-saturated materials < 0.2 μm contained essentially dioctahedral smectites as was identified by XRD with d_{001} reflections at 12.2-12.6 Å after air-drying, which expanded to 16.8-17.1 Å with EG solvation and collapsed to 9.6-9.8 Å after heating to 375 °C and to 550 °C. The d_{060} reflections occurred at ~ 1.50 Å (Table 2-1). Identification of interstratified illite-smectite (I-Sm) phases for BS-M0.2Na (Table 2-1) was supported by 0.73% of non-exchangeable potassium, corresponding to 6 to 12% of illite with a composition intermediate between 0.55K and 0.9K per $O_{10}(OH)_2$ *(Guggenheim et al., 2006; Srodon et al., 1986)* in agreement with previous studies *(Cuadros and Linares, 1996; Rozalén et al., 2009)*. Under the assumption of an illite of $K_{0.75}(Al_{1.7}Mg_{0.3})(Si_{3.55}Al_{0.45})O_{10}(OH)_2$, the resulting interstratification has a composition of I(9%)-Sm. Discrete mica $(KAl_2(Si_3Al)O_{10}(OH)_2)$ in BC-M0.2Na was quantified up to 5.4% based on the non-exchangeable potassium content and about 2% of cristobalite (SiO_2) were identified in BV-M0.2Na.
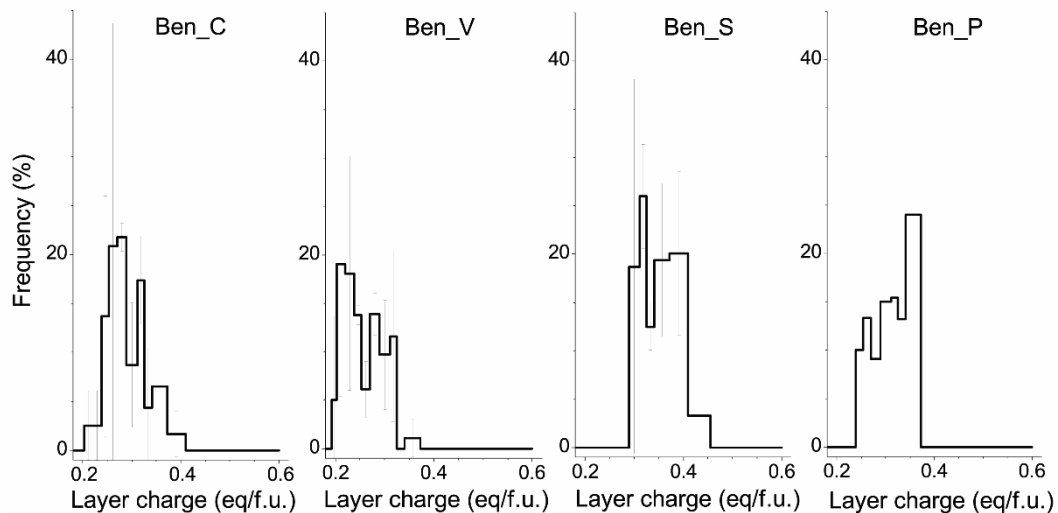
Figure 2-2: Average layer charge density distribution of Na-saturated <0.2 μm fractions with the results from (REF) for BV-M0.2Na and from (REF) for BC-MN0.2Na (33Ca), BV-M0.2Na (32Volclay), and BS-M0.2Na (28SB).

Mineralogical heterogeneity of the dioctahedral smectites is described as a function of their layer charge, octahedral distribution, iron content, and layer charge distribution (Table 2-2) *(Emmerich et al., 2009)*. Low layer charges ranging from 0.26 to 0.37 eq/f.u with a layer charge density distribution covering up to 0.2 units (Figure 2-2) were measured in agreement with previous studies *(Steudel and Emmerich, 2013; Wolters et al., 2009)* despite the influence of layer stacking during the drying process *(Lagaly, 1981)*. The layer charge distribution within the tetrahedral and octahedral sheets was first deduced from the structural formulae (Table 2-4) based on chemical analyses (Table 2-3) after impurities correction. A tetrahedral charge (ξ_T) ranging from 4% for BP-M0.2Na up to 36% for BV-M0.2Na was obtained. In the case of BS-M0.2Na, the illitic layer correction induced a decrease from 22% to 12% of the tetrahedral

charges. The Greene-Kelly test applied to the RCM samples did not reveal any re-expansion of the d_{001} peaks to 18 Å, which would be characteristic of beidellitic layers. However, slight shifts of the 001/002 and 002/004 peaks might indicate the presence of 19% to 30% of re-expandable layers (Table 2-1) *(Schultz, 1969)*. The large discrepancies from structural formula estimation found for samples with low tetrahedral charges might be attributed to non-uniform charge distribution over the layers, as was discussed by Schultz *(Schultz, 1969)*. The presence of trioctahedral domains indicated by the oversaturation in the octahedral sheet obtained from structural formula calculation *(Vogt and Köster, 1978; Wolters et al., 2009)* was not confirmed by STA measurements. Octahedral cations were distributed in a *cis-trans* vacant (*cv/tv*) man-ner, except for BV-M0.2Na. Its octahedral sheets were almost purely *cis*-vacant (*cv*) (Table 2-2). The illite layers in BS-M0.2Na, which are usually considered to be *trans*-vacant (*tv*) layers *(Drits et al., 1995)*, did not affect the classification as *cv/tv* of the smectitic layers in BS-M0.2Na.

Table 2-4: Structural formulae of Na-saturated < 0.2 μm smectites after impurities correction [mol/f.u.].

Sample	Tetrahedral cations		Octahedral cations					Interlayer cations			ξ_T	Molar mass
	Si^{4+}	Al^{3+}	Al^{3+}	Fe^{3+}	Fe^{2+}	Mg^{2+}	ΣOc	Ca^{2+}	Na^+	K^+	[%]	[g/mol]
BC-M0.2Na	3.94	0.06	1.39	0.30	0.02	0.33	2.03	0.00	0.29	0.00	20	376
BV-M0.2Na	3.91	0.09	1.60	0.17	0.03	0.23	2.03	0.00	0.25	0.00	36	372
BS-M0.2Na	3.93	0.07	1.34	0.22	0.01	0.50	2.07	0.00	0.30	0.07	22	377
BS-M0.2Na[1]	3.96	0.04	1.30	0.24	0.01	0.52	2.06	0.00	0.36	0.00	12	376
BP-M0.2Na	3.99	0.01	1.39	0.16	0.01	0.50	2.07	0.00	0.31	0.01	4	373

[1]Structural formula of smectite layers of BS-M0.2Na after deduction of illite layers.

Particle Size Distribution of Smectites. Individual particles were easily identified by coupling height and deflection images. In this way, overlapped particles or aggregates were excluded and single layer were measured (Figure 2-3). The particle shapes ranged from angular (rec-tangular or undefined) for the coarser particles (particle 3, Figure 2-3) to rounder smaller par-ticles (particles 1 and 2 in Figure 2-3). Perimeters and basal areas are parameters that can be measured directly and prevent the particle shape from being prejudged for calculation. The thickness, perimeter, and basal area were estimated statistically from a restricted number of particles (~ 40) that were considered to be sufficient for a representative overview *(Metz et al., 2005)* (Table 2-5). The thickness of the single layers was close to the expected value of 1.2 nm measured for smectites under ambient conditions, including one water layer between the particle and the substrate *(Cadene et al., 2005; Tournassat et al., 2003)*. Nevertheless, the value of 0.96 nm was used as a reference thickness of dehydrated smectite for calculation. Narrow particle size distributions for BC-M0.2Na, BS-M0.2Na, and BP-M0.2Na were observed to range from 20 to 200 nm equivalent diameter (Figure 2-4), with a mean weighted equivalent diameter of about 100 nm (Table 2-5). The particle size distribution of BV-M0.2Na, by contrast, was broader and ranged from 60 to 400 nm equivalent diameter (Figure 2-4), with a mean weighted equivalent diameter of 277 nm (Table 2-5). This was in good agreement with Cadene et al. *(Cadene et al., 2005)*. The mean weighted perimeter/basal area ratio ($\bar{R}_{P/A}$) ranged be-tween 0.024 nm^{-1} for BV-M0.2Na and 0.054-0.059 nm^{-1} for the three other materials (Table 2-5). $\bar{R}_{P/A}$ was previously measured and found to range between 0.020 and 0.023 nm^{-1} for the

material MX-80 that is related to BV-M0.2Na *(Tournassat et al., 2003)*. The total specific surface area of dispersed particles was close to 772 m^2/g with a low $a_{s,edge}$ contribution of about 1-3% (Table 2-5). The $a_{s,edge}$ of BV-M0.2Na was estimated to be around 9 m^2/g, which was close to the 8.5 m^2/g obtained for the material MX-80 *(Tournassat et al., 2003)*. BV-M0.2Na differed from the others materials by a broader particle size distribution and a higher mean particle size.

Table 2-5: Morphologic parameters of single layer distribution from AFM images and edge surface area estimation.

Sample	Thickness	Particles	$\bar{P}$	$\bar{d}^1$	$\bar{R}_{P/A}$	$a_{s,edge}$	
	[nm]	count	[nm]	[nm]	[nm^{-1}]	[m^2/g]	[%]
BC-M0.2Na	1.25 ± 0.18	79	521	118	0.054	20 ± 4	2.6 ± 0.5
BV-M0.2Na	1.22 ± 0.20	45	1242	277	0.024	9 ± 2	1.2 ± 0.3
BS-M0.2Na	1.47 ± 0.25	49	415	107	0.055	20 ± 4	2.6 ± 0.5
BP-M0.2Na	1.16 ± 0.25	35	416	101	0.059	22 ± 4	2.8 ± 0.5

[1] Equivalent mean weighted diameter calculated from the area.

Determination of the mean weighted equivalent diameter ($\bar{d}$) was used to estimate the layer stacking in dried Na-saturated powder (not shown) as well as in RCM materials (Figure 2-1). The layers per stack remained stable during lithium exchange and after the heating at 300 °C. An exception was BV-M0.2Li-300 for which the lithium exchange induced already a reduction of layer stacking, stable after heating. The reduce number of layers per stacks was reflected by an increase of $a_{s,BET}$ from 30 to 65 m^2/g. Considering the layer stacking model, the estimated layers per stack decreased from 30-60 (comparable to the 36 layers per stack estimated for SWy-2 related to BV-M0.2Na *(Le Forestier et al., 2010)*) to 12-17 after lithium exchange. For the other materials, the layers per stack were estimated to be around 6-8 (Table 2-6). The resulting $a_{s,edge}$ contribution ranged from 8 to 15%.
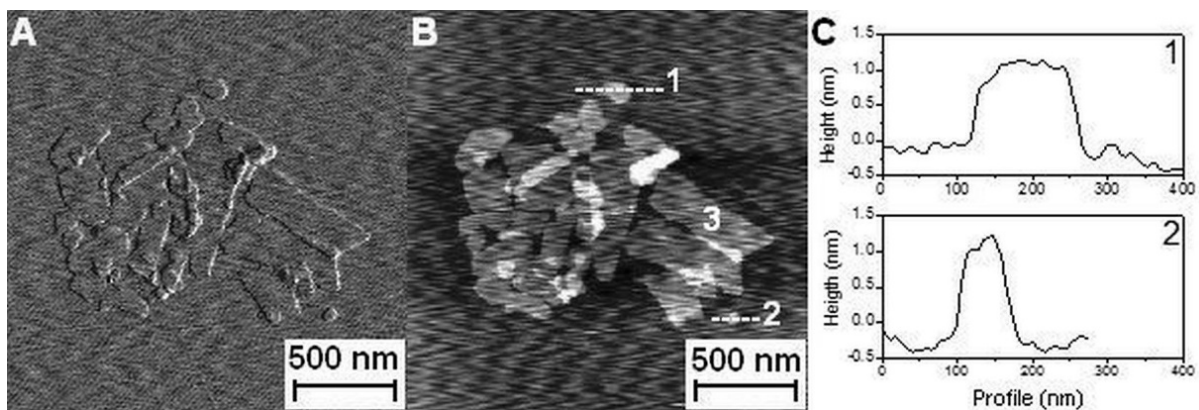
Figure 2-3: AFM images of BV-M0.2Na: Deflection (A) and height (B) images and two particle profiles (C).

Cation Exchange Behaviour. Influence of the intrinsic properties, i.e. layer charge, isomorphic substitutions, particle size, and layer stacking, on the cation exchange behaviour of the smectites was evaluated as a function of the pH.

Table 2-6: Argon gas sorption parameters, layers per stack, and edge surface area estimation of RCM materials.

Sample	$a_{s,BET}$	Micropore NLDFT				Layers per	$a_{s,edge}$
	[m²/g]	[m²/g]	[%]	[cc/g]	[%]	stack n	[%]
BC-M0.2Li-300	146	160	71	0.035	31	6-8	10-13
BV-M0.2Li-300	70	84	74	0.018	20	12-17	8-12
BS-M0.2Li-300	142	136	66	0.038	31	6-8	11-14
BP-M0.2Li-300	141	181	78	0.038	41	6-8	11-15

The CEC of the Na-saturated materials ranging from 90 to 115 cmol(+)/kg (Figure 2-5, Table 2-7) were in good agreement with previous studies *(Kaufhold and Dohrmann, 2013; Tournassat et al., 2004b)*, in which the CEC increased continuously with the pH. The heating treatment of the Li-saturated materials induced a decrease of 82 to 92% of the CEC, with a remaining CEC ranging from 7 to 16 cmol(+)/kg (Figure 2-5, Table 2-7), which is in the range of values found by Komadel et al. [67] and Skoubris et al. [68]. The reference pH was 7.1 ± 0.1 for the Na-saturated materials and around 5.4 (5.9 for BV-M0.2Li300) for the RCM corresponding to their intrinsic buffer capacity and the resulting pH during CEC measurement without pH adjustment. The amount of sodium or lithium for the Na-saturated materials and RCM materials, respectively, exceeded 93% of the CEC, which confirmed the efficiency of the homoionic exchange procedure. The amount of exchangeable cations was constant over the pH range from 4 to 9, but Si, Al and Mg were released by dissolution over the pH range (data not showed). The magnitude of CEC increase with pH was similar for Na-saturated materials and RCM materials as illustrated for BP-M0.2 in Figure 2-5. The CEC of the Na-saturated materials increased 9 cmol(+)/kg for BV-M0.2 and 12 cmol(+)/kg for BP-M0.2 (Table 2-7 between pH 4 to
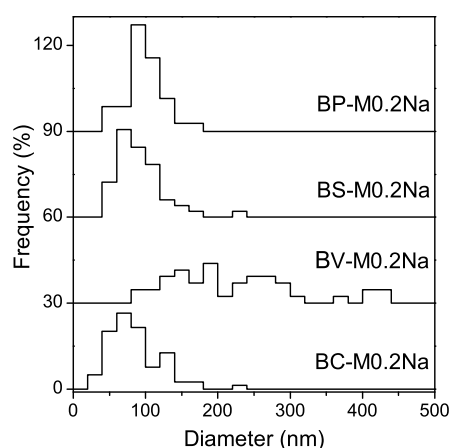
Figure 2-4: Equivalent diameter distribution from the basal area of the Na-saturated materials.

pH 9. The measurement uncertainties were set to 2% of the measured value. Comparable increase of CEC assigned to the variable charges at the edges ranging from 8 to 14 cmol(+)/kg were measured by Kaufhold and Dohrmann *(Kaufhold and Dohrmann, 2013)*.

Table 2-7: CEC_p derived from layer charge, CECNa of Na-saturated smectites measured at pH 7.1 ± 0.1, $CEC_{Na,corr}$ corrected for impurities and CEC_{RCM} measured at pH 5.4 (5.9 for BV-M0.2Li300) of RCM materials, and variable charges ($CEC_{RCM,calc}$) in cmol(+)/kg. Uncertainty of the CEC measured is estimated to amount to ± 2%

Sample	CEC_p	CEC_{Na}	$CEC_{Na,corr}$	ΔCEC_{Na} - CEC_p	$\Delta CEC_{Na,corr}$ - CEC_p	ΔCEC_{Na} pH 4-pH 9	CEC_{RCM}	$CEC_{RCM,\,calc}$
BC-M0.2	80 ± 2	90	95	10	15	10	16	11
BV-M0.2	70 ± 3	90	92	20	22	9	7	5
BS-M0.2	98 ± 2	103	112	5	14	11	16	14
BP-M0.2	86 ± 2	115	115	29	29	12	10	12

Impurities correction (5.4% mica in BC-M0.2, 2% cristobalite in BV-M0.2, and 9% of interstratified illite layers in BS-M0.2)

The point of zero net proton charge (PZNPC) *(Sposito, 1981)* or the point of zero charge at the edges ($pH_{PZC,edge}$) *(Tombacz and Szekeres, 2004)* was estimated as a function of the layer charge and the ionic strength of the electrolyte according to *(Bourg et al., 2007; Delhorme et al., 2010; Lagaly, 2006)*. The electrolyte concentration during CEC measurements was 3 mmol/L. Under this condition the $pH_{PZC,edge}$ of delaminated smectite is between pH 6 to 7 [5, 70] and between pH 5 to 6 for stacked illite layers *(Bourg et al., 2007; Delhorme et al., 2010)*. The remaining CEC of the RCM samples is comparable to stacked illite layers. Therefore, the CEC measured at pH 5.4 (5.9 for BV-M0.2Li300) results from a remaining structural charge due to an incomplete charge compensation on the external layers of the particle. An estimation of this remaining CEC ($CEC_{RCM,calc}$) (Table 2-7) based on the permanent CEC_P (Table 2-7) and the estimated layer per stacks derived from the surface measurements (Table 2-6) was in the same order of the measured CEC_{RCM}. Correlation with tetrahedral charge (Table 2-2) as commonly suggested [65] could not be confirmed. However, CEC of RCM is nearly constant at pH < 5.7 and increases with pH > 5.7 (Figure 2-5) and thus RCM might be suitable to study edge reactivity of smectites. Despite this correlation, the large difference between the measured CEC at pH 6-7 and the CEC_p of Na-saturated smectites could not be explained, yet. Therefore, the formal site densities were determined according to Tournassat et al. *(Tournassat et al., 2004a)* (

Table 2-8) as a function of $a_{s,edge}$ of each material (Table 2-5). The main sites at the edges involved in protonation/deprotonation in the pH range of 4-9 are aluminol sites ($\equiv Al\text{-}OH_n$), Al-Mg bridging sites ($\equiv AlMg\text{-}OH_n$), and Al-Si bridging sites ($\equiv SiAl\text{-}OH_n$) and, in addition, Al-Al bridging sites ($\equiv AlAl\text{-}OH_n$) at a low pH and silanol sites ($\equiv Si\text{-}OH_n$) at a high pH *(Bourg et al., 2007; Tournassat et al., 2004a)*. The formal site density for BV-M0.2 is lower than that of the other materials due to its lower $a_{s,edge}$. Variation due to isomorphic substitution in the octahedral sheet are of only slight influence [12]. The variable charges ranged from 6 to 17 cmol/kg for BV-M0.2 and from 12 to 39 cmol/kg for the other materials. The CEC measurements were consistent with these variable charge estimations between the lower and upper limits (

Table 2-8). Thus, CEC measurements provide an effective cation exchange behaviour of a certain smectite at different pH but, if applied solely, they are not appropriate to quantify the edge surface chemical reactivity. This is because of competing side reactions, such as proton

adsorption at both basal surfaces at low pH *(Amram and Ganor, 2005; Rozalén et al., 2009)* and at the edge surfaces with protonation of edge sites *(Sposito, 1981; Wanner et al., 1994)* or difficult-to-quantify clay dissolution involving the adsorption of released elements, such as Fe, Al, or Mg over the complete pH range *(Amram and Ganor, 2005; Baeyens and Bradbury, 1997; Duc et al., 2006; Rozalén et al., 2009; Rozalen et al., 2004; Tournassat et al., 2004b)* . CEC measurements combined with potentiometric titration allow modelling the clay surface reactivity *(Tournassat et al., 2004a; Tournassat et al., 2004b)*. Comparison between experimental potentiometric titration of fully delaminated Na-saturated materials and RCM materials and isolated lamella and stacked lamellae models may be used to evaluate the validity of the different models.
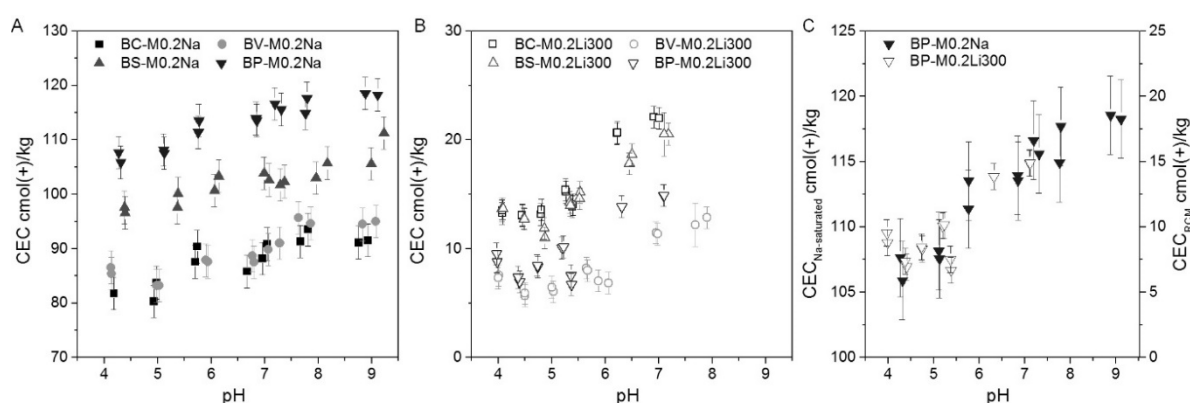
Figure 2-5: CEC as a function of Ph of Na-saturated materials (A) and RDM (B). Comparison of CECs with the same unit scale for BP-M0.2 (C).

Table 2-8: Edge site densities of dioctahedral smectites.

Surface sites / Edge site density [cmol/kg]	BC-M0.2	BV-M0.2	BS-M0.2	BP-M0.2
$\equiv$Si-OH$_n$	15.7	7.0	15.8	17.5
$\equiv$Al-OH$_n$	3.8	2.0	3.5	4.2
$\equiv$SiAl-OH$_n$	5.7	3.4	4.8	6.1
$\equiv$AlMg-OH$_n$	2.7	1.0	3.9	4.4
$\equiv$AlAl-OH$_n$	6.2	3.2	5.7	6.8
Min ($\equiv$Al-OH$_n$ + $\equiv$SiAl-OH$_n$ + $\equiv$AlMg-OH$_n$)	12	6	12	15
Max (all sites contribution)	34	17	34	39

Conclusion

A fundamental understanding of montmorillonite properties is the prerequisite for assessing the bentonite behaviour. Intrinsic properties of smectite, combined with the process parameters, modify the resulting behaviour. The influence of isomorphic substitutions was reflected by the permanent charge and resulting cation exchange capacity. The layer dimension determines edge sites properties. The widespread use of the MX-80 or SWy-1(2) as reference material could lead to some uncertainties, if structure and dimension are used as generalized

input parameters for assessment behaviour of other bentonites. Thus, comprehensive characterization of any bentonite under consideration is recommended.

2.1.1.2 Characterization and stability of bentonite dispersions with different size fractions

Introduction

High level nuclear wastes are foreseen to be placed in massive metal canisters, surrounded by a large volume of natural or compacted bentonite as engineered barrier in Swedish and Finnish repository designs *(SKB, 2010; Vieno and Ikonen, 2005)*. The role of the clay is first to stabilize the canister in case of movements in the bedrock and to seal small fractures in the vicinity of the canister. The barrier is planned to prevent corrosive elements from the surrounding, such as sulfide, thiosulfate and polythionates *(Macdonald and Sharifi-Asl, 2011)* to come in contact with the canister. In second, the barrier should retard the migration of radionuclides (RNs) present in the spent nuclear fuel in case of canister failure. Bentonite presents an excellent buffer capacity *(Karnland et al., 2006)* due to its high swelling pressure, cation exchange capacity and retention properties. It is mainly composed of montmorillonite, an Al-rich smectite, present as small particles colloidal sizes (i.e. particles of 1 nm - 1 μm in at least one dimension in dispersion *(Stumm, 1993)*). In this work, the term clay colloids refer to aggregates, consisting of stacks of several clay mineral layers. Cycles of glaciations can be expected in northern countries such as Sweden and Finland *(SKB, 2010)* over the estimated lifetime of the nuclear wastes storage (i.e. 1 million years). In the worst case scenario, a large amount of glacial melt water will be transported through fractures in the bedrock, down to repository depth and will displace the old ground water that has equilibrated with mineral surfaces for a very long time. The chemical composition of future glacial melt water is assumed to be similar to glacial melt waters of today but different from the original pore water. It can be approximated by water types of pH 8-9 and low ionic strength (IS), i.e. $5 \cdot 10^{-4}$ M in the worst case scenario cited above *(Brown, 2002)*. A decrease of the IS will increase the montmorillonite colloid stability as demonstrated in several laboratories and field experiments studies over a few months' timeframe *(Geckeis et al., 2004; Missana et al., 2003; Schäfer et al., 2012)* and also calculated from the DVLO-theory *(Liu et al., 2009b)*. A release of montmorillonite colloids from the bentonite barrier can occur in contact with glacial melt water. They can be later transported away from the barrier through the geosphere. The buffer functionality may be endangered in case of large mass loss. Furthermore, in the case of a canister failure, the transport of RNs can be enhanced, when transported by mobile montmorillonite colloids *(Möri et al., 2003)*. The colloid mobility depends strongly on physical parameters like the geometry of the fractures in the bedrock, where the fracture size distribution, the surface roughness and the surface charge are the most important characteristics *(Darbha et al., 2010; Filby et al., 2008)*. The colloid mobility is influenced as well by chemical parameters like the mineral composition of the fracture filling material (FFM) and the pore water matrix. It is also dependent on the clay aggregates properties themselves, i.e. their size heterogeneity, mineral composition and surface charge. The physico-chemical

properties of the bedrock are specific for each fracture, but a separation of particles according to their size during transport is expected in most systems. In presence of low amount of FFM (clean fracture system) but high water velocity, the flow is expected to be laminar and all the colloids will be transported more or less equally independently of their sizes *(Huber et al., 2012)*. In contrary, in presence of a large amount of FFM, the fracture will act as a porous material, where the larger particles can be transported faster as a result of size exclusion effects, sticking, clogging etc. Accordingly, the size and the stability of the clay colloids aggregates which may be detached (eroded) from the buffer are two important parameters to state on an eventual RN transport. Nevertheless those RNs being weakly bound to colloids or showing a relatively fast desorption from colloids will most likely not be carried by the montmorillonite colloids but will be adsorbed by the mineral surfaces instead *(Huber et al., 2015)*. Models of RN and clay colloid transport are currently used in safety assessments for estimating the RN transport, but presently they do not take into consideration the size heterogeneity of the clay aggregates *(Vahlund and Hermansson, 2006)*. Consequently, one may wonder whether normalized sorption coefficients (K_D) for RNs are valid expressions for quantifying RN-montmorillonite interactions, since the ratio is given for a mean particle size distribution and do not take into account polydispersity. In modelling, transport of RNs may be under- or overestimated *(Wold, 2010)*, e.g. the K_D-values are not accurate if only the smaller aggregates are transported and not the larger ones, or vice versa. An alternative may be to consider the amount of edge sites in the colloidal dispersions. With this treatment, eventual size dependent differences will be taken into account. This will be valid as long as the smaller particles are miniatures of the larger clay mineral particles, which may not be the case for nanosized particles *(Bergaya et al., 2006)*. Note that, in all cases, this approach is not adapted for RNs sorbing by cation exchange (i.e. Cs^+, Sr^+ etc.). In this work, a protocol is developed to obtain suspensions of montmorillonite aggregates with various size fractions which are further characterized (mean size, concentration, chemical composition of the dispersions). The stability of the montmorillonite aggregates present in these various suspensions is tested as actually large differences in surface structure between larger and smaller clay particles may be reflected in macroscopic properties, such as colloidal stability *(Bessho and Degueldre, 2009)*. For that purpose ions which can be present in glacial melt water (Na^+, Ca^{2+}, Mg^{2+} *(Missana et al., 2003)*) or degraded organic matter *(Bhatia et al., 2010)* are investigated. Finally, in addition to questionable normalization of sorption, i.e. the use of K_D-values in transport modelling, there is a lack of sorption and desorption kinetic data for RNs onto different size fractions of montmorillonite aggregates which should be implemented for improved safety assessments calculations *(Wold, 2010)*. This is the subject of separate studies presented in this report, see Section 2.1.2.2, presenting the RNs sorption behaviour onto the clay aggregate in the different suspensions.

Material and Methods

Clay, organic matter, chemicals, synthetic ground water. All samples are prepared with ultrapure water (Milli-Q system, 18.2 MΩ/cm resistivity) and chemicals of reagent grade. The

source of silicon was a standard solution of Si in H_2O (1000 mg/L, Spex Certiprep). The Wyoming MX-80 bentonite from American Colloid Co. is used as starting material for all experiments without any pre-treatment. The MX-80 contains approximately 82% montmorillonite with the structural formula: $Na_{0.30}(Al_{1.55}Fe_{0.21}Mg_{0.24})(Si_{3.96}Al_{0.04})O_{10}(OH)_2$, M_w = 372.6 g/mol *(Karnland et al., 2006)* and has a cation exchange capacity (CEC) of approximately 0.75 meq/g (measured according to *(Meier and Kahr, 1999)*). The fulvic acids (FA-573) used as organic matter in this study were extracted from a natural ground water (Gohy573) originating from the Gorleben site, Germany *(Wolf et al., 2004)* and subsequently purified and characterized. A detailed description can be found in *(Wolf et al., 2004)*. The elemental composition of the FA used in this work is as follows *(Wolf et al., 2004)*: C: (54.1 ± 0.1) %, H: (4.23 ± 0.08) %, O: (38.94 ± 0.04) %, N: (1.38 ± 0.02) % and S: (1.32 ± 0.01) %. The proton exchange capacity is 6.82 ± 0.04 meq/g. In this study, a small amount of FA is weighted, dispersed in NaOH and diluted in the corresponding initial clay stock dispersions as described below. The dissolved organic carbon content is measured with a TOC analyser (TOC-5000, Shimadzu). A synthetic carbonated ground water (SGW) is prepared in order to simulate a glacial melt water of low ionic strength. In the present case, we tend to the composition of the granitic groundwater coming from the Grimsel Test Site *(Geckeis et al., 2004; Möri et al., 2003)*. This is done by mixing the requested amounts of the different salts (NaOH, NaCl, $CaCl_2$, $MgCl_2$, NaF, Na_2SO_4 and $NaHCO_3$) and an aliquot of the Si standard solution in ultra-pure water. The final composition of the SGW is the following: Na^+ (28.4 mg/L, 1.2 mM), Ca^{2+} (1.49 mg/L, 0.05 mM), F^- (2.8 mg/L, 0.1 mM), Cl^- (2.64 mg/L, 0.074 mM), SO_4^{2-} (4.13 mg/L, 0.04 mM), Si (0.014 mg/L, 0.5 µM) and HCO_3^- (84 mg/L, 1.4 mM). The ionic strength is $1.6 \cdot 10^{-3}$ M and the pH is 8.4 ± 0.1.

Fractionation by sequential and direct (ultra-)centrifugation. 50 g of unpurified MX-80 bentonite is added to 5 L SGW (10 g clay/L). The dispersion is regularly stirred during one day and then let to settle during three days in order to remove the larger clay fractions and accessory mineral phases. After sedimentation the top 4 L are isolated. It constitutes the colloidal dispersion S0. Sequential centrifugation (Thermo Scientific Centrifuge 2.0, with 50 mL PE centrifugation tubes, VWR, Germany) or ultra-centrifugation (Beckmann Ultracentrifuge, XL90, with 100 mL Quick-seal centrifuge tubes, Beckmann) are then performed at increasing speeds and times to obtain various clay colloidal dispersions, starting from the supernatant S0 similarly to the protocol presented in *(Perret et al., 1994)*. The resulting supernatant after the first centrifugation step corresponds to the colloidal dispersion S1. Thereafter, the sequential centrifugation is repeated three times, where the last centrifugation step is an ultra-centrifugation, leading to the supernatant S3.5. The corresponding centrifugation times and speeds are summarized in Table 2-9. In addition to the sequential centrifugation, and for comparison, two supernatants (noted with the prefix UC and UC, FA) are collected directly from the supernatant S0 after only one ultra-centrifugation step, using the same speed and time as the ones used to obtain the dispersion S3.5. For that purpose, an initial supernatant S0 is collected after 1 d stirring and 3 d sedimentation as described above, in presence (UC, FA) or absence (UC) of 11.8 mg/L FA. Truly dissolved concentrations of Si, Al, Ca, Mg and Fe in equilibrium with clay minerals are determined after a stronger centrifugation step (1h at 235 000 g). To determine the amount of

each element in the clay particles, the truly dissolved concentration is subtracted from the total concentration measured in the dispersion.

Table 2-9: Conditions for fractionation of the clay dispersions and clay aggregate sizes expected in the supernatants (Si). (C: centrifugation; UC: ultracentrifugation)

Dispersion	Conditions of separation	Size expected in the ith
S0	3 days sedimentation	$0 \leq S0 \leq 1000$
S1	C: 30 min (S0) at 313 g	$0 \leq S1 \leq 450$
S2	C: 1 h (S1) at 700 g	$0 \leq S2 \leq 200$
S3	C: 4 h (S2) at 1200 g	$0 \leq S3 \leq 70$
S3.5	UC: 30 min (S3) at 26 000 g	$0 \leq S3.5 \leq 50$
S3.5UC	UC: 30 min (S0) at 26 000 ga	$0 \leq S3.5UC \leq 50$
S3.5UC, FA	UC: 30 min (S0) at 26 000 ga	$0 \leq S3.5UC, FA \leq 50$

a: one step ultra-centrifugation from a colloidal dispersion S0 obtained after stirring and sedimentation of a MX80 dispersion at 10 g/L in presence or absence of 11.8 mg/L FA.

The pH of all isolated supernatants is measured over a four months' time period and remains stable at 9.4 ± 0.2. All the collected supernatants and solid residues are stored at +4°C in darkness before characterization and use in stability studies.

Ion and clay particle concentrations determination. The element compositions are determined in all dispersions over time by Ion Chromatography (IC, ICS-3000) and ICP-OES (Optima 2000 DV, PerkinElmer). The samples are acidified before the ICP-OES measurements in 2% HNO_3 (Merck, ultrapure) plus a drop of HF (Merck, suprapure, 48%).

Mineral phase composition. Mineral phases composing the clay particle dispersions and the solid residues are determined by XRD. XRD data are collected on residuals and supernatants prepared as oriented samples obtained by drying on sample holders (low background Si wafers). The residuals are prepared by dilution of the solid-gel like dispersions in ultra-pure water. The SGW alone is also analysed as a reference to identify any phase that could precipitate in the supernatants or residuals upon drying. X-ray diffractograms for all samples (raw MX-80 and the supernatants) are also collected after saturation with ethylene glycol. Powder diffractograms are recorded with a D8 Advance (Bruker) diffractometer (Cu K_α radiation) equipped with an energy dispersive detector (Sol-X). The phases are identified with the DIFFRAC.EVA version 2.0 software (Bruker) by comparison with the JCPDS 2 database.

Content of organic matter. The total amount of organic carbon in the dispersions prepared in presence of FA is measured with a TOC analyser (TOC-5000, Shimadzu). A change in the FA concentration is obtained after ultra-centrifugation (final [FA] = 8.3 mg/L compared to 11.8 mg/L initially). This result indicates that a third of the organic matter might be associated with the clay aggregates while most of the FA (two thirds) remains in the dispersion under the present experimental conditions, as expected for these small-sized molecules and at the present pH.

Size distribution measurements. The size distributions of montmorillonite aggregates in all dispersions are determined by Photon Correlation Spectroscopy (PCS, homodyne single beam

ZetaPlus System equipped with a 50 mW solid-state laser emitting at 632 nm, Brookhaven Inc, USA) and Asymmetric Flow Field-Flow Fractionation system (AsFlFFF, HRFFF 10.000 AF4, Postnova Analytics, Landsberg, Germany) coupled to a UV-Vis. detector (Lambda Max LC Modell 481, Waters, Milford, USA) and an Inductively-Coupled Plasma-Mass Spectrometer (ICP-MS, X–Series2, Thermo Scientific, Germany). AsFlFFF/UV-Vis./MALLS/ICP-MS has previously been used for characterization of natural or synthetic clays colloids *(Bouby et al., 2012; Bouby et al., 2011; Bouby et al., 2004; Finck et al., 2012; Plaschke et al., 2001)*. In this study, the clay dispersions obtained after fractionation $(Si)_{i=0-3.5}$ are diluted to ~20 mg/L clay particles in SGW before injection into the system. Details on the equipment, the fractionation conditions and the calibration are given elsewhere (supporting information file of a recent paper *(Norrfors et al., 2015)* available here, http://www.sciencedirect.com/science/article/pii/S0169131715002070). For the PCS measurements, the clay dispersions are diluted to 10 mg/L in a disposable plastic cuvette and measured over 5 runs consisting of 10 measurements of 15 s each, i.e. 50 measurements, for determination of mean hydrodynamic diameters.

Clay particle stability studies. Stability studies are performed using PCS-measurements according to the experimental protocol described in *(Behrens et al., 2000; Czigány et al., 2005; Holthoff et al., 1996; Kretzschmar et al., 1998)*. The particle stability ratios (W) are calculated from the initial agglomeration rates. The stability ratio is defined as the ratio between the fast agglomeration rate to the measured agglomeration rate in the present sample (Equation 1):

$$W = \frac{\left[\dfrac{\left(\dfrac{dr_h}{dt}\right)_{t\to 0}}{C}\right]^{(f)}}{\left[\dfrac{\left(\dfrac{dr_h}{dt}\right)_{t\to 0}}{C}\right]} \qquad\qquad \textbf{Equation 1}$$

where r_h is the hydrodynamic radius (nm), t the time (s) and C the particle concentration (mg/L), the suffix f represents the fast agglomeration rate. Equation 1 is derived from the following Equation 2 and Equation 3:

$$\left(\frac{dr_h}{dt}\right)_{t\to 0} = \beta k C \qquad\qquad \textbf{Equation 2}$$

$$W = \frac{k^{(f)}}{k} = \frac{1}{\alpha} \qquad\qquad \textbf{Equation 3}$$

where ß is an optical factor (depending on the scattering angle, the wavelength of the light and the particle radius), k is the agglomeration rate and α is the particle-particle attachment efficiency and so-called the sticking probability. Consequently, W approaches 1 when the particles

are unstable under the chemical conditions tested, while for stable dispersions, W tends to go to infinity (set arbitrarily to 10^1-10^2 values in our experiments to fit into the graphs). In this study, W is determined at pH 7, while the ionic strength was varied between 0.01 and 3 M by using the electrolytes NaCl, $CaCl_2$ or $MgCl_2$. In addition, experiments in presence or absence of FA are performed, since FA is known to stabilize montmorillonite particles *(Furukawa and Watkins, 2012)*. The clay particle concentration is fixed to 10 mg/L by prior dilution throughout all measurements, and all the supernatants listed in Table 2-9 are studied. The initial intensity-weighted hydrodynamic mean diameter is measured first during 45 s before addition of the electrolyte to the dispersion. Thereafter, the evolution of the particle hydrodynamic diameter is monitored, after affecting the dispersion by simultaneous addition of concentrated electrolyte aliquots (NaCl, $CaCl_2$ or $MgCl_2$) and NaOH to reach the desired chemical conditions. All samples are measured up to between 20 and 40 min after addition of the electrolyte, with measurements of 15 s each. To investigate the effects of addition of FA, a final concentration of 10.2 mg FA/L is added to all clay dispersions. Thereafter, 0.1 M $CaCl_2$ is added to the dispersions and the results are compared to measurements in absence of FA. As the pH cannot be monitored at the same time in the cuvette used for the PCS measurement, it is measured in parallel in a second cuvette with a dispersion of identical composition. The initial agglomeration rate is determined by fitting a second-order polynomial to the experimental data, using the first 15-35 data points of each set of data. The initial agglomeration rates are then compared and normalized to the fastest initial agglomeration rate (determined for each electrolyte at 3M IS) for each colloidal fraction to obtain the corresponding W value.

Results and Discussion

Ion and colloid concentrations. The concentrations of all analysed elements are presented in Table 2-10, where the mean values obtained from several measurements are given. The clay colloid concentrations ([Coll.]) are calculated from Al-concentrations according to the theoretical structural formula *(Karnland et al., 2006)*. The molar ratios of the different elements are calculated from the ICP-OES- and IC-results and may be compared to the theoretical values based on the assumed stoichiometry. The montmorillonite colloid concentration decreases with the number of sequential centrifugation steps, for increasing centrifugation speed and time (Table 2-10), as expected. The particles consist of montmorillonite in all dispersions considering the fair agreement between the experimental and theoretical Si/Al, Al/Mg, Al/Fe and Mg/Fe (not shown) mole ratios. The free aqueous concentrations obtained after centrifugation at 235´000 g (when all clay mineral particles are removed) are subtracted to accurately determine the experimental molar element ratios. The calcium concentrations in the dispersions decrease with increasing numbers of centrifugation steps similar to the decrease of colloid concentrations (Table 2-10). This suggests its association to the clay aggregates, possibly due to ion exchange binding at the permanently charged basal plane. Furthermore, even though calcium does not appear in the theoretical formula, it is known that unpurified MX80 bentonite contains calcium based accessory minerals, like calcite *(Bradbury and Baeyens, 2002; Karnland et al., 2006; Vuorinen and Snellman, 1998)*. The results show a direct release of several elements

Table 2-10: Element and colloid concentrations in the clay colloidal dispersions measured by ICP-OES and IC; colloidal fraction distributions calculated from the mean concentration of four main and minor clay constituents (Si, Al, Mg, and Fe): amount of colloids recovered in the dispersions (%) compared to the initial colloidal concentration in S0. *: amount of stable colloids in the dispersions after letting settle the dispersions during 2 months without any shaking. The elemental mole ratios are corrected by the free aqueous concentrations determined after the strongest ultracentrifugation, which are $7.5 \cdot 10^{-5}$ M Si, $4.1 \cdot 10^{-6}$ M Mg, $7.2 \cdot 10^{-7}$ M Fe, $3.7 \cdot 10^{-6}$ M Al and $8.5 \cdot 10^{-6}$ M Ca.

Dispersion	[Coll.] mg/L	[Al] mg/L	[Mg] mg/L	[Si] mg/L	[Fe] mg/L	[Ca] mg/L	[Na] mg/L	[SO4] mg/L	[Cl] mg/L
S0	1127 ± 170	133 ± 20	20 ± 2	382 ± 110	32 ± 2	8.6 ± 0.5	87 ± 1	37 ± 3	5 ± 1
S1	746 ± 68	88 ± 8	13.6 ± 0.4	252 ± 70	21.4 ± 0.6	5.7 ± 0.1	82 ± 2	37 ± 3	3.9 ± 0.3
S2	551 ± 34	65 ± 4	9.9 ± 0.6	178 ± 46	15 ± 2	4.0 ± 0.2	76 ± 2	37 ± 4	3.9 ± 0.4
S3	280 ± 26	33 ± 3	5.5 ± 0.2	99 ± 25	8 ± 1	2.5	77	37 ± 4	3.8 ± 0.2
S3.5	96 ± 6	11.3 ± 0.6	1.9 ± 0.1	40 ± 18	2.7 ± 0.1	1.1	73	36	3.6
S3.5UC	90 ± 6	10.6 ± 0.6	1.8 ± 0.1	40 ± 18	2.8 ± 0.3	1.0	74	36	4.7
S3.5UC, FA	125 ± 3	14.7 ± 0.3	2.5 ± 0.1	51 ± 18	3.5 ± 0.1	1.6	75	36	4.8
SGW						1.6	28	3.2	2.9

Dispersion	Si/Al mole ratio	Al/Mg mole ratio	Al/Fe mole ratio	Al/Ca mole ratio	Recovered colloids (%)
S0	2.7	6.0	8.6	23.9	100 ± 0 (43 ± 1*)
S1	2.7	5.9	8.5	24.4	67 ± 4 (47 ± 2*)
S2	2.6	6.0	9.0	26.4	48 ± 5 (43 ± 2*)
S3	2.8	5.5	8.6	22.7	25 ± 2 (22 ± 1*)
S3.5	3.0	5.6	8.7	22.0	9.4 ± 0.1
S3.5UC	3.2	5.6	7.9	23.8	9.0 ± 0.2
S3.5UC, FA	3.1	5.5	8.7	17.3	12.1 ± 0.1
Theoretical values	2.49	6.62	7.57		

from the unpurified bentonite to the SGW (Table 2-10). A drastic increase of sodium and sulfate and, to a lower extend, fluoride and chloride is observed. This is consistent with literature data *(Bradbury and Baeyens, 2002; Vuorinen and Snellman, 1998)*. This can be explained, altogether, by the presence of NaCl (1.35 mmol/kg), fluorite (CaF_2), gypsum ($CaSO_4$) and celestite ($SrSO_4$) in the unpurified MX80 *(Bradbury and Baeyens, 2002; Vuorinen and Snellman, 1998)*. The dissolution of NaCl from the unpurified starting material cannot explain alone the large increase of sodium concentration in the supernatants. In addition, no increase in Ca concentration is observed (the concentration of Sr is not measured). Cation exchange reactions, where divalent cations (Ca^{2+}/Sr^{2+}) are favoured over monovalent ones (Na^+), may explain why the Na release is enhanced and no variation in Ca concentration is observed *(Gaucher et al., 2009)*. Another process involving dissolution of pyrite, which is found in the XRD analysis (not

shown), can explain the release of sulfate. However, this should be accompanied by a drop of pH. Thus, it is not considered as the most important process.

Colloidal distribution in the montmorillonite fractions and long-term stability of the dispersions. The mean clay colloidal concentrations after each centrifugation are calculated from the concentrations obtained for the four main and minor montmorillonite constituents (Si, Al, Mg, and Fe). They are compared to the initial concentration of colloids, which allows determining the colloidal recoveries, Table 2-10. From the total amount of colloids initially present in S0, approx. 9 % remain in the dispersion S3.5 (Table 2-10) which is the dispersion obtained at the last fractionation step after using 26 000 g ultra-centrifugation. The similarity of the results obtained after a single ultra-centrifugation step (S3.5^{UC}, 9.0 ± 0.2 %) is noticeable. A slightly higher recovery of clay colloids is obtained in presence of fulvic acids (S3.5^{UC,FA}, 12.1 ± 0.1 %), which indicates that the negatively charged FA may have stabilized a part of the montmorillonite colloids initially present in dispersion *(Furukawa and Watkins, 2012; Kretzschmar et al., 1998)*. To determine the long-term stability of the dispersions, the same analyses were performed 2 months later, without any shaking during that time or prior to the sampling. It is found that not all dispersions are stable over time. This is particularly true for the dispersions S0 and S1 as indicated by the percentage of colloids recovered after 2 months (Table 2-10, marked with *) showing that 57 % and 26 % of the clay colloids, respectively, have sedimented during this time period. This indicates that these dispersions contain various sizes fractions, from large to smaller clay aggregates, as expected from the sequential separation protocol.

Mineral phase composition. The as-received material, MX-80, consists mainly of montmorillonite, as indicated by the X-ray diffractogram (not shown). Accessory minerals are present in the unpurified bentonite such as quartz, cristobalite and mica, as well as trace amounts of albite, feldspar and pyrite. No attempt was made to quantify their content. This bentonite composition agrees well with reported data *(Hu et al., 2009)*. The supernatants are analyzed after each fractionation step Table 2-11. Obviously, the accessory phases settled down during the first fractionation step resulting in that cristobalite is detected only in the first sample and that quartz can be detected only in S0. All samples exhibit intense reflections at 12.2–14.6 Å (7.2–6.0° 2θ) and ~3.14 Å (28.6° 2θ) corresponding to 001 and 004 reflections of montmorillonite. The 001 reflection or basal spacing (i.e. d(001)), which corresponds to the c dimension of the elemental unit cell, is dependent on the hydration state *(Ferrage et al., 2005; Meunier, 2005)*. In this study, all supernatants have a basal spacing corresponding to the presence of one (12.2 Å) and two water molecules (14.6 Å) in the interlayer. The clay interlayer hydration state depends on the layer charge and the ambient relative humidity, not on the fractionation procedure. All samples also exhibit less intense 00l reflections typical of clay minerals, such as 002 and 006. All suspended particles in supernatants have a similar mineralogical composition, except S0, S1 and S2 that contain cristobalite and S0 that contains additionally trace amount of quartz. Finally, only halite (NaCl) and Na_2CO_3 could be detected in SGW meaning that these phases crystallized upon drying. Halite could be detected in some supernatants. All superna-

tants and residuals exhibit similar basal spacing after saturation with ethylene glycol. The expansion to 17.0 ± 0.2 Å for d(*001*) is typical of smectite swelling, and thus consistent with montmorillonite being the main component of MX-80.
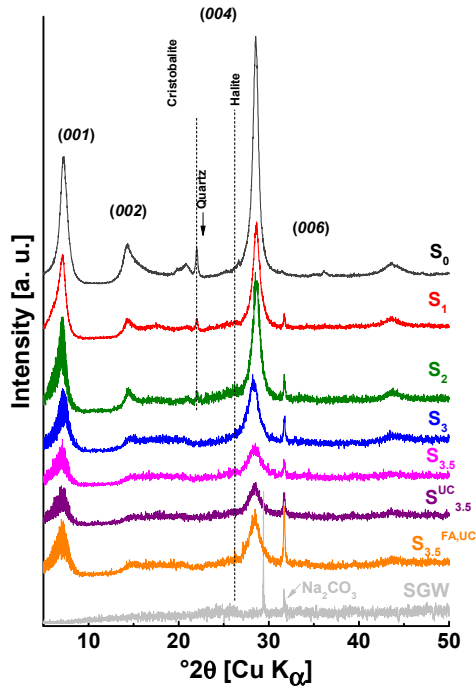
Figure 2-6: X-ray diffractograms for all supernatants right obtained by fractionation. The similarities imply a similar structure of the montmorillonite in the different suspensions. In addition, a decrease in accessory minerals with the number of centrifugation steps is seen. The montmorillonite 00*l* planes are indicated in brackets.

Clay aggregate size distribution measurements – AsFlFFF. The Al-data obtained from the AsFlFFF/ICP-MS-measurements are used as a clay indicator, since aluminium is one of the main components of montmorillonite. All Al-ICP-MS data are presented in Figure 2-7 after transformation of fractograms in mass versus size by using 1) the mass calibration method (Figure 2-7a) as developed before in previous studies *(Bouby et al., 2008)* and 2) the size calibration (Figure 2-7b), according to *(Schimpf et al., 2000)*. At a first look, a broad size distribution is obtained for each dispersion, ranging from 10 up to 275 nm. Some shoulders are clearly visible in the fractograms, indicating the presence of different size fractions in the dispersions. A separation into different well-resolved size fractions is not achieved due to the conditions selected for the AsFlFFF measurements. Nevertheless, the fractograms show clearly that the mean size of the aggregates in the dispersions is decreasing with the number of fractionation steps. This is clearly evidenced by the significant variation of the fractogram maxima and the mean sizes of the different colloidal dispersions (Figure 2-7 and Table 2-11).
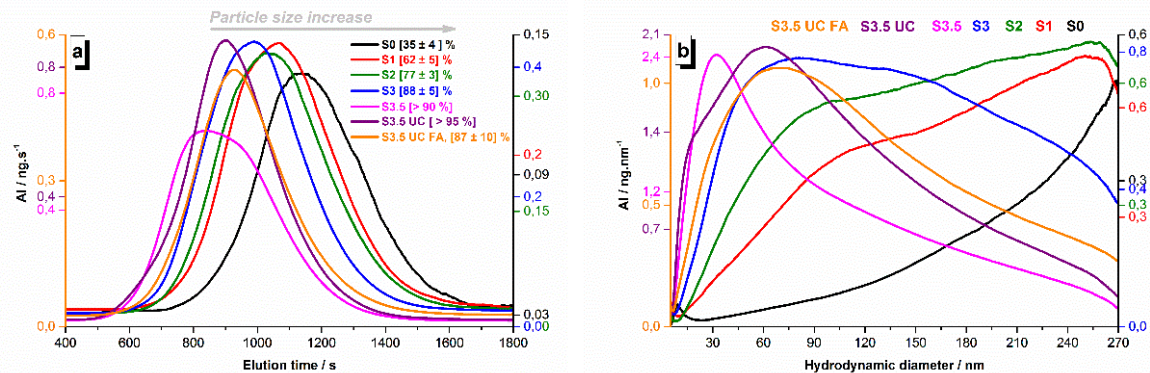
Figure 2-7: Al-ICP-MS fractograms obtained after injection (100 µL) of the different clay dispersions, all diluted to 20 mg/L clay prior to injection. a: fractograms transformed using the mass concentration calibration as a function of elution time *(Bouby et al., 2008)*. b: fractograms further transformed by using the size calibration *(Schimpf et al., 2000)*. The percentage in bracket indicates the colloid recovery in the measurements. These are all smoothed data and a mean result of two measurements.

The size distributions of the dispersions S0 to S3.5 are still broad as indicated by a rather slight decrease of the half-width. The mean clay aggregate sizes obtained in the dispersions is higher than expected (Table 2-9), especially for the dispersions where the smallest size is expected, i.e. in S3 and all S3.5 dispersions. The reason may be an incomplete sedimentation during the centrifugation by assuming a spherical shape of the particles in the Stokes' law calculation when the particle shape is of high importance *(Kunkel, 1948)*. The colloid recovery for each AsFlFFF-measurement is indicated in brackets in the legend in Figure 2-7a and in Table 2-11. It helps to understand the results. The low recoveries observed after injections of the suspensions S0 to S2 are likely due to a loss of particles in the AsFlFFF-channel due to an irreversible attachment of notably larger sized aggregates to the membrane during the fractionation process. Especially for the dispersions S0 and S1 it indicates the presence of large aggregates. This is in agreement with the slow sedimentation process observed in the unstirred dispersions S0 and S1 over time (Table 2-10). The recovery increases significantly with higher centrifugation forces, especially for the dispersions obtained after the ultra-centrifugation step (S3.5 and S3.5^{UC}).

Table 2-11: Peak maxima and mean aggregate sizes of the dispersions obtained from AsFlFFF-/ICP-MS measurements with the corresponding mean volume (V)-weighted sizes determined from PCS analysis from the multimodal size distribution (MSD). The colloid recovery in the AsFlFFF-measurements increases with decreasing sizes. d_T/d_S: equivalent spherical diameter (ESD) ratios, where d_T is the ESD for a translating disc-shaped particle determined by PCS (mean volume-weighted value, PCS_V) and d_S is the equivalent Stokes' spherical diameter for a sedimenting particle determined by AsFlFFF (mean value).

| Sample | AsFlFFF | | | PCS | | Mean (nm) | | |
	Mode (nm)	Half-width	Recovery (%)	Average count rate (kcps)	PCS_V (dT) (MSD)	AsFlFFF (dS)	dT/dS
S0	264 ± 9	64 ± 47	35 ± 4	118 ± 7	962 ± 225	229 ± 5	4.20
S1	243 ± 28	183 ± 24	62 ± 5	87 ± 2	610 ± 57	198 ± 13	3.07
S2	255 ± 21	217 ± 4	77 ± 3	53 ± 1	337 ± 29	189 ± 7	1.78
S3	80 ± 5	232 ± 18	88 ± 5	37 ± 1	186 ± 64	151 ± 14	1.23
S3.5	33 ± 3	83 ± 15	> 90	20 ± 1	172 ± 49	84 ± 8	2.06
S3.5UC	61 ± 6	142 ± 12	> 95	25 ± 1	167 ± 50	95 ± 13	1.76
S3.5UC, FA	70 ± 6	167 ± 1	87 ± 10	29 ± 1	143 ± 43	124 ± 24	1.16

PCS. To complement the AsFlFFF analysis, the dispersions are monitored by PCS after dilution to 10 mg/L clay. The results of the PCS analyses are presented in Table 2-11. The table presents the average count rates (in kilo counts per second (kcps)) which clearly decrease for centrifugation steps with higher rotation rates, even though the colloid mass concentrations are the same. Since the scattered intensity is highly dependent on the particle size, this is in line with the size variations seen in the AsFlFFF-measurements (Table 2-11). The corresponding values for the mean diameters of the clay aggregates are given as volume-weighted (PCS_V) in Table 2-11 as obtained from the measurements by considering the multimodal size distribution using the Non-Negatively constrained Least Squares (NNLS) algorithm to fit the data *(Bro and De Jong, 1997)*. The volume-weighted diameter values (PCS_V) are those which can be compared directly with the AsFlFFF data. Looking into Table 2-11, the results are comparable. The differences are explained by losses of large particles in the AsFlFFF channel (especially for samples S0 and S1) and by recalling that the PCS preferentially detect larger sized entities. Several techniques have to be used to draw a more realistic description of a natural or synthetic sample, containing particles of irregular shapes, especially clay nanoparticles *(Beckett et al., 1997; Bowen, 2002; Bowen et al., 2002; Cadene et al., 2005; Gallego-Urrea et al., 2014; Gantenbein et al., 2011; Plaschke et al., 2001; Veghte and Freedman, 2014)*. Following the development of *(Jennings and Parslow, 1988)* extended by e.g. *(Bowen et al., 2002)*, *(Pabst and Berthold, 2007)* and *(Gantenbein et al., 2011)*, more information can be obtained from the AsFlFFF and PCS data. Whatever the equipment used, the dimensions obtained are equivalent sphere diameters (ESD) i.e. the diameters of spheres that would behave the same as the particles in the sample, as a function of the method used. The ESD describes a 3-dimensional

object with only one number. Flow FFF provides the Stokes' diameter d_S *(Schimpf et al., 2000)*. The PCS gives access to the equivalent diameter from frictional translatory diffusion data, d_T *(Jennings and Parslow, 1988)*. Except for spherical particles, one cannot expect the derived ESD to be identical from the two techniques as different physical phenomena are the basis of the measurements. This is presently an advantage as no identical results reveal the non-sphericity of the particles to be analysed and is used to measure it. This is developed in the following with the ESD values (d_S) obtained with the AsFlFFF and the ESD values (d_T) obtained with the PCS. According to Jennings *(Jennings, 1993)*, the ESD values from the AsFlFFF (d_S) and PCS (d_T) are related to the mean clay axial ratio (ρ) of the aggregates in each dispersions which is defined as the aggregate surface diameter to thickness ratio. In previous works *(Jennings, 1993; Jennings and Parslow, 1988)*, the mathematical expressions of the equivalent spherical diameter (ESD) are given as a function of the axial ratio (ρ) according to the analytical method used for its determination. The equations are given in general and for two limiting geometry cases, i.e. the rod and the disc, to which the clay aggregate geometry may refer. The ESD expressions are the following *(Jennings and Parslow, 1988)* (Equation 4 and Equation 5):

$$\frac{d_T}{\delta} = \frac{\sqrt{\rho^2 - 1}}{\rho \cdot \arctan\left(\sqrt{\rho^2 - 1}\right)} \qquad \textbf{Equation 4}$$

$$\frac{d_S}{\delta} = \sqrt{\frac{\arctan\left(\sqrt{\rho^2 - 1}\right)}{\sqrt{\rho^2 - 1}}} \qquad \textbf{Equation 5}$$

where $\rho = \delta/t$ is the axial ratio of the disc-shaped particle, with δ being the surface diameter of the disc-shaped particle and t its thickness. Inversely, for a given particle, the ratio of the two ESD expressions may be used *a posteriori* to evaluate the axial or aspect ratio (ρ) of the particle and thus to obtain the value of δ and t, if the clay aggregate is approximated by a disc of diameter δ and thickness t. In the present work, the ratio d_T/d_S correspond to the ratio of the ESD determined by AsFlFFF (d_S) and PCS (d_T) (volume-weighted mean value, PCS$_v$). The calculated d_T/d_S from the experimental mean diameters are presented in Table 2-11. We can presently only propose a graphical solution. The theoretical curve $d_T/d_S = f(\rho)$ obtained from Equation 4 and Equation 5 is plotted in Figure 2-8 and is used to deduce the axial ratio (ρ) for each clay colloid dispersion reported in Table 2-11.
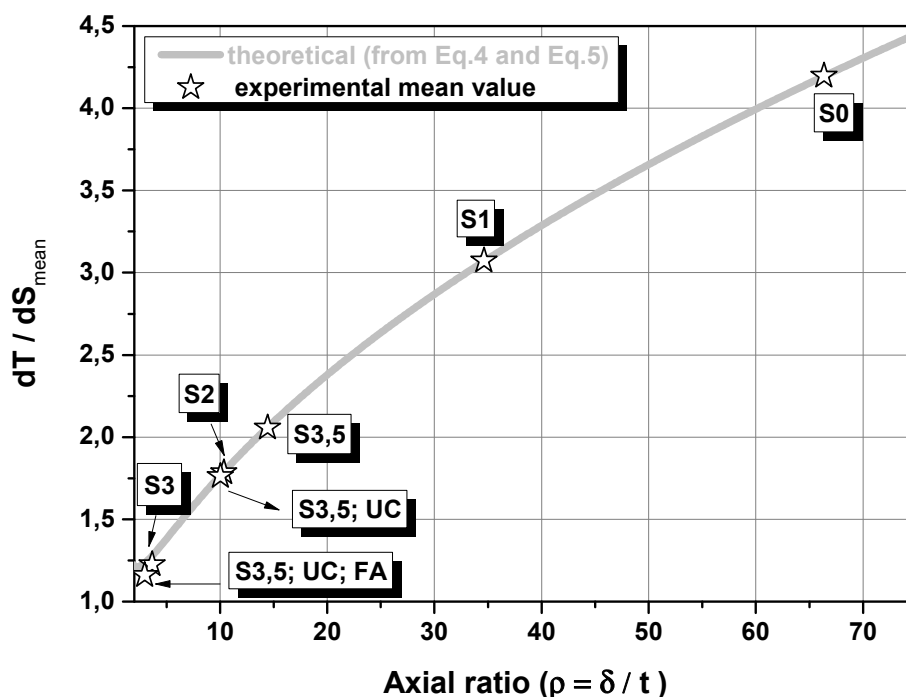
Figure 2-8: Theoretical d_T/d_S-ratio values calculated as a function of the axial ratio (grey line) using equations (4) and (5). The d_T/d_S-ratio values determined from the experimental mean PCS and AsFlFFF ESD data are reported for each dispersion. *A posteriori*, the corresponding axial ratio is obtained and presented in Table 2-12.

Obviously, $\rho > 1$ for each dispersion as expected for clay aggregates having a disc-shaped geometry. Interestingly, the ρ-values are decreasing with increasing fractionation steps from ~35 (S1) down to ~3.7 (S3). (Note: due to the low AsFlFFF recovery, the ρ-value obtained for S0 (~66) is not thought to reflect the reality). Once ρ-values are known for each dispersion, one can back-calculate the corresponding mean surface diameter, δ, and thickness, t, by using Equation 4 and Equation 5. The number of clay layers is calculated by taking 1.3 nm as the thickness of one single clay mineral layer (basal spacing) obtained by XRD results and according to *(Meunier, 2005)*. The results are summarized in Table 2-12 and the reported dimensions of the clay aggregates agree with literature data *(Bergaya et al., 2006; Bouby et al., 2011; Hauser et al., 2002; Missana et al., 2003; Plaschke et al., 2001; Schramm and Kwak, 1982; Sposito, 1992; Tournassat et al., 2011; Tournassat et al., 2003)*. The aspect ratio values are consistent with previous work *(Ali and Bandyopadhyay, 2013; Cadene et al., 2005; Gélinas and Vidal, 2010; Plaschke et al., 2001; Tournassat et al., 2011; Tournassat et al., 2003; Veghte and Freedman, 2014; Weber et al., 2014)*. A raw evaluation of the AsFlFFF/MALLS data according to *(Baalousha et al., 2005; Baalousha et al., 2006; Kammer et al., 2005)* allows to compare the hydrodynamic (R_h) versus gyration (R_g) radius. The corresponding ratio (R_g/R_h), called the shape factor, varies consistently in the range [1.5-4] for the present measurements

as it equals to 1 for spherical particles but increases as soon as the particles deviate from a spherical shape as supposed for the present montmorillonite aggregates.

Table 2-12: Mean disc surface diameters (δ) and number of layers calculated from PCS and AsFlFFF mean equivalent sphere diameters (ESD) and the mathematical equations 4 and 5, according to *(Jennings and Parslow, 1988)* for the clay aggregates. The number of layers is calculated by taking 1.3 nm as the thickness, t, of one clay sheet, according to XRD results when considering one water layer. Estimation of the mean number of edge sites for each clay dispersion from PCS- and AsFlFFF-data. The perimeter of a clay stack is noted as P and is calculated by using the clay aggregate disc diameter δ. The clay disc area (A) is calculated by using δ as the mean diameter of the clay aggregate.

Sample	Axial ratio $\rho = \delta/t$	PCS dT/δ	AsFlFFF dS/δ	δ (disc Ø; nm)	t (disc thickness; nm)	Number of layers
S0	66.3	0.643	0.226	1496	23	17
S1	34.6	0.648	0.325	940	27	21
S2	10.3	0.675	0.449	500	48	37
S3	3.7	0.743	0.546	250	68	52
S3.5	14.4	0.664	0.303	258	18	14
S3.5UC	10.0	0.676	0.385	246	25	19
S3.5UC,FA	3.0	0.767	0.546	187	63	48

Sample	Ratio (P/A) nm^{-1}	nAl mmol/kg	nSi mmol/kg	nTot mmol/kg
S0	0.0027	4.9	6.3	11.2
S1	0.0042	7.8	10.0	17.8
S2	0.0080	14.7	18.8	33.5
S3	0.0161	29.4	37.6	67.0
S3.5	0.0152	28.4	36.3	64.7
S3.5UC	0.0162	29.8	38.1	67.9
S3.5UC,FA	0.0214	39.3	50.2	89.5

For both measurement techniques used in this study, the ESDs are found smaller than the true dimension, δ, as expected *(Jennings and Parslow, 1988)*. From S0 to S3, the surface diameter, δ, is significantly decreasing, while the thickness, t, increases. The results can be considered as partly representative of the complete samples due to the low recoveries in the AsFlFFF-measurements but this remains true even if one considers only the dispersions where ≥ 50% of the mass is recovered (S1 and smaller). The difference between the dispersion S3 and S3.5 appears only in the thickness of the clay aggregates. As expected, comparable results are obtained for the dispersions S3.5 and S3.5[UC]. Interestingly, the thickness, and thus number of clay sheets, appears slightly higher in presence of FA during the fractionation, which may indicate that the presence of FA could stabilize thicker clay aggregates, i.e. maintain a larger number of stacked clay mineral layers together. In conclusion, dispersions of clay aggregates have been obtained by using the fractionation protocol described above which leads to some still broad but decreasing particle size distributions. Assimilating the clay aggregates to discs of surface diameter δ and thickness t, the results indicate the presence of aggregates with

mean surface diameters ranging from ~245 nm up to 1500 nm and with mean thicknesses ranging from ~18 up to 70 nm (~14 to 52 clay layers). The presence of FA during the fractionation allows to isolate clay aggregates with a surface diameter of ~190 nm, which present a slightly larger thickness (~63 nm) than those obtained under the same fractionation conditions in absence of FA. The use of other microscopy techniques like AFM will advantageously complement the present investigations. Finally, estimations of the mean number of edge sites in each clay dispersion were performed according to the work of White and Zelazny *(White and Zelazny, 1988)* and Tournassat et al. *(Tournassat et al., 2003)*, assuming a clay density of 2.7 g/cm³, and are presented in Table 2-12. The main assumption is that the stacking of clay mineral layers does not change the accessibility to the lateral surfaces, only the interlayer basal surfaces are not accessible. The results show variations up to a factor ~8, but they are only considered as approximations since the aggregate dimensions are underestimated. Taking a regular disc to mimic smectite aggregates does not take into account their convexities and concavities which lead to an increase in their surface area and perimeter. When considering the dispersions with the smaller mean clay size (S3.5, S3.5^{UC} and S3.5^{UC,FA}), the results are in agreement with those of Tournassat et al. *(Tournassat et al., 2003)*.

Stability studies. The data obtained from the stability studies are very scattered (Figure 2-9) which is certainly due to the broad clay particle size distribution in each suspensions. It is thus challenging to determine the mean particle size increase in order to determine the corresponding agglomeration rate (especially for the dispersion S0, which cannot be further considered). In addition, the agglomeration behaviour of smaller sized particles is probably hidden by the dominant scattered light intensities from larger particles which are those preferentially detected by the PCS. Nevertheless, better results are obtained from the less scattered data of the suspensions (S3 and S3.5). The stability ratios (W) calculated for all dispersions at pH 7 and for different ionic strengths in different electrolytes (NaCl, CaCl$_2$ or MgCl$_2$) are presented (Figure 2-10). W decreases with increasing ionic strength, as expected. This is obvious after addition of NaCl (Figure 2-10a) and is consistent with the DLVO-theory. The montmorillonite particles are more easily destabilize by addition of CaCl$_2$ and MgCl$_2$. Actually, the lowest concentrations tested (0.01 M resulting in a IS of 0.03 M) are enough to agglomerate the clay particle in suspensions (Figure 2-10b and Figure 2-10c), as expected from previous studies *(Schudel et al., 1997)*. This is in line with the well-known Shulze-Hardy rule *(Overbeek, 1980)*. The decrease in stability ratio in presence of divalent cations is partly explained by specific interaction of divalent cations as previously reported in the literature *(French et al., 2009; Keiding and Nielsen, 1997; Norrfors, 2015; Oncsik et al., 2014; Pantina and Furst, 2006)*. According to the DVLO-theory, the calculated Van der Waals (VdW)-forces increase for increasing particle size of two identical spherical particles *(Ottewill and Shaw, 1966; Reerink and Overbeek, 1954; Shah et al., 2002)*. However, when no electrostatic repulsions are present, the kinetic energy dominates over the VdW-forces and the agglomeration rate constants of spherical latex particles are therefore independent of the particle size *(Henry et al., 2015)*.
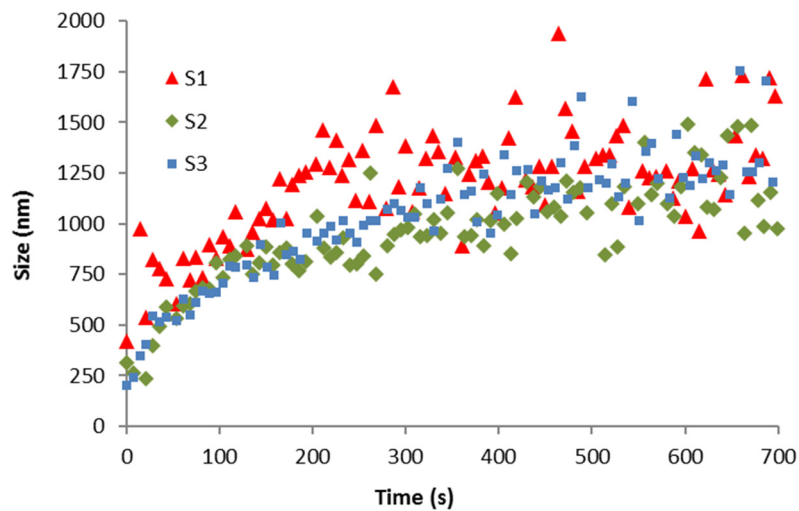
Figure 2-9: Evolution of the hydrodynamic diameter for three montmorillonite dispersions after adding 0.01 M CaCl$_2$ at pH 7.

Even though clay aggregates are known to have different shapes and compositions than the latex particles present in the previous study *(Henry et al., 2015)*, the domination of the kinetic energy can be one explanation of the absence of significant differences between the colloidal dispersions in this study (Figure 2-10). The absence of particle size dependency on the stability ratios is further in agreement with previous studies *(Behrens et al., 2000; Ottewill and Shaw, 1966)* but once again, one should have in mind that PCS favours the detection of larger sized entities. In poly disperse dispersions, it renders difficult the detection of the primary agglomeration of the smaller size entities. Previous studies of polydisperse dispersions *(Chang and Wang, 2004; Jia and Iwata, 2010)* indicate that their stability ratio is smaller than for a mono disperse system, which seems consistent with the present observations.
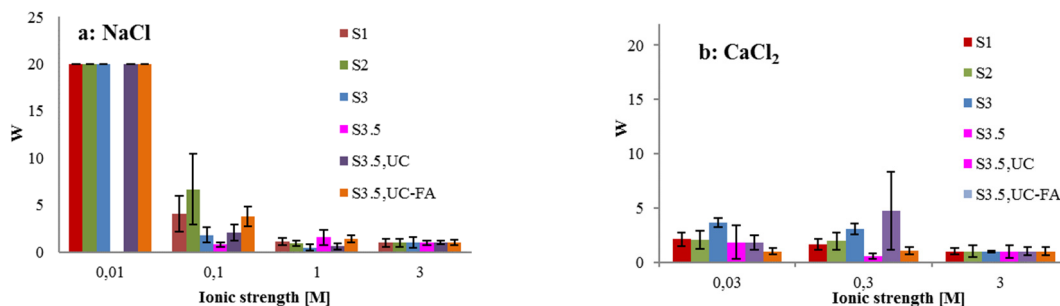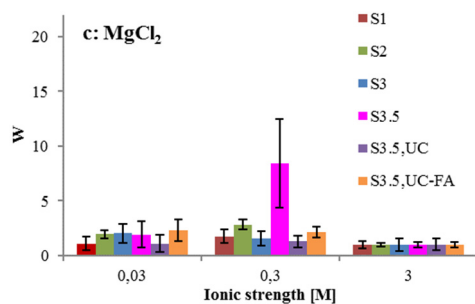
Figure 2-10: Stability ratios (W) calculated at different ionic strengths in a) NaCl b) CaCl$_2$ or c) MgCl$_2$, at pH 7. Infinity is arbitrarily set to 20 in the figures.

Finally, the presence or absence of FA in the dispersions does not change the results. Previous studies present a stabilization of the clay particles in presence of FA *(Kretzschmar et al., 1998)* but notice that the stabilization properties of FA decreases with increasing pH, due to the lower FA adsorption to clay surfaces.

Conclusions

A protocol to obtain montmorillonite colloid dispersions with different size fractions is proposed. It is based on a sedimentation step followed by sequential or direct (ultra-)centrifugation.

Montmorillonite aggregates found in the different dispersions present the same composition as seen from both the chemical analysis and the XRD results. Calcium is associated to the clay particles as natural calcite or due to the fast ionic exchange processes arising under the present experimental conditions. An instant release of sodium and sulfate occurs when the bentonite is suspended in the SGW. This is explained by dissolution of the gypsum or/and the celestite naturally present in the unpurified MX-80 bentonite.

Mean equivalent sphere diameters (EDS) values of the clay aggregates obtained by different methods vary from ~960 nm down to ~ 85 nm. After applying mathematical treatments, the differences recorded in the initial data between the AsFIFFF (giving the Stokes diameter) and the PCS (giving a frictional translatory diffusion diameter) are used to estimate the mean diameter, δ and the thickness, t, of the clay aggregates in the different dispersions after approximating those to regular disc-shaped aggregates consisting of stacked clay mineral layers. According to our calculations,   varies from 1.5 µm down to ~ 190 nm and t lies in the range of 18 to 70 nm. The number of sheets (clay mineral layers) is determined by dividing the thickness t by 1.3 nm (thickness of one single clay layer in basal spacing). The corresponding axial (or aspect) ratios ($\rho=\delta/t$) agree with literature data. An estimation of the number of edge sites in each clay dispersions is given.

The stability of montmorillonite aggregates is higher in NaCl solution than in CaCl$_2$ and MgCl$_2$ for the same ionic strength, which is in line with the Schulze-Hardy rule. In addition, the stability ratio is independent on the colloidal size initially present.

2.1.2   Radionuclide interaction studies

2.1.2.1   Reversibility studies on fracture filling material in support of the field program

R. Rinderknecht, F. Huber, S. Heck, T. Schenk, C. Walschburger, F. Geyer, T. Schäfer

Introduction

One of the reference evolution scenarios of a high-level nuclear waste disposal in crystalline formations (e.g. granitic rock) in e.g. Sweden and Finland foresees the intrusion of low mineralized glacial melt water down to repository depth (~500m below surface) *(Bath, 2011)*. Under these hydrogeochemical conditions, erosion of the geotechnical barrier consisting of bentonite may occur leading to the formation of bentonite colloids. Radionuclides sorbed to these colloids may be transported over longer distances than in the absence of a colloidal phase *(Kersting et al., 1999)*. Laboratory batch studies on the reversibility of the sorption process to the colloids leading a decrease in transport distances have been carried out in the past years for the ternary system radionuclide-colloid-fracture filling/fault gouge material (e.g. *(Huber et al., 2011; Huber et al., 2015)*). Moreover, field scale experiments on colloid facilitated radionuclide transport in the framework of the Colloid Formation and Migration project (CFM (www.grimsel.com) have been conducted corroborating the occurrence of sorption reversibility. Derived desorption rates out of the experimental datasets can be directly used in performance assessment codes like e.g. *(Reiche et al., 2016)* to simulate the effect of sorption reversibility on the long-term migration behaviour. Surprisingly, up to now, only little data is available on the binary system radionuclide-fracture filling/fault gouge material under these low ionic strength meltwater conditions *(Alonso et al., 2006a)*. Reliable distribution coefficients (Kd values) and kinetic rates for the binary system are needed to decrease the uncertainties in the transport simulations. To close the data gap, a new experimental program was initiated focusing on the following aspects:

➢ Determination of Kd values for ^{99}Tc, ^{233}U, ^{237}Np, ^{242}Pu and ^{243}Am on fault gouge material from Grimsel under Grimsel groundwater conditions

➢ Study potential sorption competition effects by comparison of single radionuclide batch experiments with radionuclide cocktail batch experiments

➢ Examine a possible impact of the initial sorption time on the desorption kinetic process

Material and Methods

Fault gouge material (FG). The FG material was collected at the Grimsel Test Site (GTS), Switzerland. The main rock type in the Grimsel area is the so-called Grimsel "granodiorite" *(Nagra, 2006)*. It consists of plagioclase, quartz, K-feldspar, biotite and accessory minerals like muscovite/sericite, apatite, sphene, epidote, zircon, calcite and opaque minerals (e.g. Fe-oxides like magnetite) *(Alexander et al., 2001)*. The material was extracted from an outcrop of the Colloid Formation and Migration (CFM) project shear zone at the tunnel wall. FG was transferred to KIT-INE, crushed and separated under ambient conditions using sieves with meshes between 63 µm up to 5 mm. Thereby, FG in seven different grain sizes (<63 µm (VII), 63-125 µm (VI), 125-250 µm (V), 250-500 µm (IV), 500-1000 µm (III), 1-2 mm (II) and 2-5 mm(I)) was generated. Only the size fraction IV was used for the sorption reversibility experiments. These fractions were washed and equilibrated using natural Grimsel groundwater (GGW) over a period of two weeks and exchanged regularly several times to remove any leftover fines.

Environmental Scanning Electron Microscopy (ESEM) analysis of the size fraction was carried. The FG material was dried at 60°C and transferred to the ESEM device. Results are shown in Figure 2-11 corroborating the sieved size fraction of 250µm – 500µm. By application of energy-dispersive X-ray spectroscopy (EDX) mineralogical characterization was possible yielding mainly feldspar, plagioclase, quartz and phyllosilicates. As expected the artificially and freshly crushed grains show a very rough and irregular shape.
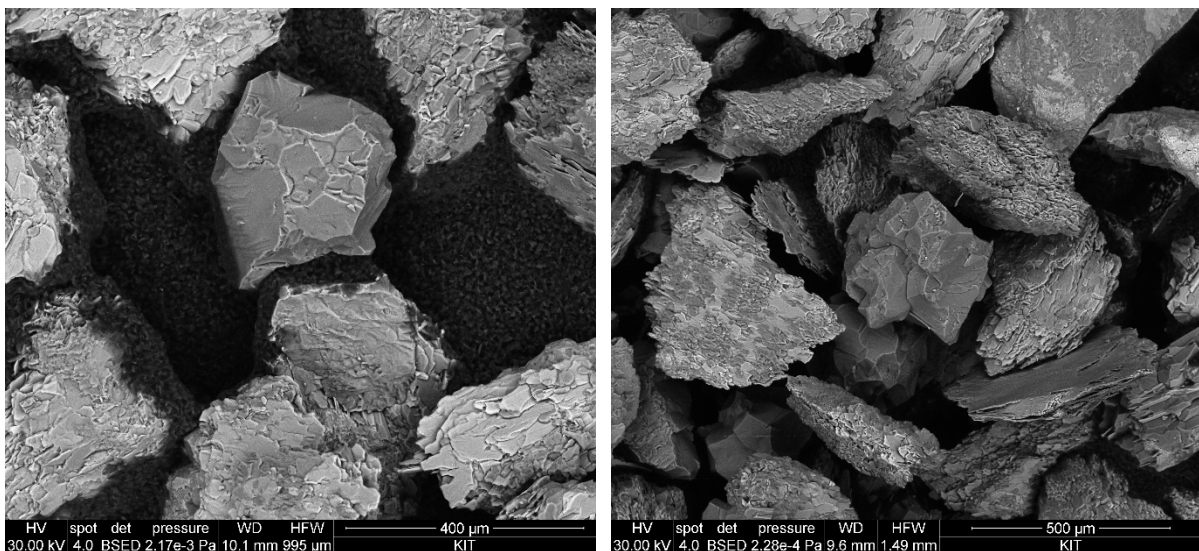
Figure 2-11: ESEM shots of 250 - 500 µm grain sized FG. EDX verifies quartz, feldspars and phyllosilicates.

Powder X-ray diffraction analysis was conducted to determine the mineralogical composition of the size fraction used. XRD spectra were recorded from 5° - 90° 2*Θ* with a Siemens D5000 powder diffractometer equipped with a scintillation detector an Cu K*α* radiation. Results of the

40

analysis yield mainly mineral phases like quartz, plagioclase, K-feldspar in line with literature data given. Chemical rock composition was traced by XRF for determining the major and trace elemental composition of the FG material used. In line with general granitic rock composition SiO_2, Al_2O_3, N_2O, Fe_2O_3 and K_2O dominate reflecting the main minerals plagioclase, feldspar and quartz. The dominating Fe redox state is Fe(II) with 2.71% of 3.87% total Fe present in the sample. The specific surface area of the FG was measured by classical BET N_2-adsorption. All samples were heated to 90°C and degassed for 18h. Using multi point analysis the BET isotherm was fitted to obtain the surface area. A total surface area of > 1m^2 was used in all measurements. Results for the BET analysis is given in Table 2-13. Additionally, the geometrical surface area was calculated and with a density of 2.7 g/cm^3 for the FG the specific surface area was determined. Comparing the measured BET with the calculated specific surface area it is obvious that the FG material specific surface area is fully dominated by inner porosity in pores or cracks rather than the surface area only. Despite the assumption of perfect smooth spherical particle shapes in the calculations compared to the SEM pictures shown above for the FG material grains this conclusion still holds and allows the comparison in terms of mass based Kd values to similar experiments using the same type of FG material but with a different size fraction (1160 µm) *(Nagra, 2006)*.

Table 2-13: Specific surface area of the FG material used in the batch experiments.

FG grain size fraction (µm)	Specific surface area (m^2/g)	
	BET	calculated (sphere)
250 – 500	22.8	$8.8 \cdot 10^{-3}$ (250µm) / $4.4 \cdot 10^{-3}$ (500µm)

Radionuclides and cocktail preparation. Two experimental series were prepared: (i) single radionuclide and (ii) radionuclide cocktail samples, respectively. The radionuclides used are listed in Table 2-14 in conjunction with their respective concentration and oxidation states. The concentrations are very similar in both sample series. ^{233}U was used in the cocktail experiments only. Radionuclide concentrations have been selected to not exceed the solubility limit under the geochemical conditions given therefore avoiding any precipitation which could bias the analysis of the experiments and the experimental results itself. Measurement of the radionuclide concentrations in the samples was done by either ICP-MS (THERMO X-Series II) or high-resolution (HR) ICP-MS (THERMO Element XR).

Table 2-14: Concentrations of the radionuclides used in the different batch experiments.

Nuclide	C $_{single\ radionuclide}$ [M]	$C_{RN\text{-}cocktail}$ [M]
^{99}Tc(VII)	$1.5 \cdot 10^{-7}$	$1.5 \cdot 10^{-7}$
^{233}U(VI)	Not used	$8.2 \cdot 10^{-8}$
^{237}Np(V)	$5.5 \cdot 10^{-9}$	$5.4 \cdot 10^{-9}$
^{242}Pu(IV)	$5.9 \cdot 10^{-10}$	$6.4 \cdot 10^{-10}$
^{243}Am(III)	$4.2 \cdot 10^{-10}$	$3.3 \cdot 10^{-10}$

Experimental procedure and conditions. Both batch sorption and desorption (reversibility) experiments have been conducted in a glove box under anaerobic conditions (Ar atmosphere) and room temperature (22°C). Single samples have been prepared using HDPE 20ml vials

(ZINSSER) for each sampling time. This allows the use of the sorption samples subsequently as samples in the desorption experiments. A duplicate has been prepared for each sample to check for reproducibility. Diluted stock solutions (RN-GGW) for each single radionuclide and for the cocktail sample series were prepared by mixing fresh GGW with the concentrated radionuclide stock solutions to reach the desired radionuclide concentrations. Afterwards pH of the RN-GGW solutions were re-adjusted to the original Grimsel pH of ~9.5. In each vial 1.5g (dry weight) of the FG (250-500µm size fraction) was brought in contact with 8.5ml of the different RN-GGW stock solutions yielding a V/m ratio of 5.7 ml/g. The samples prepared were stored in the glove box during the whole experimental duration. Sampling times were as follows: 1d, 3d, 7d, 14fd, 28d, 100d, 200d and 300d. After the desired contact time, an aliquot of the sample was diluted in 5% HNO3 and analysed by (HR)-ICP-MS. Again, pH was measured to check for any drift over the experimental duration. After the sorption time, the remaining solution in each vial was discarded carefully and fresh RN free GGW was added (8.5ml to keep the V/m ratio constant). A similar sampling schedule was chosen in the desorption experiments as used in the sorption experiments, namely 1d, 3d, 7d, 14fd, 28d, 100d, 200d and 300d. That is, for the 7d sorption sample for instance, after a desorption time of e.g. 1d an aliquot was taken for RN analysis by (HR)-ICP-MS and pH of the sample was measured. Subsequently, the remaining solution was completely discarded from the sample vial and fresh GGW was added. After additional 2days (that is 3d desorption time in total), the same procedure of sampling, pH measurement and exchange of solution with fresh GGW was carried out. This procedure was repeated for all samples and desired desorption times. In other words, every sample out of the sorption series experiments was exchanged with fresh GGW 8 times (once for each desorption time) within the desorption experiment series. Subsequently to the desorption kinetics experiments, the FG material containing sorbed RN (only for the single radionuclide series of Am, Pu and cocktail series samples, respectively) was brought in contact with 8.5 ml of synthetic Ni montmorillonite containing colloid suspension *(Huber et al., 2015; Reinholdt et al., 2013)* to study a possible remobilization of RN due to the presence of an additional concurrence surface. The colloid concentration in the sample was around 36 mg/L. The samples were contacted for 1d, 5d, 14d, and 28d and afterwards immediately prepared for elemental composition analysis.

Results and Discussion

Evolution of pH-Eh-conditions. In each single sample pH was measured at the time of sampling using a semi-micro Ross electrode (81-03, Orion Co.) in combination with a digital pH meter (720A, Orion Co.). Calibration of the pH setup was carried out using at least 5 commercial buffer solutions (Merck). The evolution of both the sorption and desorption experiments are shown in Figure 2-12. In case of the sorption samples, the pH shown is an average of 34 single samples in total (total amount of samples for 1d contact time for each radionuclide and cocktail plus additional blank samples with GGW and FG only). Regarding the very small error bar (~0.1 pH unit) the reproducibility of the measured pH values are in very good agreement. A constant pH was observable within the first 14d contact time. Afterwards a drift from initially

pH of ~9.3 down to pH of ~8.2 was detectable during the contact time of 232d. This drift might be attributed to two possible reasons: (i) a disequilibrium between the FG and the GGW inducing mineral dissolution and precipitation processes which consume OH^- ions shifting pH to lower values or (ii) intrusion of trace amounts of CO_2 (which could be present in the glove box Ar atmosphere) into the samples by diffusion. The former explanation might be favoured over the latter explanation when looking at the pH evolution during the desorption experiments. Here the pH stayed very much constant (9.3 ± ~0.1 pH unit) over 300d despite having contact to the FG all the time. The pH during the desorption experiments is shown in Figure 2-12 as a greyish area instead of single values. This was necessary since for each sorption time 14 pH values (7 samples with duplicates) have been measured for each desorption step for each single radionuclide and cocktail samples (6 RN series sums up to > 500 values).
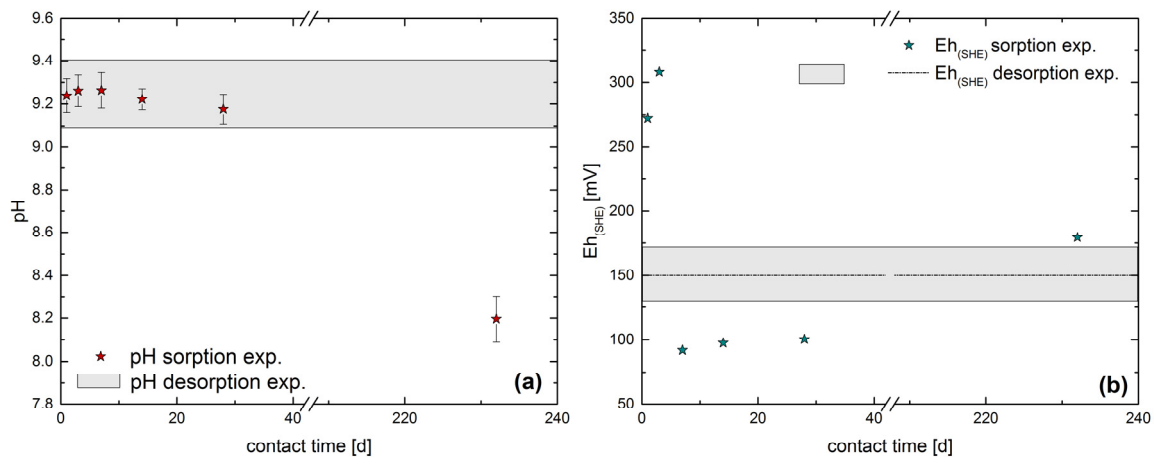
Figure 2-12: (a) pH evolution for both the sorption (symbols) and desorption (grey area) experiments, respectively. (b) Eh evolution for both the sorption (symbols) and desorption (grey area) experiments, respectively.

The redox potential was measured in blank samples (GGW and FG only) in absence of RN to evaluate only the influence of the FG material on the Eh evolution and to avoid any leakage of the electrode inner filling electrolyte (3M KCL) into the sample solution during long measurement times. Measurements have been carried out with a Pt combined electrode (Metrohm) connected to the pH meter (Orion). $Eh_{(SHE)}$ was consistently monitored in the blank samples until a plateau value was reached. With respect to the sorption experiments, an initial drop from ~+250 mV down to ~+ 90 mV was detected within the first 7d which stayed constant until 28d. Afterwards $Eh_{(SHE)}$ drifted to a value of ~+175 mV after 232d. The drift for the long term samples might be explained by trace amounts of O_2 diffusing into the vials. Regarding the desorption experiments, $Eh_{(SHE)}$ was very constant over the whole experimental duration in line with the pH behaviour. Generally speaking, the measured redox potentials of the GGW are much more positive than the in-situ $Eh_{(SHE)}$ value measured in the field. Here values of around -300 mV have been measured by *(Möri et al., 2003)*. Similar low redox potentials have also been measured within very similar laboratory batch experiments by *(Huber et al., 2015)*. The

discrepancies between the measured values in this study and reported values in the literature display the general high uncertainties in reliably measure $Eh_{(SHE)}$ values in systems where only very little amounts of redox active elements like e.g. Fe(II)/Fe(III) are present. For a thorough discussion on this topic the reader is referred to e.g. *(Grenthe et al., 1992)*.

RN sorption kinetics

^{99}*Tc(VII),* ^{233}*U(VI) and* ^{237}*Np(V).* The results for the ^{99}Tc(VII) sorption kinetics are shown in Figure 2-13 for both the single RN experiments and the RN cocktail experiments. Less than 10% sorption was observed for the cocktail samples after 28d contact. The same is true for the single RN samples except the values after 28d which is around 17%. For the long term sample after 232d both the single RN experiments yielded values of 60% and only ~45% for the RN cocktail samples, respectively. The removal process leading to the decrease in aqueous ^{99}Tc(VII) concentration is most probably a redox transformation of ^{99}Tc(VII) to ^{99}Tc(IV). It is well known that a dramatic change in the sorption properties is accompanied with the reduction process *(Bondietti and Francis, 1979)*. While Tc(VII) behaves like a conservative tracer and is therefore not interacting with the FG surface, Tc(IV) shows a very strong sorption behaviour. Thus, it seems likely that during the experimental duration a coupled process of reduction and subsequent sorption occurred (sorptive reduction). As potential redox partner Fe(II) might be responsible which is found in the Grimsel FG material as verified by XRF measurements (2.7% FeO). A similar behaviour of ^{99}Tc sorptive reduction in the same system has been observed e.g. by *(Huber et al., 2011; Huber et al., 2015)*. Regarding thermodynamic simulation results, no reduction should be expected based on the measured pH-Eh range. This might be in good agreement for the short term kinetics with less than 10-20% removal but not for the long-term sample after 232d with fractions removed of ~45-60%. Though one has to state clearly that the determination of the redox potential in natural systems is associated with very high uncertainties due to local redox dis-equilibriums for example *(Grenthe et al., 1992)*. A study by *(Marsac et al., 2015b)* investigated Np(V) interaction with illite and found that although the measured redox potential measured in solution would predict Np(V), the reduced Np(IV) species was detected on the illite surface. That is, the redox potential measured in solution with a redox electrode can be different to the redox potential prevailing at the solid-liquid interface. Sorption kinetics for ^{233}U(VI) are shown in Figure 2-13. Only values for the cocktail samples are shown since no single RN experiment has been conducted for ^{233}U(VI). A maximum of ~40% sorption was observed which was obtained already after 14d contact time. Afterwards only a very small increase could be observed until 228d (~2%). This might be interpreted as a faster initial sorption followed by a very slow sorption kinetic as long-term behaviour or already as an equilibrium state. Regarding the thermodynamic modelling a reduction of U(VI) to U(IV) as proposed for e.g. ^{99}Tc is rather unlikely since the measured redox potentials are several 100 mV above the 50/50% borderline for U(VI)/U(IV) reduction. It seems more reasonable to assume a U(VI) sorption kinetic. It has been shown that the $CaUO_2CO_3$ species is rather weakly sorbing and thus also very stable against reduction when assuming a sorptive reduction process. This would be in line with the results observed.
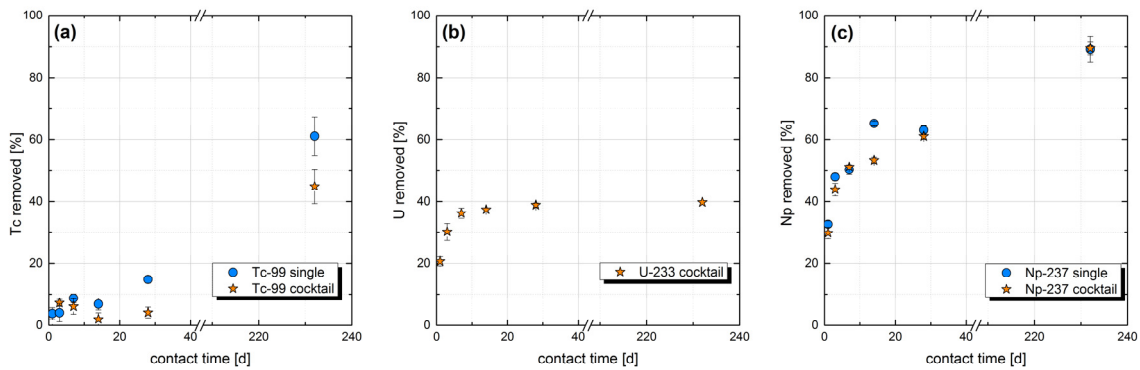
Figure 2-13: Results of (a) ^{99}Tc, (b) ^{233}U and (c) ^{237}Np batch kinetic sorption experiments.

Both single RN and cocktail experiments have been conducted for ^{237}Np(V). Results are depicted in Figure 2-13. The results indicate the absence of an equilibrium state within the experimental duration of 232d. There is a steady increase in sorption for ^{237}Np(V) up to ~90% after 232d contact time. No difference is observable between the cocktail and the single RN samples indicating the absence of any competition effects. Since the pentavalent Np is known to sorb rather weakly the removal process might again be explained by a sorptive reduction process to Np(IV) at the surface of the FG material. This seems to be corroborated by thermodynamic considerations which predict Np(IV) species at around -10 to -50 mV in the pH range 8 to 10. Given the uncertainties of the Eh$_{(SHE)}$ measurements as noted above, the measured values are relatively close to the Np(V)/Np(IV) borderline. A transformation of Np(V) to Np(IV) and a subsequent sorption to the FG material can therefore be hypothesized as Np removal process occurring.

^{242}*Pu(IV) and* ^{243}*Am(III).* With respect to ^{99}Tc, ^{233}U and ^{237}Np, ^{242}Pu(IV) shows a much faster sorption kinetic since more than 80% is already sorbed after 3d contact time as can be seen in Figure 2-14. The high degree of sorption was expected since the tri- and tetravalent RNs are known to sorb very strongly onto various mineral phases *(Geckeis et al., 2013)*. The sorption increases to more than 90% after 7d to 14d possibly reaching already a steady state equilibrium process. After 228d contact time, the sorption is even slightly higher at around 98%. This increase between 28d and 228d might indicate a very slow sorption kinetic although the analytical uncertainty is rather pronounced at this high sorption values. Again, no difference was observed between single RN experiments and cocktail experiments, respectively.
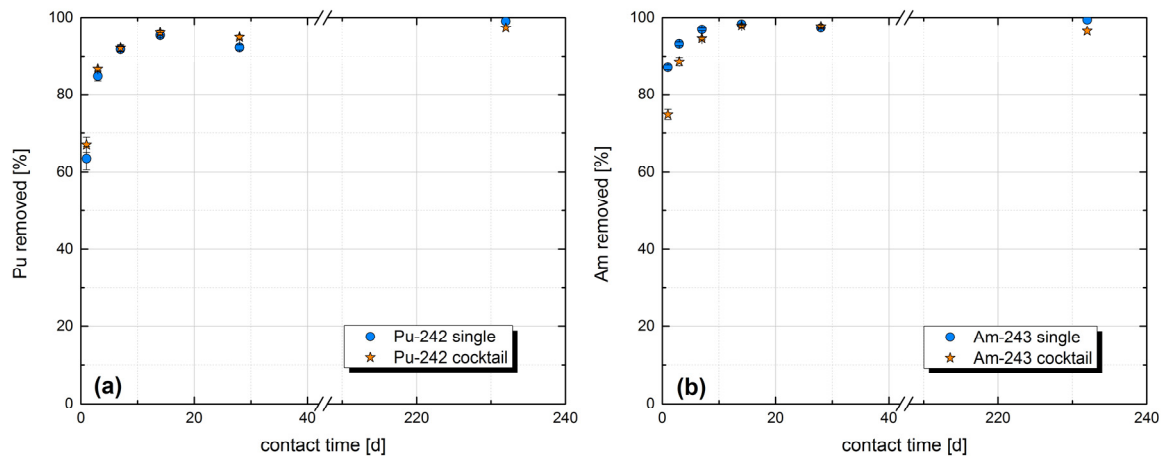
Figure 2-14: Results of ^{242}Pu (a) and ^{243}Am (b) batch kinetic sorption experiments.

A very similar sorption behaviour was found for ^{243}Am(III) compared to ^{242}Pu(IV). The removal kinetic is even slightly faster for ^{243}Am(III) and clearly attributed to a sorption process since ^{243}Am(III) is not redox sensitive. After 7 to 14d, the sorption is >95% reaching a plateau which can be interpreted as an equilibrium state. No difference is found between single RN experiments and cocktail experiments. Using an exponential growth equation (Equation 6) sorption rates k [1/T] were fitted to the experimental datasets.

$$y = A_1 \cdot e^{\frac{x}{t_1}} + y_0 \quad with \; k = \frac{1}{t_1} \qquad \textbf{Equation 6}$$

The fitting results are given in Table 2-15. These rates are needed as input parameters in numerical codes for performance assessment calculations like e.g. COFRAME *(Reiche et al., 2016)*. The fastest rates were found for Pu with values of ~-0.52 to -0.54 [1/d]. Am and U show very similar rates of -0.37 to -0.45 [1/d] (^{243}Am(III)) and -0.38 [1/d] (^{233}U(IV)). Although the rates for ^{243}Am(III) and ^{233}U(IV) are very similar the amount sorbed is totally different between the two radionuclides. That is, because the fit does not account for the actual amount sorbed but only how fast the equilibrium approach is required. Rates of around one order of magnitude lower were found in case of Np yielding values of -0.027 to 0.037 [1/d]. For ^{99}Tc(VII), the fitting routine was not successful due to the very low amount of ^{99}Tc(VII) sorbed within the first month of the experiments.

46

Table 2-15: Radionuclide sorption rates fitted to the batch sorption experiment results.

	Rate [1/d]	Error [±]	R^2 [-]
	^{242}Pu(IV)		
Single RN exp.	-0.52	0.15	0.948
Cocktail exp.	-0.54	0.1	0.976
	^{243}Am(III)		
Single RN exp.	-0.37	0.088	0.962
Cocktail exp.	-0.45	0.059	0.934
	^{233}U(VI)		
Cocktail exp.	-0.38	0.053	0.98
	^{237}Np(V)		
Single RN exp.	-0.037	0.017	0.84
Cocktail exp.	-0.027	0.011	0.9
	^{99}Tc(VII)		
Single RN exp	No fitting possible		
Cocktail exp.	No fitting possible		

RN desorption kinetics. Subsequent to the sorption studies, desorption experiments were conducted to examine a possible sorption reversibility as function of the previous sorption time. The desorption data is presented in the following way: (i) the amount sorbed after the desired contact time is set to 100%, (ii) the amount desorbed after each desorption step is plotted as cumulative concentration as function of time

^{99}Tc(VII), ^{233}U(VI) and ^{237}Np(V). Desorption kinetics for ^{99}Tc(VII) are depicted in Figure 2-15. Since the ^{99}Tc(VII) amount sorbed was very little and scattered within the first 28d contact time, the desorption data values for this time range is attached with a high uncertainty. Thus, no clear correlation is visible between the previous sorption time and the desorption time. The most certain values are clearly the values for the sorption time of 232d where ~40-60% Tc was found on the FG surface. The desorption was found to be in the range of ~10% after 28d contact time. Due to the high scatter in the data fitting of the desorption rate was very hard to accomplish. In contrast to ^{99}Tc(VII), data for ^{233}U(VI) show a clearer trend between the sorption time and the reversibility. While the samples for short sorption contact times (1-28d) are very similar compared to each other showing a desorption of ~30-70% for desorption times between 1d and ~400d, the data for 232d sorption time clearly show less desorption. Even for the highest desorption time of 400d only a maximum desorption of 30% was found. This result highlights that the previous sorption time has a direct influence on the desorbable amount. A possible explanation for this observation might be found in a coupled sorption reduction transformation over time. That is, ^{233}U was sorbed initially as hexavalent ^{233}U on the FG material and was reduced to U(IV) by e.g. Fe(II) during the course of the experiment especially for the long-term samples. Since ^{233}U(IV) is showing a stronger sorption behaviour as ^{233}U(VI), the total

desorption and the desorption rate is expected to be less which is in line to the results described above.

Figure 2-15: Results of (a) ^{99}Tc and (b) ^{233}U batch kinetic desorption experiments.

An even clearer correlation between the previous sorption time and the amount of reversibility is found for ^{237}Np(V) shown in Figure 2-15a and Figure 2-15b. Again, the longer the sorption time, the lesser pronounced the desorption. The maximum desorption increases from ~30% after 1d desorption up to ~68% after 399d desorption for the 1d sorption sample. For the 232d sorption samples, the desorption values increase only from below 10% after 1d up to a maximum of only ~20% after 168d desorption. Moreover, the desorption kinetic is slowing down between 28d and 168d desorption time indicating near equilibrium conditions. Slightly higher desorption values (~5 to 10%) were observed for the cocktail samples compared to the single RN samples. A very similar explanation for the correlation between the sorption time and the Np desorption behaviour is postulated as above for U and Tc. Np(V) was reduced to Np(IV) during the sorption experiments and removed via sorption to the FG material. The increasing amount of stronger sorbing Np(IV) for longer contact times during the sorption experiments is directly visible in the decreasing amount of desorbed Np for the longer contact times of the sorption samples within the desorption experiments.

^{242}*Pu(IV) and* ^{243}*Am(III).* The results of the desorption experiments for both ^{242}Pu(IV) and ^{243}Am(III) show a very similar behaviour (Figure 2-17a and Figure 2-17b and Figure 2-18a and Figure 2-18b). Both radionuclides are strongly and fast sorbing in the sorption experiments. Their desorption is only very weakly from values of ~1% after 1d desorption time to a maximum of ~15% (or even less) after 232d desorption time. No clear trend of the amount desorbed with respect to the sorption time was observed. A very slow desorption kinetic might be seen in case of the single RN experiments especially for Pu. Even slower kinetics were observed for the cocktail experiment samples for Pu and Am single RN experiments. Unfortunately, no results for ^{243}Am cocktail sample series have been obtained due to very little amount of desorption lying below the detection limit of the ICP-MS. New measurements of these samples using

the HR-ICP-MS are currently conducted. To conclude, both radionuclides show no tendency for desorption possibly due to the lack of any concurrence surface or ligand present which could trigger a desorption process. Therefore, experiments adding bentonite colloids as concurrence ligand to the RN containing FG material samples were conducted.
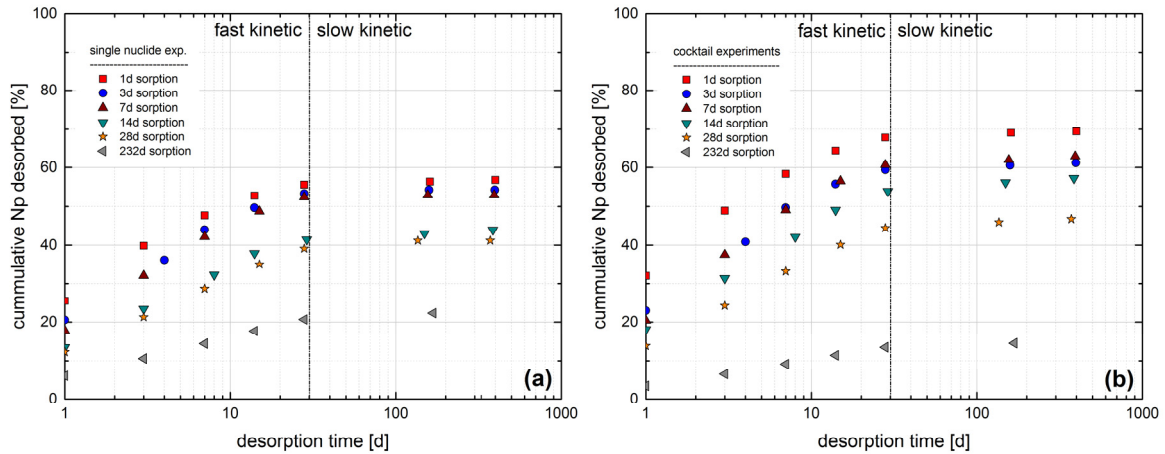
Figure 2-16: Results of (a) ^{237}Np single radionuclide and (b) ^{237}Np cocktail kinetic desorption experiments, respectively.
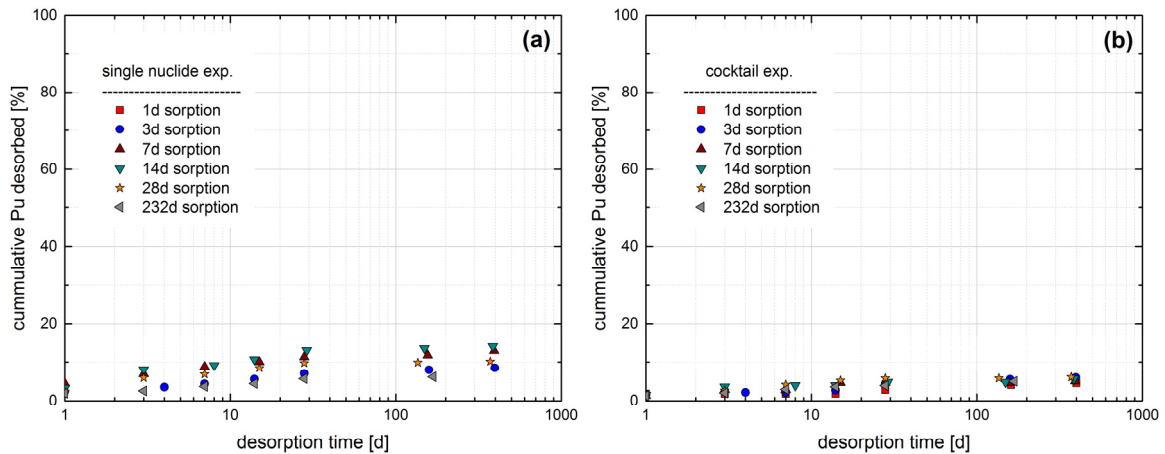
Figure 2-17: Results of (a) ^{242}Pu single radionuclide and (b) ^{242}Pu cocktail kinetic desorption experiments, respectively.
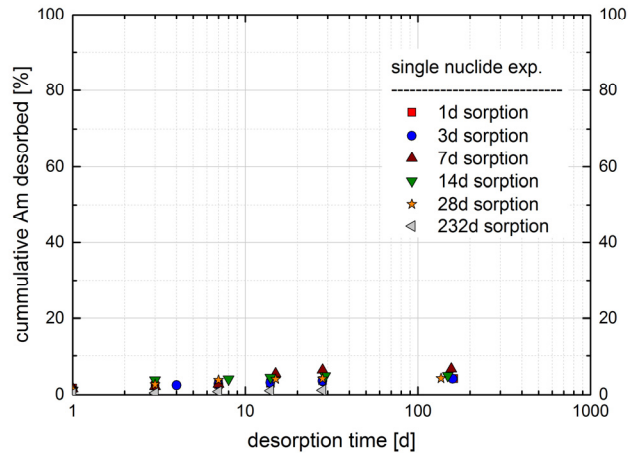
Figure 2-18: Results of ^{243}Am single radionuclide sample series.

Table 2-16: Overview of the fitted desorption rates and measured radionuclide recoveries. Recovery denotes the amount of radionuclide found in solution after the desired contact time of desorption.

| | | Single nuclide samples | | | | RN cocktail samples | | | |
| | | 1-rate fit | 2-rate fit | | | 1-rate fit | 2-rate fit | | |
Sorption time [d]	Desorption time [d]	k [1/a]	k_1 [1/a]	k_2 [1/a]	Recovery [%]	k [1/a]	k_1 [1/a]	k_2 [1/a]	Recovery [%]
					^{237}Np				
1	399	147 ± 24.2	409 ± 23.4	48 ± 3.5	57	150 ± 25.7	424 ± 28.0	47 ± 4.0	70
3	397	96 ± 12.9	479 ± 117.3	57 ± 7.8	55	95 ± 13.0	446 ± 115.0	56 ± 9.2	61
7	393	100 ± 89.2	296 ± 24.3	47 ± 3.4	53	93 ± 12.8	254 ± 24.0	38 ± 4.1	63
14	386	66 ± 10.7	351 ± 74.7	39 ± 4.6	44	68 ± 11.8	336 ± 57.4	36 ± 4.1	57
28	372	58± 10	323 ± 29.7	33 ± 1.9	42	67 ±10.0	319 ± 47.8	37 ± 3.4	46
232	168	50 ± 8.7	331 ± 35.5	29 ± 1.8	22	81 ± 11.8	273 ± 13.3	29 ± 0.8	15
					^{233}U				
1	399					132 ± 28.6	403 ± 51.8	33 ± 6.3	65
3	397					76 ± 12.9	301 ± 60.8	30 ± 7.0	67
7	393					69 ± 14.2	250 ± 31.0	23 ± 3.3	58
14	386		no single nuclide samples for U-233			47 ± 9.8	275 ± 61.5	21 ± 4.1	68
28	372					37 ± 8.2	260 ± 69.2	19 ± 3.7	58
232	168					52 ± 11.9	376 ± 52.4	25.4 ± 2.6	0.3
					^{99}Tc				
232	168	163 ± 41.9	380 ± 61.2	18.9 ± 8.0	14	217 ± 62.2	654 ± 128.3	32 ± 10.3	6.5
					^{242}Pu				
1	399	41 ± 16.2	622 ± 148.3	14 ± 3.1	13	9 ± 4.1		5 ± 2.2	5
3	397	27 ± 5.2	664 ± 297.3	20 ± 2.6	9	15 ± 3.4	13 ± 3.0	168167 ± 0	6
7	393	51 ± 14.1	351 ± 131.5	23 ± 7.8	13	57 ± 13.6	386 ± 530	39 ± 27.2	5

14	386	48 ± 11.0	253 ± 116.5	21 ± 9.3	14	52 ± 18.8	196 ± 53.3	1 ± 2.7	6
28	372	65 ± 12.4	227 ± 115.0	28 ± 13.7	10	58 ± 5.3	159 ± 81.7	41 ± 11.8	6
232	168	38 ± 7.8	1024 ± 1101.4	27 ± 4.5	6	32 ± 7.7	195 ± 86.4	12 ± 5.7	5
			[243]Am						
1	399	36 ± 11.6	494 ± 73.9	15 ± 1.6	4				
3	397	39 ± 10.8	308 ± 57.8	11 ± 2.3	4				
7	393	32 ± 4.6			7		below ICP-MS detection limit		
14	386	100 ± 27.0	175± 44.1	3 ± 3.1	5				
28	372	113 ± 11.6	138 ± 11.6	3 ± 3.0	4				
232	168	34 ± 5.3	75 ± 37.9	9 ± 11.8	1				

Summary and Conclusions

Batch studies on radionuclide sorption and desorption on fault gouge material from Grimsel have been conducted. Both single radionuclide sample series and radionuclide cocktail sample series have been used to examine possible sorption competition effects. The tri- and tetravalent radionuclides [242]Pu and [243]Am show a fast sorption kinetic reaching equilibrium between 7-14d with sorption values > 95%. The redox sensitive radionuclides [99]Tc(VII), [233]U(VI) and [237]Np(V) behave differently. [99]Tc(VIII) shows only a very weak sorption (< ~15%) within the first month contact time and increases to ~42 (single radionuclide series)-60% (radionuclide cocktail series) after 232d sorption time. This removal from solution and attachment to the FG material is explained by a reductive sorption to Tc(IV). The same process is made responsible for the decrease in concentration for [237]Np(V). Here [237]Np shows a steady increase in sorption up to 232d without reaching an equilibrium even for the long term contact time. Np(V) is likely be reduced to the more strongly and sparingly soluble Np(V). Measured redox potentials are in general to oxidizing to reduce ^{99}Tc and [237]Np from a thermodynamically point of view. Nevertheless, the redox potential determination is always accompanied with a high uncertainty and there has been moreover indications, that surface redox potentials might be more reducing as measured redox potentials in solution *(Marsac et al., 2015b)*. In case of [233]U(VI) a sorption equilibrium is obtained quite fast after ~14d contact time. Though a maximum of only 40% is removed from solution. Needing even more negative redox potentials than for ^{99}Tc and [237]Np, [233]U is assumed to be not reduced showing a U(VI) sorption only.

With respect to a possible sorption competition effect no clear trends are visible for all radionuclides within the analytical uncertainty. It seems that there is an excess of sorption sites on the FG material for all radionuclides available.

Rates for the sorption kinetics have been derived by fitting an exponential growth equation to the datasets. Due to the very weak interaction of ^{99}Tc with the FG material no fitting was possible. [242]Pu shows the fastest kinetic (k = ~ -0.5 [1/d)] closely followed by Am and U [k = ~ -0.4]. One order of magnitude lower rate (k = ~-0.03 [1/d]) has been found for [237]Np.

A correlation between the initial sorption contact time and the subsequent amount of desorption has been observed to some part for ^{99}Tc and ^{233}U and very pronounced for ^{237}Np whereas no trend has been observed in case of the strongly sorbing ^{242}Pu and ^{243}Am. ^{237}Np clearly shows a decrease in desorption for longer sorption times. That is, the sorption sample after 232d contact time, shows a maximum value for desorption of ~20% whereas the short term sorption sample after 1d contact time reaches up to almost 60% desorption. All the other contact times in between follow nicely the same trend.

Again kinetic rates for desorption have been fitted using both a 1-rate and 2-rate exponential equation approach. The tri- and tetravalent radionuclides ^{242}Pu and ^{243}Am can be satisfactorily fitted using the 1-rate model showing a simple sorption/desorption process taking place only. In case of especially ^{237}Np the 2-rate model gave better fits than the 1-rate model likely indicating the coupled sorption-reduction process occurring.

The extension of available models for radionuclide transport to additionally include a two rate desorption process in combination with more accurate sorption kinetics (or Kd values) will likely improve the current simulation results. Especially the simulation of the long-term tailing behaviour of the breakthrough curves measured by AMS (accelerated mass spectrometry) within the CFM project might be better predicted by the rates presented in this study (see Section 2.1.3 and 3.1.1).

2.1.2.2 Colloid size dependent radionuclide sorption studies

Reprinted with permission from Elsevier Ltd: "*Montmorillonite colloids: II. Characterization and stability of dispersions with different size fractions*" K.K. Norrfors, R. Marsac, M. Bouby, S. Heck, S. Wold, J. Lützenkirchen and T. Schäfer. Applied Clay Science 123 (2016) 292-303.

Introduction

Since size separation of montmorillonite colloids may occur in bedrock fractures, their size, morphology, stability and RN adsorption capacities are among the important parameters for estimating colloid facilitated transport of RNs, and are required in reactive transport modelling. According to the results presented in this report (Section 2.1.1.2) on the montmorillonite particles stability at various ionic strengths *(Norrfors et al., 2015)*, no dependency on the montmorillonite size was observed. Consequently, under defined geochemical conditions, all clay colloidal size fractions are supposed to remain simultaneously or not. Nevertheless, due to natural hydrodynamic chromatography effects (like the natural filtration occurring due to the presence of FFM as mentioned above), not all the size fractions may migrate and be disseminated. It is thus of high importance to examine if and how the RN adsorption depends on the clay colloid size and thus, the total exposed surface area. A size-dependent reactivity of hematite nano-mineral surfaces on Cu^{2+} adsorption has been previously demonstrated *(Madden et al., 2006)*. The amount of RNs transported through the bedrock via montmorillonite particles can be over- or underestimated in the reactive transport models used today *(Vahlund and Hermansson, 2006)* if the RN adsorption, via the exposed lateral surface area, is montmorillonite particle size dependant. In addition, the particle charge can change for nano-sized particles of several different materials *(Abbas et al., 2008; Madden et al., 2006; Vayssieres, 2009)*. Accordingly, the adsorption capacity of the particles may change with particle size as well. Therefore, adsorption study onto nano-sized material is of high importance. RN surface complexation to edge sites of clay particles is an important sorption mechanism at circum-neutral to alkaline pH. Tournassat et al. suggested a model where the amount of edge sites can be calculated from the aspect ratio and the density of the clay particles by assuming a site density of silanol and aluminol edge sites per mass of clay *(Tournassat et al., 2003)*. Given the same density for all clay particles, the amounts of edge sites are proportional to the aspect ratio. These calculations were done and reported in this report (see Table 2-12) for different montmorillonite suspensions. The results showed that mass normalized site density may vary by a factor of six between the suspensions containing the largest or the smallest isolated clay fractions. This may lead to variations in the mean sorption properties for the different suspensions. Present approaches neither account for surface site heterogeneity nor the possible effects of particle morphology and roughness (see e.g. *(Boily and Kozin, 2014; Hiemstra and Van Riemsdijk, 1991; Lützenkirchen et al., 2002)*) on clay edge surface reactivity. On the basis of the bond valence principle *(Hiemstra et al., 1996)*, Tournassat et al. *(Tournassat et al., 2004a)* showed that montmorillonite particles exhibit a large variety of surface sites, whose proportions vary depending on exposed crystal faces at the solid-water interface. Since all this suggests that clay colloid sorption properties may vary between different isolated clay size fractions, this

work aims at investigating the influence of the exposed lateral surface area of montmorillonite colloids (which is related to their size) on the adsorption of trace concentrations of RNs in the synthetic groundwater (SGW, see Section 2.1.1.2) representing a glacial meltwater type *(Geckeis et al., 2004; Kunze et al., 2008; Möri et al., 2003)*. The term "clay colloids" will refer to aggregates, consisting of stacks of several clay mineral layers. Aggregates were chosen to name the colloids due to their thickness (from 18 up to 70 nm), based on previous work *(Norrfors et al., 2015)*. The seven montmorillonite dispersions used for adsorption studies with different mean particle sizes and particle size distributions, including one that contains fulvic acids (FA), are those described previously (see § 2.1.1.2). The RNs are the following: ^{232}Th(IV), ^{99}Tc(VII), ^{233}U(VI), ^{237}Np(V) and ^{242}Pu(IV). The equilibration time varies from 3 days up to six months. The 2 sites protolysis non-electrostatic surface complexation and cation exchange (2 SPNE SC/CE) model *(Bradbury and Baeyens, 2011)* is used to predict the uptake of RNs. In addition, an attempt to estimate the influence of the expected amounts of edge sites on the RN adsorption process is done.

Material and Methods

Montmorillonite colloids, fulvic acids, synthetic ground water (SGW). The description of the preparation of the clay colloidal suspensions, fulvic acids and synthetic ground water can be found in the present report, Section 2.1.1.2.

Radionuclide cocktail. A radionuclide cocktail containing the elements: ^{232}Th, ^{99}Tc, ^{233}U, ^{237}Np and ^{242}Pu was prepared in a glove box under Ar atmosphere in 0.1 M HCl. The seven clay dispersions, diluted to 20 mg colloids/L in the SGW, were spiked with the cocktail. The pH was 8.9 ± 0.3 in all samples after addition of RNs without any pH adjustments. The initial RN concentrations were checked by ICP-MS and were $[^{232}$Th(IV)$]$ = 10^{-8} M, $[^{99}$Tc(VII)$]$ = $5 \cdot 10^{-9}$ M, $[^{233}$U(VI)$]$ = 10^{-8} M, $[^{237}$Np(V)$]$ = 10^{-8} M and $[^{242}$Pu(IV)$]$ = $2 \cdot 10^{-9}$ M. These values were used as total concentrations in all calculations. ^{242}Pu added as ^{242}Pu(III) was expected to oxidize to Pu(IV) under the SGW experimental conditions. All RN concentrations except for Pu were below the respective solubility limits in the carbonated SGW, according to literature (Np(V) *(Guillaumont and Mompean, 2003; Neck et al., 1992; Runde et al., 2002)*, Tc(VII) *(Alliot et al., 2009)*, U(VI) and Pu(IV) *(Huber et al., 2011)*, Th(IV) *(Östhols et al., 1994)*).

Experimental conditions and procedure. All experiments were performed at room temperature in a glove box under Ar atmosphere (<1 ppm O$_2$). pH was measured with a semi micro Ross electrode (81-03, Orion Co.) in combination with a digital pH-meter (720A, Orion Co.). This set-up was calibrated using four commercial buffer solutions (Merck). The redox potentials in the clay dispersions were measured using an Orion 525A (Eh meter) and a Pt electrode combined with Ag/AgCl reference system (Metrohm). Raw data were converted into Eh vs. standard hydrogen electrode (SHE) by correcting for the potential of the reference electrode. A commercial redox-buffer (+220 mV, Schott instruments) was used for calibration. An equilibration time of

30 min (while softly stirring) was applied for all Eh measurements. Uncertainties in Eh measurements were ± 50 mV *(Altmaier et al., 2010; Kirsch et al., 2011)*. Each batch adsorption sample was prepared in duplicate. For monitoring radionuclide adsorption, aliquots of the samples were taken after 72 h (~3 days), 260 h (~2 weeks), 580 h (~1 month) and 3800 h (~6 months). During the equilibration times, the samples were sealed and remained unshaken in the glovebox. Initially, the top 0.5 mL of the sample was analysed by ICP-MS to obtain the amount of stable montmorillonite colloids in the dispersion. Thereafter, approximately 4 mL of each sample was transferred into ultra-centrifugation vials, sealed by welding inside the glove box and afterwards ultra-centrifuged (Beckman XL-90, rotor type 90Ti) for 1h at 90.000 rpm (centrifugal force of approximately $7 \cdot 10^5 \times g$). Subsequently, a volume of 0.5 mL of the ultra-centrifuged supernatants was sampled and analysed by ICP-MS. This ultra-centrifugation procedure has been proven to effectively remove montmorillonite colloids and thereby the RNs associated to colloids *(Altmaier et al., 2004)*. When the experiment ended (i.e. after 6 months), all samples were characterised by pH = 8.9 ± 0.3 and $Eh_{(SHE)}$ = +230 ± 50 mV. The distribution of RNs was calculated and defined as (i) the amount of soluble species RNs in dispersion (%Free), (ii) RNs associated to montmorillonite colloids (%Colloid) and (iii) the amount of RNs associated to particulates (i.e. settled particles, %Part). When FA was present initially, 70% of it was found free in the dispersion after fractionation. No distinction between soluble RNs species and dissolved FA-RN complexes is therefore possible. The concentration of RNs as soluble species was measured in the supernatant after ultra-centrifugation. Colloidal RN concentration was determined from the difference in concentration before and after ultra-centrifugation. Particulate RNs corresponds to the fraction that was the remaining based on the initial concentration. All results presented are mean values of duplicate samples with their standard deviation. Dispersion S3.5 had the same size distribution as S3.5^{UC}, and identical adsorption results were obtained for these two dispersions, indicating a good reproducibility of the fractionation procedure developed *(Norrfors et al., 2015)*. Results from the sorption experiments are expressed as distribution coefficients (K_D) for each RN. K_D values were calculated for the overall RN adsorption as "average K_D values", which does not distinguish between suspended (%Colloids) and particulate (settled particles, %Part) clay. The expression for K_D is given in Equation 7:

$$K_D = \frac{[RN]_{Tot} - [RN]_{free}}{[RN]_{free}} \cdot \frac{1}{m_{Clay}} \ (dm^3/kg)$$

Equation 7

where $[RN]_{Tot}$ and m_{Clay} are the total, initial concentrations of RNs and montmorillonite, respectively. $[RN]_{free}$ is the concentration of soluble species of RNs in solution after a given equilibration time. Uncertainties associated to log K_D refer to the standard deviation (σ) calculated from the results of duplicates. Additionally, with the mean amount of adsorption sites estimated for each clay dispersion, a K_D value normalized to the amount of sites ($K_{D,sites}$) was calculated. The relationship between the mass-normalized (K_D), the sites-normalized values ($K_{D,sites}$) and the amount of sites in one clay dispersion ([Sites]) is given by Equation 8:

$$\log K_{D,sites} \; (dm^3/mol \; of \; sorption \; sites)$$
$$= \log K_D \; (dm^3/kg) - \log[Sites] \; (mol/kg) \qquad \textbf{Equation 8}$$

As mentioned above, the montmorillonite dispersions (S0 and S1) containing the largest clay particles contain a mixture of colloidal sizes. In these dispersions, the larger clay particles sedimented with time, whereas the smaller clay colloids remained suspended. Therefore, a better evaluation of RN adsorption onto different colloid sizes could be made in these dispersions if the average K_D value was compared to the K_D value for the particulates (settled, large particles) in the clay dispersion, i.e. $K_{D,part}$, defined as (Equation 9):

$$K_{D,part} = \frac{[RN]_{Tot} - [RN]_{free} - [RN]_{colloid}}{[RN]_{free}} \cdot \frac{1}{m_{part}} \; (dm^3/kg) \qquad \textbf{Equation 9}$$

where $[RN]_{colloid}$ is the amount of RNs associated to stable, suspended clay colloids and m_{part} the amount of clay particulates.

Geochemical speciation modelling. Predominance diagrams were plotted with PhreePlot *(Kinniburgh and Cooper, 2009)*, which contains an embedded version of the geochemical speciation program PHREEQC *(Parkhurst and Appelo, 1999)*. Stability constants for dissolved species and solubility calculations were included in the NEA database (U/Np/Pu: *(Guillaumont and Mompean, 2003)*, Tc: *(Rard, 1999)*, Th: *(Rand et al., 2009)*). Fluoride and carbonate complexes for all RNs were considered in the calculations. The fluoride complexes did not play here a significant role. The formation constants of $Pu(OH)_2(CO_3)_2^{2-}$ and $Np(OH)_2(CO_3)_2^{2-}$ selected by THEREDA (Release 2013-08-02) were used in all calculations. The selected constants (in the NEA and THEREDA databases) were consistent with each other. The Davies equation was used for activity coefficient calculations. Reduction of sulfate and CO_2 was suppressed in the calculations. The cation exchange capacity (CEC) was 0.87 eq/kg *(Marques Fernandes et al., 2012)*. Preliminary tests showed that cation exchange reactions had no significant influence at pH 8.9, so that they were subsequently neglected. Bradbury and Baeyens *(Bradbury and Baeyens, 2011)* applied a linear additive model (LAM) to predict adsorption on natural clay rocks. For bentonite, they considered montmorillonite as the only adsorbent for radionuclides. In the present case, montmorillonite represents 75 wt.% of MX80 bentonite. The 2 Site Protolysis Non Electrostatic Surface Complexation and Cation Exchange (2SPNE SC/CE) model for surface complexation and cation exchange reactions at montmorillonite surfaces *(Bradbury and Baeyens, 2005; Bradbury and Baeyens, 2006)* involves two types of proton active sites to describe the titration data, but only one type to bind cations by the model approach. Cation binding occurs on weak sites ([≡WOH] = $4 \cdot 10^{-2}$ mol/kg) as well as on less abundant strong sites ([≡SOH] = $2 \cdot 10^{-3}$ mol/kg) with identical acid-base properties. Bradbury and Baeyens *(Bradbury and Baeyens, 2005; Bradbury and Baeyens, 2006)* determined surface complexation constants for Np(V), U(VI) and Th(IV) to strong sites of montmorillonite. Due to the low RN concentrations investigated in this study and the lack of RN surface complexation

constants for the weak sites, only the strong sites were considered as adsorption sites. In solution, all actinides were predominately present as neutral or negative species due to complexation with OH^-/CO_3^{2-}, and Tc(VII) was present as a negative species (TcO_4^-). Marques-Fernandez et al. *(Marques Fernandes et al., 2012)* determined thermodynamic constants for the formation of ternary montmorillonite-U(VI)-carbonate surface complexes. Ternary montmorillonite-Np(V)-carbonate surface complexes were not considered to exist in our conditions, and therefore were not included *(Turner et al., 1998)*. Adsorption of TcO_4^- to clays can be neglected *(Guillaumont and Mompean, 2003; Ticknor et al., 1996)*. After addition, Np(V) might be reduced to Np(IV) at the clay surface, especially at long equilibrium times, as observed in the Np-illite system *(Marsac et al., 2015b)*. The oxidized form adsorbs less strongly to minerals than Np(IV). Surface complexation constants for Np(IV) are unknown for montmorillonite, but Bradbury and Baeyens *(Bradbury and Baeyens, 2005; Bradbury and Baeyens, 2009)* proposed linear free energy relationships (LFER) between cation hydrolysis constants (Equation 10) and surface complexation constants (Equation 11) for illite and montmorillonite within the 2SPNE SC/CE model.

$$M^{n+} + xH_2O \rightleftharpoons M(OH)_x^{(n-x)} + H^+, \text{ giving } ^{OH}K_x \qquad \textbf{Equation 10}$$

$$\equiv SOH + M^{n+} + (x-1)H_2O \rightleftharpoons\ \equiv SOM(OH)_{(x-1)}^{(n-x)} + xH^+, \text{ giving } ^{S}K_{(x-1)} \qquad \textbf{Equation 11}$$
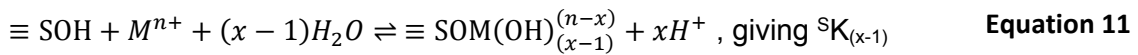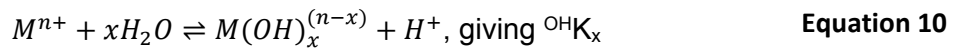
The LFERs for montmorillonite (Equation 12) and illite (Equation 13) are:

$$\log {}^{S}K_{(x-1),mont} = 8.1 + 0.90 \times \log {}^{OH}K_x \qquad \textbf{Equation 12}$$

$$\log {}^{S}K_{(x-1),ill} = 7.9 + 0.83 \times \log {}^{OH}K_x \qquad \textbf{Equation 13}$$

Uncertainties associated to the parameters of the LFERs were omitted for simplicity. According to Marsac et al. *(Marsac et al., 2015b)* the formation of $\equiv SONp(OH)_4^-$ is required to describe Np(IV) adsorption to illite. The same might be true for montmorillonite, as in the Th(IV) case *(Bradbury and Baeyens, 2005)*. Unfortunately, the formation constant of $\equiv SOAn(OH)_4^-$ is not available from a LFER due to lack of the formation constant for the corresponding aqueous species ($An(OH)_5^-_{(aq)}$). However, the combination of Equation 12 and Equation 13 can be used to generate an illite-montmorillonite LFER, which can be applied to Np(IV), using surface complexation constants determined by Marsac et al. *(Marsac et al., 2015b)* (Equation 14):

$$\log {}^{S}K_{(x-1),mont} = 1.08 \times \log {}^{S}K_{(x-1),ill} - 0.46 \qquad \textbf{Equation 14}$$

Based on similar hydrolysis, the Np(IV) constants were used for Pu(IV). This procedure ensures that the sets of surface complexation constants and hydrolysis constants are consistent with each other for Pu(IV). By analogy with Np(IV), U(IV) and Tc(IV) surface complexes might form at the montmorillonite surface. Given the lower redox potentials of the U(VI)/U(IV) and Tc(VII)/Tc(IV) couples compared to Np(V)/Np(IV), reduction of U(VI) or Tc(VII) was not expected at the relatively high Eh in our experiments (see the results and discussion section). Thus, U(IV) and Tc(IV) adsorption to montmorillonite was not further considered. Cations with different chemical behaviour (related to their oxidation state) do not compete for the same

adsorption sites *(Bradbury and Baeyens, 2005)*. They have to be modelled by considering several types of binding sites for the different RNs, the different sites exhibiting the same surface site density. The tetravalent RNs Th(IV), Np(IV) and Pu(IV) were expected to compete for the same strong sites. Applying the concept further, Np(V) and U(VI) have no competitor for their respective sites in our study. The natural occurrence of ^{238}U, was not taken into account in the calculations, which apply only to the ^{233}U added to the clay dispersions. The surface complexation reactions and constants used in the modelling can be found in the supporting information file (supplementary data) of a recent publication *(Norrfors et al., 2016a)*, see here: http://www.sciencedirect.com/science/article/pii/S0169131716300187. Our simulations were based on the estimations and assumptions discussed above. The impact of carbonates on the adsorption of most RNs onto clays has not been investigated. Therefore, these modelling results should only be considered as semi-quantitative and are mainly used as a guide for experimental data interpretation.

Results and Discussion

Batch adsorption results - Stability of montmorillonite colloids. The evolution of the suspended Al-concentration at a given time, relative to the initial Al-concentration, allows to estimate the montmorillonite particle stability. The percentages of stable colloids in the different dispersions were determined after 3 days, 2 weeks, 1 month and 6 months. No significant sedimentation was observed after 3 days in any dispersion except in those containing larger montmorillonite colloids, i.e. S0. Sedimentation was observed at longer times (e.g. only 55% and 82% remain suspended after 6 months in the dispersions S0 and S1, respectively). The long term stability of the undiluted clay dispersions was already examined (see Section 2.1.1.2) where, in agreement, 43% and 70% of the colloids remained stable in dispersions S0 and S1 after 2 months without shaking *(Norrfors et al., 2015)*. No spontaneous agglomeration of the colloids was observed and the clay dispersions with smaller colloids (i.e. S3, S3.5, S3.5^{UC} and S3.5^{UC,FA}) remained stable during the two months period. Similar trends were found here, even though the dispersions were diluted to 20 mg/L. Interestingly, the colloidal dispersion obtained after sequential (ultra-) centrifugation (S3.5) and the dispersion obtained from one direct ultra-centrifugation step (S3.5^{UC}), have a similar size distribution *(Norrfors et al., 2015)*, and exhibit the same high colloidal stability. Predominance pH-Eh diagrams, speciation and elemental distribution. The predominance pH-Eh diagrams for Tc, U, Np and Pu in solution are calculated by Phreeplot and shown in Figure 2-19. The pH-Eh conditions measured at the end of the experiment (after 6 months, pH = 8.9 ± 0.3 and Eh = 230 ± 50 mV) are shown as a black square in each diagram. The elemental distribution of the different elements between clay particulates, stable clay colloids and soluble species are reported exemplary for the suspension S0 over time in Figure 2-20.

Technetium adsorption. The pH-Eh conditions measured at the end of the experiment (after 6 months, pH = 8.9 ± 0.3 and Eh = 230 ± 50 mV) are in the stability field of Tc(VII) (i.e. TcO$_4^-$$_{(aq)}$).
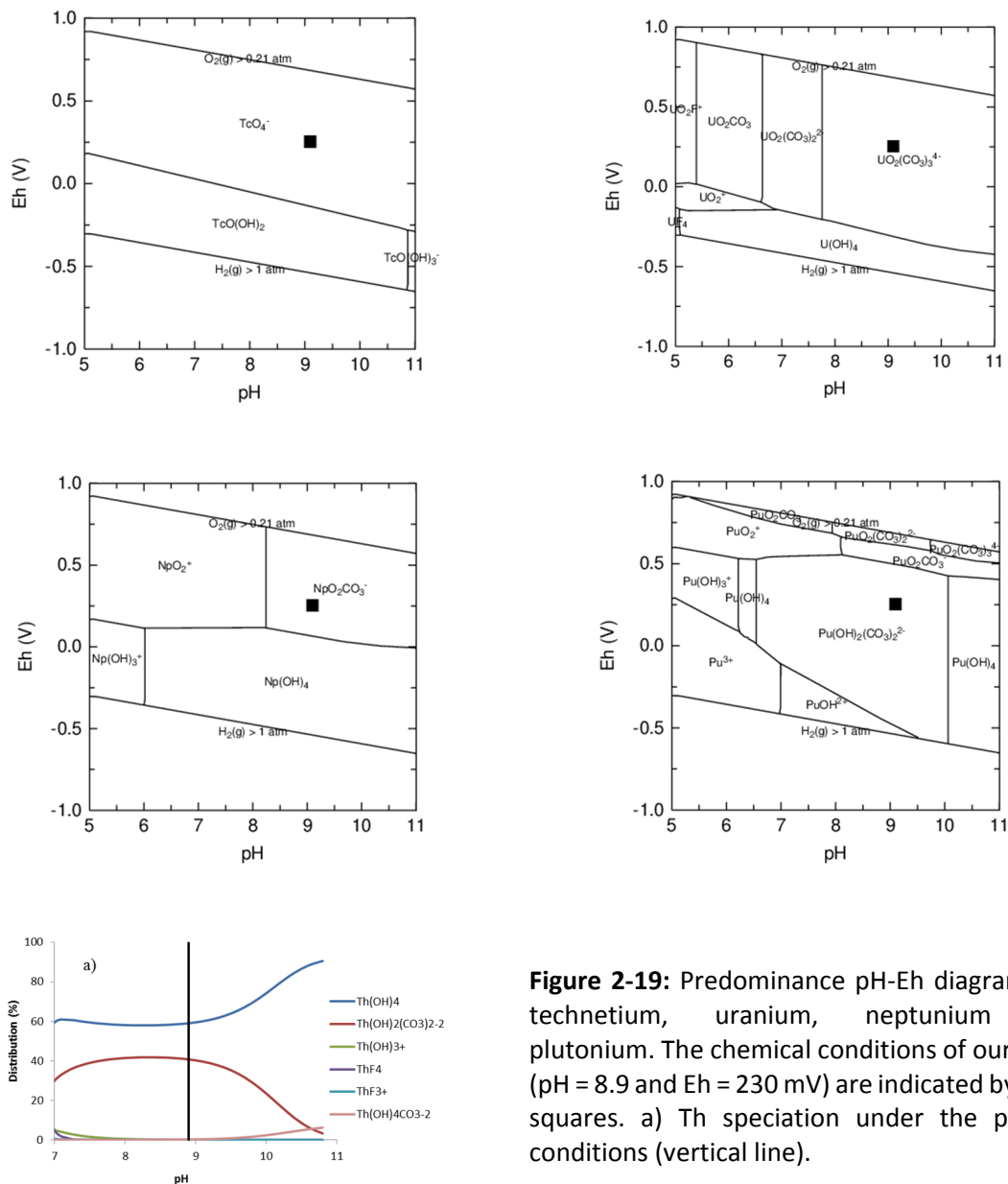
Figure 2-19: Predominance pH-Eh diagrams for technetium, uranium, neptunium and plutonium. The chemical conditions of our study (pH = 8.9 and Eh = 230 mV) are indicated by black squares. a) Th speciation under the present conditions (vertical line).

No reduction of Tc(VII) to Tc(IV) was thus expected. In addition, no adsorption of Tc was expected due to the low solid to liquid ratio investigated and because of weak adsorption of TcO$_4^-$ $_{(aq)}$ onto mineral surfaces *(Guillaumont and Mompean, 2003; Huber et al., 2011; Ticknor et al., 1996)*. The distribution of Tc between particulates, suspended colloids and soluble species in the suspension S0 is shown Figure 2-20 and for all other dispersions, results are accessible as supplementary data of the published work of Norrfors et al. *(Norrfors et al., 2016a)*. The concentrations of Tc(VII) remain constant in solution over the 6 months of measurements in all dispersions within the analytical uncertainties. This construes the expectations that no reduction of technetium or adsorption onto clay colloids occurs. Slow reduction of Tc(VII) to Tc(IV) in presence of synthetic or Febex montmorillonite colloids has been previously noted in natural groundwater of similar low ionic strength (~1 mM), at pH = 9 after 1 month *(Huber et*

59

al., 2015), which was related to a decrease in Eh to approximately -200 mV after 1 month, as reported by the authors. Since most FA remains free in dispersion, distinction between Tc-FA complexes and soluble species of Tc is not possible and Tc distribution in S3.5, S3.5^{UC,FA} and S3.5^{UC} was identical, as expected.

Uranium adsorption. Due to the presence of carbonate in the SGW and based on the geochemical calculations, uranium should be mainly present as $UO_2(CO_3)_3^{4-}{}_{(aq)}$, as seen on the pH-Eh predominance diagram (Figure 2-19). U(VI) is known to form highly soluble complexes with carbonate at pH 9 *(Bernhard et al., 2001; Bradbury and Baeyens, 2011; Hartmann et al., 2008; Marques Fernandes et al., 2012; Regenspurg et al., 2009)*. In a previous study *(Marques Fernandes et al., 2012)*, a log (K_D (dm^3/kg)) value of 2.7 was reported for U(VI) adsorption onto montmorillonite in 1 mM HCO$_3^-$ and 0.1 M NaClO$_4$ at pH 9. It would correspond to an uptake of 1% uranium with the present clay concentration (20 mg/L). Our simulation for the SGW indeed predicts ~1% uptake. In Figure 2-20, the experimental results for uranium adsorption for dispersion S0 are presented as the distribution of U between particulates, suspended colloids and soluble species as a function of equilibration time. The results for the other clay dispersions can be found in the supporting information file (supplementary data) of a recent publication *(Norrfors et al., 2016a)*, see here: http://www.sciencedirect.com/science/article/pii/S0169131716300187 .

Within the experimental uncertainties, no significant uranium (^{233}U) adsorption onto montmorillonite was detected, in any of the clay dispersions, at any equilibration time. Instead, in line with published studies *(Marques Fernandes et al., 2012)* and model predictions, uranium remains as aqueous carbonate complexes in all clay dispersions. Since FA does not strongly adsorb onto montmorillonite at pH 8.9, the results for dispersion S3.5^{UC,FA} were not expected to differ from those for dispersions in absence of FA, which agrees with the distribution presented. Interestingly, a significant release of naturally occurring ^{238}U in the raw MX80 clay was observed in all dispersions, attributable to the presence of carbonates in the SGW, in line with the predominance of soluble U-carbonate complexes.

Neptunium adsorption. Np should prevail as Np(V) as NpO$_2$CO$_3^-$ in the SGW (pH = 8.9 and Eh = 230 mV) according to the pH-Eh predominance diagram (Figure 2-19) and remain in solution due to weak Np(V) uptake onto montmorillonite *(Missana and Geckeis, 2006; Turner et al., 1998; Wu et al., 2009)*. The Np distribution in the S0 dispersion is presented in Figure 2-20 at different equilibration (sorption) times. The results for the other clay dispersions can be found in the supporting information file (supplementary data) of a recent publication *(Norrfors et al., 2016a)*, see here: http://www.sciencedirect.com/science/article/pii/S0169131716300187 No Np uptake on montmorillonite was detected for any clay dispersion at any equilibration time, as expected and consistently with recently developed predictions considering plausible Np induced reduction onto montmorillonite surface to occur *(Marsac et al., 2015b)*. As for U and Tc, the presence of FA in S3.5^{UC,FA} did not change the Np uptake as expected, since FA remains predominantly in solution.
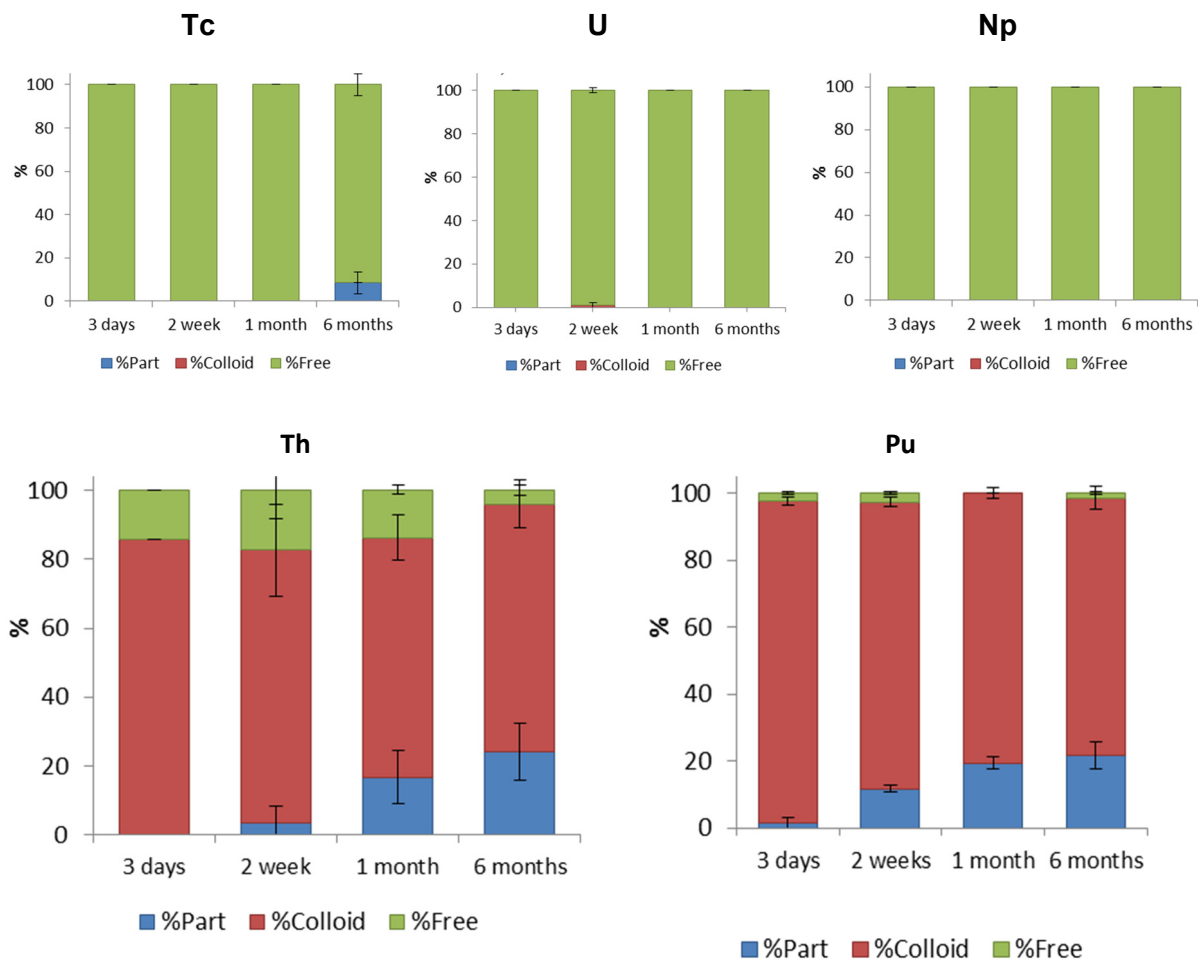
Figure 2-20: Elemental distribution, in percentage, between particulates (%Part, blue), stable clay colloids (%Colloid, red) or soluble species (%Free, green) measured in the dispersion S0, at different equilibration (sorption) times. The results obtained for the other clay dispersions are presented in the Supporting Information of the work of Norrfors et al. 2016.

Thorium adsorption. Thorium speciation in the SGW is shown as a function of pH in (Figure 2-19a). Th was predicted to be present as $Th(OH)_4(aq)$ (60%) and $Th(OH)_2(CO_3)_2^{2-}$ (40%) at pH 8.9, marked as a vertical line in (Figure 2-19a). The model predicts 83% of Th(IV) uptake onto montmorillonite, corresponding to log (K_D (dm^3/kg)) = 5.4. The distribution of Th in the S0 dispersion between particulates, suspended colloids or soluble species as a function of equilibration time is presented Figure 2-20. The results for the other clay dispersions can be found in the supporting information file (supplementary data) of a recent publication *(Norrfors et al., 2016a)*, see here: http://www.sciencedirect.com/science/article/pii/S0169131716300187. Thorium was strongly adsorbed in all clay dispersions. The amount of Th which settled increased with time in S0 (Figure 2-20). This agrees with the amount of clay particles which sedimented, as already mentioned. This indicates that a fraction of Th is associated with the unstable, large montmorillonite particulates. For the clay dispersions containing smaller colloids (S2→S3.5^{UC}),

no sedimentation was expected in line with the experimental results, according to the experimental uncertainties. The K_D values for Th in the different clay dispersions are presented as a function of equilibration time in Figure 2-21.
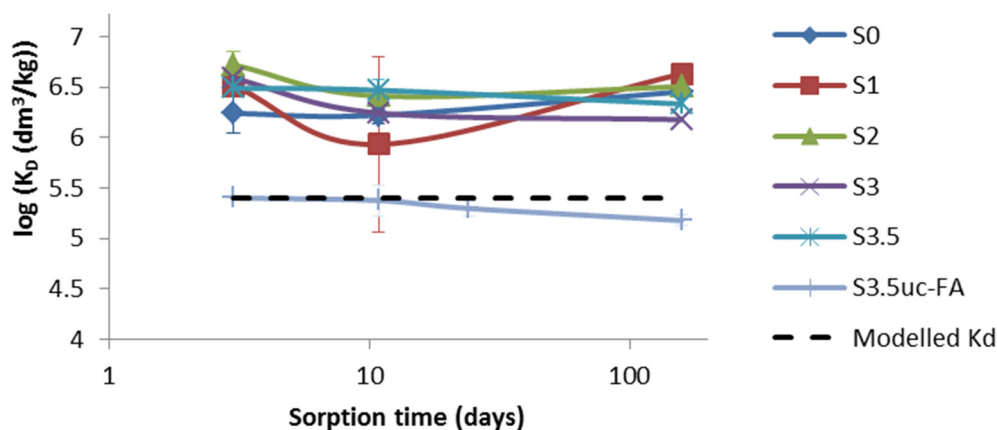
Figure 2-21: log (K_D (dm³/kg)) value with its standard deviation as a function of equilibration (sorption) time corresponding to the adsorption of Th in the different montmorillonite dispersions. The dashed line corresponds to the predicted value from modelling.

Data points for samples where the concentration of Th as soluble species were below the detection limit are not shown. No significant variations in Th uptake were found. Overall, no kinetic effects were observed. Our log (K_D (dm³/kg)) = 6.4 ± 0.5 was similar to log (K_D (dm³/kg)) = 6.4 ± 0.5 and log (K_D (dm³/kg)) = 5.3 ± 0.5 for batch adsorption experiments by Huber et al. *(Huber et al., 2011; Huber et al., 2015)* and Bouby et al. *(Bouby et al., 2011)*, respectively, in a low ionic strength (~1 mM) groundwater at pH = 8.3 - 9.5 at carbonate concentrations of ~0.05 mM, comparable to the SGW used in our study. The experimental K_D value was slightly higher than expected from modelling (dashed line in Figure 2-21). The model for Th(IV) uptake had been calibrated with the experimental results of Bradbury and Baeyens *(Bradbury and Baeyens, 2005)*, involving a measured log (K_D (dm³/kg)) ≈ 5.5 for Th at pH = 9 in 0.1 M NaClO₄, i.e. in higher ionic strength and in absence of carbonate. In presence of FA (S3.5[UC,FA]), the Th uptake onto clay colloids was significantly lower. Log (K_D (dm³/kg)) was reduced to 5.3 ± 0.5 and remains constant over time (Figure 2-21). FA complexed Th(IV) compete with Th-montmorillonite surface complexes. This measured K_D value corresponds to a decrease in the amount of adsorbed Th by approximately 15%. Pan et al. *(Pan et al., 2011)* reported a decrease in log (K_D (dm³/kg)) from ~6.0 to ~5.4 after addition of FA in absence of carbonate, at pH = 9 and in 50 mM NaCl, with a FA to Na-bentonite ratio of 1:5 compared to 1:10 in our study. Yu et al. *(Yu et al., 2008)* reported an even larger decrease in log (K_D (dm³/kg)) value in presence of FA (from ~5.2 to ~3.9) with a FA to bentonite ratio of 1:30 at pH = 9, at slightly higher ionic strength (0.1 M NaNO₃). Overall, the present results can be considered to be in line with literature data.

Plutonium adsorption. In the SGW, Pu was expected to prevail as Pu(IV) mainly Pu(OH)$_2$(CO$_3$)$_2^{2-}$(aq) according to the predominance pH-Eh diagram (Figure 2-19). Pu(IV) is known to strongly adsorb onto montmorillonite *(Geckeis et al., 2004; Latrille et al., 2006; Lujanienė et al., 2007; Zavarin et al., 2012)* and to be stabilized at mineral surfaces beyond the predominance field of aqueous Pu(V/VI) *(Hixon et al., 2013; Kalmykov Stepan et al., 2015; Marsac et al., 2015a; Powell et al., 2005).* Even though the total amount of Pu would exceed the solubility limit of Pu(IV) *(Huber et al., 2011)*, the final aqueous Pu concentration was always below the saturation with respect to PuO$_{2(am,hydr)}$ due to strong adsorption onto montmorillonite. Furthermore, since adsorption is usually faster than nucleation and precipitation, precipitation of Pu was not expected *(Zhao et al., 2011)*. An uptake of 97% Pu(IV) was predicted by the model, which corresponds to log (K$_D$ (dm^3/kg)) = 6.3 in our experimental conditions. The distribution of Pu as a function of equilibration time is presented for the clay dispersion S0 in Figure 2-20. Pu was largely associated to montmorillonite. The distribution of Pu in the other clay dispersions is presented in the supporting information file (supplementary data) of a recent publication *(Norrfors et al., 2016a)*, see here: http://www.sciencedirect.com/science/article/pii/S0169131716300187,and was comparable to the results for S0. Similarly, to Th, a part of Pu is associated with sedimenting particulates present in the clay dispersions S0. In the dispersion with smaller colloids, no Pu association to particulates was found. K$_D$ values for Pu adsorption to each clay suspension are presented as a function of equilibration time in Figure 2-22. Pu uptake does not significantly evolve over the first month, with an average distribution coefficient for all dispersions of log (K$_D$ (dm^3/kg)) = 5.7 ± 0.5. The predicted log (K$_D$ (dm^3/kg)) = 6.3 (dashed line in Figure 2-22) agrees well with the experimental data, though the Pu(IV) surface complexation constants for the 2 SPNE SC/CE model used in this study were based on several approximations. Pu(IV) predominated in the SGW, as seen by its high uptake even if the uptake was slightly lower than for Th (Figure 2-21). The slight increase in Pu uptake over time (almost insignificant given the error bars) might suggest the initial presence of a small fraction of Pu(III). Pu(III) oxidation to Pu(IV) may be kinetically controlled. Consistently, after 6 months equilibration time, the Pu uptake was similar to values reported for Th and predicted by the model. All this indicates a consistent high adsorption of the two tetravalent RNs. Previous studies *(Geckeis et al., 2004; Huber et al., 2015)* reported log (K$_D$ (dm^3/kg)) = 5.4 ± 0.5 and log (K$_D$ (dm^3/kg)) = 6.4 ± 0.5 in ground waters of low ionic strength (~1 mM) and pH = 9.5 – 9.6 for adsorption of Pu(IV) to montmorillonite. These values were consistent with the present work despite higher Eh in our study (0 to -200 mV in *(Geckeis et al., 2004; Huber et al., 2015)*), due to the large stability field of Pu(IV) at pH ≈ 9. As for Th, in presence of FA, a lower Pu uptake is noticed since FA was acting as a competing ligand (Figure 2-22). Pu adsorption in the presence of FA remained constant at log (K$_D$ (dm^3/kg)) = 5.1 ± 0.5. In previous published work, the reported competitive effect of added FA differed. Ticknor et al. *(Ticknor et al., 1996)*
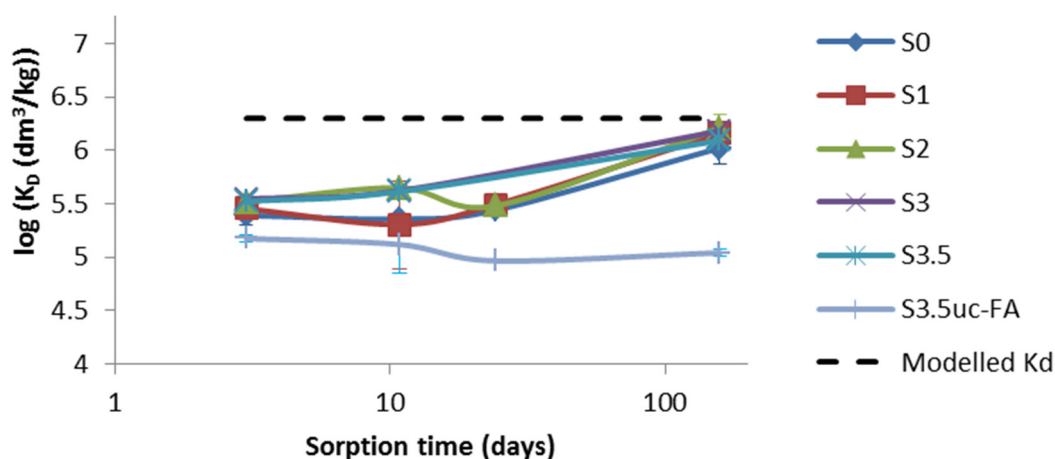
Figure 2-22: log (K_D (dm^3/kg)) value with its standard deviation as a function of equilibration (sorption) time corresponding to the adsorption of Pu in the different montmorillonite dispersions. The dashed line corresponds to the predicted value from modelling.

investigated Pu uptake by montmorillonite ([Pu(IV)] = $1.1 \cdot 10^{-10}$ M, m/V = 25 g/L) in the presence of FA (0 – 4.84 mg/L) at pH = 7.7, with 56 mg/L HCO$_3$ and ionic strength of ~0.2 M, and observed a maximum decrease in log (K_D (dm^3/kg)) from ~4.8 to ~3.5, even though their FA to montmorillonite ratio was far less than in our study. On the opposite, Boggs et al. *(Boggs et al., 2015)* did not find any effect of FA addition at pH = 8 in 0.01 M NaCl. In that study, the FA to montmorillonite ratio was higher (m/V = 0.1 g/L, [FA] = 1.5 mg/L, [Pu(IV)] = 10^{-10} M). A decrease in Pu adsorption was expected under our conditions as suggested by the Th results (Figure 2-21) and similar studies with gibbsite, FA and Pu(IV) at pH 8 – 10 in 0.1 M NaCl *(Simpkins, 2011)*.

Colloidal size effect on adsorption of RNs onto montmorillonite. Within the analytical uncertainties (see Figure 2-21 and Figure 2-22) any of the tested clay colloid dispersions particularly favour adsorption of Th(IV) and Pu(IV). To better compare the amount of adsorbed RNs, the estimated amounts of edge sites (Section 2.1.1.2) were used. It suggests (Table 2-12) an increase by a factor of approximately six in the amount of sites (corresponding to both weak and strong sites according to the 2 SPNE SC/CE model) between the dispersions containing all the clay particle sizes (S0) and those more restricted to smaller sizes (S3.5^{UC}). A factor of six difference in the amount of adsorbed RNs could be expected, based on these estimations. K_D values normalized to the amount of sites ($K_{D,sites}$), instead of mass, using equation 2, yielded a maximal theoretical difference of log(6) = 0.8 units between the two dispersions S0 and S3.5. This value was similar to the experimental uncertainty for log K_D measurements often considered for strongly adsorbing elements (± 0.5 log units *(Bradbury and Baeyens, 2011)*), and explains why no significant difference in adsorption between the clay dispersions was detected in our study. To better compare the adsorption onto smaller and larger clay colloids, K_D values for the montmorillonite pertaining to the particulate phase ($K_{D,part}$, for the larger particles) were calculated using equation 3. This $K_{D,part}$ value can be compared to the K_D value of stable, suspended montmorillonite colloids (corresponding to smaller colloids). All clay dispersions were

poly disperse and in the dispersions with the largest colloids, the smaller colloids were present as well. From the amount of settled colloids, compared to the amount of Th in the particulate phase in dispersion S0 after 6 months (Figure 2-20), a log ($K_{D,part}$ (dm^3/kg)) = 6.2 ± 0.5 was obtained. This was similar to log (K_D (dm^3/kg)) = 6.3 ± 0.5 obtained for the smaller, stable dispersion S3.5. Consequently, the amount of adsorbed Th was similar for these two clay dispersions and no difference in K_D values related to the mean colloidal size in the clay dispersions could be inferred. Accordingly, if theoretically any difference in particle morphology and roughness depending on the size fraction might influence the mean clay reactivity, this was presently not evidenced. To summarize, no significant differences between adsorption of strongly adsorbing RNs onto the smallest and largest montmorillonite colloids could be deduced, so that an "average log (K_D)" should provide sufficient estimates for RN adsorption to bentonites. This "average log (K_D)" can be used in reactive transport modelling with confidence, which simplifies models for RN migration accordingly. To better study a potential effect of colloidal size, one may recommend the use of RNs which adsorb to clays more strongly than penta- hexa- and heptavalent RNs but more weakly than tetravalent RNs in these experimental conditions. For those RNs, the variation in RN uptake with size (if any) should be larger than the experimental errors. Accordingly, the task will be easier if very well size defined clay colloidal fraction may be isolated and used separately for comparison. While an ultimate statement concerning desorption properties related to the mean colloidal (particle) size for the added RNs cannot be made, an effect did occur for natural [238]U which varied significantly with the clay dispersion properties.

Conclusions

RN uptake onto size separated montmorillonite colloids was examined. Np(V), Tc(VII) and U(VI) were not found to adsorb onto montmorillonite under our experimental conditions. They remain present as aqueous species, mainly as $NpO_2CO_3^-$(aq), TcO_4^-(aq) and $UO_2(CO_3)_3^{4-}$(aq), respectively, while Th(IV) and Pu(IV) strongly adsorbed onto montmorillonite. If FA were present (as here during the fractionation step of the clay colloids), the amount Pu and Th associated with clay was significantly decreased. During the experimental observation period (up to 6 months), larger clay particles settled with time. A fraction of Th and Pu were adsorbed on these larger, unstable montmorillonite particles (i.e. in the particulate phase) and remained so. Although more accurate model parameters than the presently estimated ones would be required to predict RN sorption to clays, model predictions were qualitatively in line with experimental results. It is worth noting that further experimental and modelling studies for more reducing conditions are required to evaluate the impact of clay colloids on Np(IV), U(IV) and Tc(IV) transport.

No significant changes in adsorption behaviour of Th and Pu onto different sized clay colloids, expressed as mass-normalized K_D values, were found. Between the clay dispersions with smallest and the largest mean sizes, an estimated difference by a factor of six in the amounts

of edge sites was calculated. This was too small to be detected given the experimental uncertainties. Therefore, based on our experimental results for MX-80, it seems appropriate to implement an "average log K_D" for all colloidal sizes in reactive transport modelling codes. While a variation in the montmorillonite colloidal size does not seem to influence the adsorption behaviour of strongly adsorbing RNs, the question remains if it affects RN desorption and desorption kinetics. This is presently investigated in a separate study.

2.1.3   Accelerated Mass Spectrometry (AMS) of Actinides in Ground- and Seawater: Simultaneous Analysis of U, Np, Pu Am, and Cm Isotopes below ppq Levels

Introduction

At the Grimsel Test Site, two in-situ field experiments devoted to investigate the colloid medi-ated transport and retention of actinides were performed in 2012 and 2013. In the first experi-ment, named RUN 12-02, ^{237}Np, ^{242}Pu and ^{243}Am, among other radionuclides dissolved in a solution of Grimsel groundwater, were injected into a dipole of a water conducting granodiorite shear zone fracture in the presence of bentonite colloids. Details on the setup of the experiment are given in Section 2.2.2. Groundwater samples sized 250 to 500 ml were continuously col-lected at the exit of the dipole employing an extraction flow close to natural conditions. The concentration of the injected actinides in the eluted groundwater samples was determined with SF-ICPMS. In this way, a high number of data were obtained that described the peak of the breakthrough curve that appeared within 27 days from the injection of the actinide tracers. In the tailing of the curve the actinides were present in the samples at levels lower than the de-tection limits (DL) of SF-ICPMS that are equal to 10 ppb (ca. 2×10^7 atoms of an actinide nu-clide). The limited sample size, which for the actual study was of 250 ml, taken together the ultra-trace concentration of the actinides (< 10 ppb) required the use of an appropriately sen-sitive analytical technique. Accelerator mass spectrometry (AMS) is presently the most sensi-tive analytical techniques for the determination of actinides. The key feature of AMS is that of being composed by two mass spectrometers linked by a tandem accelerator, which provides the dissociation of molecular ions and in this way the suppression of molecular isobaric back-ground. Furthermore, the acceleration of the ions to MeV energies in the tandem accelerator provides a strong reduction of tailing interferences. At the Vienna Environmental Research Accelerator (VERA), ^{236}U, ^{237}Np and ^{239}Pu can be discriminated relative to the highly abundant neighbouring mass of ^{238}U at levels ≤ 10^{-15} (1). Detection limits (DL) for actinide nuclides at a value of 10^4 atoms per sample are presently achieved. With such AS and DL, actinides nu-clides can be determined at levels down to 10^5 atoms in a sample (2) and with a relative sta-tistical uncertainty of ca. 32%. The determination of 10^7 atoms in a sample is then associated with a relative statistical uncertainty of ca. 0.02%. Another challenge in the ultra-trace determi-nation of ^{237}Np and of ^{243}Am lies in the non-availability of pure enough isotopic tracers for their mass spectrometric measurements. We have, therefore, investigated the use of non-isotopic tracers and developed an analytical method for the group determination of actinides with AMS (1). In the developed analytical method, the use of non-isotopic tracers is combined with a simplified chemical procedure, namely one concentration step using Fe(OH)$_3$ as actinides scavenger, that once converted to oxides, is directly used as cathode material for AMS. In the actual sample preparation, the chemical separation of the actinides from each other is avoided,

exploiting the exceptional AS of AMS instead. In this way different actinide nuclides can be measured sequentially from the same AMS sample. Such simplified chemical treatment is, furthermore, favoured by the reduced amount of matrix elements that is a consequence of the small sample size employed. The accuracy of the developed method was validated by analysing the Reference Material (FM) IAEA-443 – *Radionuclides in Irish Seawater* (3).

In the present study we have analysed with AMS six groundwater samples collected far in the tailing of the tracer pulse experiment breakthrough curve up to six months after the injection was initiated.

Materials and Methods

In order to find actinide tracers suited to our experiment, we have investigated several solutions of actinides for the presence of non-negligible concentrations of the isotopes under investigation, or of their isobars, namely nuclides with mass 237, 242 and 243. A reference solution of ^{239}Pu (Isotope Products Laboratories) and an in-house ^{248}Cm solution were found to have the degree of purity required by our objectives and were thereby chosen as double non isotopic tracers for the samples of RUN 12-02. The amount of each tracer added to the samples was ~ 10^8 atoms. New Teflon vessels were used for each sample and high purity water (18.2 MΩ) from a Milli-Q Element (Millipore) water supply system was employed for the preparation of the reagents. Nitric and hydrochloric acids of Rotipuran® Ultra quality, Metallic iron (Alfa Aesar Puratronic) and Ammonia of Suprapur grade were used as reagents. The tracers were gravimetrically added to the 250 ml groundwater samples together with 5 mL conc. HNO_3. The so obtained solutions were evaporated in 250 mL PFA beakers on a hot plate until the volume was reduced to 100 mL. Then, further 5 mL conc. HNO_3 were added. When the samples were evaporated almost to dryness, 5 mL conc. HNO_3 were added and fumed off until almost dryness; this step was repeated once more. After that, 5 mL conc. HCl were added three times and fumed off almost to dryness; the last time, together with the HCl also 1.5 mg Fe from a Fe solution in 1 M HCl were added. The residue was dissolved in 1 mL conc. HCl and transferred to a 50 mL centrifuge tube; 4 x 5 mL of 0.1 M HCl were sequentially used in order to rinse the beaker and transferred into the centrifuge tube. The concentration of Fe in the final solution was ~ 70 mg Fe/L. $Fe(OH)_3$ co-precipitation was obtained increasing the pH of the sample solutions to a value of ~ 8 with 25% NH_3. The samples were centrifuged at a RCF of ~ 1700 (corresponding to 3,500 rpm) for 8 minutes with a Heraeus Sepatech Centrifuge Varifuge 3.0, Thermo Scientific. The supernatants were discharged and 5 mL Milli-Q H_2O were added to the precipitates. Such suspensions were centrifuged at 3,500 rpm for 5 minutes. After the supernatants were discharged, the precipitates were dried at 80°C for 12 h and converted to Fe-oxides at 800°C for 3 h in a muffle furnace. The temperature was increased stepwise through 170°C, 210°C (melting and boiling points, respectively, of NH_4NO_3), 338°C and 520°C (decomposition and boiling points, respectively, of NH_4Cl) with each temperature step lasting two hours. The obtained samples were pressed into the sputter cathodes suited for the 3 MV tan-

dem accelerator VERA. Stripping with helium to the 3+ charge state at 1.65 MV terminal voltage was employed and the background caused by ^{235}U hydrides was suppressed with the 90° magnet in the analyser before the actinide ions were detected with a Bragg-type energy detector. Four procedural blanks (B1-B4), spiked with ^{233}U, were prepared and measured together with the water samples, following the same chemical procedure and with the same AMS setup. The actinide nuclides were sequentially scanned from the same sample. The measuring time dedicated to each nuclide was defined as inversely proportional to the square root of its count rate. In this way, the duration of the measurement of all nuclides in a sample was optimized so that the relative uncertainty due to counting statistics lay on the same order of magnitude for the investigated nuclides. In the measurement setup, the samples were periodically alternated with the procedural blanks, with the tuning cathodes containing the in-house reference material for U, Vienna-KkU (^{236}U/^{238}U ratio of $(6.98 \pm 0.32) \times 10^{-11}$) (4), with an in-house reference material for Pu isotopic ratios and with samples used to compensate for the different chemical and ionization yields of the actinides, as described in the following section. More details on the analytical method can be found in (2).

ACCURACY OF THE METHOD. The count rate associated with a certain concentration of an actinide nuclide depends on both the chemical yield of the sample preparation and the ionization yield of the Cs negative ions sputtering source of AMS. In order to study these two effects, six Grimsel groundwater samples, 250 ml each, were spiked with a multi-isotope solution obtained with known amounts of ^{233}U, ^{237}Np, ^{239}Pu, ^{243}Am and ^{248}Cm and submitted to the same chemical procedure of the samples. Reference solutions of ^{233}U (IRM040-1), ^{239}Pu (Isotope Products Laboratories) and ^{243}Am (P624735, Eckert & Ziegler Nuclitec GMBH), and in-house ^{237}Np and ^{248}Cm solutions were used to compose such calibration samples. The so obtained calibration samples were repeatedly measured together with the investigated samples in order to compensate for the different chemical and ionization yields of the several actinides. Since in this experiment these two effects are not separable, we define their combination as "chemical and ionization yield" (CIY) of the actinide element. The measured CIYs increased with the atomic number of the actinide element, according to literature data (5, 6). A precision between 8 % for Np and up to 40 % for Cm was observed in their determination relative to U. However, a precision of 16% and between 20 and 24% characterized the quantification of Np relative to Pu and of Am relative to Cm. The method was validated with the analysis of the Reference Material (RM) IAEA-443, radionuclides in Irish Seawater. The concentrations of ^{236}U, ^{237}Np and ^{239}Pu were measured in four aliquots, 100 g mass each, of the RM by using ^{233}U as non-isotopic tracer. The signals of ^{236}U, ^{237}Np and ^{239}Pu relative to ^{233}U were normalized with the corresponding values of the CIYs determined in two seawaters similarly like for the Grimsel groundwater samples. The obtained values were, within the uncertainties, consistent with literature data (7, 8, 9), as depicted in Figure 2-23. These results prove that the performed correction by the CIYs provides accurate determinations.
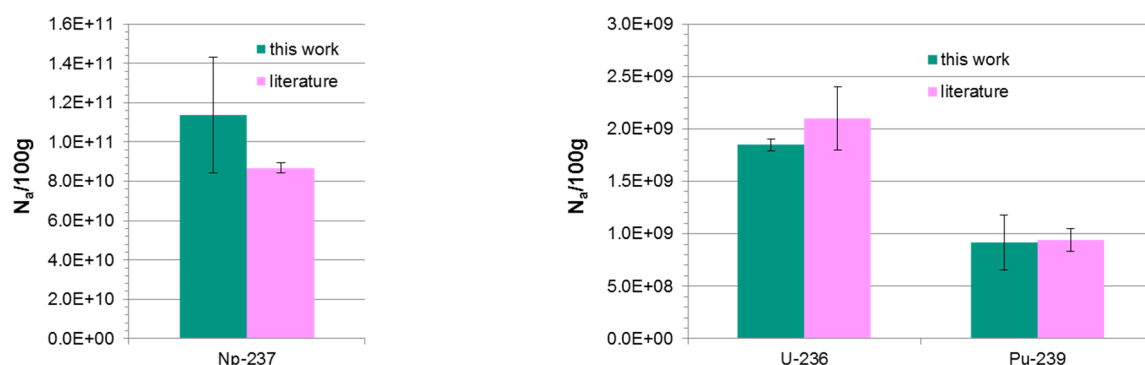
Figure 2-23: Agreement between the concentrations of ^{236}U, ^{237}Np and ^{239}Pu of the RM IAEA 443 measured in the actual study (green) and literature data (rosa).

Results and Discussion

Four procedural blanks were investigated. ^{236}U and ^{237}Np were detected in the blanks with maximum concentrations of $(1.1 \pm 0.3) \times 10^5$ atoms and $(1.2 \pm 0.4) \times 10^5$ atoms, respectively. The detection of mass 239, 242 u and 243 u in procedural blanks was also investigated, and found being below the DL. The six investigated groundwater samples from RUN 12-02 were collected from 60 up to 195 days after the start of the experiment. The detection of the injected tracers, ^{237}Np, ^{242}Pu and ^{243}Am by AMS was successful in the samples even down to the levels of fg/g and ag/g, corresponding to the lowest concentration of ~ 8×10^{-6} ppt for ^{243}Am and the maximum of ~ 8×10^{-3} ppt for ^{237}Np, as represented in Table 2-17. These values range down to three orders of magnitude below the DL of the employed SF-ICP-MS. The concentrations of ^{237}Np and ^{242}Pu have been determined by using ^{239}Pu as CIY spike and that of ^{243}Am by using ^{248}Cm.

Table 2-17: Concentrations of the injected tracers ^{242}Pu, ^{237}Np and ^{243}Am in the six investigated samples from the tailing of the breakthrough curve of RUN 12-05. The sample code and the corresponding sampling time are also listed.

sample code	days from injection	^{242}Pu (ppt)	^{242}Pu Rel. Unc (%)	^{237}Np (ppt)	^{237}Np Rel. Unc (%)	^{243}Am (ppt)	^{243}Am Rel. Unc (%)
BG-02	60	$(3.2\pm0.1)\times10^{-4}$	3	$(1.2\pm0.2)\times10^{-3}$	16	$(1.3\pm0.3)\times10^{-5}$	22
BG-09	75	$(2.51\pm0.09)\times10^{-4}$	4	$(8\pm1)\times10^{-4}$	16	$(7\pm1)\times10^{-6}$	23
BG-22	105	$(2.38\pm0.07)\times10^{-4}$	3	$(1.3\pm0.2)\times10^{-3}$	16	$(1.1\pm0.2)\times10^{-5}$	21
BG-25	165	$(6.1\pm0.1)\times10^{-4}$	2	$(1.7\pm0.3)\times10^{-3}$	16	$(3.4\pm0.7)\times10^{-5}$	20
BG-27	195	$(2.72\pm0.08)\times10^{-4}$	3	$(6\pm1)\times10^{-4}$	16	$(9\pm2)\times10^{-6}$	22
BG-47	210	$(8.6\pm0.4)\times10^{-5}$	5	$(5.4\pm0.9)\times10^{-4}$	16	$(8\pm0.2)\times10^{-6}$	24

The use of non-isotopic tracers has led to a higher uncertainty in the determination of ^{237}Np and ^{243}Am than of ^{242}Pu. In fact, the maximum relative uncertainty on the measured values of

^{242}Pu, solely due to the counting error, was equal to 5%. The relative uncertainties of the measured values of ^{237}Np and ^{243}Am reached 16% and 24%, respectively, since they were propagated from the uncertainties of the CIYs of Np relative to Pu, and Am relative to Cm, respectively, in the Grimsel groundwater (Table 2-17). The use of non-isotopic tracers, even though accompanied by an uncertainty higher than that associated solely to the counting statistics of the nuclides, made possible the quantitative determination of ^{237}Np and ^{243}Am in the samples far below the DL of SF ICP-MS as depicted in Figure 2-24. This outcome is of particular importance since such samples were unique and available to the present study only in a size of 250 ml. Furthermore, notwithstanding this higher uncertainty, a trend of concentration over time was visible in all investigated isotopes with a local maximum at the sampling time of 165 days, as shown in Figure 2-24. This can presently be interpreted as concentration fluctuations in the frame of an almost constant release of the tracers from the fracture zone where the migration experiment has been performed before and where a part of the injected actinide species had been retarded. These findings prove that the long term release and retention of actinide tracers can be studied with the developed analytical method in samples collected up to 6 months after the start of the experiment. Such data will provide extremely valuable information on the long-term retention and migration behaviour of actinide ions under geochemical conditions expected in crystalline formations at near natural conditions.
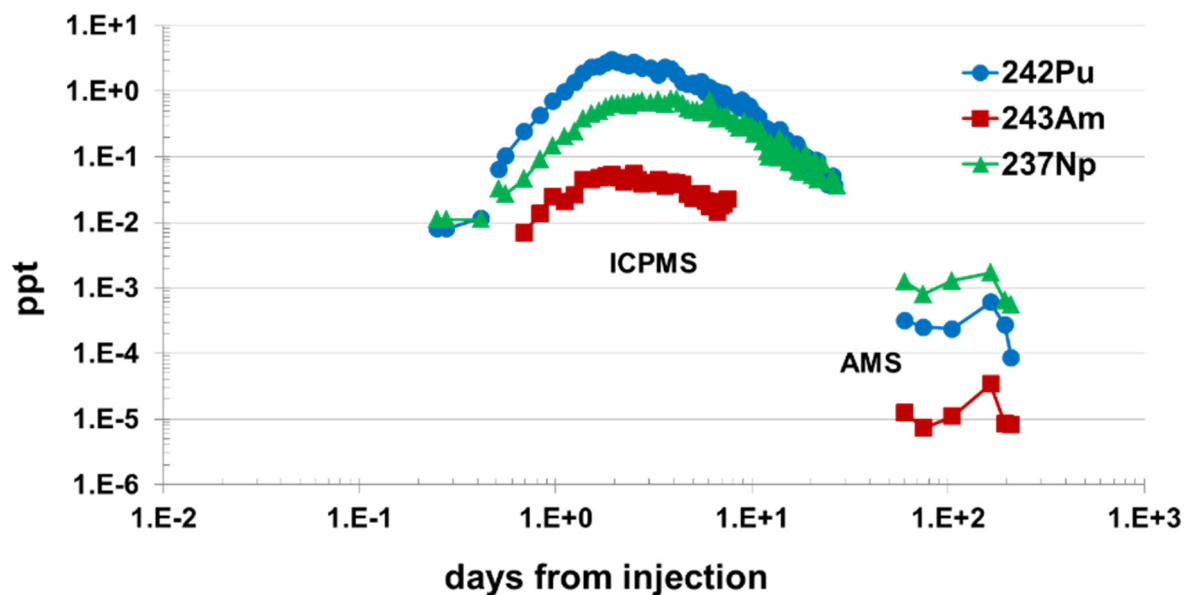
Figure 2-24: ^{242}Pu (blue circles), ^{237}Np (green triangles) and ^{243}Am (red squares) concentrations, expressed in ppt of the effluent fractions collected during of the experiment RUN 12-02. On the horizontal axis, the sampling times are indicated. The data obtained with AMS lie in a range from one to three orders of magnitude below the DL of the employed SF ICP-MS (0.01 ppt equal to ~ 2.5×10^7 atoms/g).

2.1.4 Hydration of compacted bentonite: An ESEM approach

Introduction

Bentonite erosion experiments play an important role within the Kollorado-e project. These experiments showed strong swelling of the hydrated bentonite clays and the formation of a clay gel-layer within the aperture of the erosion cell. In this context the water uptake and the swelling or shrinkage behaviour of bentonite is a very important question. Especially smectites have an excellent ability to adsorb water, leading to a strongly increased particle volume and finally in a complete delamination of the particles forming colloidal suspensions. This water adsorption phenomenon of smectites is a complex process related to their structural and physical-chemical properties. The structure of smectites is characterized by isomorphous ion replacements, which cause a deficit of positive charge in their octahedral and sometimes tetrahedral sheets. This deficit is balanced by interlayer cations like Na^+, K^+, or Mg^{2+} and Ca^{2+}. In an aqueous environment in smectites these cations are accessible for water molecules. There the water molecules are arranged in a partly ordered structure forming one or two water layers around the interlayer cations, leading to an increased interlayer space. Hence, these interlayer cations play an important role in the smectite-water interaction. Not only the interlayer spacing of the clay mineral depends on the kind of cation, but also the amount of adsorbed water. Thus leading to a strongly increased particle volume and finally resulting in a complete delamination of the aggregates, forming colloidal suspensions or voluminous clay gels. Therefore, the focus of this study was set to the visualization and in-situ electron microscopic quantification of these effects on the swelling behaviour of Febex-bentonite by environmental scanning electron microscopy (ESEM), as it reveals the unique possibility to investigate sensitive and even wet materials (e.g. *(Donald, 1998; Kloprogge et al., 2013; Stokes, 2008)*).

Materials and Methods

In our study the Spanish Febex bentonite from Almeria was used. According to *(Fernández et al., 2004)* this raw bentonite is very rich in montmorillonitic clay minerals (> 90 %), with minor amounts of quartz, feldspars and cristobalite. For the hydration experiments the fraction < 2 μm of the untreated bentonite with its natural exchangeable cation population was used. In the following, this sample is called "untreated bentonite". Therefore, 20 g of the clay were purified according to the procedure established by *(Tributh and G., 1986)*. X-ray diffractometry and FTIR-spectroscopy of this fraction revealed only traces of quartz besides the clay mineral. According to our measurements the clay consists of an illite-montmorillonite interstratified mineral with 13 % of non-swellable layers (data not shown), which is in good agreement with *(Cuadros and Linares, 1996)*. According to the procedure of *(Glaus et al., 2007)* Li-, Na-, and

Sr-exchanged samples were produced by adding 250 mL of 1 M metal chloride solutions to 2 g of the bentonite fraction < 2 µm and shaking the suspensions for 24 h. Then the clay was separated by centrifugation (10 min at 4000 rpm) and decantation of the supernatant solutions. This procedure was repeated three times. To remove excessive salts, dialysis of the suspensions in dialysis tubes (Nadir, pore size 2.5 nm) was conducted. Prior to that, the tubes were boiled in water to remove soluble organics. Afterwards the cation-saturated samples were filled in and were dialyzed in deionized water until conductivity in the water was below 5 µS/cm. Then all materials were dried at 60 °C for 72 h and finally were ground. To achieve a layer charge reduced smectite, 2 g of the Li-exchanged sample were heated to 300 °C. At this temperature the Li$^+$ cations migrate from the interlayer space into the mineral framework of the smectite and remarkably reduce its layer charge *(Hofmann and Klemen, 1950)*.

Environmental scanning electron microscopy (ESEM). Microscopic hydration experiments were carried out in a FEI Quanta 650 field emission gun environmental scanning electron microscope (FEG-ESEM), which was equipped with a gaseous secondary electron detector (GSED). The microscope was operated at 20 kV in wet-mode under varying water vapour pressures between 130 and 870 Pa and at a fixed working distance of 9.5 mm. To control the sample temperature during the hydration experiments a water cooled peltier cooling stage was used. With this equipment it is possible to create a defined relative humidity around the specimen by varying water vapour pressure in the microscope chamber and temperature of the peltier stage (Figure 2-25).
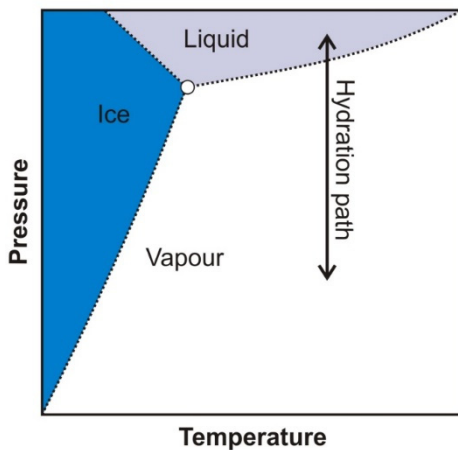
Figure 2-25: Phase diagram of water. Hydration path for in-situ experiments at fixed temperatures (e.g. 5°C) in the microscope.

For the measurements small amounts of clay powder were poured on the stainless steel sample holder and stage temperature and chamber pressure were set to 5 °C and 130 Pa, respectively. According to these parameters the relative humidity around the sample was 15 %. The specimen was allowed to equilibrate at these parameters for at least 15 minutes prior to the start of the experiments. Swelling isotherms were measured by increasing the water vapour pressure in five steps from 130 Pa to 862 Pa, which correspond to relative humidities of 15, 35, 55, 75, 85, and 95 % RH respectively. At each step of pressure an image was taken after

an equilibration time of 15 minutes. The last step of the hydration cycle at 862 Pa (95 % RH) was used as the first step of the dehydration cycle. Then the chamber pressure was decreased via the same five steps as in the hydration cycle until the starting conditions were achieved (130 Pa, 15 % RH). The sample temperature was always kept constant at 5°C. For digital image analysis the open source software *ImageJ* was used *(Rasband, 2015)*. Bentonite aggregates with diameters between 30 and 50 µm were selected for area measurements. The selected ESEM-images were converted to 8-bit and covered 1024 x 943 pixels. The area of interest (AOI) was isolated by applying a grey level threshold Figure 2-26. Therefore, *ImageJ* considered a grey level range of 0-255 for all area measurements. Then the increase in area was calculated from the following Equation (Equation 15):

$$Swelling\ (\%) = \left((A_h - A_0)/A_0\right) \cdot 100 \hspace{2cm} \textbf{Equation 15}$$

Where A_h represents the area (µm^2) of the hydrated sample and A_0 represents the initial area (µm^2) of the dry sample at 5 °C and 15 % RH. The data are displayed as relative expansion (swelling %) versus relative humidity at a fixed temperature and therefore can be indicated as isotherms. To determine the precision of the hydration experiments, the average standard deviation was calculated for each hydration step after the measurement of hydration isotherms of five different particles. It is worth mentioning, that the standard deviation is constant between 0.9 and 1.4 % for relative humidities up to 85 %. Only at highest relative humidities it slightly increased to 2.5 %.
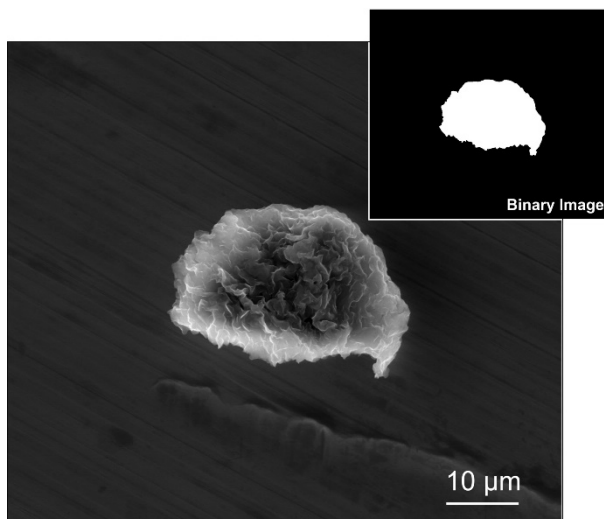
Figure 2-26: Creation of a binary image out of the ESEM micrograph with the software ImageJ. These binary images are used for the calculation of the swelling areas.

Results and Discussion

Scanning electron microscopy reveals 2D-images of three-dimensional particles, this means only a projection of the clay aggregate surface on the xy-plane is measurable. Information along the z-direction is not accessible. To investigate the behaviour of the Febex bentonite along the z-axis during hydration a thin clay film with oriented clay platelets was produced by

sedimentation from a suspension of the Na-exchanged material with a clay concentration of 5 g/L. A small piece of freshly broken film was then glued vertically on the stainless steel sample holder with a conductive adhesive (Leitsilber, Plano GmbH, Germany). Afterwards, the edge of the clay film was directly observable during hydration in the ESEM.
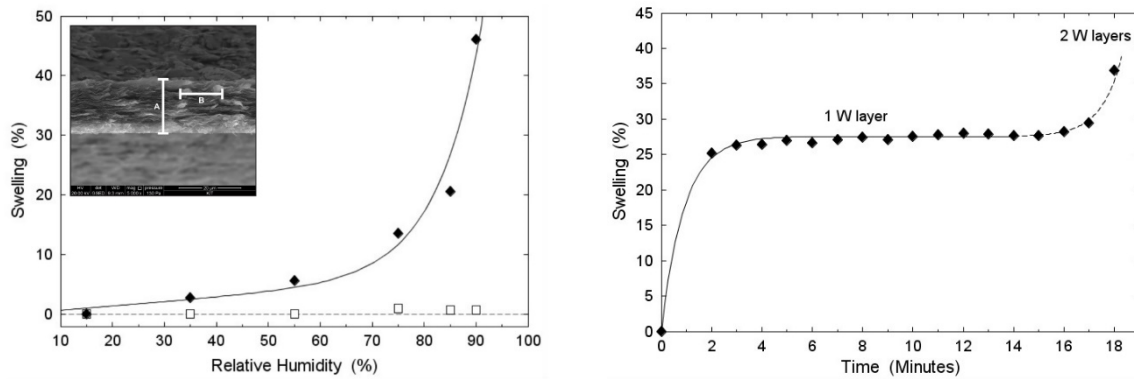
Figure 2-27: (left) Anisotropic swelling behaviour parallel and perpendicular to the clay c-axis. Black rhombs: swelling parallel to c-axis of the clay platelets (line A), white squares: swelling perpendicular to the c-axis (line B). (right) Swelling-shrinkage cycle of Na-Febex at 90 % (and after 12 minutes at 97 % RH) to determine equilibration time and occurrence of discrete water layers (1W, 2W) within the smectite interlayer. Experimental data fitted by exponential functions.

Figure 2-27 compares the swelling behaviour of the film along the c-axis of the oriented clay mineral particles, to the swelling along their ab-plane. The clay particles show a very aniso-tropic swelling behaviour. While the clay film strongly swells perpendicular to the clay layers (along the c-axis), along the ab-plane swelling occurs only at high relative humidities (> 75 %) to a very low degree. *(Carrier et al., 2013)* attributed this behaviour to irregularities and misa-lignments in the particle orientation. As a simplified assumption it can be stated, that in clay aggregates the particles are randomly oriented. According to the results displayed in Figure 2-27, an equidimensional swelling of these aggregates during a hydration experiment in the ESEM can be assumed. Hence, the measured area data display a 2D-projection of the volu-metric expansion and can be used for quantification of the observed clay swelling without a further transformation into a coefficient of volume expansion. Similar approaches were used by a number of earlier studies (e.g. *(Carrier et al., 2013; Montes-H, 2005; Montes-H et al., 2003b; Romero and Simms, 2008)*). The changes in morphology of the bentonite aggregate during hydration are shown in Figure 2-27. The aggregate size remarkably increased with in-creasing humidity and also the typical rough smectite morphology changed considerably. An overlay image of the isolated AOI's illustrates the swelling process. Based on X-ray diffracto-metric investigations or water vapour adsorption-desorption experiments many authors re-ported a stepwise increase of interlayer spacing and were able to calculate discrete hydration states with one or more water layers (1W, 2W) in smectite interlayers during hydration (e.g. *(Cases et al., 1992; Emmerich et al., 2015; Ferrage et al., 2005; Ferrage et al., 2007)*). How-

ever, this behaviour of smectites cannot be observed in microscopic swelling vs. relative humidity hydration experiments. Only *(Montes-H et al., 2003b)* found three stages of hydration during an experiment with relative humidities fixed at 90 % or 95 % respectively. We tested a similar setup with a Na-exchanged Febex sample. In our experiment first we increased RH from 15 % to 90 % in one step and held it for 12 minutes and then increased RH to 97 % and held it for another five minutes. Figure 2-27 shows the swelling behaviour of the aggregate versus time. The initial swelling was very fast. As explained earlier, it was not possible to image this. A plateau at 18 % RH was already reached after two minutes. Thereafter no further increase could be detected, until RH was increased to 97 %. Again, this caused a fast and very strong increase in aggregate swelling up to 52 %. At this latest stage also water droplets are visible on the aggregate surfaces. To estimate if these data display the occurrence of 1W layer and 2W layer states within the sample, two equations (Equation 16 and Equation 17)developed by *(Ferrage et al., 2005)* were used:

$$\text{Layer thickness (1W)} = 12.556 + 0.3525 \times (v/r - 0.241) \times (v \times RH - 0.979) \quad \textbf{Equation 16}$$

$$\text{Layer thickness (2W)} = 15.592 + 0.6472 \times (v/r - 0.839) \times (v \times RH - 1.412) \quad \textbf{Equation 17}$$

Where *v* is the cation valence, *r* is the ionic radius and RH the relative humidity. For Na^+ $v = 1$ and $r = 0.102$ nm. Thus, Equation 16 gives a layer thickness of 1.253 nm at 90 % RH and with Equation 17 a layer thickness of 1.553 nm at 97 % RH was calculated. Furthermore, *(Ferrage et al., 2005)* calculated a layer thickness of 1 nm at dry state (0W) for smectites. Strictly speaking, the smectite-equations of *(Ferrage et al., 2005)* cannot be used for an illite-montmorillonite interstratified mineral like the Febex-bentonite. But to demonstrate the general correctness of our assumptions we use a smectite as simplified model particle. Thus, the correct values should be lower than the values we calculated here. Figure 2-28 shows a sketch of this simplified smectite particle with assumed typical dimensions of 200 nm (a), 350 nm (b) and the above calculated layer thicknesses at 0W, 1W, 2W (c).
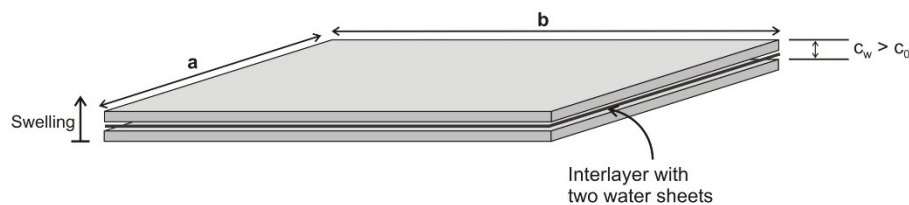
Figure 2-28: Sketch of a simplified smectite particle for calculation of maximum swelling. C_0: layer thickness without water layer, C_w: layer thickness with one or two water layers incorporated in smectite interlayer.

As demonstrated in Figure 2-27, swelling occurs only along the c-axis. Thus, by comparing the sizes of the ac- or bc-planes before and after hydration, the swelling percentage can easily be calculated. Using the assumed dimensions and layer thicknesses, it is possible to estimate an

area increase of 16 % for one water layer (1W) and an increase of 32 % for two water layers (2W). This is in good agreement with the measured data in Figure 2-29 (18 % and 42 % swelling). The higher swelling up to 50 % at very high relative humidities could possibly be explained by a strong contribution of so-called osmotic swelling in the inter particle space as proposed by *(Baker et al., 1995)* and *(Salles et al., 2008)*. A water adsorption isotherm of Na-Febex at 5 °C is displayed in Figure 2-29**.** The swelling rates are very low at the beginning of the experiment. Not till relative humidities of 55 % the changes in particle morphology are clearly visible. The swelling finally increases exponentially at high humidities above 75 %. The dehydration path proceeds at slightly higher swelling percentages with decreasing relative humidities. In gas adsorption (BET-) measurements of smectites similar types of hysteresis are observed. There, this kind of hysteresis loop is called type H3, and is typical for plate-like particles giving rise to slit shaped pores (e.g. *(Sing et al., 1985)*). A logarithmic representation of the swelling data is shown in Figure 2-29. The measured data were fitted with a linear function. The slope of the hydration path (0.061 ± 0.01, $R^2 = 0.914$) is larger than the one determined for the dehydration (0.036 ± 0.004, $R^2 = 0.967$). Thus, hydration and dehydration can be assigned to a first order reaction, where the water availability is the driving force. Furthermore, the hydration exhibits a more pronounced dependency on the value of the relative humidity, than on the reverse action.
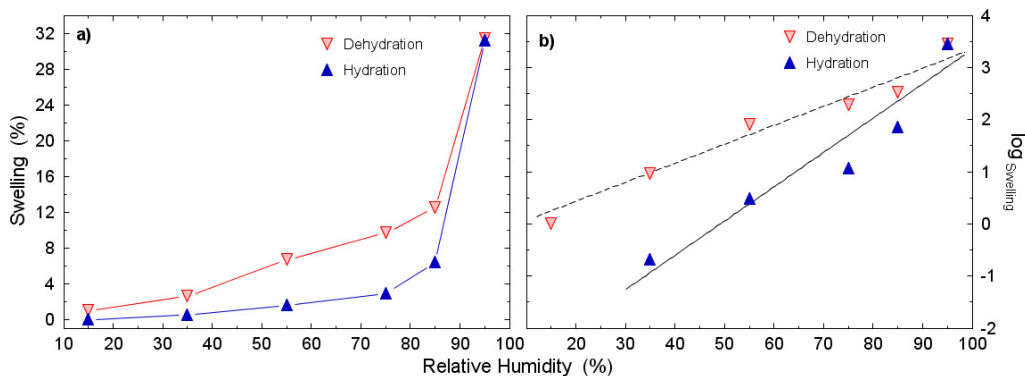
Figure 2-29: a) Measured isotherms of Na-Febex bentonite at 5 °C. Blue triangles: hydration path, red triangles: dehydration path. b) Logarithmic plot of swelling vs. relative humidity representing a first order reaction of the hydration process with hindered dehydration (t_{equil} = 15 min).

Similar behaviour was observed by several authors using different techniques (e.g. *(Cases et al., 1992; Fu et al., 1990; Keren and Shainberg, 1975)*). But its interpretation still is under discussion. From XRD data, the hindered desorption was attributed to a decreased entropy *(Fu et al., 1990)* or to geometrical factors like changes in particle arrangement and interlayer distances *(Cases et al., 1992)*. In addition, based on Monte Carlo simulations *(Tompsett et al., 2005)* suggested network effects and cavitation phenomena for wide hysteresis loops in mesoporous materials. Hydration experiments with various cation exchanged bentonite samples (Figure 2-30) did not yield as many differences as reported by earlier studies (e.g. *(Keren and Shainberg, 1975)*). Untreated, Na- and Sr-exchanged samples swell to a similar maximum

(max. swelling 29 and 28 %), while the swelling of Li-exchanged bentonite was slightly lower (max. swelling 18 %). Apart from that, the shapes of the hydration paths are very similar. In the layer charge reduced Li-sample (300°C) the migration of water molecules into the interlayer is hindered, thus it swelled only to 6 %. This behaviour may have two reasons: First, the heat treatment leads to the migration of the lithium cations into the di-trigonal cavities of tetrahedral sheet, resulting in both a reduction of layer charge and the amount of interlayer cations. Secondly, this causes a collapse of the interlayer sheet to an illite-like d-spacing (e.g. *(Pálková et al., 2003)*). The behaviour of the untreated sample was similar to that of the Na- and Sr-samples with a slightly higher maximum swelling (31 %), which is related to a mixed cation occupancy of its interlayers (Na, Ca). Beyond that, the Sr-saturated bentonite showed a significantly higher swelling already at low relative humidities compared to the other samples. This can be assigned to the much higher hydration energy of divalent cations like Strontium ($\Delta H_h°$ = - 1415 kJ/mol) compared to alkali metals like Lithium or Sodium ($\Delta H_h°$ = - 499 and - 390 kJ/mol) *(Wiberg et al., 2007)*. *(Bol et al., 1970)* suggested, that divalent cations form two clear-cut hydration shells. This increases the hydration force within the clay interlayers, and results in large water spheres around the cation *(Keren and Shainberg, 1975)*. Nevertheless, the effect of the kind of interlayer cation on the swelling behaviour of the clay aggregates was not as pronounced as it was discussed by earlier studies (e.g. *(Keren and Shainberg, 1975; Montes-H et al., 2003a)*).
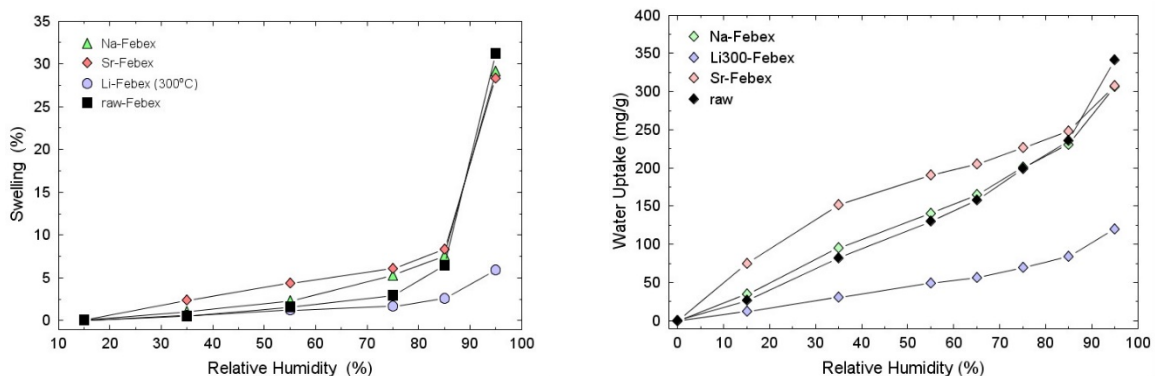
Figure 2-30: Comparison of the water adsorption isotherms of Na, Li(300°C) and Sr-exchanged bentonite vs. the untreated raw-material. Figure 8. Water uptake of Febex bentonite in dependence of interlayer cation.

This behaviour is supported by water uptake experiments conducted under defined relative humidities 15, 35, 55, 65, 75, 85 and 95 % (Figure 2-30). As could be expected, the charge reduced Li-sample had the lowest water uptake ability. In contrast Sr-Febex sorbed the highest amount of water at low and medium relative humidities, while at 95% RH it has the same value (310 mg/g) as the Na-exchanged sample. Here the untreated raw sample shows the highest water sorption ability (345 mg/g). Figure 2-31 shows the morphological changes during hydration experiments on a compacted bentonite sample (1640 kg/m³). The massive surface of the dry sample (13% RH) has only a few small cracks. During hydration the surface morphology changes drastically. Not only swelling of the clay particles is visible, but also the opening of

large cavities and translations or rotations of larger units occur (yellow arrows). A quantification of all observed morphological changes is very difficult. *(Carrier et al., 2013)* suggested a digital image correlation technique (DIC) where small squares are used as correlation windows on which grey levels are compared between reference and deformed image to compute the displacement.
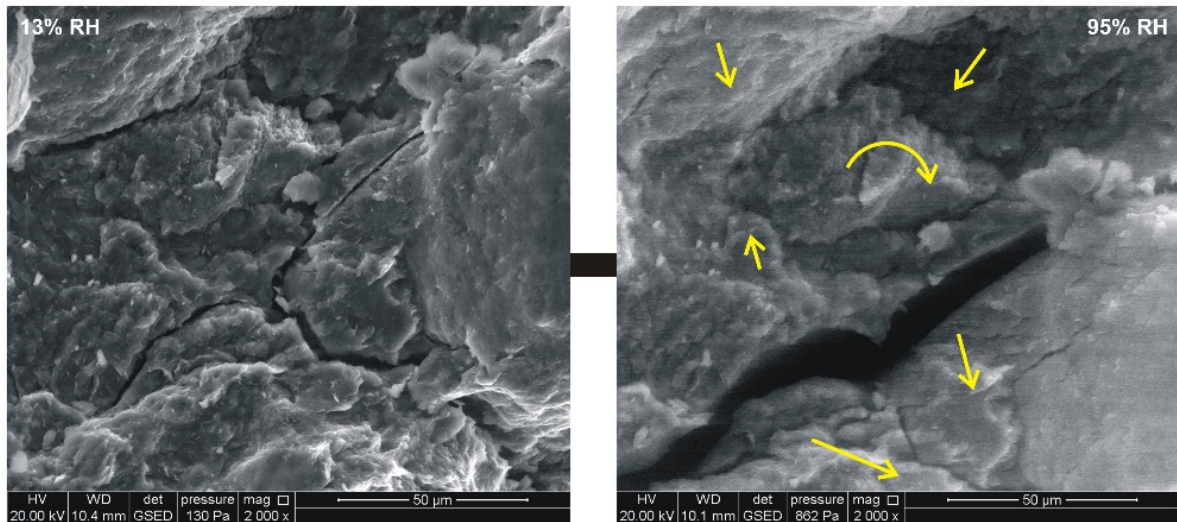
Figure 2-31: Surface of a compacted bentonite sample (Na-Febex). During hydration strong morphological changes like translations and rotations of larger clay units are visible (yellow arrows). Furthermore, a large cavity opens up.

Conclusions

Environmental scanning electron microscopy coupled with digital image analysis allowed for in situ observation and measurement of the swelling behaviour of Febex bentonite in the RH range of 15 – 95%. New discoveries in terms of the hydration behaviour of smectite were not expected from the present study. The behaviour of Febex-bentonite in this regard had not been investigated previously, though it has been used in many studies. The hydration behaviour of Febex is very significant. Examination of the swelling behaviour of Febex, by means of ESEM, showed that it is different from other bentonites, such as MX80, in this regard.

Measurements of the humidity-induced swelling of an oriented Na-exchanged clay film showed a strongly anisotropic swelling behaviour with swelling only in the direction perpendicular to the clay stacking. According to these results, and to the simplified assumption of a random distribution of the clay particles in the aggregates, an equidimensional swelling during hydration experiments in the ESEM was a correct assumption.

The hydration isotherms of various cation-exchanged Febex bentonite samples have exponential form with strongly increasing swelling at high RH values. The effect of the kind and

charge of interlayer cation seems to be insignificant in this bentonite. The maximum swelling of the Sr, Na, and Li samples is very similar. The hydration paths of the Na, Li, and untreated samples also coincide. Only the Sr-exchanged sample showed significantly more swelling at low RH values, which can be explained by the much greater hydration energy of Sr in comparison with the other ions, and thus its greater hydration force within the clay interlayer.

2.1.5 Colloid generation at the compacted bentonite water interface (laboratory erosion experiments)

2.1.5.1 Mineralogical characterization of the gel layer

F. Friedrich, F. Rinderknecht, F. Huber, T. Schäfer

Introduction

In this study the erosion and swelling behaviour of the FEBEX bentonite has been investigated during erosion experiments conducted in a custom-made flow through cell. The focus was set on the mineralogical investigation of the eroded material located in the gel layer.

Materials and Methods

Erosion Experiments (artificial fracture tests). The housing of the erosion cell was made of acrylic glass and had a diameter of 18 cm. Two apertures were available: 1 mm and 0.1 mm. For the tests compacted rings of FEBEX bentonite and of a commercial sodium montmorillonite (Nanocor, PGN grade) were used, with an inner diameter of 4 cm, an outer diameter of 8 cm and a height of 2.5 cm. Their dry density was 1650 and 1400 kg/m^3 respectively. The rings were placed in a cavity in the centre of the cell and were dry prior to the experiment. Grimsel groundwater was pumped through the cell by a peristaltic pump with an initial flow velocity $v_{init.}$ = 10^{-5} m/s. Furthermore, this cell was equipped with a pressure sensor (disynet XP1103-A1-100BG) to monitor the evolution of the bentonite swelling pressure during the experiment (Figure 2-32a).
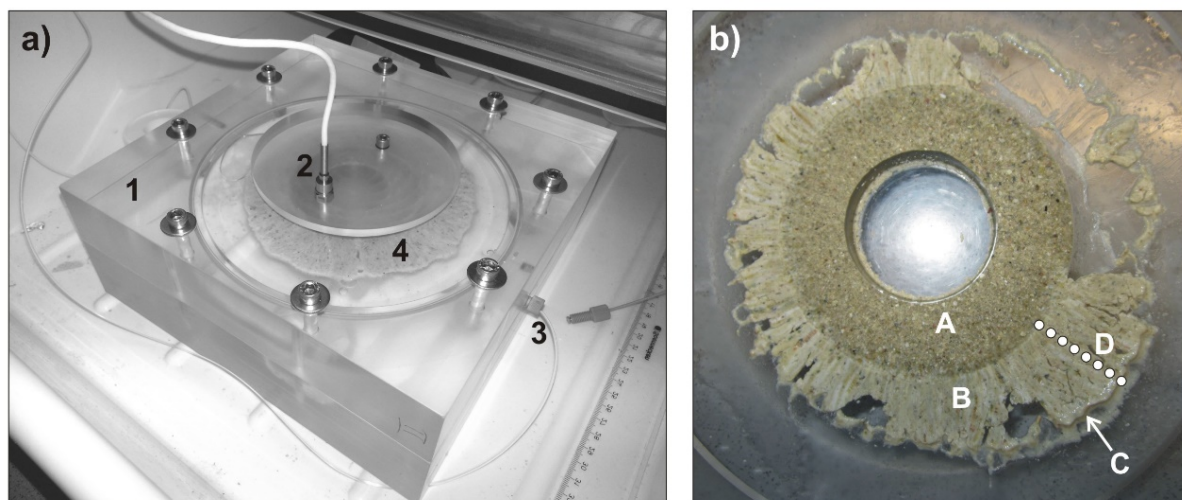
Figure 2-32: a) setup of the flow through cell; visible are the acrylic glass housing (1), the pressure sensor (2) with the (dark) bentonite ring beneath, the water inlet (3) and the erosion

halo (4). b) Halo of eroded material around the bentonite ring. (A) compacted bentonite ring, (B, C) eroded material (gel layer), (D) sample locations for XRD measurements.

X-Ray Diffractometry (XRD). XRD patterns were recorded over the range of 3° to 63° 2Θ using a Bruker D8 Advance diffractometer, equipped with a graphite secondary monochromator and a Sol-X detector. Counting time was 6s in 0.02° steps and CuKα radiation (λ = 1.5418 Å) was used for measurement.

Environmental Scanning Electron Microscopy (ESEM). The morphologies of the samples were examined by a FEI QUANTA FEG ESEM and a Phillips XL30 FEG ESEM. During preliminary investigations at a chamber pressure of 130 Pa the samples showed no damage due to beam energy and low pressure. Thus to improve the image quality the samples were sputtered with a thin conductive layer (5 nm Au/Pd 80/20) and were investigated under high vacuum using an acceleration voltage of 15 kV.

Fourier Transform Infrared Spectroscopy (FTIR). A Bruker IFS 55 EQUINOX spectrometer, equipped with a DTGS (deuterated triglycine sulphate) detector was employed to obtain IR-spectra. 64 scans in the 4000 – 400 cm^{-1} spectral range were recorded with a scanner velocity of 5 kHz and a resolution of 4 cm^{-1}. For ATR measurements a MIRacle single reflection diamond attenuated total reflection (ATR) cell (PIKE Technologies) was used. Band component analysis was undertaken using the Jandel Peakfit software package, which enables the type of fitting function to be selected and allows specific parameters to be fixed or varied accordingly. A linear two-point background was chosen and fitting runs were repeated until reproducible results were obtained with a squared correlation parameter r^2 better than 0.998.

X-ray disc centrifuge (XDC). For the measurement of the particle size distribution an X-ray disc centrifuge system (Brookhaven Instruments Corporation, USA) was used. The XDC method allows the measurement of suspensions in a centrifugal field, reducing the measurement time dramatically. In principle X-rays from a low power X-ray tube are passed through the disc. The intensity of the beam is attenuated in proportion to the concentration of the suspension through which it passes; the transmitted beam is then measured with a detector consisting of a scintillation counter whose output is recorded by the computer as a function of time. For a homogeneous suspension, the attenuation of the X-ray beam is proportional to the mass concentration of the suspension at the measurement radius. 500 mg of sample powder were dispersed in 20 ml ultrapure water using an ultrasonic horn (200 watts) for two minutes. The rotation speed was set to 3500 RPM and the measurement time was set to 60 minutes, thus covering a size range from 1.6 to 0.01 μm.

Results and Discussion

Within the first 24 h after the start of the experiment with an aperture of 1 mm the swelling pressure rapidly increased to 2.6 MPa (Figure 2-33a). During the following days the pressure

decreased to a constant value between 1.7 to 1.8 MPa implying steady state conditions (Figure 2-33). This pressure drop coincides with the bentonite swelling into the 1 mm aperture.
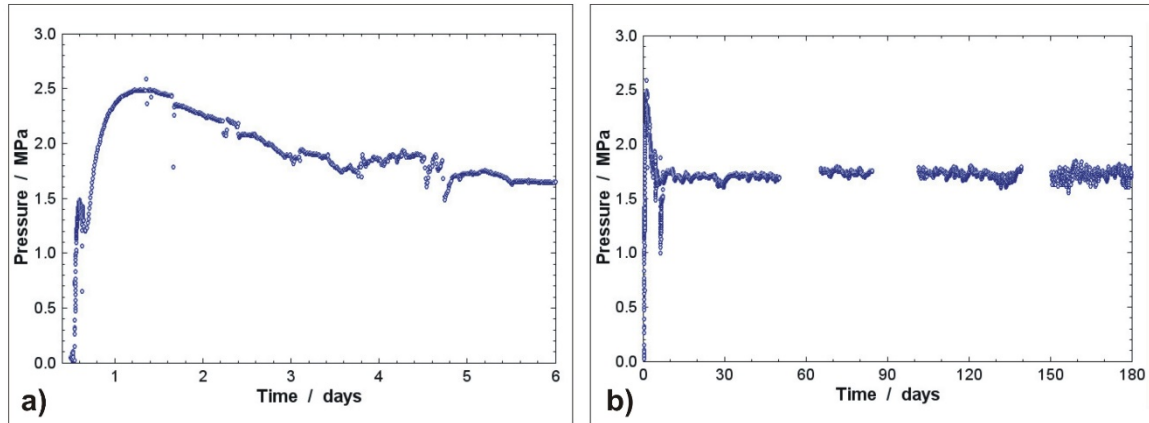
Figure 2-33: Results of pressure measurements over a time period of 180 days.

In the course of the experiment a "halo"-like structure of eroded material was formed within the aperture ("gel layer"), which did not expand any further after 40 days and had a final diameter of 3.2 cm. The experiment was stopped and the eroded material was sampled along a traverse from the outermost part of the gel layer into the bentonite ring, in total eight samples were taken (Figure 2-32). In contrast the swelling behaviour and the gel layer formation within a smaller aperture of 0.1 mm is remarkably different. The swelling pressure slowly increased to 1.5 MPa and further to 1.85 MPa within the first ten days. After this initial phase it slowly increased to a final pressure of 2.05 MPa after 65 days (Figure 2-34a). In contrast, the formation of the gel layer started much later. Only after 25 days a very small "halo" of eroded material was visible and it slowly increased to a plateau at 0.8 cm (after 80 days). A further swelling occurred after 190 days and reached a maximum thickness of 1.1 cm after 280 days. A comparison with the swelling data from the erosion cell with 1 mm aperture illustrates the much slower evolution of the gel layer during the benchmark test (Figure 2-34b). During this experiment it was not possible to fill the aperture volume completely with water. At least 10% of the volume was filled with air bubbles. Under these conditions it was not possible to apply a water flow through the aperture. Probably this behaviour is related to the large dimensions of the bentonite sample associated with a very slow hydration of the ring through the thin aperture (small contact area bentonite/water of only 25 mm^2), as the hydration was going on over the entire experiment duration without reaching equilibrium state. Figure 2-35 displays diffraction patterns from sample points along the gel layer. The analysis of these data reveals, that not only clay minerals like montmorillonite and traces of illite were eroded, but also Na- and Ca-feldspars, quartz and carbonate particles (calcite, dolomite) migrated far into the outer parts of the gel layer.
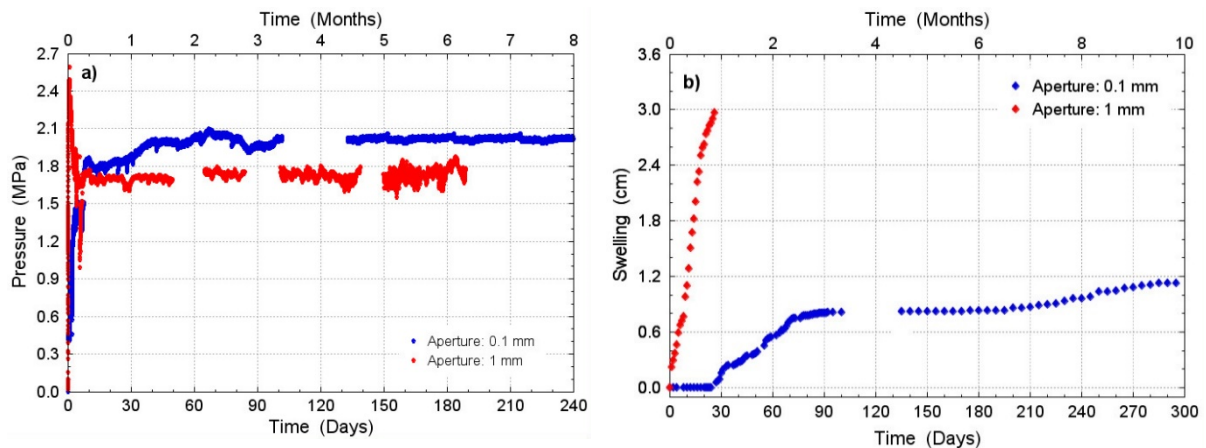
Figure 2-34: a) Comparison of swelling pressures in the bentonite ring over the entire duration of the experiments with 1 mm and 0.1 mm aperture size. b) Comparison of gel layer sizes around the bentonite ring**.**
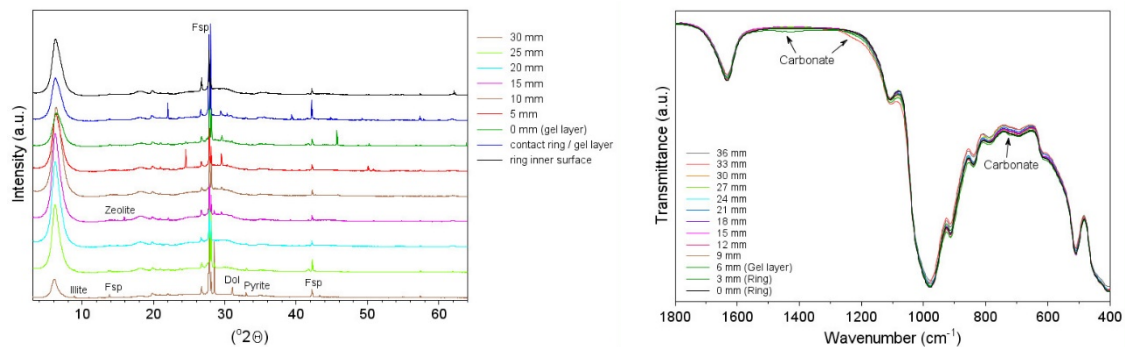
Figure 2-35: X-ray patterns of ring and gel layer samples. all patterns show peaks of smectite (Sm), feldspars (Fsp), quartz (Qz) and traces of illite, zeolite (analcime), pyrite, calcite (Cc) and dolomite (Dol). FTIR spectra of gel layer samples. Only a few very small and brought carbonate bands are visible between the smectite vibrations.

Infrared spectra show only bands which can be assigned to smectite vibrations (Figure 2-35). Only three very small and brought vibrations at 1430, 1223 and 727 cm^{-1} can be assigned to carbonate vibrations. No further information can be derived from FTIR spectroscopy. This means that besides smectite only very low amounts of further minerals are present in the gel layer. But the appearance of further mineral phases can be proved by means of scanning electron microscopy. The gel layer consisted of strongly agglomerated clay material (Figure 2-36a) in its outer area, while in the inner parts a thick and massive clay matrix (Figure 2-36b) is visible with partly typical smectite morphology (Figure 2-36c, d, g). This clay matrix consisted a few large mineral grains of Na- and Ca-feldspars (Figure 2-36e, f), silica (Figure 2-36d, g) or mica flakes (Figure 2-36i). The grainsizes were always lying in the range of 50 µm and much

larger, even in the gel layer. As could be expected, the overall grainsize distribution data obtained by XDC in the range below 2 µm, showed remarkable differences between gel layer and ring material (Figure 2-37). The main peak was visible at 40 nm in both graphs. Furthermore, the compacted ring showed two peaks at larger grainsizes (0,25 µm and 0,55 – 1,1 µm) which could not be observed in the graph of the eroded gel layer material.
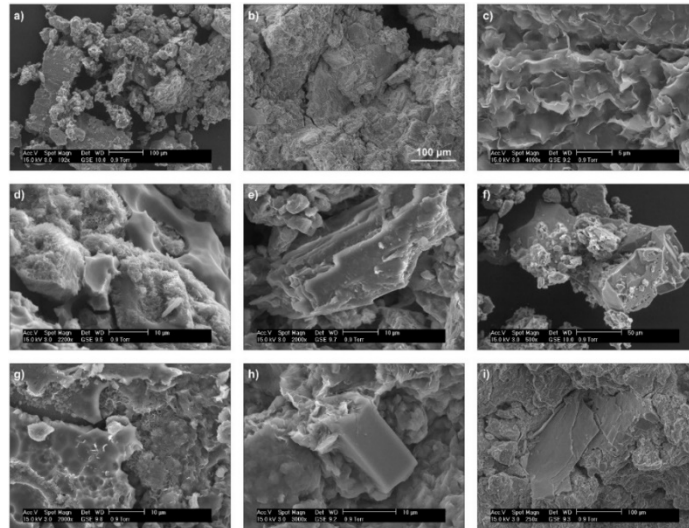
Figure 2-36: ESEM-images of the gel layer. A) and b) massive gel layer matrix with strongly agglomerated material. C) typical smectite morphology, d) and g) large rounded silica masses together with smectite, e) and f) large crystals of Na- and Ca-feldspar, h) zeolite block, i) large mica flake in smectite matrix.
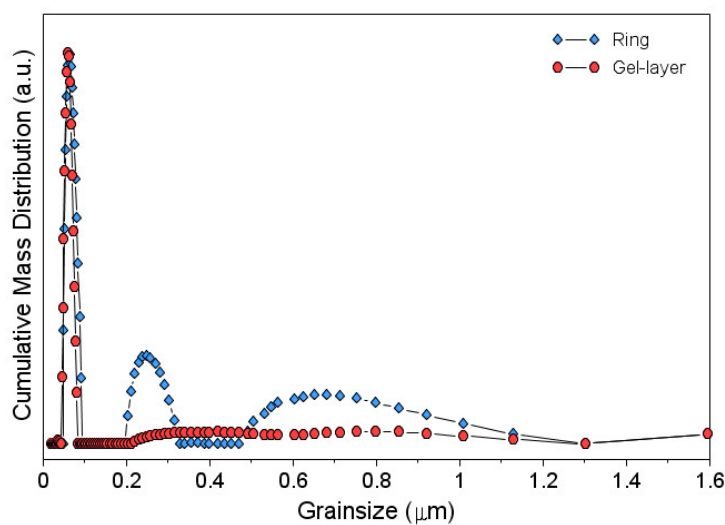
Figure 2-37: Grainsize distribution data in the range below 2 µm show remarkable differences between ring material and gel layer.

The results of the erosion experiments show that the hydration of the bentonite sample leads to a strong pressure increase within the compacted sample. This forces the movement of large amounts of mainly small clay particles into the aperture forming the gel layer. Due to the high swelling pressure also traces of other minerals like feldspars, micas or carbonates are carried along into the gel layer. To some extend these mineral grains have sizes of more than 100 µm. Furthermore, as could be expected the size of the aperture plays an important role in the formation and size of the gel layer around a compacted bentonite.

2.1.5.2 Colloid generation and characterization

2.1.5.2.1 2-side erosion reactors

M. Bouby

Introduction

Compacted bentonite is considered to be suitable for use as geotechnical barrier in a high level radioactive waste repository in crystalline host rocks. The radionuclides are safely enclosed in the geotechnical barrier if it stays intact, i.e. as long as no water enters the repository. Considering for example the Scandinavian glacial cycles scenario *(SKB, 2011)*, melt water may flow down to repository and enter in contact with the compacted bentonite inducing its swelling and a gel formation at the water interface. Accordingly, the bentonite erosion processes and the interaction of the eroded material with radionuclides may play an important role in the safety assessment of a deep radioactive waste repository in crystalline host rock which has to be fully understood (*(Missana et al., 2003)*). To simulate erosion processes under dynamic conditions is the aim of this work. The results obtained will be compared with other ones obtained with different or same bentonite material. This is greatly useful to validate and select the data which can be further used for performance assessment (PA).

Material and Methods

The experimental set-up used to perform bentonite erosion experiments in this study is shown in Figure 2-38. The bentonite used in these experiments is the Volclay bentonite MX80. The brand name MX-80 represents a western, or Wyoming, sodium dominated bentonite supplied by the American Colloid Company. The montmorillonite content is ~ 82 %. The raw material is the one used in two other recent studies *(Norrfors et al., 2015; Norrfors et al., 2016b)*. The raw material is first sieved and the fraction < 63 µm is used to prepare Na- and Ca- homo ionic MX80.

Raw, Na- and Ca-exchanged MX80 bentonite samples or mixture of both have been compacted in pellets at a density of 1.6 g/cm³ and placed in 4 double-side reactors. Erosion experiments are conducted by using a synthetic low ionic strength carbonated water (SGW) to simulate the potential effect of glacial melt water on the bentonite stability (see Table 2-18 for details). Main and trace elements were analysed over time in the collected SGW. The element compositions were determined by Ion Chromatography (IC, ICS-3000), ICP-OES (Optima 2000 DV, Perkin Elmer) or ICP-MS (X-Series 2, Thermo Scientific, Germany). This allows to plot the breakthrough curves (BCs) for each element of interest. The BCs represent the evolution of the elemental mass concentrations. The presence of clay colloids is revealed by the detection of their main or trace constituents. This may be confirmed via the calculation of the experimental mole ratios which can be compared to the theoretical ones, obtained from the

structural formula (see Table 2-18). Finally, one can follow any mineral dissolution (especially NaCl and $CaSO_4$).
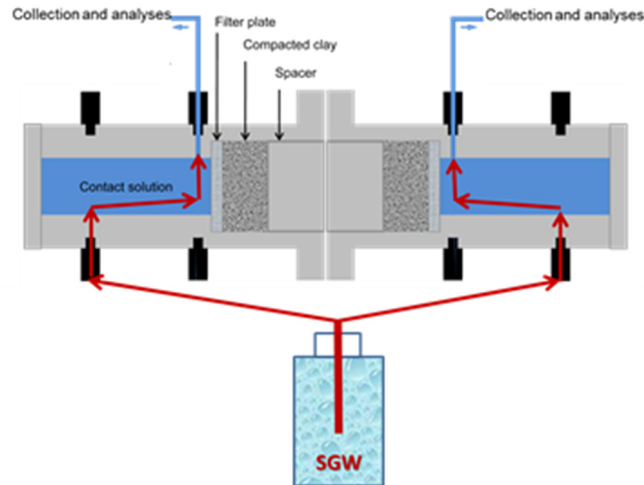
Figure 2-38: Scheme of one of the double-side reactor used for the erosion experiments.

Results

Samples are regularly taken and analysed since the beginning of the experiment running for almost 3 years. The present data summarize the results of the first 2.5 years (907 days), see Table 2-18. The results are very reproducible. The pH (8.3 ± 0.3) and flow rate (3.0 ± 0.1) $\mu L.min^{-1}$ remain constant over the investigated time period. Some material is clearly produced (detached) and identified as clay according to the concentrations of Si, Al, Mg and Fe recorded (see Figure 2-39). A clear effect of the initial bentonite pellet composition is evidenced. The highest erosion occurs for the Na-exchanged MX80 pellets while (almost) no erosion is observed when using Ca-exchanged ones and it is much more limited when using raw MX80 or the Na-Ca-MX80 pellets. When effective, the colloid production presents maxima after ~ 25 or 50 days to reach a colloid concentration up to ~ 500 mg/L (for Na-exchanged MX80 compacted pellets). Afterwards, the clay colloid concentration is decreasing to level off after 6 months at ~ < 2 mg/L. These data are used to determine the mass loss rates (MLR) and average mass loss rates (AMLR) under those specific conditions (see Table 2-18). The sizes of the eroded material collected after ~ 1 month were determined by PCS and presented Table 2-18. They agree with the sizes already previously reported for clay colloids extracted by centrifugation *(Bouby et al., 2011; Missana et al., 2003; Norrfors et al., 2015)*.
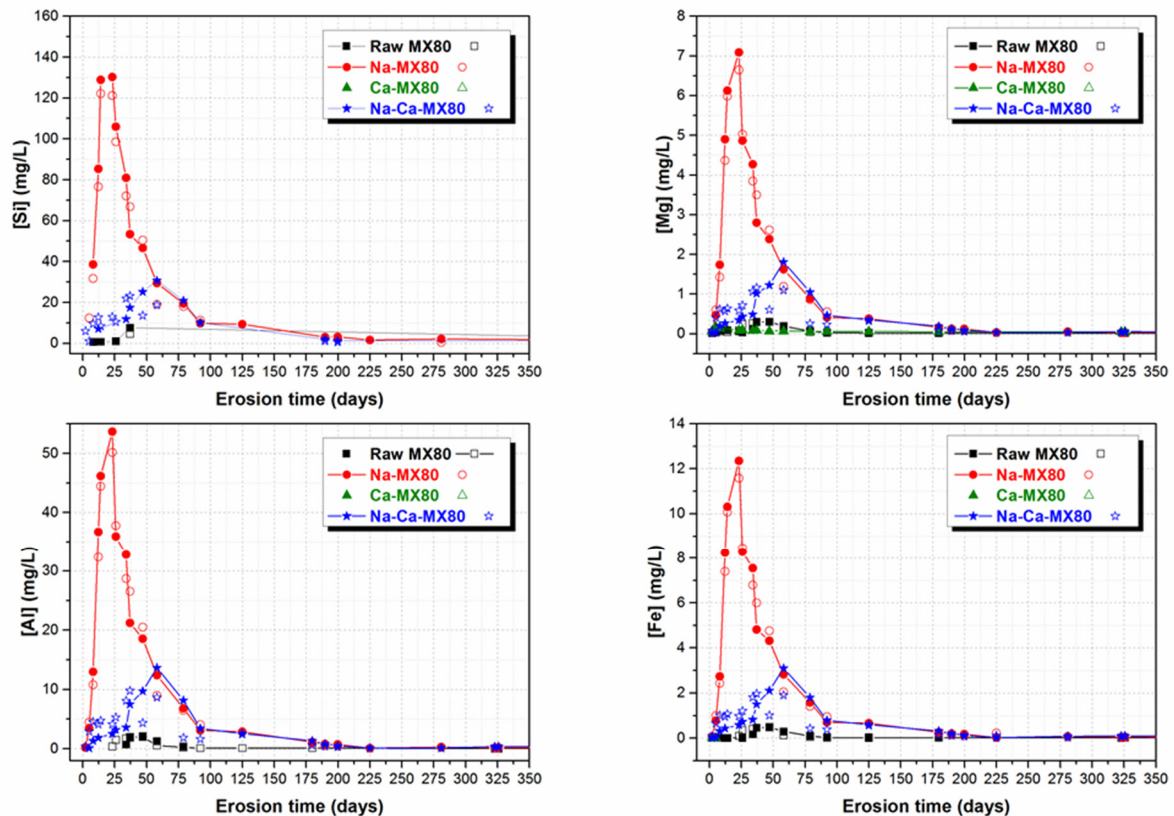
Figure 2-39: Si, Al, Mg and Fe breakthrough curves (BCs) over the first 9 months.

A Cs, Eu and U sorption test was performed with the eroded material. Cs is not sorbed. No U sorption can be demonstrated which agrees with our latest results (Norrfors et al., 2016). As only a partial removal of the clay colloids was possible in this single test (centrifugation at 16192 x g), one can only state that a minimum of 20 % up to 40 % of Eu is sorbed under the present conditions, with apparently a lower sorption on the eroded material obtained from the raw MX80 pellets. Further work is in progress to obtain a more precise Eu sorption quantification as done in (Bouby et al., 2011). Interestingly, in agreement with literature data and other works (Norrfors et al., 2015), instant releases of sodium, sulfate and chloride are clearly evidenced and attributed to the dissolution of accessory minerals present in the raw bentonite (like gypsum or halide) followed by cationic exchange process. For the first time, the release of Cs, Th and U have been quantified additionally. Cs behaves, as expected as a cationic exchanger. Th and U BCs behave like the Al ones and can thus be considered as clay trace components. This is very interesting as these elements are more easily detectable by ICP-MS. In the present case, it permits to detect the non-expected erosion occurring for the Ca-MX80 compacted clay pellet. The Cs, Th and U amounts released have been calculated and normalized (see Table 2-19). It is thus possible to take into account the potential amount of natural radionuclides released by the backfill material itself. This has probably to be consider in PA.

Table 2-18: Results of the dynamic erosion experiment performed in double-side reactors.

CLAY PELLET Main characteristics					
		Raw MX80	Na-MX80	Ca-MX80	Na-Ca-MX80
Pre - conditioning		No	Homo ionization in NaCl (1M)	Homo ionization in CaCl2 (1M)	Mixture
Mass	g	4.90 and 4.88	4.25 and 4.45	4.90 and 4.89	4.80 and 4.81
Dry Density		1.6 g/cm3			
Dimensions		ø:19 mm; h: 10 mm			
Na- or Ca-MX80 in pellet		100 % of raw material	100 % Na-MX80	100 % Ca-MX80	50:50 % Na- : Ca-MX80

EROSION CONDITIONS		
Synthetic carbonated ground water (SGW)		pH = 8.4 ± 0.1 and Eh(SHE) = +0.35 ± 0.05 V
Composition		[Na+] = 1.2 mM, [Ca2+] = 0.05 mM, [F-] = 0.1 mM, [Cl-] = 0.074 mM, [SO42-] = 0.04 mM, [HCO3-] = 1.0 mM, Si traces
Ionic Strength		1.6 mM
Volume		11.6 mL in the reactor (see Fig. 2.1.5.2.2.1)
Dynamic conditions (time)		907 days (2.5 years)
Test duration		21768 hours
Flow		(3.0 ±0.1) µL / min 2.3 10-4 m/s
Sloped		yes (180o)
Free swelling		no
Confined		yes
Fracture dimensions	cm2	Stainless Steel Porous filter: 20 µm; Surface area: 2.86 cm²; porosity 29.4%. frit volume 134.7 µL. real surface contact area: 0.842 cm²
Extrusion distance (filter thickness)		0.16 cm

RESULTS					
		Raw MX80	Na-MX80	Ca-MX80	Na-Ca-MX80
pH		8.3 ± 0.3	8.3 ± 0.3	8.3 ± 0.3	8.3 ± 0.3
Eluted mass (colloids)	mg	5.5 ± 0.1	77.8 ± 2.1	none	31.2 ± 6.3
Eluted mass loss/initial mass	%	0.11 ± 0.01	1.8 ± 0.1	none	0.6 ± 0.1
Eluted mass loss	kg/m²	0.065 ± 0.001	0.92 ± 0.2	none	0.37 ± 0.07
Average eluted mass loss rate (AMLR)	kg/(a·m²)	0.026 ± 0.005	0.37 ± 0.01	none	0.15 ± 0.03
Time used for AMLR calculations ↑: 21768 hours / 907 days					
Eluted mass loss rate (MLR)	kg/(y·m2)	0.051 ± 0.007	1.01 ± 0.02	none	0.37 ± 0.08
Time used for MLR calculations ↑: 7800 hours / 325 days					

CLAY COLLOIDS CHARACTERIZATION					
Size: hydrodynamic diameter		Raw MX80	Na-MX80	Ca-MX80	Na-Ca-MX80
PCS. f(I)	nm	162 ± 32	131 ± 3	-	132± 7
PCS. f(V)	nm	131 ± 98	93 ± 52	-	83± 40
Mean mole ratios (325 days)	Theoretical				
Si/Al	2.49	-	2.54 ± 0.04	-	2.8 ± 0.6
Al/Mg	6.62	5.6 ± 1.2	6.75 ± 0.02	-	6.66 ± 0.01
Al/Fe	7.57	10.2± 2.5	8.93 ± 0.13	-	9.0 ± 0.1

Table 2-19: Cs, Th and U releases during the dynamic MX80-bentonite erosion experiments.

		CATION RELEASES			
		Raw MX80	Na-MX80	Ca-MX80	Na-Ca-MX80
Cs	Days (d)				
Mass Released	325				
(μg/g)		0.013 ± 0.002	0.015 ± 0.001	0.87 ± 0.02	0.16 ± 0.06
(μg/g/a)		0.015 ± 0.002	0.016 ± 0.001	0.98 ± 0.02	0.17 ± 0.06
Mass Rate Release					
(kg/m^2)		$(7.8 \pm 1.1) \times 10^{-7}$	$(7.51 \pm 0.01) \times 10^{-7}$	$(5.0 \pm 0.1) \times 10^{-5}$	$(8.9 \pm 3.3) \times 10^{-6}$
(kg/m²/a)		$(8.8 \pm 1.3) \times 10^{-7}$	$(8.43 \pm 0.01) \times 10^{-7}$	$(5.7 \pm 0.2) \times 10^{-5}$	$(9.9 \pm 4.0) \times 10^{-6}$
Mass Released	907				
(μg/g)		0.04 ± 0.02	0.036 ± 0.002	1.58 ± 0.05	0.4 ± 0.1
(μg/g/y)		0.017 ± 0.008	0.015 ± 0.001	0.64 ± 0.02	0.14 ± 0.05
Mass Rate Release					
(kg/m2)		$(2.4 \pm 1.2) \times 10^{-6}$	$(1.87 \pm 0.02) \times 10^{-6}$	$(9.2 \pm 0.3) \times 10^{-5}$	$(2.0 \pm 0.7) \times 10^{-5}$
(kg/m²/y)		$(9.7 \pm 4.7) \times 10^{-7}$	$(7.53 \pm 0.07) \times 10^{-7}$	$(3.7 \pm 0.2) \times 10^{-5}$	$(8.1 \pm 2.7) \times 10^{-6}$
Th					
Mass Released	325				
(μg/g)		0.043 ± 0.001	0.52 ± 0.02	0.009 ± 0.004	0.19 ± 0.05
(μg/g/a)		0.048 ± 0.001	0.58 ± 0.02	0.01 ± 0.001	0.22 ± 0.06
Mass Rate Release					
(kg/m^2)		$(2.48 \pm 0.08) \times 10^{-6}$	$(2.67 \pm 0.01) \times 10^{-5}$	$(5.2 \pm 2.3) \times 10^{-7}$	$(1.1 \pm 0.3) \times 10^{-5}$
(kg/m²/a)		$(2.78 \pm 0.09) \times 10^{-6}$	$(3.0 \pm 0.01) \times 10^{-5}$	$(5.8 \pm 2.6) \times 10^{-7}$	$(1.2 \pm 0.3) \times 10^{-5}$
Activity Rate Release					
(Bq/m²/a)		11.3 ± 0.4	121.7 ± 0.1	2 ± 1	51 ± 13
Mass Released	907				
(μg/g)		0.056 ± 0.003	0.53 ± 0.02	0.012 ± 0.004	0.21 ± 0.05
(μg/g/a)		0.023 ± 0.001	0.21 ± 0.01	0.005 ± 0.002	0.08 ± 0.02
Mass Rate Release					
(kg/m^2)		$(3.3 \pm 0.2) \times 10^{-6}$	$(2.73 \pm 0.02) \times 10^{-5}$	$(7.2 \pm 2.4) \times 10^{-7}$	$(1.2 \pm 0.3) \times 10^{-5}$
(kg/m²/a)		$(1.32 \pm 0.08) \times 10^{-6}$	$(1.1 \pm 0.01) \times 10^{-5}$	$(2.9 \pm 0.9) \times 10^{-7}$	$(4.8 \pm 1.2) \times 10^{-6}$
Activity Rate Release					
(Bq/m²/a)		5.4 ± 0.3	44.7 ± 0.1	1.2 ± 0.4	20 ± 5
U					
Mass Released	325				
(μg/g)		0.06 ± 0.02	0.142 ± 0.004	0.09 ± 0.05	0.06 ± 0.01
(μg/g/a)		0.06 ± 0.02	0.159 ± 0.005	0.11 ± 0.05	0.07 ± 0.02
Mass Rate Release					
(kg/m^2)		$(3.2 \pm 1.0) \times 10^{-6}$	$(7.33 \pm 0.02) \times 10^{-6}$	$(5.5 \pm 2.8) \times 10^{-6}$	$(3.48 \pm 0.09) \times 10^{-6}$
(kg/m²/a)		$(3.6 \pm 1.2) \times 10^{-6}$	$(8.23 \pm 0.02) \times 10^{-6}$	$(6.2 \pm 3.1) \times 10^{-6}$	$(3.9 \pm 1.0) \times 10^{-6}$
Activity Rate Release					
(Bq/m²/a)		45 ± 14	102.1 ± 0.1	51 ± 3	49 ± 12
Mass Released	907				
(μg/g)		0.07 ± 0.02	0.154 ± 0.005	0.13 ± 0.07	0.07 ± 0.02
(μg/g/y)		0.026 ± 0.007	0.062 ± 0.002	0.05 ± 0.03	0.029 ± 0.006
Mass Rate Release					
(kg/m^2)		$(3.8 \pm 1.0) \times 10^{-6}$	$(8.0 \pm 0.02) \times 10^{-6}$	$(7.8 \pm 4.0) \times 10^{-6}$	$(4.2 \pm 0.9) \times 10^{-6}$
(kg/m²/a)		$(1.5 \pm 0.4) \times 10^{-6}$	$(3.21 \pm 0.01) \times 10^{-6}$	$(3.1 \pm 1.6) \times 10^{-6}$	$(1.7 \pm 0.4) \times 10^{-6}$
Activity Rate Release					
(Bq/m²/a)		19 ± 5	39.8 ± 0.1	24 ± 1	21 ± 4

Conclusions

Bentonite erosion experiments, with raw or cation exchanged clay material, have been carried out under realistic scenario i.e. with highly compacted and confined bentonite under dynamic conditions simulating the presence of a hydraulically active fracture. The erosion was investigated by circulating a low ionic strength (1.6×10^{-3} M) carbonated water at pH 8.4. The swelling

was confined by stainless steel filter plates. Breakthrough curves (BCs) were acquired which represented the mass concentration evolution of the main clay components and ions released.

Erosion (clay colloid detachment) was detected whatever the clay pellet composition, which means even unexpectedly for the Ca-MX80 bentonite too, even if to a much lower extent than for the raw-MX80, mixed Na-Ca-MX80 or Na-MX80 bentonite. The results confirm that, at fixed flow rate, the amount of exchangeable Na^+ and the presence of Ca^{2+} are the most important parameters with respect to clay colloidal particle detachment.

The BCs monitoring of trace actinide like Th and U allows to quantify the amounts of natural RNs potentially eluted from the backfill material itself. Finally, the Ca-homo ionization process is shown to drastically decrease the Cs retention capacity of the Ca-exchanged clay and that might have strong consequence on the sink properties of the backfill material. Accordingly, all those data can be useful in performance assessment (PA).

The experiments will be continued by reversing the elution pathway as it is easily feasible with our experimental set-up (see Figure 2-38) in order to collect some material detached during the erosion which has eventually sedimented. This will allow to complete the present calculations that refer to the total eluted mass and not to the total eroded mass *(Schatz, 2013)*. The final step will be to open the reactors in order to collect and analyse the residual material. Experiments are thus on-going.

2.1.5.2.2 Long-term bentonite erosion in an artificial fracture under near-natural advective conditions

F. Rinderknecht, F. Friedrich, F. Huber, S. Heck, T. Schäfer

Introduction

In the Scandinavian region, for example, crystalline rock like e.g. granite is the only possible option for the deposition of radioactive waste *(SKB, 2006b)*. In crystalline host rocks compacted bentonite is considered to be suitable for use as geotechnical barrier in a high level radioactive waste repository. Montmorillonite is a clay mineral of the di-octahedral smectite 2:1 group and the major constituent (>90%) of most bentonites. It is characterized by good swelling abilities that enable clogging of water bearing fractures and thereby safely enclosure of the containing waste *(Missana et al., 2003)*. The outstanding sorption capacity by cationic exchange reactions and metal surface complexation resulting in a high retention capacity for many radionuclides is another key feature of the bentonite barrier. The function of the geotechnical barrier lays in the retention of the radioactive waste after the breakdown of the technical barrier as the therefore used canisters have a finite life span. In the case of a canister failure due to corrosion, radionuclides get in contact with the surrounding bentonite buffer under porewater conditions and sorption may occur *(Fernández et al., 2004)*. The radionuclides are safely enclosed in the geotechnical barrier as it will stay intact as long as no water enters the repository. One of the reference scenarios in the Swedish safety case foresees the intrusion of dilute glacial melt water in the repository *(Bath, 2011; SKB, 2011)*. Under these hydro-geochemical perturbations the compacted bentonite will swell with the formation of gel at the water interface. Eventually, radionuclide bearing bentonite colloids may leave the repository into the repository farfield due to advection. Therefore, bentonite erosion processes need to be considered in the safety assessment of a deep radioactive waste repository in crystalline host rock.

Materials and Methods

Artificial fracture set-up and sample geometry. The artificial fracture set-up consists of an acrylic glass housing that is built up by three parts, namely a lower and an upper shell and a cylindrical spacer that is placed inside the arrangement (Figure 2-40). A ring shaped compacted bentonite sample with inner diameter of 40 mm, outer diameter of 80 mm and 25 mm in height is located in the middle of the setup and the spacer is placed in the centre of this ring. The parts of the housing around the bentonite ring are not in contact. Thereby a slit with an aperture of 1 mm height and 180 mm in diameter is formed that mimics a parallel-plate synthetic fracture around the bentonite source and allows the granitic groundwater to reach the bentonite. Natural Grimsel groundwater is pumped through the synthetic fracture with constant flow rate. The dimensions of the compacted bentonite ring are identical to the long-term in-situ test (LIT) which is running since May, 2014 within the **C**olloid **F**ormation and **M**igration project (CFM) located at the Grimsel Test Site (GTS, Switzerland).
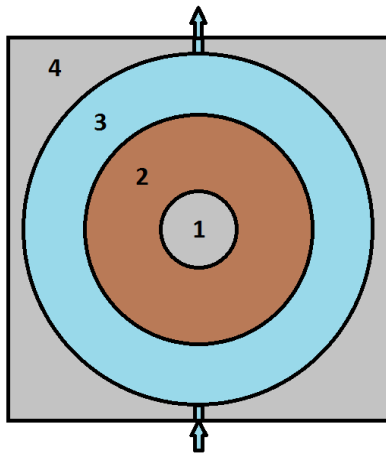
Figure 2-40 (left): Schematic arrangement of the bentonite erosion experiment. 1. spacer 2. compacted bentonite 3. aperture of 1 mm height fracture 4. acrylic glass in contact, seals the arrangement; Arrows at top and bottom: water inlet and water outlet. (right): Bentonite erosion experiment set-up as installed in the lab. Pressure monitoring sensor on top (white cable).

Febex Bentonite characterization. Previous to the **f**ull-scale **e**ngineered **b**arriers **ex**periment (FEBEX) which started in 1997 at the GTS (www.grimsel.com), a suitable bentonite for the construction of the engineered barrier system was selected. The so-called Febex bentonite originating from the Cortijo de Archidona deposit exploited by Minas de Gádor, located in south Spain was chosen and is also used in the experiment presented in here. Characteristics of the Febex bentonite is a very high montmorillonite content, large swelling pressure, low permeability, good retention properties and the ease of compaction. Febex bentonite consists mostly of smectite with minor quantities of quartz, plagioclase, cristobalite and gypsum. *(Fernandez, 2005)* (Table 2-20). The interlayer composition of the smectite phase is given in Table 2-21. A compacted bentonite ring of untreated Febex with a dry density of 1600 kg/m^3 is used for this experiment (Figure 2-41).

Table 2-20: Mineralogical composition of the Febex bentonite.

Mineral	Content [%]
Smectite	92 ± 3
Quartz	2 ± 1
Plagioclase	2 ± 1
Cristobalite	2 ± 1
Gypsum	0.14 ± 0.01

Tracer characterization. Eight thin glass vials containing 220 mg synthetic Ni-labelled montmorillonite (as paste) (*(Reinholdt et al., 2013)*) spiked with 10 mg uranine in each vial as conservative tracer and the homologues Eu, Th, Hf and Tb (25 µg per vial, respectively) are emplaced in the bentonite ring. For this, 8 holes are drilled laterally in the sample ring to mount the glass vials (Figure 2-41). Due to the swelling of the clay the glass vials are supposed to

break and release the labelled montmorillonite and associated homologues as well as the conservative tracer.

Table 2-21: Exchangeable cation composition of the smectite interlayer within the Febex bentonite. Total cation exchange capacity (CEC) and the main cations for charge compensation are listed.

Exchangeable Cation	Content to CEC [meq/100g]
Ca^{2+}	42 ± 3
Mg^{2+}	32 ± 2
Na^+	25 ± 2
K^+	2.5 ± 0.3
CEC_{total}	102 ± 4

Grimsel groundwater composition. Natural ground water from the Grimsel test site is used as contact water in the experiment. It is sampled from the CFM migration shear zone and transferred and stored in 50 L Al barrels under anoxic conditions (Ar overpressure) to prevent oxidation and carbonisation. High pH values, low natural colloid concentration and very low salinity make this groundwater an ideal analogue for glacial melt water (Table 2-22).

Laser Induced Breakdown Detection (LIBD). The laser-induced breakdown detection method has been developed particularly for the characterization of aquatic colloidal nanoparticles in dilute concentrations. The principle of LIBD is based on the generation of a dielectric breakdown in the focus region of a pulsed laser beam. As the threshold energy to incite breakdown for solid is lower than for liquid or gas, the breakdown can be generated selectively on particles dispersed in solution at suitable pulse energy *(Hauser et al., 2002)*. The pulsed laser beam is focused in the centre of the colloid suspension containing sample vial. Closed vials or flow-through cuvettes are suitable. Assumed that the laser energy exceeds a certain irradiance threshold a breakdown is generated when a colloidal particle enters the focal region of the laser. The plasma can be detected by its optical emission or by recording the acoustic signal of the plasma expansion with a piezo detector coupled to the sample cell. By counting the number of breakdowns during a predefined number of laser pulses (breakdown probability), the particle number density in the suspension can be determined. Through optical data acquisition, size information is gained by measuring the breakdown distribution along the laser beam axis at constant laser pulse energy *(Hauser et al., 2002; Walther et al., 2004)*. S-curve LIBD is an advanced LIBD method to investigate colloidal size distributions in multimodal size suspensions by varying the laser pulse energy. As bigger particles form breakdowns more easily, size distributions can be analysed by recording the breakdown probability while step-wise increasing the laser pulse energy followed by computational data evaluation. The method is called s-curve LIBD as the resulting breakdown probability over laser energy diagram has an s-curve shape.

Table 2-22: Granitic groundwater composition from the CFM shear zone at the Grimsel Test Site. The extraction point is located at the intersect of the migration shear zone with the main tunnel of the test site (D.L. = detection limit) *(Huber et al., 2011)*.

Parameter	Value
pH	9.67
Ionic strength	1.2 mM
Mg^{2+}	12.6 µg/L
Ca^{2+}	5.3 mg/L
$Fe^{2+/3+}$	< D.L.
Mn^{2+}	< D.L.
Sr^{2+}	182 µg/L
Cs^+	0.79 µg/L
La^{3+}	<D.L.
U	0.028 µg/L
Th	0.00136 µg/L
Al^{3+}	42.9 µg/L
Na^+	14.7 mg/L
Cl^-	6.7 mg/L
Si	5.6 mg/L
SO_4^{2-}	5.8 mg/L
F^-	6.3 mg/L
NO_3^-	< D.L.
HCO_3^-	2.0 mg/L

ICP-MS. The effluent samples have been measured by ICP-MS (THERMO X-Series II). Therefore, the samples were ten times diluted in 2% HNO_3 and hydrofluoric acid was added to dissolve any bentonite colloids.

Experimental procedure and sampling strategy. The experiment is continuously running since October 29th, 2013. As the bentonite used contains a high amount of swellable clay (smectite), a swelling pressure builds up in the cell during the saturation of the bentonite with the Grimsel groundwater. The bentonite swelling pressure evolution is monitored by a pressure sensor (disynet XP1103-A1-100BG) installed on the top housing part of the cell above the bentonite ring (Figure 2-40). The experiment is conducted at room temperature (~21 °C) under ambient conditions for the first seven months and afterwards transferred to anoxic conditions in a glove box under Ar atmosphere (<1 ppm O_2). The pH measurements were undertaken using a semi-micro Ross electrode (81-03, Orion Co.) in combination with a digital pH meter (520A, Orion Co.). The set-up was calibrated using five commercial buffer solutions covering a pH region of 2 to 10. Samples are taken daily for the first 11 weeks of the experiment and weekly afterwards. During the first seven months, samples are taken in 15 mL sample vials and the remaining effluent is discarded. Once the set-up is in the glove box all the effluent has to be collected and in order to recover as much released colloidal material as possible the total effluent is sampled weekly (~500 mL per week). The samples are analysed with regard to pH, fluorescence intensity (conservative tracer), chemical composition by ICP-MS and IC. Eluted colloid

size, colloid size distribution and colloid concentration were determined by LIBD systems. Flow rate is determined over the eluted volume weighted on a balance during each sampling period.

Figure 2-41: (right) Bentonite sample with holes on side of the ring containing filled glass vials. (left) Top view of the bentonite ring in the swelling stage.

Results

Monitoring of bentonite swelling distance and pressure. Swelling of the bentonite ring takes place during the first weeks of the experiment and is monitored with a camera which is installed only while the experiment is running in the glove box. Pictures have been taken regularly every 20 minutes for the first three weeks and every 3 hours afterwards. Swelling starts immediately upon contact of the bentonite sample with GGW in conjunction with the built-up of a swelling pressure. The biggest difference in swelling distance is observed during the first days of the experiments. After 2 d the sample expanded already 6.1 mm into the fracture. From this point on the swelling distance linearly increases over time with a rate of 0.7 mm per day and reaches a steady state at a distance of 18 mm after ~21 d. Within the first 10 h after the start of the experiment the swelling pressure increased up to ~2500 kPa. During the following days pressure decreased to a constant value between 1700 to 1800 kPa (Figure 2-42) implying steady state conditions after 5 days. The pressure drop coincided with the bentonite swelling into the fracture. As an unsaturated Febex bentonite sample was used in the experiment, a water saturation process took place in the initial phase of the experiment. Groundwater was sucked into the Febex cavities and replaced entrapped air. As a consequence, air bubbles occurred regularly at the rim of the swelling zone during the first days of the experiment which were removed by slightly tilting of the set-up and moderately increasing the flow rate in parallel. This was necessary as the air bubbles otherwise would have stayed in the system effectively preventing the bentonite swelling process. The bentonite ring was fully saturated after three weeks and the swelling distance reached a steady state. Three pressure drops on the third, the forth and the sixth day can be explained by the removal of air bubbles (Figure 2-42This procedure had only a minor effect on the system as the swelling pressure recovered within 3 hours after each

manual disturbance. Pressure monitoring was stopped in May, 2014 as the setup was moved to the glove box.
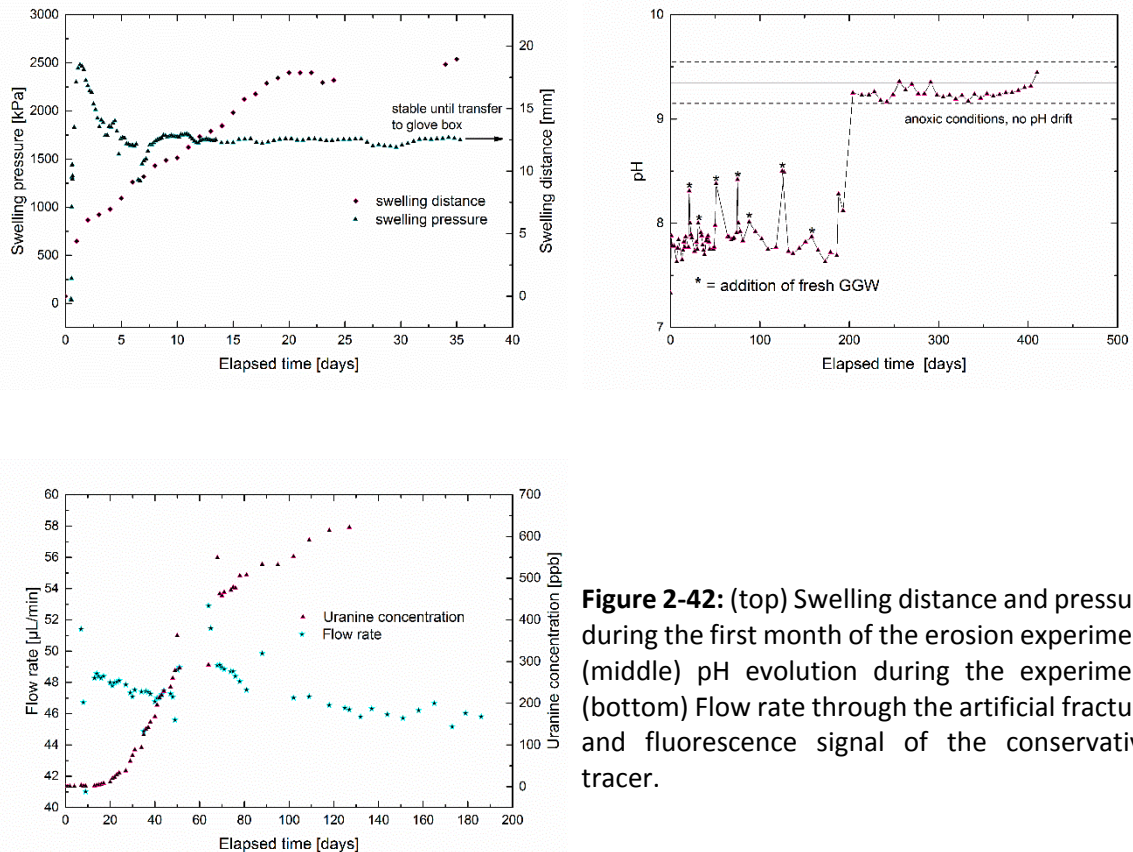
Figure 2-42: (top) Swelling distance and pressure during the first month of the erosion experiment (middle) pH evolution during the experiment (bottom) Flow rate through the artificial fracture and fluorescence signal of the conservative tracer.

Hydro-geochemical monitoring - pH, flow rate and conservative tracer. GGW is continuously pumped through the artificial fracture. A 1 L GGW reservoir is used and refilled if necessary. As the experiment is set up under ambient conditions for the first months, surrounding carbon dioxide and oxygen interacted with the reservoir water which resulted in a fast pH drift towards values around 7.8 due to carbonisation. The repeatedly addition of fresh GGW led to an immediate increase in pH. This pH drift disappeared once the experiment was transferred to the glove box (anoxic and CO_2- free conditions) and the measured pH-values stayed close to the GGW value indicating that the glove box provides an O_2 and CO_2-free atmosphere. Flow rates were monitored during each sampling as the eluted mass over time gives the volumetric flow rate. It was initially adjusted to 49 µL/min but due to some alterations of the tubing the rate decreased to 46 ± 0.5 µL/min within the first months (Figure 2-42). After the transfer to the glove box the pump was changed and again fresh tubing was used. In this case the flow rate was again initially adjusted to 49 µL/min and decreased to 45 ± 0.5 µL/min within four weeks. The breakthrough of the conservative tracer uranine was investigated by fluorescence on a Aminco-Bowman Series 2 Luminescence Spectrometer (Thermo Inc.). After 13 days the first tracer signal was detected rising to a plateau value around 600 ppb after120 days experimental run-time. Based on the results obtained the experiment can be divided into three consecutive

phases namely (i) an initial washing phase in which loosely bound particles are removed, (ii) a dissolution phase in which Febex bentonite accessory phases start to dissolve and finally (iii) an erosion phase with increased bentonite colloid release. Additionally, a cation exchange process occurs during the total duration of the experiment though playing only a minor role. Here, magnesium and sodium in the smectite interlayer is exchanged constantly with calcium.

Phase I (Washing phase): As the raw and un-purified bentonite ring material gets in contact with the GGW, loosely bound particles of the bentonite ring were washed out. The colloidal size distribution and concentration monitored by optical LIBD, s-curve LIBD during the first weeks of the experiment is depicted in Figure 2-45. During the first days a high colloid concentration was detected by LIBD (initially ~10 mg/l) which is explained by the release of loosely aggregates and accessory minerals during the initial bentonite saturation step. The washing phase is followed by a decrease of colloid concentration to values around 0.02 to 0.3 mg/l within 10 d which coincided with increased Ca^{2+}-concentrations.

Phase II (Dissolution phase). The second phase of the bentonite erosion experiment is dominated by the dissolution of accessory minerals like halite and gypsum which are accessory components of natural Febex *(Missana et al., 2011)* bentonite. Simultaneously a cation exchange process occurred in which Ca is intercalated and Na and Mg are released from the Febex interlayer. Dissolution of accessory minerals can be followed by the evolution of sodium, calcium, chloride and sulphate concentrations, respectively (Figure 2-43). This process dominates the experiment during the first 3 months of the total run-time and reaches maximum values between 7 days (Na and Cl evolution, Figure 2-43) for readily soluble phases like halite and 35 days in the case of slightly soluble minerals like gypsum (SO_4, Figure 2-43). These concentrations decrease and reach steady states after 200 days. It is remarkable that in the case of Na, Cl and SO_4 steady state values are still above the respective background levels. Assuming that all sulphate originates from gypsum a total amount of 2.3 mmol is dissolved within 750 days. This sums up to a total gypsum content of 0.19 % in good agreement to literature data (0.14 % ± 0.1 % *(Fernandez, 2005)*). Over this period 16 mmol sodium but only 5.4 mmol chloride have been collected in the effluents.
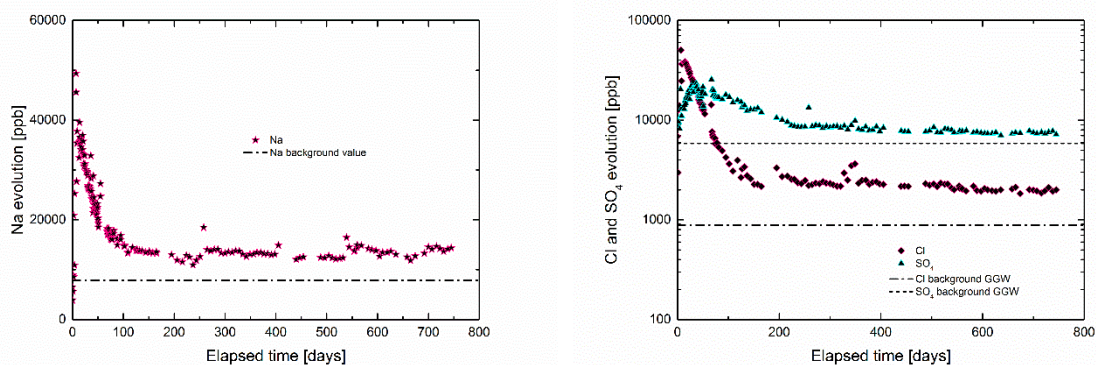
Figure 2-43: Evolution of Na (left) and Cl⁻ and SO_4^{2-} (right) during the experiment.

An additional sodium source can be found in the bentonite itself as 24 % of the interlayer is Na-occupied. In the course of the experiment sodium is exchanged against divalent cations and released from the interlayer. Over the total experimental duration 16 mmol Na is released from the system. Under the assumption that the total amount originates from the Febex interlayer 40 % of the interlayer inventory is exchanged at most. Limited calcium concentrations (Figure 2-44.) that drop after a previous increase due to dissolution processes even under the GGW background level and reach steady state at this reduced concentration are an additional indication for this process and demonstrate that it is still ongoing.

Besides sodium and calcium magnesium with a ratio of 30 % is referred to the CEC part of the Febex interlayer composition. Mg concentrations are only displayed for the first 200 days of the experiment. These values can be correlated to dissolved Mg from dissolution and cation exchange processes. Colloid release is suppressed as dissolution results in higher ionic strength decreasing colloid stability. A maximum value of 2.9 mM is reached during the dissolution phase. Regarding the calcium concentration only, the highest concentration of 0.32 mM alone is already sufficient to inhibit colloid release *(Schäfer et al., 2012)*. Colloids as additional Mg-source turn out to gain importance in the continuation of the experiment and are discussed in detail later. The evolution of magnesium and calcium concentrations both show a maximum after 20 days of the experiment and decrease to reach steady state after 150 days. Released magnesium sums up to a total amount of 0.2 mmol over the first 200 days which correlates to 0.8% of the interlayer Mg-inventory at most.
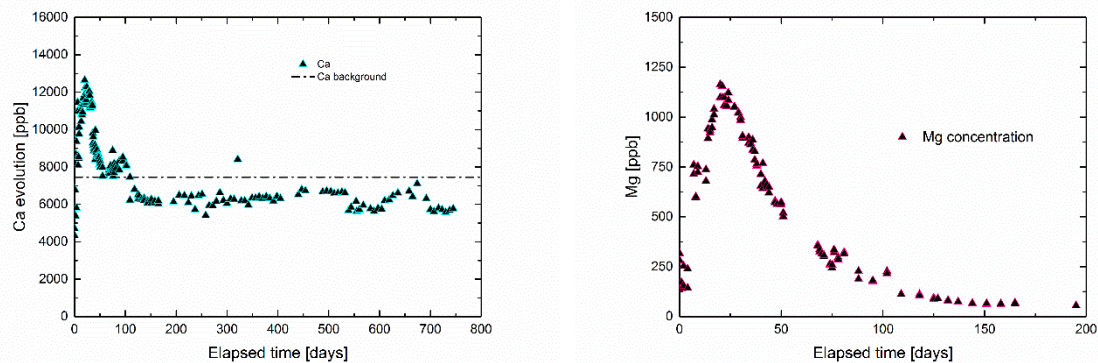
Figure 2-44: Ca (left) and Mg (right) evolution during the experiment.

Phase III – (Erosion phase). Colloid concentrations obtained by optical LIBD increase after 150 days which goes along with a decrease in concentrations of the aforementioned elements. Depletion of the accessory minerals lead to a decrease in ionic strength and consequently in a higher colloid stability. As a result, mean colloid concentrations of 1.05 mg/L with a deviation between 0.1 – 6.1 mg/L are detected during the further run-time. Size distributions obtained by s-curve LIBD show a bimodal distribution of 20 -25 nm particles with a larger size fraction in the range of 150 - 300 nm in the early stage of the experiment. A software update of the system necessitated a new calibration of the system and is responsible for the gap in the s-curve LIBD

data. Thereby the upper end of the calibration was expanded from 400 nm to 900 nm whereas the smallest measureable particle size remained at 20 nm. The newly calibrated system detected smaller particles mainly in the range of 20 - 85 nm and no significant amount of a bigger fraction. Indirect comparison of the colloid size in the effluents over the optical LIBD data is possible. Thereby colloid mean size and concentration have been determined in parallel to the s-curve measurement. The older calibration delivered higher total concentrations compared to the optical LIBD but after the update measured concentrations have mostly been below values obtained by optical LIBD (Figure 2-45). But s-curve LIBD follows the changes in colloid concentrations at all times.
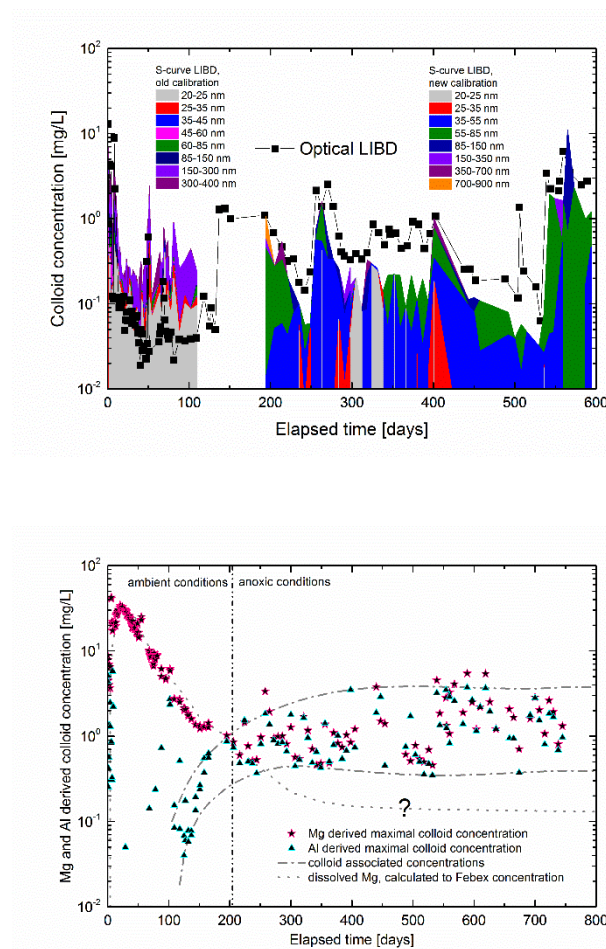
Figure 2-45: (left) Colloid concentration measured by LIBD and s-curve LIBD. The s-curve measurement gives a total concentration and a size distribution. The size fraction is given in the respective stacked diagram. The gap in the s-curve data is due to a software update during the experiment. (right) Colloid concentration calculated from the Mg and Al signal measured by ICP-MS.

Colloid concentrations are calculated from the elemental composition of the effluents. Al, Mg and Si concentrations can be used as they are main components of the Febex bentonite, which shows the structural formula $(Na_{0,31}K_{0,06})(Si_{3,91}Al_{0,09})(Al_{1,32}Fe_{0,24}Mg_{0,52})O_{10}(OH)_2$. Si values are

increased due to the use of hydrofluoric acid which is used for colloid dissolution during the sample preparation and therefore discarded for colloid quantification. Low Al and Mg background in the GGW makes the calculation more reliable. Under the assumption that the total amount of Mg and Al is originating from colloids, total colloid concentrations can be found in Table 2-23. As previously discussed Mg is also released from the bentonite interlayer. This process dominates the Mg concentration for the first 150 days of the experiment. During this period very low Al derived colloid concentrations are detectable. Therefore, one can assume that a colloid phase originating from the Febex sample is not present at this point because of the higher ionic strength from the dissolution and cation exchange reaction which decreases bentonite colloids stability. Al derived colloid concentrations start to increase after 100 days experimental duration and converge to Mg derived values after 200 days (Figure 2-45). After that colloid release (erosion) becomes the Al and Mg concentration dominating process. Measured colloid concentrations scatter between 0.4 and 4 mg/L with a mean value of 1.4 mg/L but the trend is comparable to the LIBD measurement.

Table 2-23: Colloid mean concentration measured by three different methods over the bentonite erosion phase. Mean values, lowest and highest limits are given.

Method	Mean colloid concentration	Lowest colloid concentration	Highest colloid concentration
Optical LIBD	1.05 mg/L	0.06 mg/L	3.72 mg/L
s-curve LIBD	0.69 mg/L	0.03 mg/L	10.9 mg/L
ICP-MS (Mg/Al-signal)	1.42 mg/L	0.40 mg/L	4.59 mg/L

Mg/Al derived colloid ratios of 1.25 and decreased Ca concentrations in comparison to the GGW background value over all samples in this period indicate the release of dissolved Mg in minor concentrations by continuous cation exchange process.

Conclusion

It has been shown that bentonite erosion of an untreated Febex sample using natural GGW can be divided into a washing phase of the sample that only lasts for the very first days and in which colloid concentrations are increased due to the removal of loosely bound particles followed by an up to 150 days lasting dissolution of accessory mineral phase. Thereby, bentonite erosion is limited due to increased ionic strength. Divalent ions like Ca^{2+} and Mg^{2+} in particular have an impact on the colloid stability. Once the accessory minerals are fully depleted and the elemental concentrations level off towards the background values, colloid stability increases and higher colloid concentrations are detected. The bentonite erosion phase lasts over the remaining run-time of the experiment. An additional cationic exchange reaction takes place during the whole experiment. Thereby calcium is stripped from the solution and incorporated in the bentonite interlayer. In exchange sodium and small amounts of the interlayer magnesium are released and can be detected in the effluent. It is remarkable that the exchange of sodium is faster compared to magnesium as the binding strength increases with the valence. In case of the bivalent cations the selectivity of magnesium to bind in the interlayer is higher compared

to calcium *(Li et al., 2012)* but as calcium is part of the GGW in at least 150-fold excess compared to magnesium, a slow exchange of ~1% of the interlayer amount of magnesium over 750 days could be observed.

Furthermore, it has been shown that bentonite erosion scatters quite varying in the size of one order of magnitude concerning colloid concentrations. Changes in colloid concentration have been detected simultaneously by LIBD, s-curve LIBD and ICP-MS. Mean values and limits can be found in Table 2-23. Erosion rates can be calculated from the mean colloid concentration normalized to the contact area between the swelling zone and the surrounding groundwater. Concerning the swelling distance of 18 mm into the fracture colloids are released over a contact area of $3.71 \cdot 10^{-4}$ m^2. Taking in account that roughly 25 L GGW are pumped through the system in a year the erosion rate for natural Febex bentonite in GGW can be determined to 71.0 ± 20.1 g/m^2*a.

2.1.6 Colloid – Mineral surface interactions (microscopic approach)

Introduction

Colloids such as clay minerals and humic substances are ubiquitous in surface and subsurface waters. Because of the low settling velocity, small colloids (≤ 1 µm) can travel long distances, e.g. through fractures or porous media *(Kim et al., 1983; Schäfer et al., 2012)*. Colloid transport in geological formations has been studied for decades. For example, there are environmental issues such as contaminant transport in groundwater *(Chrysikopoulos, 1999; Kretzschmar and Schäfer, 2005; McCarthy and McKay, 2004; McCarthy and Zachara, 1989; Weisbrod et al., 2002)* and more specifically colloid facilitated radionuclide transport *inter alia* at the Nevada Test Site and in the Underground Research Laboratory (URL) experiments at the Grimsel Test Site *(Geckeis et al., 2004; Kersting et al., 1999; Möri et al., 2003; Utsunomiya et al., 2009)*. Besides negative economic issues such as pore clogging (formation damage) during extraction of fluids from the subsurface *(e. g. Civan, 2011; Rosenbrand et al., 2014)*, in fractured reservoirs, deposition of clay colloids enhances reactivation potential and thus, permeability *(Evans et al., 2005; Geiermann and Schill, 2010)*. In this study we focus on fractured media. Fractures serve as preferential conduits for colloids. This is due to (i) large flow diameters that enable high flow velocities compared to the surrounding matrix, (ii) mostly unfavourable conditions for attachment due to negatively charged surfaces of colloids and fractured walls and (iii) negligible matrix diffusion of colloids in contrast to solutes *(Alonso et al., 2007b; Chrysikopoulos, 1999; McKay et al., 2002; Schäfer et al., 2012)*. The mechanistic understanding of colloid transport determining processes in fractured rocks is a key to make reliable long-term predictions on the fate of hazardous elements attached to colloids. Major processes acting on colloids during the transport in saturated fractures are advection, dispersion, adsorption, desorption and physical straining *(Zhang et al., 2012)*. Colloids are transported through conductive fractures by advection. Under high groundwater flow conditions it has been shown that the mean colloid transport velocity is enhanced in contrast to solute conservative tracers *(Becker et al., 1999; Champ and Schroeter, 1988; Geckeis et al., 2004; Hinsby et al., 1996; Knapp et al., 2000; McCarthy et al., 2002; McKay et al., 2002; Möri et al., 2003; Reimus, 1995; Tang and Weisbrod, 2009; Zvikelsky and Weisbrod, 2006; Zvikelsky et al., 2008)*. This can be explained by a combination of three effects: size exclusion, charge exclusion and Taylor dispersion *(Becker et al., 1999; Zvikelsky and Weisbrod, 2006)*. Thus, colloids migrate through a comparably smaller effective volume and due to their small diffusivity the colloids diffuse too slowly to enter low or stagnant flow zones *(Reimus, 1995)*. According to the Stokes-Einstein equation *(Einstein, 1905)* this effect increases with increasing colloid size because of a colloid radius dependent lower diffusion coefficient. *James and Chrysikopoulos (2003)* showed that colloids follow the highest flow velocities in the centre of the fracture. Thus, colloids follow a parabolic velocity profile and travel midstream while migrating through a fracture. Beside the

fraction that is transported unretarded, colloid retention occurs to a certain extent. The main mechanisms for retention are physical straining, sedimentation, (matrix) diffusion, and adsorption/desorption *(Zhang et al., 2012)*. Colloid deposition on solid surfaces is subdivided into two processes: transport and attachment *(Elimelech and O'Melia, 1990)*. The transport process can be described by advection-diffusion equations and it depicts the movement of the colloids from the bulk fluid to the vicinity of the fracture surface. The attachment process depends on the interaction forces between the colloids and the collector surface (e. g. fracture wall) discriminating between electrostatically favourable and unfavourable conditions of attachment *(Chinju et al., 2001)*. This electrostatic dependent interaction is often described by the DLVO-Theory (for further information see e. g *van Oss et al. (1990)*). However, both field- and laboratory experiments found significant colloid retention even under electrostatically unfavourable conditions, where repulsive forces dominate *(Missana et al., 2008; Schäfer et al., 2004; Shen et al., 2010)*. For example *Albarran et al. (2013)* analysed the transport behaviour of artificial (gold and latex) and natural (smectite) colloids in colloid transport experiments through a rough granite fracture under unfavourable attachment conditions. They observed colloid retention for all colloid types and sizes. They concluded that this retention is not driven by the chemical composition of the minerals but rather by mineral porosity, surface roughness, crystal defects, grain boundaries or small scale chemical and/or charge heterogeneities. This conclusion was made in several comparable studies as well *(e. g. Bradford and Torkzaban, 2013; Chinju et al., 2001; Darbha et al., 2012a; Fischer et al., 2012)*. On a bigger scale, in colloid transport experiments through a natural fractured granite block (83 × 90 × 60 cm) *Vilks and Bachinski (1996)* investigate the influence of colloid size, velocity, flow direction and flow path on colloid retention. They showed that the transport of colloids is highly sensitive to variations in flow path and flow direction. In studies on low density carboxylated polystyrene spheres *Cumbie and McKay (1999)* discovered a significant influence of colloid diameter on transport and retention in fractured shale saprolite. The optimum transported colloid size was found to be 500 nm. In accordance with filtration theory *(Tufenkji and Elimelech, 2004; Yao et al., 1971)* both smaller (50–100 nm diameter) and bigger colloids (1000 nm diameter) showed higher filtration factors and therefore lower recovery - the smaller colloids due to diffusion and the bigger colloids due to sedimentation. This conclusion verifies the experimental results and conceptual model of *Reimus (1995)*. The influence of collector surface orientation on colloid deposition was investigated in detail by *Dokou et al. (2001)* by means of static batch experiments using colloids of different sizes and densities and vertical or horizontal coated glass surfaces. They found that under stagnant conditions gravity is negligible for low density colloids (1.05 g/cm³) with sizes < 1 µm. In experiments using bigger or denser colloids (2.07 g/cm³ or 19.20 g/cm³) they observed a higher amount of colloids on horizontal glass samples than on vertical glass samples. The impact of gravity on transported colloids was shown in numerical studies of *James and Chrysikopoulos (2011)* who investigate the influence of fracture orientation on colloid transport through a single fracture. In all these studies mentioned above the influence of collector roughness on colloid retention as a function of colloid size was not investigated in detail. Therefore, the aim of this study is to gain process understanding of colloid size dependent transport and deposition on cut granodiorite surfaces by a combination of the following methodical approaches:

(i) Macro-scale colloid transport experiments under laminar flow conditions (7 mL/h) using a parallel plate type fracture flow cell and a background electrolyte of 1 mM NaCl at pH 5 establishing bulk unfavourable colloid attachment conditions.

(ii) Micro- to nano-scale investigations on the colloid–collector interaction by means of atomic force microscopy (AFM) characterizing (a) the collector surface roughness and (b) the interaction forces using the colloid probe technique.

(iii) The experiments are accompanied by 2-D numerical simulations using COMSOL Multiphysics®. The laminar flow and the colloid transport are solved using the Navier-Stokes equation and a Lagrangian particle tracing approach. Implemented forces which are acting on the colloids are gravity, drag force and Brownian motion.

Parameter variations in the macro-scale experiments included (a) the flow velocity with flow interruptions ("stop-flow") to simulate long residence times, (b) the collector surface roughness in comparison to acrylic glass as reference material, (c) the fracture orientation to sound the potential influence of gravity and (d) the colloid size by using 25 nm and 1000 nm polystyrene carboxylated spheres.

Material and methods

Artificial fracture flow cell. A parallel plate type fracture flow cell made of acrylic glass (Polymethyl methacrylate, PMMA, trademark Plexiglas®) has been designed and constructed. The scheme in Figure 2-46a shows the fracture cell dimensions and design. The main parts consist of two cylindrical bodies: one larger body with an inlet and an outlet and one disc like body. A cavity with the dimensions of 38.3 mm diameter and 0.75 mm depth has been drilled into the bottom side of the larger upper body. After assembling the flow cell, the cavity represents the artificial fracture aperture with the top side surface always consisting of acrylic glass, whereas the lower body can be exchanged to, e.g. granodiorite as shown in Figure 2-46b or acrylic glass. The volume of the fracture is 0.86 mL (inclusive inlet and outlet channels 0.99 mL in total). With the help of an O-ring the fluid cell is sealed and leak-proof. The construction is fixed along its sides by six screws (shown in Figure 2-46b). The advantage of this set-up is the possibility to open it after each experiment for post mortem analyses.
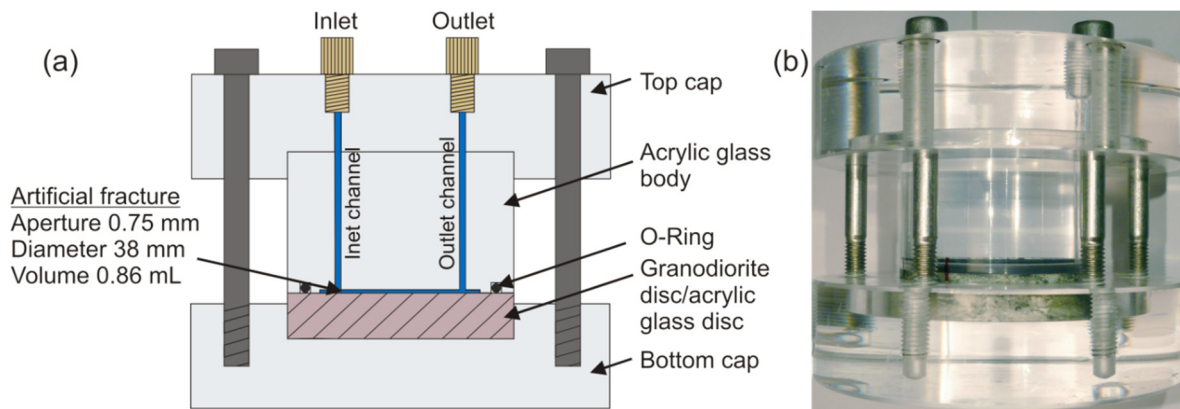
Figure 2-46: (a) Scheme of the synthetic fracture flow cell. The exchangeable disc is marked in purple. (b) Fracture flow cell with installed granodiorite disc. Marks on the rim of the disc assure the correct position of the disc in the casing each time after assembling.

The granodiorite disc used with a diameter of 54 mm originates from the Aar Massif in Switzerland taken at the Grimsel Test Site (GTS, Switzerland). This disc is cut without further treatment (e.g. polishing). After installing the disc in the fracture cell, the flow-wetted surface is 2236 mm². The Grimsel granodiorite consists mineralogically of quartz (32.8 vol%), K-feldspar (17.2 vol%), plagioclase (36.5 vol%), biotite (6.4 vol%), mica and sericite (2.1 vol%) and accessory minerals (5.0 vol%) (mean values taken from *Jokelainen et al. (2013)*). The acrylic glass disc (Polymethyl methacrylate, PMMA, trademark Plexiglas®) with a cut and polished surface (preparation of the acrylic glass disc see SI) has the identical dimensions as mentioned above.

Collector material properties. Streaming potential measurements have been carried out to determine the zeta potential under the geochemical conditions prevailing in the experiments for both collector surface materials: granodiorite and acrylic glass. To determine the zeta potential, streaming current measurements are carried out using the SurPass Apparatus (Anton Paar, dimensions streaming channel: 10 × 20 × 0.5 mm) *(Lützenkirchen and Richter, 2013)*. For an ionic strength of 1 mM NaCl and pH 5.1 the obtained overall zeta potential for the Grimsel granodiorite is -38 mV and for acrylic glass -48.7 mV, respectively. In order to determine the interactions between colloids and the different mineral phases of the granodiorite sample in AFM measurements (Dimension 3100 atomic force microscope equipped with a nanoscope IV controller, Bruker, Germany), the mineralogy of a narrow area on the sample is characterized using scanning electron microscopy (SEM) and energy-dispersive X-ray spectroscopy (EDX). SEM analyses are performed using a QUANTA 650 FEG environmental scanning electron microscope (FEI, USA). Furthermore, the detection of characteristic X-rays allows quantitative determination of atomic concentrations at a micrometer scale (EDX).

Colloid suspension and conservative solute tracer. The colloids used for the investigations presented here are monodisperse fluorescent carboxylated polystyrene spheres with diameters of 25 nm (Postnova Analytics GmbH, Germany) and 1000 nm (Sigma Aldrich GmbH, Germany). Important properties are summarized in Table 2-24. Under the chemical conditions present in the transport experiments, the stability of the colloid suspension (stock diluted in background electrolyte to 0.001 M NaCl and pH 5) is controlled by Photon Correlation Spectroscopy; PCS (ZetaPlus system, Brookhaven Inc., USA). For both colloid types the measured size stays constant for > 24 h, thus, no coagulation occurs and the colloid suspensions are considered stable throughout the transport experiments (Table 2-24).

Table 2-24: Colloid properties implemented in the studies. Improvement of Henry's mobility formula by Ohshima (2001) used to calculate zata potential values.

Colloid size stated [nm]	Colloid size measured [nm]	Ex./Em. wavelength [nm]	Density [g/cm³]	Experimental concentration [ppm]	Colloids per mL stock	Colloids per 5 mL pulse	Zeta potential [mV] at pH 5
25	35 ± 1	552/580	1.030	1.00	1.20E+15	6.00E+11	46.3 ± 1.0
1000	1181 ± 29	470/505	1.045	1.00	4.55E+10	9.09E+06	42.0 ± 1.8

To characterize the hydrodynamics and residence time distribution in the fracture flow cell, conservative tracer experiments have been conducted using a conservative solute tracer. The conservative tracer used is a 10 ppb UV-fluorescent 7-amino-1.3-naphthalene disulfonate (Amino-G, Postnova Analytics GmbH, Germany) dye.

Experimental set-up. A scheme of the experimental set-up is shown in Figure 2-47. The fracture flow cell is connected to a peristaltic pump (REGLO Digital MS-4/8, Ismatec, Germany) during the transport experiments. In order to prevent colloid sorption to the experimental set-up, PEEK tubing has been used whenever possible. The outlet of the fracture cell is connected to a flow-through cuvette (100 μL, Hellma) inside a luminescence spectrometer (Luminescence Spectrometer 55, Perkin Elmer, USA). The fluorescence signal of the tracer and the colloids is measured continuously yielding residence time distributions (breakthrough curves; BTC). The "Time Drive" application software (BL studio, Germany) enables time-dependent fluorescence measurements at a fixed wavelength. A short data interval (interval between two measuring points: $\Delta t = 3$ s) and the low dead volume of the flow-through cuvette result in a high time resolution dataset. In order to measure the pH and determine the exact flow rate, the eluate is collected and weighed after passing the fluorescence device at the outlet using a balance. The length of the tubing has been kept to a minimum to minimize artificial dispersion by the experimental set-up. The pump is installed directly after the fluorescence spectrometer to limit tubing length before the fluorescence measurement device. The total dead volume of the set-up has been quantified to be 330 μL by performing experiments bypassing the fracture cell. In comparison to the dead volume the fracture volume is 860 μL (inclusive inlet and outlet channels 990 mL in total). Three-way valves (3-Way Flow Switching Valve, Upchurch Scientific, Germany) are utilized for switching between colloid and background electrolyte and for switching between fracture flow cell and bypass in the stop flow experiments.
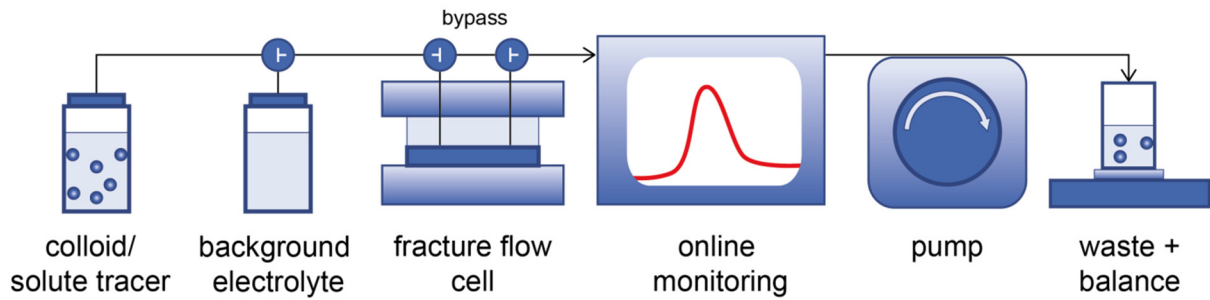
Figure 2-47: Scheme of the experimental set-up (horizontal fracture orientation).

For all experimental conditions and both colloid types calibration curves are taken to convert the fluorescence intensity into a concentration value. Before each experiment, fresh background electrolyte is prepared, in which the granodiorite disc is saturated and equilibrated overnight. After installing the disc and flushing it for at least one hour, the pH of the eluate is checked. Before and after every experiment the initial concentration C_0 of the tracer/colloid suspension is measured by injecting the tracer or colloid suspension directly into the flow-through-cuvette using a syringe. Thus, slight fluctuations of the output signal can be compensated by taking the mean fluorescence intensity of both measurements. To start a continuous flow experiment, the colloid suspension or the solute tracer is pumped into the fracture flow cell. A pulse of 5 mL is used to ensure a constant colloid concentration in the whole fracture. The flow rate in all experiments is set to 7 ± 0.1 mL/h. After saturating the fracture flow cell, the injection fluid is switched to the background electrolyte and the system is flushed. The flushing step is stopped when the fluorescence intensity value reaches the background level. Due to the small spatial dimensions and void volume of the fracture flow cell and the limitation of the pump in performing small flow rates (min. 2 mL/h), the longest residence time in a continuous flow experiment is ≈ 30 min. Therefore, to achieve longer residence times (> 1 h), flow interruptions ("stop-flow") are conducted. After injecting 5 mL of the colloid suspension, the cell is disconnected by switching to the bypass and the injection solution is switched to the background electrolyte. Thereby the colloids within the cell are captured and the whole tubing is flushed to be colloid free. After the desired residence time is reached, the cell is reconnected to the flow and the mobile colloids can be detected as a breakthrough curve. With the help of the stop flow method, residence times of 1 h, 3 h, 14 h and 24 h are achieved. Furthermore, the fracture is either orientated vertically or horizontally to investigate the influence of gravity on colloidal transport. In case of the vertical fracture orientation, the inlet and the outlet channels are oriented in the horizontal direction (injection always from the bottom), whereas for the horizontal fracture orientation the inlet and the outlet channels are positioned vertically. In order to assure that the material surfaces are colloid free before starting an experiment, the set-up is opened and the single parts are ultra-sonicated in a slight alkaline solution (pH 7–9) after each experiment. Additionally, in case of 1000 nm colloids the colloid free surface is verified using fluorescence microscopy.

To normalize the data, the ratio of measured concentration C(t) to initial concentration C_0 is plotted as a function of replaced pore volume PV [-], which is defined as (Equation 18):

$$PV = \frac{Q \cdot t}{V} \qquad \textbf{Equation 18}$$

where Q [m³/s] is the estimated flow rate, t is the time [s] and V is the volume of the artificial fracture [m³].

Converting the concentration C(t) into a colloid number per mL c [colloids/mL] the total recovery [%] can be calculated using (Equation 19):

$$Recovery\ [\%] = 100 \cdot \sum_{i=1}^{n} \frac{c_i \cdot \Delta t \cdot Q}{N_0} \qquad \textbf{Equation 19}$$

where Δt is the interval time [s] and N_0 is the total number of colloids contained in the tracer pulse.

For continuous flow experiments the average residence time t_R [s] is defined as (Equation 20):

$$t_R = \frac{V}{Q} \qquad \textbf{Equation 20}$$

where V [m³] is the fracture volume and Q [m³/s] is the applied flow rate. For stop flow experiments the residence time is taken as the duration time of the stop plus the calculated residence time of the continuous flow.

AFM and colloid probe technique. AFM in combination with the colloid probe technique is used to study (i) the roughness that a colloid experienced while moving along the granodiorite surface and (ii) the interaction forces between a colloid and the different mineral phases composing the granodiorite (quartz, plagioclase, K-feldspar and biotite) and the acrylic glass surface. With the colloidal probe technique, the interacting forces between colloids and/or planar surfaces can be measured. The cantilever probes modified with carboxylated polystyrene colloids (Ø = 1000 nm) are purchased from Novascan Technologies (USA). The properties of the colloid attached to the cantilever are similar to that used in the transport experiments. Due to the limitation of the colloid size that can be attached to the cantilever, to mimic the 25 nm colloid, a sharp silicon tip (Ø = 25 nm) (Bruker, Germany) is used.

The surface topography and the surface profile of the collector surfaces are obtained using both the colloid probe and the sharp tip in contact mode. The obtained data sets are processed for tilt correction and image analysis using scanning probe image processing software (Image metrology, Denmark). The surface topography is quantified using the roughness parameter Rq (Equation 21) which is defined as the root mean square deviation of the profile.

$$Rq = \sqrt{\frac{1}{n}\sum_{i=1}^{n} z_i^2}$$

Equation 21

where n is the number of points in the profile, and z_i [nm] is the height value at point i.

(In order to determine the diffuse layer potential of the collector surface materials, force-volume measurements are conducted. The force-volume measurements are obtained over 256 data points using the colloid probe technique between the 1000 nm probe and the granodiorite surface in the electrolytic media. For a specific mineral, an average of these 256 data points is considered to be a representative force curve. From the spring constant of the cantilever (0.12 N/m), the force-voltage curves are converted to force-distance curves. Initially, the force curves between polystyrene colloid against a surface with known surface potential, e.g. acrylic glass, is obtained. The DLVO equation is applied to fit the approach force curve to predict the unknown potential of the sphere attached to cantilever. Next, using the same colloid, the force curves are obtained on the granodiorite surface at varying surface sites and the potential distribution is determined using DLVO equation as described before.

Modelling. To facilitate the analysis and interpretation of the experimental findings, numerical flow and colloid transport calculations have been conducted using the Finite Element code COMSOL Multiphysics® (Version 5.0) (COMSOL Multiphysics, 2015). A 3-D computational model of the artificial fracture flow cell has been constructed with COMSOL. Based on the 3-D model, a 2-D model has been extracted using one of the two symmetry planes of the fracture (Figure 2-48). To accurately resolve the flow within the fracture cell a hybrid mesh (prismatic boundary layers and triangular elements) consisting of in total 87187 elements has been generated.
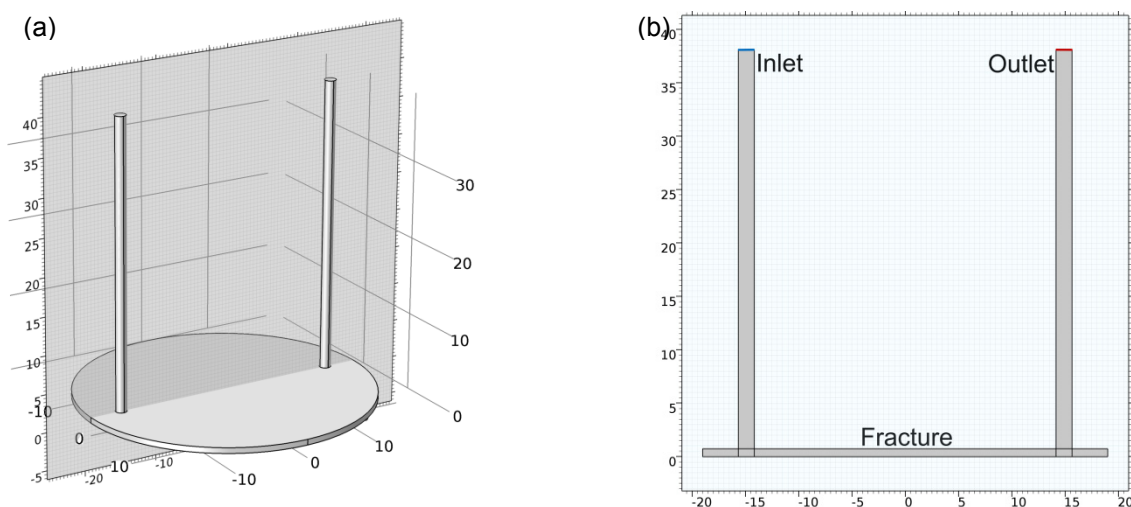
Figure 2-48: (a) 3-D model of the fracture flow cell. The grey plane indicates the symmetry plane used in the construction of the 2-D model; (b) 2-D model of the fracture flow cell used in the simulations. Blue indicates the inlet, red the outlet of the model (numbers given in the figures are length units in mm).

111

Colloid-wall interaction boundary conditions. Since both the colloids and the collector (fracture; acrylic glass and/or Grimsel granodiorite) surface are negatively charged, only a very weak electrostatic interaction is expected. Though, it has been shown by e.g. *Darbha et al. (2012a)* that even under unfavourable attachment conditions colloids may be deposited or even attached on the surface due to surface roughness effects or surface charge heterogeneities.

This is why two different cases have been considered in the model to approach the experimental results:

1) No sorption (unfavourable attachment conditions): When a colloid hits the collector surface, it is reflected with the same angle and velocity with which it has hit the surface. This case accounts for sedimentation only without any attachment (attractive forces acting) of the colloid to the surface.

2) Full sorption (favourable attachment conditions): When a colloid hits the surface, it immediately sticks irreversibly to the surface and cannot be removed again from the surface afterwards. This condition may represent an extreme unlikely case given the experimental conditions presented in the manuscript. Nevertheless, it offers an impression of the maximum attachment possible under the hydrodynamic conditions within the fracture flow cell (including also all the additional forces acting on the colloid as mentioned below (section 0)).

Since there can be also a retention of colloids on acrylic glass, both cases (no sorption and full sorption) are applied for the whole model and not exclusively for the collector surfaces within the fracture. Therefore, a possible retention within the channels which connect inlet/outlet with the fracture is implemented.

Simulation set-up. The Navier-Stokes equations are solved using the Laminar Flow option of COMSOL Multiphysics®. A mass flow rate boundary condition is applied at the inlet and a pressure condition at the outlet, respectively. The mass flow rate from the experiment (1.972E-6 kg/s) is divided by 2π to account for the 2-D model dimension. No-slip flow boundaries (v = 0) are applied to the fracture walls. The COMSOL Particle Tracing Module® is used to solve the colloid transport. Colloid-fluid interaction is modeled by one-way coupling. That is, since the colloid volume fraction in the injection suspensions used in the experiments are below 10 %, it is justified to assume no influence of the colloids on the flow field *(COMSOL Multiphysics, 2015)*. Moreover, under this diluted conditions, colloid-colloid interactions can be neglected as well. This allows solving for the steady state fluid flow and using the simulated stationary flow field in the colloid transport simulation. The colloids are distributed to the flow field at the inlet as a function of the flow velocity distribution. Thus, in the center of the inlet the colloids are more densely distributed compared to the outer area of the inlet. This boundary condition is chosen for both the 1000 nm and the 25 nm colloids. Especially for the 1000 nm colloids, it has been shown that bigger colloids tend to be transported in the center where the highest flow velocities occur *(James and Chrysikopoulos, 2003)*. In all the experiments, a 5 mL pulse of colloid suspension is used. In the model, this pulse is modeled by injecting every second 25

colloids at the inlet for the duration of the pulse. After 2535 s injection time no further colloids are injected. In case of the stop-flow experiments, the flow field is re-initialized after 2535 s to set all flow velocities to zero. Thus, the only forces acting on the colloids during the stop flow conditions are Brownian motion and gravity. After the desired flow interruptions, the original flow field is re-initialized again and the transport of the colloids resumed. In all simulations, the total number of colloids introduced accumulates to 63400. This number of colloids accounts to 0.7 % of the total number of colloids used in the 1000 nm experiments (9.09E+06 colloids) and 0.00001 % in the 25 nm experiments (6.00E+11 colloids), respectively. Nevertheless, this number is a compromise concerning the computational duration increasing with the modeled particle number. A sensitivity study with varying particle number was performed to assure that the chosen colloid number is high enough.

Post mortem analyses on 1000 nm colloids retention on granodiorite. Post mortem analyses of the granitic fracture surface using a fluorescence microscope is done to obtain information on the colloid deposition/attachment behaviour and spatial distribution as function of e.g. mineralogy or surface roughness. In order to prove the feasibility, post mortem analyses are performed for three different continuous flow experiments with the 1000 nm colloids. In these experiments the flow rate (7 mL/h and 2 mL/h) and the colloid concentration (1 ppm and 10 ppm) was varied. An aluminium pinhole aperture containing twelve randomly chosen holes (Ø = 2 mm) and an apparatus for adjusting it precisely allow the investigation of different spots on the granodiorite surface. For this the granodiorite disc is fixed in an acrylic glass case underneath the pinhole aperture (Figure 2-49(a) & (b)). Important properties that will be investigated include roughness and mineralogy. For analysing the surface roughness of each spot Laser Scanning Microscopy (LSM, VK-9700 Color 3D Laser Scanning Microscope, Keyence) is used, with a 10x magnification (1401*1048 µm²). The roughness Rq is automatically determined. This value represents the bulk roughness information for each spot. The mineralogical composition of the granodiorite at each spot is determined by using Scanning Electron Microscopy (SEM). Because of the small colloid size, a post mortem analysis was not feasible for 25 nm colloids. After the transport experiment the flow cell is opened and the granodiorite disc is taken out to let it dry by room temperature. When the sample is totally dry, it is carefully placed inside the acrylic glass case at the marked positions. The pinhole aperture is installed and adjusted. Using a fluorescence microscope (Axioplan 2 Imaging, Fluorescence Microscope, Zeiss, 10x magnification, image size 1401*1048 µm²) the colloids are observed directly. Focus stacking, also known as z-stacking, is used in this case for getting images with a greater depth of field (DOF), so every colloid gets in focus. To compare the results with the LSM and SEM measurements the same areas on the surface are investigated. Using ImageJ (public domain Java image processing and analysis program *(Schneider et al., 2012)*) the z-stacking files are displayed on one plane. With the help of SPIP™ (3-D Image Processing, Image Metrology) the colloids are counted and quantified in size by application of a tool named "Particle & Pore". The kinetics of the colloid deposition is determined by calculating the dimensionless Sherwood number Sh *(Darbha et al., 2012a)* (Equation 22):

$$Sh = \frac{J \cdot R}{C_0 \cdot D_\infty}$$

Equation 22

where J [1/(m²·s)] is the deposition flux, R [m] is the mean colloid radius, C_0 [colloids/m³] is the bulk colloidal concentration and D_∞ [m/s²] the bulk diffusion coefficient. D_∞ is defined by the Stokes-Einstein equation *(Einstein, 1905)* (Equation 23):

$$D_\infty = \frac{k_B \cdot T}{6 \cdot \pi \cdot \eta \cdot R}$$

Equation 23

where k_B is the Boltzmann constant [1.3806481E-23 m²·kg/(s⁻²·K)], T is the temperature [K], η is the dynamic viscosity [N·s/m⁻²]. J is defined as *(Darbha et al., 2012a)* (Equation 24):

$$J = \frac{N}{t_R \cdot A}$$

Equation 24

where N represents the number of the deposited colloids, t_R [s] is the average residence time in the fracture and A [m²] the field of view.
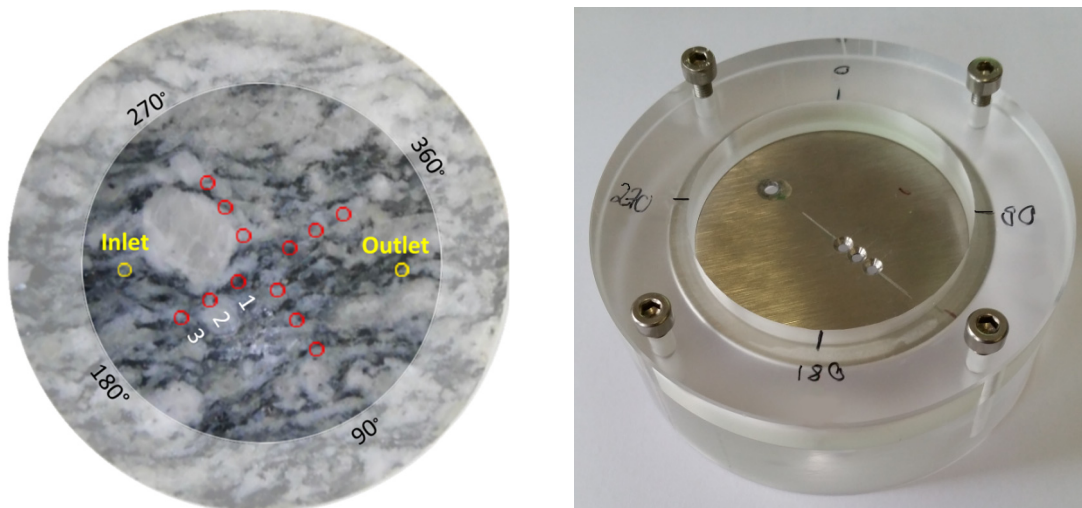
Figure 2-49: (left) Top view on the granodiorite disc. Yellow marked are inlet and outlet. Red marked are the chosen spots in order to direct investigation. (right) Pinhole aperture inside acrylic glass case.

Results and Discussion

This section is subdivided in the results of the continuous flow experiments and the "Stop Flow" experiments. The reproducibility of the experiments was confirmed by repeating experiments randomly.

Continuous Flow experiments and conservative solute tracer. Continuous flow experiments with a flow rate of 7 mL/h for both colloid sizes and both fracture orientations have been conducted. According to Equation 20 the residence time of the colloids in the fracture is 7.4 min. Figure 2-50 shows the BTCs of the experiments conducted with a horizontal fracture orientation (left) and with a vertical fracture orientation (right). Compared to the conservative tracer Amino-G, the colloid results show earlier first arrivals for both colloid types and slightly more pronounced tailings in the measured breakthrough curves for the 1000 nm colloids. As mentioned before, the earlier arrival of the colloid is likely due to size exclusion, charge exclusion and Taylor dispersion (e.g. *Becker et al., 1999; Zvikelsky and Weisbrod, 2006)*. The recoveries of the colloid experiments (Table 2-25) deviate in < 4 % and all recoveries are > 95 %. No dependency of fracture orientation on colloid retention can be detected for both colloid types. Slightly less recovery is observed for 25 nm colloids compared to 1000 nm colloids for equal transport conditions but this deviation is in the range of the error (≈ 2-3 %).
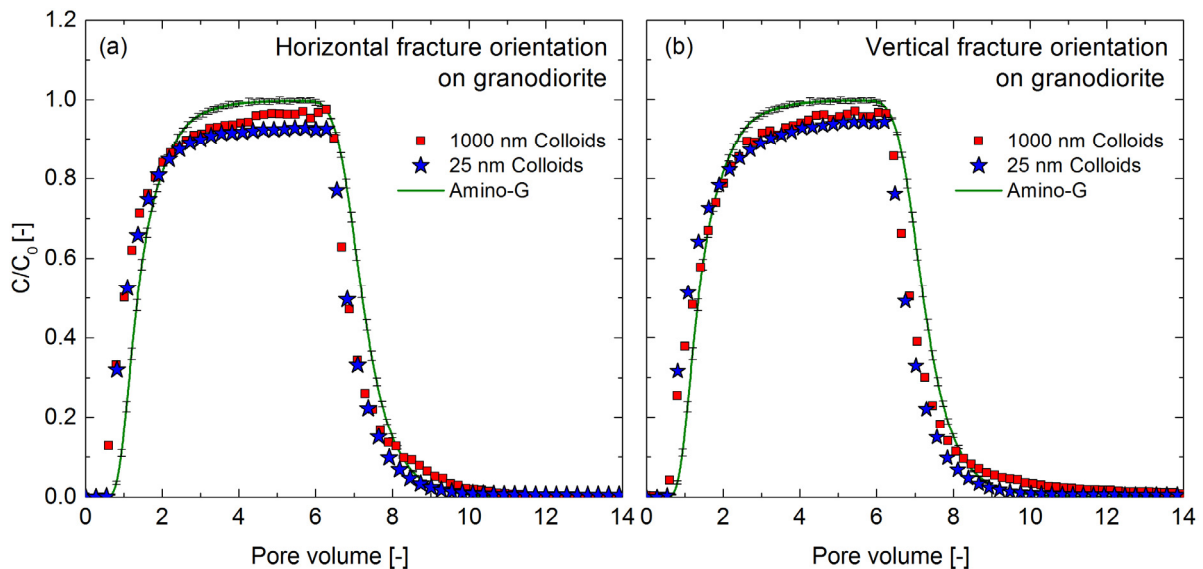
Figure 2-50: BTCs of continuous transport experiments using 25 nm and 1000 nm colloids and Amino-G on granodiorite (Colloid/Tracer pulse: 5 mL).

Table 2-25: Recoveries of the continuous flow experiments (uncertainties of the recovery calculation 2–3 %).

Experiment	Flow rate [mL/h]	Residence time [min]	Recovery [%] Horizontal fracture orientation	Recovery [%] Vertical fracture orientation
1000 nm	7	7.4	98	97
25 nm	7	7.4	95	96
Amino-G	7	7.4	99	99

Stop flow experiments. To investigate whether an increase in residence time has an effect on colloid retention, "stop flow" experiments are performed (Table 2-26). In this section only the BTCs obtained flushing the fracture flow cell after the stop phase are shown. That means the injection of the colloids into the fracture flow cell and the flushing of the tubing during the stop phase are not shown.

Table 2-26: Experimental cases and residence times of the "stop flow" experiments.

Fracture Orientation	*1000 nm Colloid*		*25 nm Colloid*	
	Granodiorite	Acrylic glass	Granodiorite	Acrylic glass
Horizontal	1 h, 3 h, 14h , 24h	1 h, 3 h, 14h , 24h	1 h, 3 h, 14h , 24h	1 h, 3 h, 14h , 24h
Vertical	1 h, 3 h, 14h , 24h	1 h, 3 h, 14h , 24h	1 h, 3 h, 14h , 24h	1 h, 3 h, 14h , 24h

Figure 2-51(a–d) shows the breakthrough curves of the 1000 nm polystyrene colloids and Figure 2-52(a–d) of the 25 nm polystyrene colloids, respectively. In all cases the heights of the BTCs decrease with increasing residence time. In case of the 1000 nm colloids Figure 2-51(a–d)) for the same fracture orientation (a & b or c & d), no striking difference between experiments using granodiorite or acrylic glass can be observed. By comparing the vertical and the horizontal experiments using the same collector surface, both the heights and the shapes of the breakthrough curves differ for residence times ≥ 3 h. For example, with increasing residence time the BTCs of the vertical experiments decrease in height but the shape of the BTC stays constant. In contrast, in the horizontal experiments after 3 h residence time the peak of the BTC is broadened and a flat plateau shape evolves. After 14 h and 24 h the BTCs have a double peak shape with a larger first peak and a smaller second peak. This feature is not visible in the vertical experiments. Regarding these results, for 1000 nm polystyrene colloids there is an influence of fracture orientation on colloid retention, but no influence of collector surface, respectively.
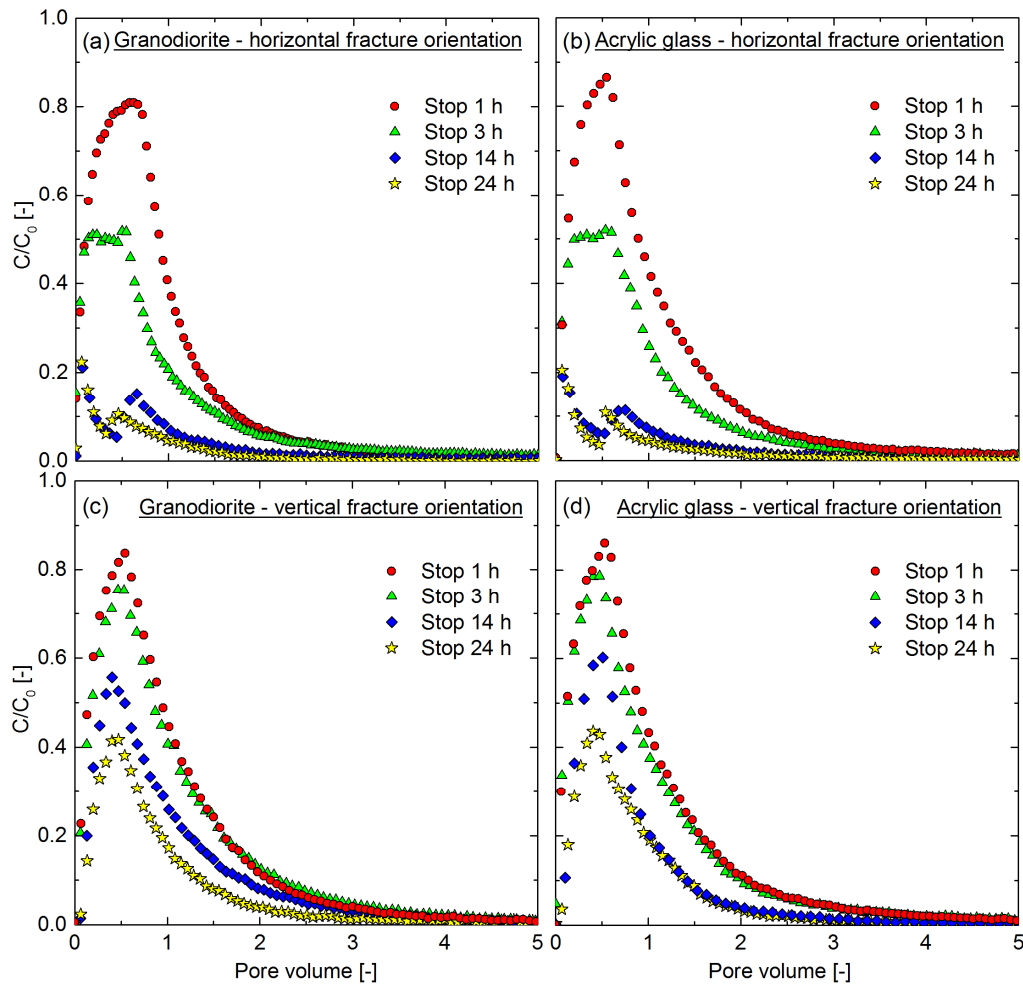
Figure 2-51: BTCs of "stop flow" experiments on granodiorite (a & c) and acrylic glass (b & d) using 1000 nm colloids for horizontal (top) and vertical (bottom) fracture orientation.

Contrary to that, the BTCs of the 25 nm colloid experiments (Figure 2-52(a–d)) show an influence of the collector surface on colloid retention but an influence of fracture orientation is not visible. For equal fracture orientation the heights of the BTCs differ between granodiorite and acrylic glass with higher BTCs in experiments on acrylic glass. Comparable with the horizontal 1000 nm colloid experiments after residence times of 14 h and 24 h, a double peak shape evolves in all cases.
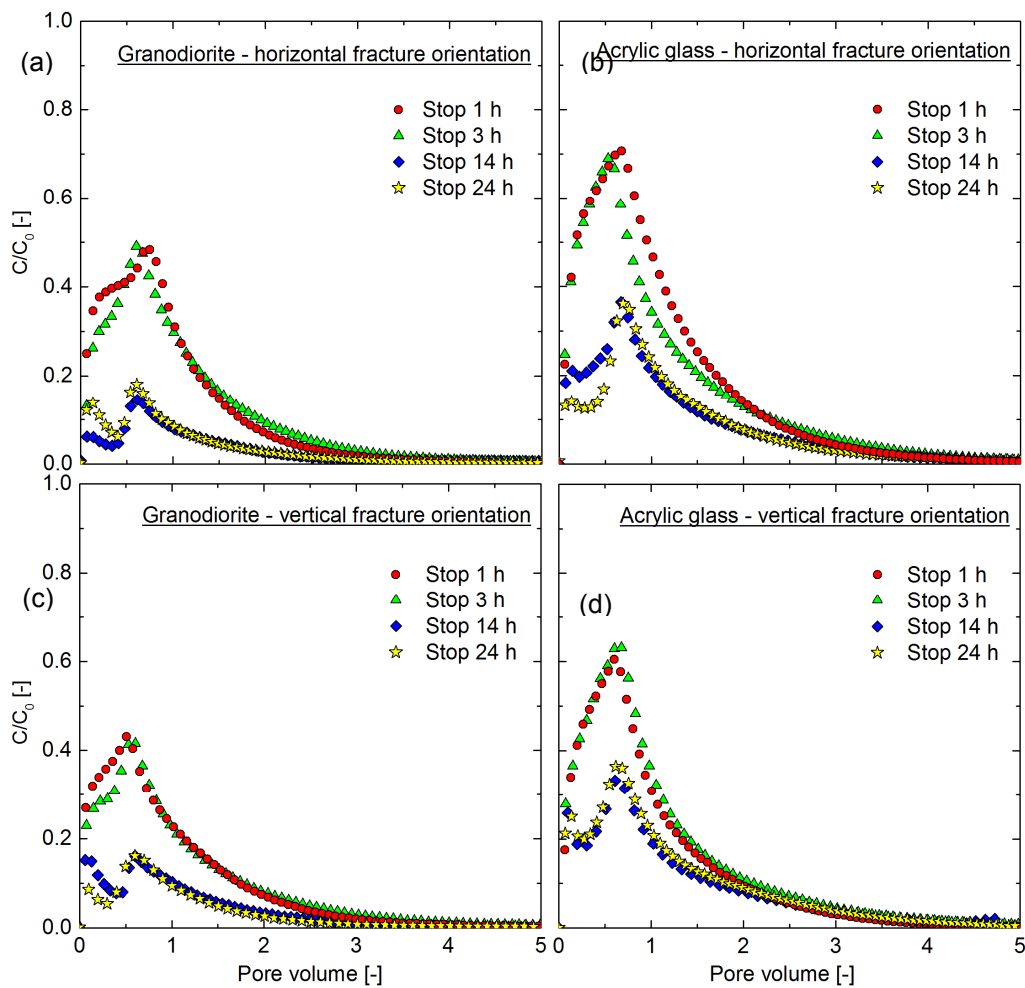
Figure 2-52: BTCs of "stop flow" experiments on granodiorite (a & c) and acrylic glass (b & d) using 25 nm colloids for horizontal (top) and vertical (bottom) fracture orientation.

Figure 2-53 shows the corresponding recoveries as a function of residence time for 1000 nm colloids and 25 nm colloids. An exponential fit (first order exponential decay function) is used to describe the 1000 nm colloid data. However, a second order exponential decay function is needed to describe the 25 nm colloid data due to the comparably high colloid retention within the first hour of stop flow in all experimental cases. By comparing the recoveries with the obtained BTCs, the observed features are visible as well. In all cases the recovery decreases with increasing residence time. In case of the 1000 nm colloids for short residence times (1 h and 3 h) the recoveries are similar between the vertical and the horizontal case. But for the long residence times in the vertical case the recoveries are more than three times higher compared to the horizontal case. The deviation between horizontal and vertical cases increases with increasing residence time. In case of the 25 nm colloids, the colloid recovery decreases with increasing residence time more pronounced in the experiments using granodiorite compared to acrylic glass. In experiments using granodiorite, after 1 h residence time the recovery is < 50 %. The adaption of a second order exponential decay function shows that two mechanisms influence the colloid retention both on granodiorite and on acrylic glass for the 25 nm

colloids. Within the first hour a fast kinetic prevails with the rate of > 4 h^{-1}. With increasing residence time the kinetic slows down which leads to smaller rates (< 0.1 h^{-1}). The progress of the recoveries shows a correlation between fracture orientation and colloid retention for the 1000 nm colloids and a correlation between collector surface material and colloid retention for the 25 nm colloids. This indicates that the 1000 nm colloids undergo sedimentation during their residence within the fracture and that the 25 nm colloids interact with the collector material.
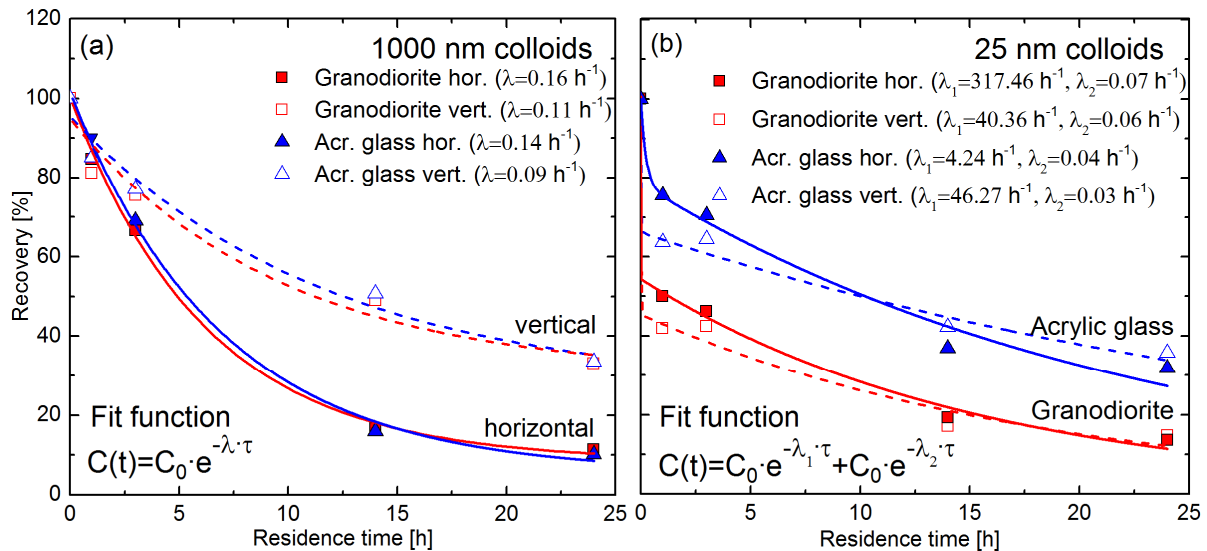
Figure 2-53: Colloid recovery over residence time of "stop flow" experiments using (a) 1000 nm colloids and (b) 25 nm colloids. The solid lines represent the fit function of the horizontal experiments and the dotted line of the vertical experiments.

Based on the results of the breakthrough curves, it is not possible to differentiate, whether the retained colloids are attached irreversibly to the fracture set-up or if all colloids are flushed out as soon as the flushing time is long enough. Because colloids which are deposited to the fracture surface, need longer to leave the fracture due to low flow velocity in the vicinity of the surface than colloids which are in the middle stream assuming a parabolic flow field. This might lead to a dilution effect and generates a concentration beneath the detection limit. The BTCs generated with the 2-D model (see SI 3 and SI 4) show comparable results. In case of the 1000 nm models with and without sorption, an evolution of double peaks is visible for horizontal fracture orientation. In case of the vertical simulations with increasing residence time, the evolution of one single peak is visible with and without sorption. This supports the observation that the retention of the 1000 nm colloids is not dependent on the collector surface material. The model also confirms the experimental results for the 25 nm colloids. There are no differences between vertical and horizontal cases with and without sorption which supports the experimental observations. In case of sorption, double peak shapes evolve in both vertical and horizontal cases which also supports the experimental results that the retention of 25 nm colloids are influenced by the collector material and not by the fracture orientation. A comparison is not made between the experimental recoveries and the modelled recoveries because of the geometrical deviation between the real fracture flow cell and the 2-D model.

Impact of colloid size. To clarify the impact of colloid size on colloid retention, it is important to understand the dominating forces acting on the colloids during the stop flow phase. The prevailing deposition mechanism that brings a colloid to the fracture surface during the stop flow phase is either sedimentation or Brownian motion and it is dependent on the density and size of the colloids. The relative influence of both mechanisms can be analysed by comparing the ratio of the characteristic sedimentation length and diffusion length for both types of colloid sizes. The sedimentation length L_S [m] for spherical colloids is defined as the product of the Stokes settling rate and the residence time of the colloids in the fracture *(Becker et al., 1999)* (Equation 25):

$$L_s = \left(\frac{1}{18\eta}\right)(\rho_p - \rho_f)gd_p^2 t_R \qquad \textbf{Equation 25}$$

where η [kg/ms] is the dynamic viscosity in water, ρ_f and ρ_p [kg/m³] are the fluid density and the colloid density, g [m/s²] is the acceleration of gravity, d_p [m] is the colloid diameter, and t_R [s] is the particular residence time in the fracture.

The diffusion length L_D [m] is defined as *(Becker et al., 1999)* (Equation 26):

$$L_D = \sqrt{2Dt_R} \qquad \textbf{Equation 26}$$

where D [m²/s] is the Stokes Einstein diffusion coefficient which is defined by the Stokes-Einstein equation *(Einstein, 1905)* (Equation 27):

$$D = \frac{k_B \cdot T}{6 \cdot \pi \cdot \eta \cdot R} \qquad \textbf{Equation 27}$$

where k_B [m²·kg/(s²·K)] is the Boltzmann constant and T [K] is the temperature.

The ratio of L_S/L_D represents the relative influence of the two deposition mechanisms: sedimentation or Brownian motion. If the ratio is ≈ 1, both mechanisms are expected to be in equilibrium. Otherwise, sedimentation (ratio > 1) or Brownian motion (ratio < 1) dominates *(Becker et al., 1999)* (Equation 28).

$$L_S/L_D > 1 \qquad\qquad L_S/L_D < 1 \qquad \textbf{Equation 28}$$
$$\text{Gravity prevailing} \qquad \text{Diffusion prevailing}$$

In Figure 2-54 the ratio of L_S/L_D is shown for 1000 nm and 25 nm colloids as a function of residence time. Already after 1 h the dominating force acting on the 1000 nm colloids is gravity. For the 25 nm colloids the overall force bringing colloids to the surface is Brownian motion because the ratio of L_S/L_D stays for all residence times < 1. The L_S/L_D ratio stays in close relation to the dimensionless Péclet number which describes colloid motion as well and which is defined as the ratio of sedimentation and diffusion (*Pe* > 1: sedimentation dominated system; *Pe* < 1: diffusion dominated system) (Equation 29):

$$Pe = \frac{v_{sed} \cdot L}{D} \qquad \textbf{Equation 29}$$

The sedimentation velocity v_{sed} [m/s] is obtained by Equation 25 setting t_R to 1 s. The aperture of the artificial fracture represents in our case the characteristic length L [m]. This results in Pe = 47.59 for the 1000 nm colloids and Pe = 4.46E-4 for the 25 nm colloids. By comparing the obtained recoveries of the 1000 nm colloid and 25 nm colloid experiments (Figure 2-53) with the L_S/L_D ratios and the Péclet numbers, it is reasonable to assume that two mechanisms, are responsible for 25 nm colloid retention and only one mechanism, namely sedimentation, for 1000 nm colloid retention. The working hypothesis for the 25 nm colloid retention is that beside Brownian motion an influence of surface roughness might be responsible for the measured surface retention difference between acrylic glass and the granodiorite surface.
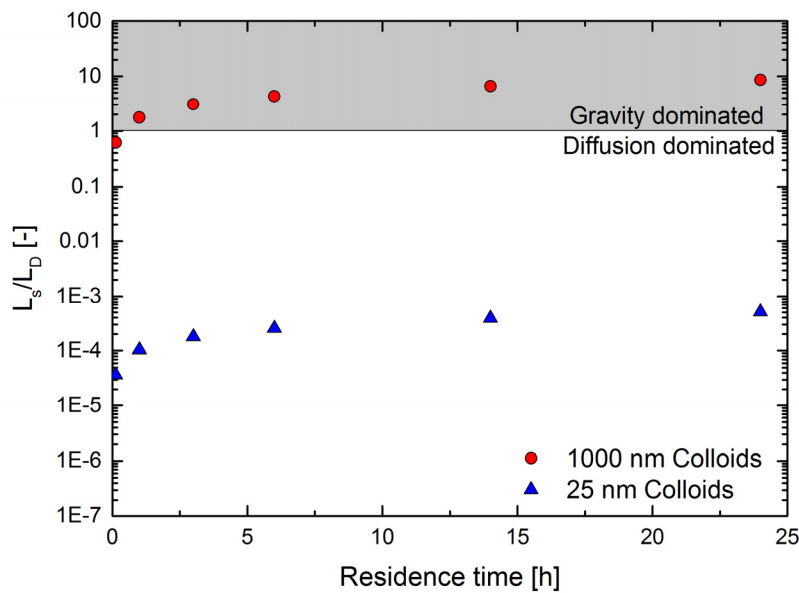
Figure 2-54: Calculated ratio of LS/LD as a function of residence time (7.4 min, 1 h, 3 h, 6 h, 14 h, 24 h) for 1000 nm and 25 nm colloids.

Impact of collector surface material on colloid retention. Both electrostatic interaction and surface inhomogeneities, e.g. surface roughness, may trigger the observed colloid retention. In respect to the negative zeta potentials of the bulk materials (Grimsel granodiorite: -38 mV and acrylic glass: -48.7 mV) and the negative diffuse layer potentials of the mineral phases (K-feldspar: -55 mV; biotite: -51 mV; plagioclase: -62 mV; quartz: -68 mV; more information on the force curves see SI 4) we assume that the observed colloid retention is not due to electrostatic interactions with the collector surfaces. For the measurement on the granodiorite disc, a feldspar crystal and on acrylic glass a random area has been chosen to be representative. Each area is first scanned using the 1000 nm colloid attached to the cantilever and in the next step with the sharp silicon tip as a representative of the 25 nm polystyrene colloid. Figure 2-55 shows the topographic images of the investigated area of the granodiorite (a & b) and the acrylic glass (c & d) surface, scanned by either a 1000 nm colloid or the sharp silicon tip. The 3-D topographic data are projected to denote lateral and height variations on the granodiorite/acrylic glass surfaces as indicated by the colour bar with the scale (notice the changing scale range in the colour bars). Comparing the topographic images of granodiorite obtained by a 1000 nm colloid versus a 25 nm tip, there are significant differences. The images obtained

with a 1000 nm colloid are blurred with rounded edges. No sharp features are visible and the surface is smoother in contrast to the images received by the 25 nm sharp tip. The images of the tip show more details and depth. A four times higher root mean square roughness value (Rq) is calculated for the same surface region for the 25 nm sharp tip in comparison to the 1000 nm colloid. In contrast, in case of the acrylic glass data this difference is less pronounced. Rq increases only by a factor of about 1.2 times.
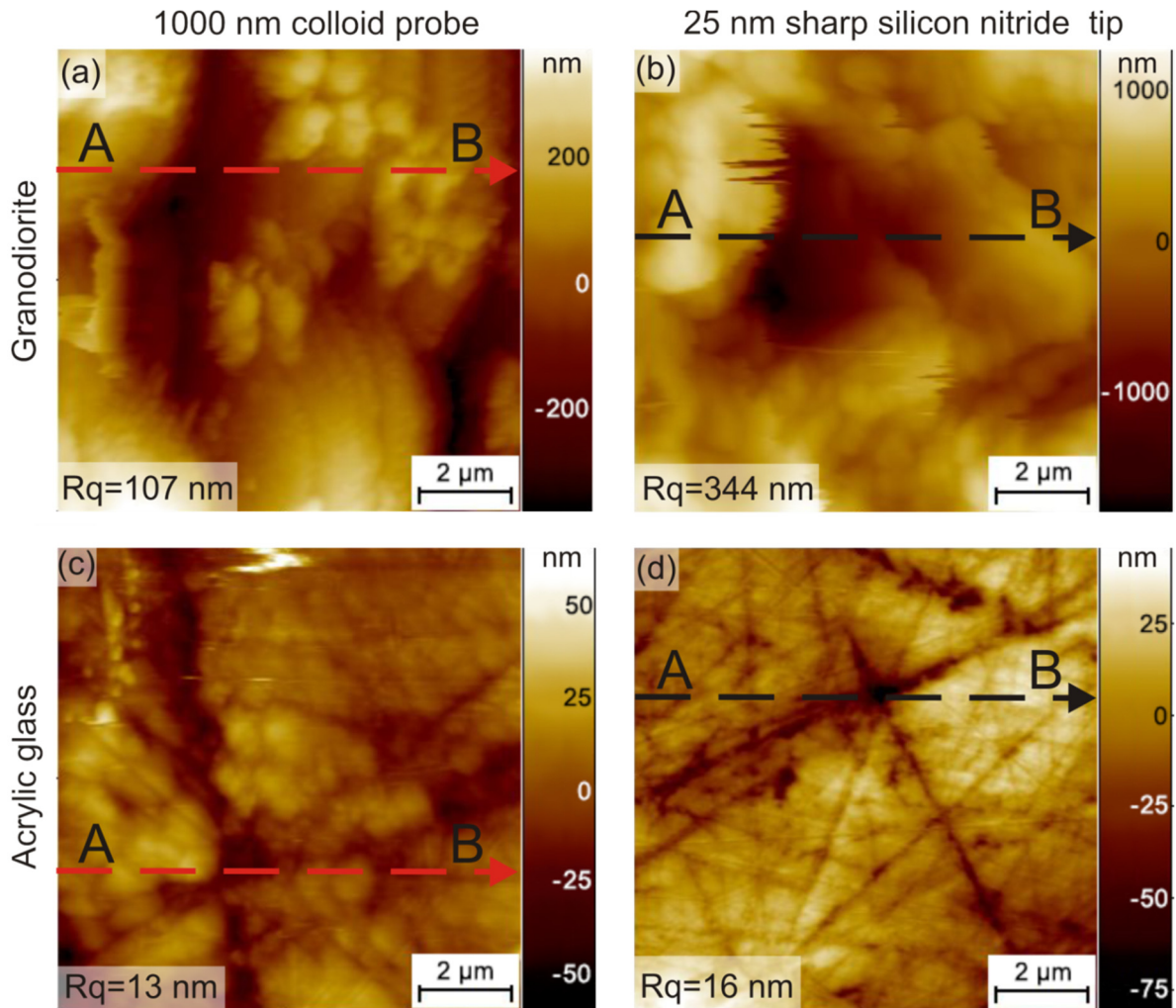
Figure 2-55: Topographic data obtained from AFM by scanning the granodiorite (top) and the acrylic glass (bottom) surfaces using (a & c) a tip modified with a 1000 nm polystyrene colloid or (b & d) a 25 nm sharp silicon nitride tip. The investigated areas are 8 x 8 µm each. The red and black dotted arrows mark the scanning path and direction of the surface profile scan (Figure 2-56).

In the form of surface roughness profiles of the same area, Figure 2-56 illustrates this increase in surface roughness by changing from the 1000 nm colloid (red line) to the 25 nm sharp tip (black line). This means for granodiorite (Figure 2-56a) that smaller colloids see higher surface roughness in the vicinity of the granodiorite fracture surface. For this particular area Rt (maximum height of the profile from the lowest point to highest point) is around 2000 nm. This cor-

responds to 80 times the colloid size of the 25 nm colloids. Using the sharp tip, grain boundaries and also deep structures within minerals can be visualized. This is not possible with a 40 times bigger 1000 nm colloid. This explains the increase in roughness of the same surface area using a sharper tip. The difference by scanning acrylic glass (Figure 2-56b) is less significant. The roughness stays more or less constant. This is because acrylic glass is much smoother and homogeneous compared to the granodiorite disc.
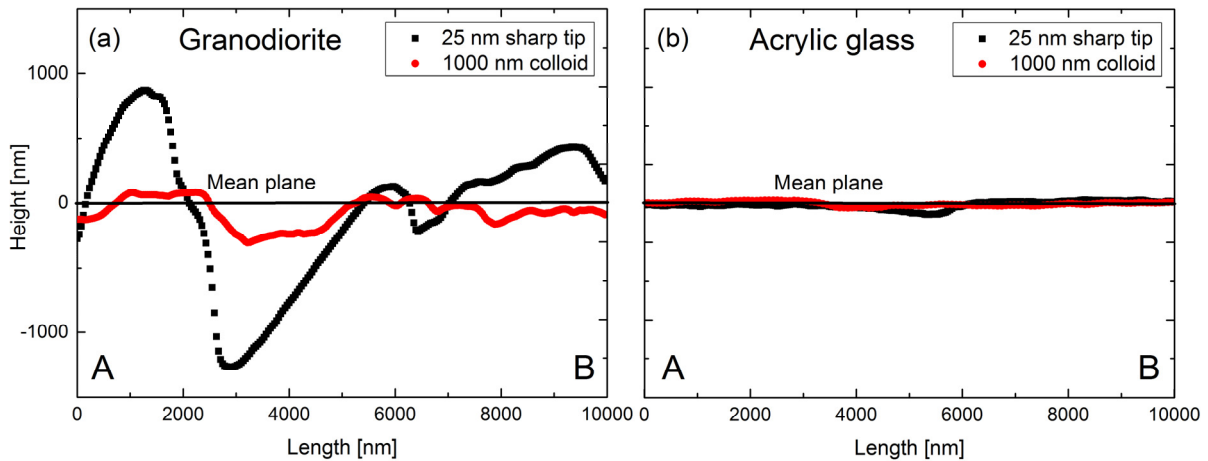
Figure 2-56: Surface roughness profiles obtained on the granodiorite (a) and the acrylic glass (b) surfaces using a tip modified with a 1000 nm polystyrene (red line) colloid or a 25 nm sharp silicon nitride tip (black line).

These results support the working hypothesis that the colloid retention can be directly correlated with the increased roughness seen by the smaller colloids (25 nm) compared to bigger colloid sizes (1000 nm). Therefore, the higher colloid retention on granodiorite is due to the higher surface roughness compared to acrylic glass. As observed by *Darbha et al. (2012b)*, the effect of surface roughness is dependent on the ratio between the asperity to the interacting colloid. For a constant asperity, smaller colloid sizes experience more surface roughness as clearly documented here. This result explains the double peak shape in the BTC of the 25 nm experiments for long residence times. As already mentioned, the double peak shape is not an effect of the fracture orientation. The colloids which are inside the fracture show a higher retention than the colloids which are inside the inlet channel and the outlet channel made of acrylic glass. The roughness and the surface area of both granodiorite and acrylic glass are so high that the colloids are retained on these collector surfaces rather than in the inlet and the outlet channels. In consequence, a double peak shape in the BTC evolves under both fracture orientations and collector surface materials.

Impact of fracture orientation on colloid retention and the shape of the BTC. To understand the impact of the fracture orientation on the colloid retention, the colloid distribution within the fracture flow cell during the stop phases has been investigated with the help of the 2-D model. The black boxes in Figure 2-57 and Figure 2-58 show the regions of interest (ROIs) that are investigated more closely of (a) the inlet channel and the fracture in horizontal fracture orientation

and (b) the outlet channel and the fracture in the vertical fracture orientation. In both cases the results are shown for the colloid distributions in the flow cell after injection (2,535 s), 6 h stop flow and 14 h stop flow under conditions without sorption (unfavourable attachment conditions). It can be seen that after injection the colloids are homogeneously distributed in the whole flow cell. Only the stagnant flow areas in the fracture part of the cell are free of colloids. In case of the 1000 nm colloids (Figure 2-57), with increasing stop flow time the colloids settle due to gravity. In the horizontal case (a) after 14 h all colloids which are initially homogeneously distributed in the fracture have settled to the fracture bottom. Below the inlet (and outlet) there are still colloids since these colloids settle from the inlet area into the fracture area. In contrast, in the vertical case (b) after 14 h almost all colloids initially homogeneously distributed in the outlet channel (and inlet channel) have settled to the outlet channel bottom (and inlet channel bottom). Contrariwise, the fracture stays colloids filled. Based on these results, the development of the double peak in the horizontal case is due to the colloid filled inlet and outlet channels which form the two peaks in the BTC. The colloid free fracture forms the gap between those peaks. In the "no sorption" case, these colloids are mobilized little by little which results in the pronounced and long tailings. In the vertical case, the single peak represents the signal of the homogeneously distributed colloids in the fracture because in these cases the settled colloids in inlet and outlet channels need to be mobilized in the first place as well. Differences in the BTCs between no sorption and full sorption arise in the subsequent flushing stages of the flow cell after the different stop flow times since in case of the favourable conditions, the attached colloids cannot be mobilized again.
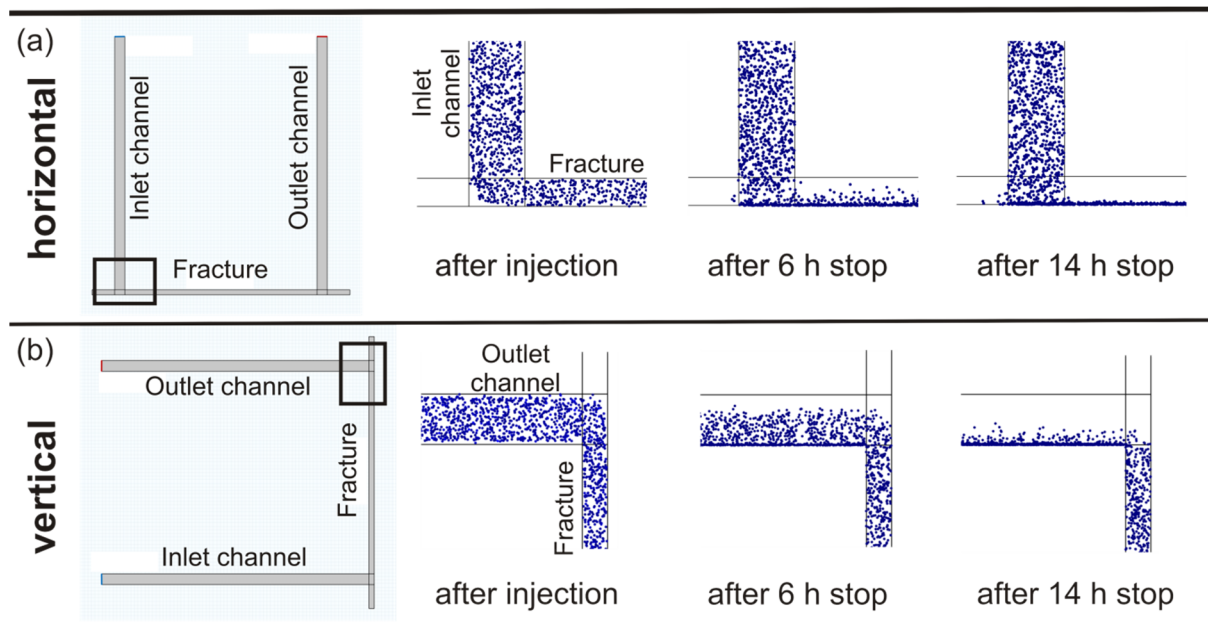
Figure 2-57: Colloid distribution after injection, after 6 h stop and after 14 h stop of 1000 nm colloids in case of (a) horizontal fracture orientation and (b) vertical fracture orientation. The pictured size of the colloids is out of scale.

In contrast to that, for 25 nm colloids (Figure 2-58), it can be seen that after injection the colloids stay evenly distributed within inlet/outlet channels and fracture with increasing residence

time. The stagnant flow areas become more colloid filled because of undirected colloid diffusion. This corroborates that the colloids will not undergo sedimentation and that the development of the double peaks in the experimental BTCs is due to higher retention of the colloids within the fracture than in inlet and outlet channels for both collector surface materials. In addition, the retention on granodiorite is higher compared to acrylic glass. But there is no effect of gravity and fracture geometry on colloid retention for 25 nm colloids.
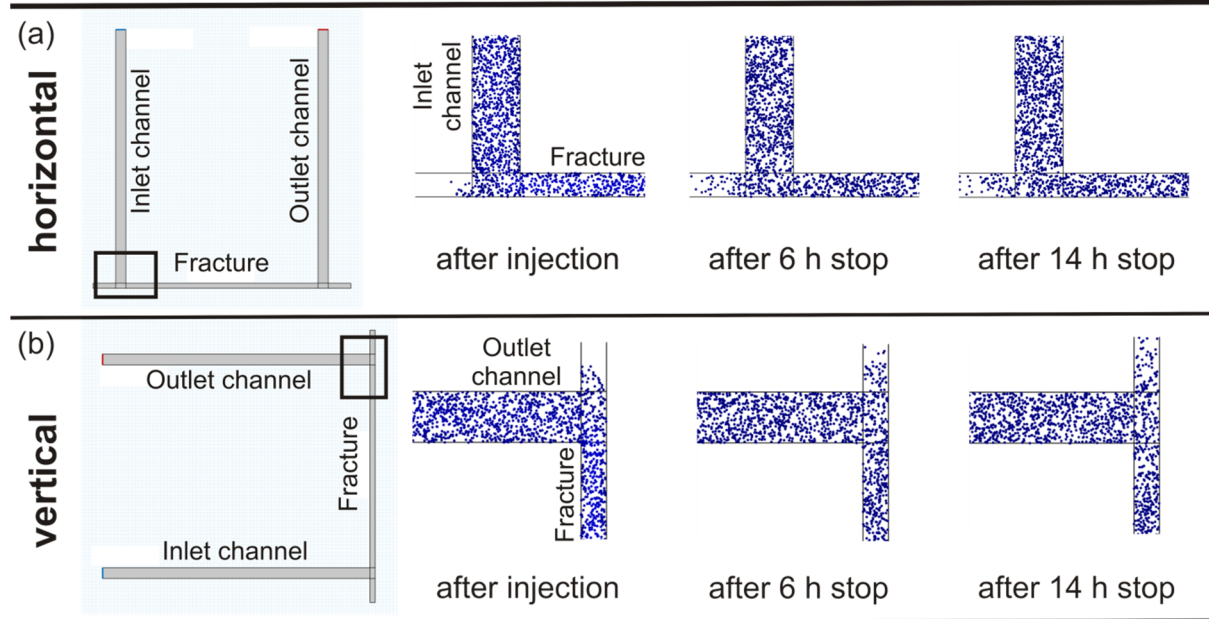
Figure 2-58: Colloid distribution after injection, after 6 h stop and after 14 h stop of 25 nm colloids in case of (a) horizontal fracture orientation and (b) vertical fracture orientation. The pictured size of the colloids is out of scale.

Post mortem analyses after continuous flow experiments. The post mortem analysis was performed on twelve regions of interest (ROIs) on the granodiorite surface after performing continuous flow experiments using 1000 nm colloids. The insights/comprehension gained in the last section will be used for the later understanding. Colloid retention values calculated on basis of the measured BTCs (Table 2-27) show that the colloid retention increases with decreasing flow velocity (=increasing residence time) and decreasing colloid concentration slightly. But this deviation is in the range of the error (~2-3 %). The retention on the granodiorite surface obtained by fluorescence microscopy is an extrapolated value based on the sum of the counted colloids in twelve ROIs. The investigated surface area is 1.5 % (17.63 mm²) of the whole granodiorite surface area involved in the experiments (1134.12 mm²). In the range of the error the extrapolated percentage is in all cases comparable or higher than the percentage obtained by the BTCs (Table 2-27). Comparable with the colloid retention obtained on basis of the BTCs there is an influence of colloid concentration on colloid retention detectable. However, using this method there is no influence of flow rate detectable, respectively.

Table 2-27: Calculated colloid retention of continuous flow experiments using 1000 nm carboxylated polystyrene colloids (uncertainties of the recovery calculation 2–3 %).

Concentration [ppm]	Flow rate [mL/h]	Retention [%] Breakthrough curve	Retention [%] Fluorescence microscopy
10	7	0	3
1	7	2	7
1	2	5	7

By comparing the calculated Sherwood numbers as a function of surface roughness (Figure 2-59), a slight linear correlation between colloid attachment and roughness can be observed for the experiment using the low colloid concentration at high flow rate (1 ppm, 7 mL/h), which means an increase in Sherwood number with increasing surface roughness. In contrast to that, no correlation is visible for the experiment including the high colloid concentration at high flow rate (10 ppm, 7 mL/h). However, against the expectation that a decrease in flow rate (=increase in residence time) has an influence on colloid attachment, no correlation of Sherwood number and surface roughness is detectable in the case using the low colloid concentration at low flow rate (1 ppm, 2 mL/h) and even a lower Sherwood number could be detected.
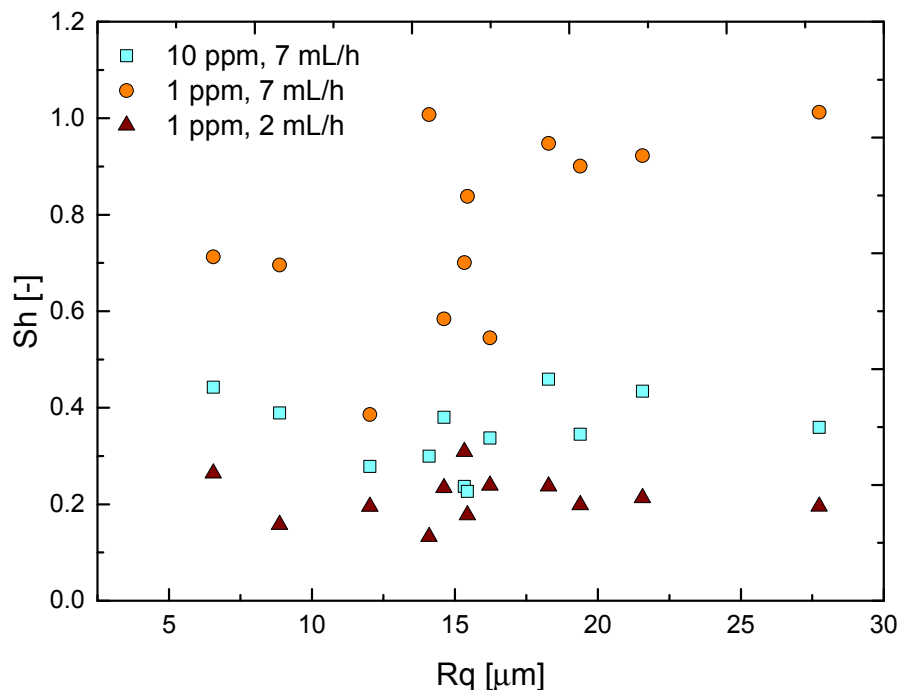
Figure 2-59: Sherwood number as a function of surface roughness of continuous flow experiments with varying colloid concentration and flow rate for 1000 nm colloids.

By comparing these findings with the AFM measurements it is safe to assume that there is no influence of surface roughness on colloids retention on 1000 nm colloids. The L_s/L_B ratio for 1000 nm colloids at 2 mL/h (residence time 27 min) is 1.19. Due to that the colloid deposition at 2 mL/h is neither only dominated by gravity or diffusion. Both forces act equally on the colloids. For these conditions a significant effect of colloid deposition by gravity compared to the higher flow rate is not expected.

To investigate the colloid retention on the granodiorite minerals the self-fluorescent signal of the minerals obtained by changing the filter cubes of the microscope was taken and compared with the mineral deposition information. This additional procedure was done exclusively for the experiment using 1 ppm colloid suspension at 2 mL/h. The information of SEM/EDX measurements of each ROI helps identifying the mineral phases. In Figure 2-60 the combined image of ROI 90_2 is shown with marked mineral phases. It can be seen that the colloids are distributed evenly over the whole investigated ROI. There is no mineral dependent higher or lower colloid deposition detectable. This finding supports the surface potential measurements and the force volume measurements using AFM which show overall negative surface potentials. Comparable observations are made for the other ROIs.
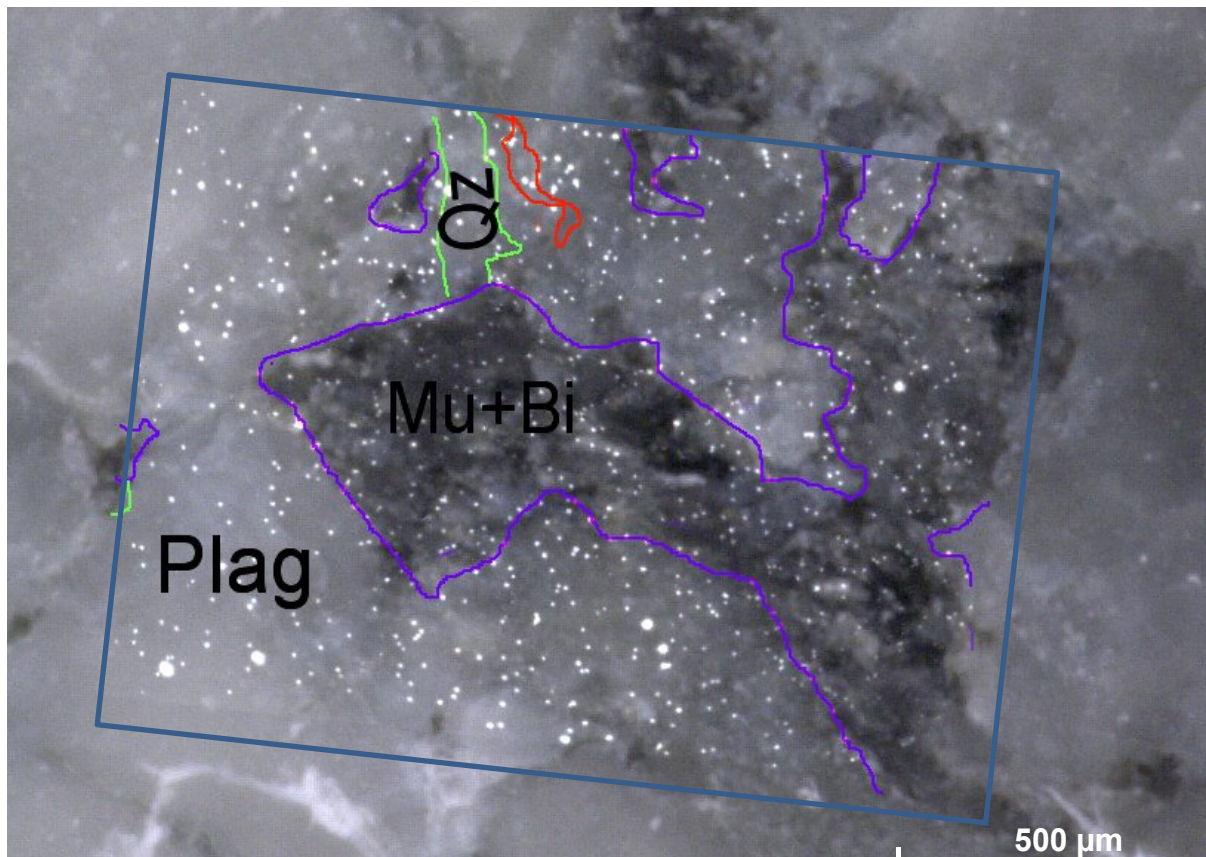
Figure 2-60: Colloid distribution (white spots) on granodiorite minerals phases (plagioclase, quartz muscovite and biotite) ROI 90_2.

Summary and Conclusion

In this study the interaction of monodisperse fluorescent carboxylated polystyrene colloids with a cut granodiorite surface (Grimsel granodiorite; Switzerland) and with an acrylic glass surface was investigated both experimentally and numerically. For this, 1000 nm and 25 nm carboxylated polystyrene colloids were used. By means of colloid transport experiments in an artificial fracture flow cell, residence time and fracture orientation were varied for both collector surface materials and for both colloid types. The experiments were conducted at pH 5 under low ionic strength (1 mM NaCl) and under laminar flow (7mL/h) conditions. For 1000 nm and for 25 nm

colloids a positive correlation between residence time and colloid retention was found on both collector surfaces. Due to the geometry of the fracture set-up it was possible to see a dependence of fracture orientation, more precisely the effect of gravity over Brownian motion on 1000 nm colloid retention. This was not found for 25 nm colloids. In our case, the deposition of 25 nm colloids is controlled by Brownian motion. However, it was found that the colloid retention of 25 nm colloids is influenced by the collector surface material with a higher retention on granodiorite. This was confirmed by AFM measurements using the colloid probe technique. Compared to 1000 nm colloids, 25 nm colloids are exposed to a higher surface roughness on granodiorite, whereas the "felt" roughness for acrylic glass is comparable. Additionally, according to the small colloids the roughness of granodiorite is many times higher than on acrylic glass. This difference is less for 1000 nm colloids. Thus, 1000 nm colloids overcome this surface roughness without significant retention. These findings led to the conclusion that 1000 nm colloids undergo sedimentation due to a higher influence of gravity over Brownian motion. 25 nm colloids are retained by surface roughness due to their small colloid size and higher diffusivity into cracks and scratches of the material. The BTCs generated with the help of the 2-D model represent qualitatively the experimental findings for both colloid sizes. The observed double peak (in the horizontal experiments using 1000 nm colloids and all experimental cases using 25 nm colloids) and the single peak (in the vertical experiments using 1000 nm colloids) after long residence times (14 h and 24 h) can be reproduced/simulated by the 2-D model. The colloid deposition and diffusion behaviour was well shown by means of visualizing the colloid distribution in the inlet/outlet channels and the fracture after distinct residence times. The experimental findings for the 1000 nm colloids are supported by fluorescent microscopy which was used for post mortem analysis. For low colloid concentrations ~1 ppm neither a mineral dependency nor roughness dependency was observed for the 1000 nm colloids in a continuous flow experiment at 2–7 mL/h.

These findings have applications in very different fields:

Polystyrene microspheres can be seen as an analogue to micro plastics, which are frequently found in surface waters *(Teuten et al., 2009)*. The transport of these polystyrene nano-particles in fractures and the identification of the dominant retention processes are of paramount importance to evaluate the risk for these vulnerable groundwater systems.

The erosion of compacted bentonite under low ionic strength groundwater conditions and the long-term prognoses of the integrity of the so called geo-engineered barrier in contact with a water conducting feature/fracture is a key topic for the safety assessment of deep geological repositories in crystalline rocks. Numerous experiments on the bentonite erosion issue have been performed within the CP BELBaR project using acrylic glass as a synthetic fracture material, partly implementing the natural surface roughness *(Reid et al., 2015)*. However, the fracture surface interaction of released clay colloids in the size range of 20 nm–1000 nm is not investigated in detail. The use of monodisperse colloidal material covering the smallest and largest size class observed in the released clay material covers the spectrum of surface interaction processes potentially occurring. This study gives mechanistic details on the retention

processes expected in fractures under unfavourable conditions as a function of the fracture orientation and shows the size dependent retention.

Although obtained in simplified geometries and under low ionic strength groundwater conditions the data presented here shows the significant effect of fracture orientation on colloid deposition. Having high suspension load, as expected in geothermal reservoirs, permeability variation with orientation of the fracture network due to reactivation potential might be triggered additionally by colloid/particle deposition. The experiments presented here, using low colloid load and very simplified fracture orientation, are a first step towards this problem.

2.2 Field experiments at Grimsel Test Site (GTS)

2.2.1 The Colloid Formation and Migration (CFM) project: Background and project organisation

The Colloid Formation and Migration (CFM) project is conducted in the framework of Phase VI of the research program of the Grimsel Test Site (GTS). GTS Phase VI runs from 2004 to 2013 and is dedicated to repository-relevant (i.e. large-scale, long-term) in-situ experiments. An extension of Phase VI until 2018 is under discussion. The CFM project is the current project in a series of experiments conducted within the Radionuclide Retardation Programme of the GTS since 1984. Phase 1 began in 2004 and ended early in 2008. The main tasks were preparatory studies concerning in-situ boundary conditions, predictive modelling and supporting laboratory programs.

Experimental aims and boundary conditions

The aims of the CFM long-term colloid project are listed in Table 2-28.

Table 2-28: CFM project aims and approaches.

Aim	How it is addressed in the CFM project
Examine colloid generation rates and mechanisms at the engineered barrier system (EBS) – host rock boundary under in-situ conditions	Laboratory (e.g. Bentflow and mock-up tests) and in-situ test
Evaluate the long-distance migration behaviour of EBS-derived colloids in a water-conducting feature in a repository-relevant flow system (i.e. with a very low flowrate/water flux)	Colloid tracer tests and monitoring of release from in-situ test
Study the long-term geochemical behaviour (mobility, mineralisation, colloid formation etc.) of radionuclides at the EBS-host rock boundary	Laboratory tests (including mock-ups) and monitoring of in-situ test near field
Examine reversibility of radionuclide uptake onto colloids	Laboratory, possibly mock-ups
Gain experience in long-term monitoring of radionuclide/colloid propagation near a repository	Design, development, implementation and "post-mortem" examination of in-situ test monitoring system
Apply the results to improve repository performance assessments, optimise EBS design and contribute to the "monitoring" debate	

History of field activities for site selection, characterization and preparation from 2005 on:

The field activities conducted in Phase 1 of the CFM experiment focused on site selection, site characterization and site preparation. Colloid transport in a water-conducting feature is expected to take place in an advective flow regime. At the onset of Phase 1 it was clear, therefore, that the key element for the selection of a suitable site at GTS for the CFM experiment was the availability of a water-conducting feature with a well characterized natural flow field. The migration (MI) shear zone at tunnel position AU96 met many expectations. As the focus structure of earlier MI, EP (Excavation project) and CRR (Colloid and Radionuclide Retardation) experiments, it had been studied already and instrumentation was in place. Numerous hydro- and tracer tests had been conducted, some with active tracers which required the temporary transformation of the AU gallery into a radiation controlled zone. The MI shear zone is an almost two dimensional feature extending from the KWO (Kraftwerke Oberhasli AG) access tunnel towards the VE gallery. An early task of the CFM Phase 1 site characterization was the investigation of the tunnel surface of the roughly 7 m marked by the MI shear zone (tunnel coordinates AU93 to AU100). Focus was on (i) detailed mapping of major structural features like ductile shear zones, brittle fractures and fault gouge and (ii) hydrological investigations in terms of localizing major water inflow points and measuring the groundwater flow rates of these features. Figure 2-61: shows the result of the geological mapping of the MI shear zone. The main foliation in the granodiorite is defined by biotite and feldspars which are aligned in parallel to each other. The shear zone was originally formed by ductile deformation. In a later stage of alpine deformation and following uplift, the shear zone was reactivated. In this brittle deformation phase, cohesionless fault gouge material formed along discrete fracture planes. The complete MI shear zone is represented by 3 steep (>70°) shear planes striking WSW-ENE. They are hydraulically connected and represent a complex water conducting feature. The transmissivity of the shear zone was found to be, in general, between 10^{-8} and 10^{-6} m^2 s^{-1} with very low transmissivity parts where transmissivity is $<10^{-10}$ m^2 m^{-1}. The main shear plane in the northern part of the mapped zone shows a high degree of brittle deformation overprinting the older ductile features. This main shear plane is also characterized by distinct inflow points where surface packers have been installed (red circles in Figure 2-61:). These inflow points are openings of up to 10 mm in width and deliver continuous water inflow into the tunnel. The water conducting features tend to be filled with fault gouge. More detail on the deformation history and fracture geometry is found in *(Möri and Blechschmidt, 2006)*. The results of the mineralogical analyses and investigations of the chemical composition of discharging groundwater from the MI shear zone are found in *(Blechschmidt et al., 2006)*. The hydraulic characterization of the test site could build on tests from the existing boreholes and results from earlier MI, EP and CRR activities. Figure 2-61 shows the test site in a 3D block model with the MI shear zone and boreholes at the onset of Phase 2 of the CFM project. The 86 mm boreholes are equipped with inflatable multi-packer systems isolating the MI shear zone interval in each borehole. The isolated intervals are equipped with pressure lines allowing permanent monitoring of groundwater pressure in the MI shear zone as well as flow lines for hydro- and tracer testing. Preliminary hydraulic tests were conducted at the CFM site in March 2005. Hydraulic testing focused on the MI shear zone with the intention to estimate the shear-zone transmissivities T and to provide data for numeric modelling. Other objectives of the field campaign were to document 'static' interval pressures, to measure the natural inflow into the tunnel from

the so-called Pinkel and Kalotte inflow points and to assess the impact of the sealed boreholes. The 2-day hydraulic testing campaign confirmed the heterogeneous properties of the MI shear zone. For the majority of the investigated shear-zone intervals, the estimated T values vary between $6 \cdot 10^{-8}$ m^2 s^{-1} and $1.4 \cdot 10^{-6}$ m^2 s^{-1}. The measured hydraulic heads vary within 12.8 m. Interference reactions were recorded in all but two monitored boreholes. Further results are provided in *(Blechschmidt et al., 2006)*. Preparation of the test site started with cleaning the rock surface using sandblasting and pressure washing. The cleaning campaign allowed detailed geological mapping and detection of the major inflow points which were then equipped with surface packers (Figure 2-61: for locations). The next step involved sealing the shear planes and, eventually, the entire tunnel surface over a 6 m stretch with special cements and resins. Tunnel inflow continued to be monitored throughout these activities. Pressures have also been recorded continuously since March 2005 in the packed off borehole intervals in the MI shear zone. The pressure records show responses to tests of the sealing quality, renewed sealing activities, pressure conditions created for tracer tests etc. Two tracer tests were performed after the resin sealing (but prior to establishing low gradient flow fields) within the MI shear zone using uranine (Na-fluorescein) doped water. #1 was the first tracer test performed after the shear zone was sealed in the second half of 2005. The sealing was a requirement to achieve lower hydraulic gradients. Tracer Test Run #2 was performed in January 2006 after a fissure near the Pinkel surface packer was sealed and the shear zone pressures had recovered and stabilized. The objectives of the tracer tests were to obtain advective travel times, assess the recovered tracer and estimate the dispersion parameters in the shear zone flow field from boreholes to the tunnel surface packer intervals when the shear zone was sealed but allowed to freely flow from surface packers. Two boreholes, CFM 06.001 and CFM 06.002, were drilled and equipped for testing and observation in August 2006 (Figure 2-62). In particular, the hydraulic modelling results showed the boreholes could fill existing data gaps. An inspection with a borehole camera was carried out in both boreholes. The camera logs confirmed the position of the shear zone and identified lamprophyre intrusions in the core of CFM 06.001, whereas in CFM 06.002 no clear fractures were observed, except a water outflow point at the borehole end (6.85 m). Some weeks later, borehole CFM 06.002 was extended to penetrate the shear zone. Both boreholes were equipped with packer systems and saturated. By the time of the 3rd CFM Project Meeting in May 2006 it was apparent that the status of the sealing of the MI shear zone did not fulfill the requirements for the in-situ experiment. The hydraulic gradients within the MI shear zone towards the AU tunnel were too steep. It was decided to install a 5 m long steel mechanical tunnel packer (referred to as mega-packer or sub-mountain packer) to resist higher pressures in the MI shear zone. The annular space between the tunnel wall and the packer can be pressurized to support the resin sealing. In February 2007 the mega-packer and the new boreholes were instrumented and connected to the GeoMonitor II automatic data acquisition system (DAS).
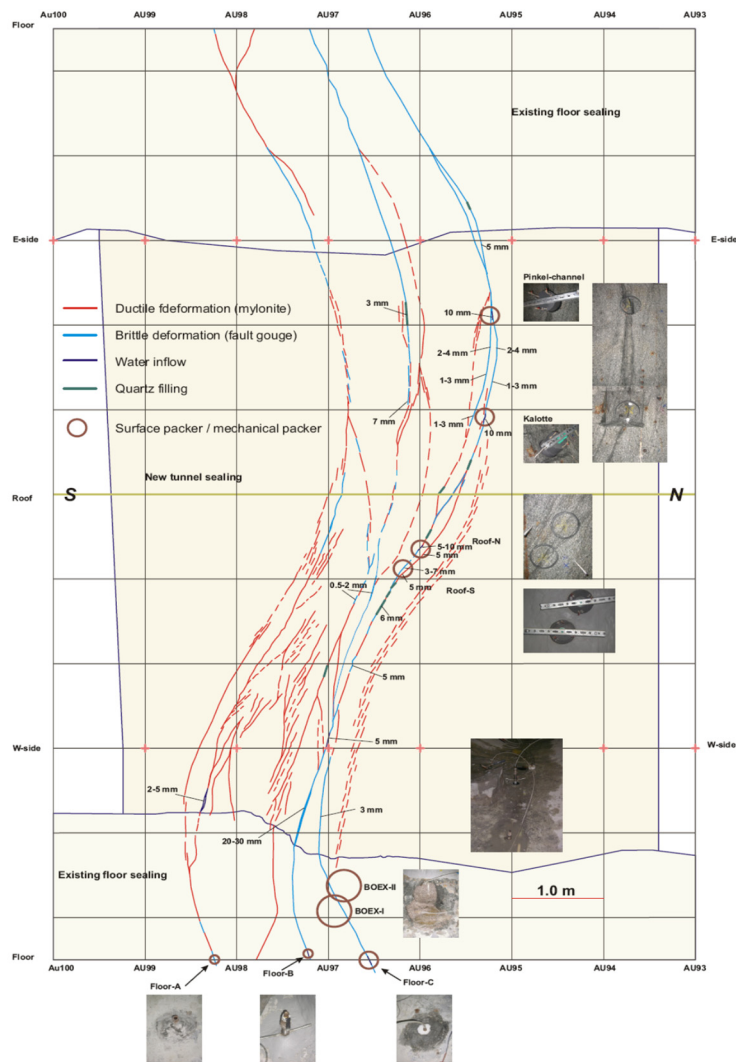
Figure 2-61: Detailed geological mapping of the MI shear zone between tunnel meters AU93 and AU100 with surface-packer locations (Blechschmidt et al., 2006).

In the immediate area around the tunnel intersection, the MI shear zone is effectively isolated and does not intersect any other large scale structure. At a greater distance it is believed that the shear zone intersects the lamprophyre that crosses the tunnel at about tunnel meter AU73 close to the site of the LTD (Long Term Diffusion) monopole experiment (over-cored in 2010). The local transmissivity of the shear zone around borehole CFM 06.001 ($\sim 10^{-9}$ m^2 s^{-1}) is slightly lower than the average of the CFM/MI zone (between 10^{-8} and 10^{-6} m^2 s^{-1}). The hydraulic properties of the lamprophyre and observed pressure interferences with the MI shear zone were analysed in *(Lanyon and Blechschmidt, 2008)*. Throughout 2007, a series of five tracer tests (Tracer Test Runs 07-01 to 07-05) was conducted with dyed water to further evaluate the flow field for the colloid migration experiment. Homologue Tracer Test 08-01 was carried out in January 2008 and followed by companion Tracer Test Run 08-02 with uranine injection in February into approximately the same flow field. It had been decided that the conservative tracer might cause complexation and so the test needed to be performed separately. The flow

field selected was similar (in terms of outflow from the shear zone) to that used in Tracer Test Run 07-01. The results from runs 08-01 and 08-02 are discussed in more detail in a later section.
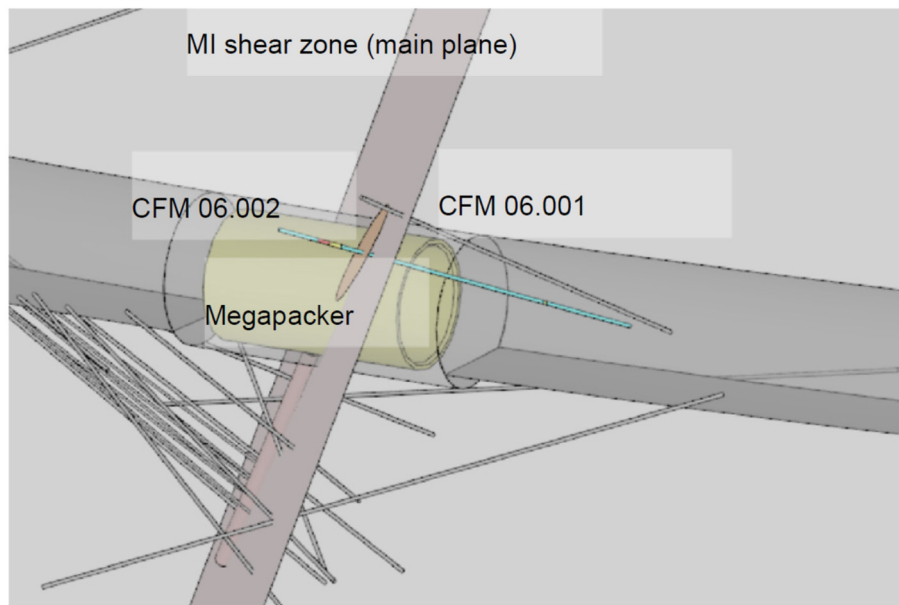
Figure 2-62: Schematic of the site of the CFM in-situ experiment. Boreholes CFM 06.001 and CFM 06.002 were drilled in 2006. They are shown in the foreground (CFM 06.002 coloured by lithology). The location of the main plane of the shear zone is also shown, as is the main flowing feature in borehole CFM 06.002. The other boreholes are from previous investigations.

One of the three key objectives for 2008/2009 was the development and demonstration of an adequate and robust sealing system suitable for the performance of a long-term in-situ test. Since the beginning of the project in 2004, numerous considerations eventually resulted in the implementation of three increasingly complex sealing concepts. It was recognized at the beginning of Phase 2 that further improvements would be necessary. Eventually, the 5 m long steel liner of the mega-packer installed in Phase 1 was left in place while the cement-filled Bullflex packers on each end were replaced with inflatable rubber packers. The new system was put into operation in September 2009 and provided reliable sealing over a range of conditions with no indication of significant leakage over the first few months of observation. The second key objective concerned the characterization of borehole CFM 06.002 and the key feature in it as a possible emplacement location for the bentonite source for the in-situ test. For this, the lithological and structural features were analysed with an optical borehole scan, core mapping and an impression packer survey. A hydraulic screening test campaign with test intervals in borehole CFM 06.002 and monitoring intervals in this and neighbouring boreholes supported the hydrogeological characterization of the MI shear zone. The highest transmissivities were associated with the borehole section between 6.40 and 7.10 m which contains a single fracture identified in the core (), images and the impression packer data. The design of the final borehole instrumentation was optimized accordingly. Interval 2 of the triple packer

134

system installed in May 2009 covers this 0.7 m section and was equipped with a PEEK (Poly-etheretherketon) dummy to reduce its volume.

The results from Tracer Test Run 09-01 demonstrated that the interval around the candidate feature is suitable for the in-situ test. The attributes include:

- There is a well-characterized distinct flow feature in interval 2 (6.40 – 7.10 m).

- The feature is well connected to flow paths in the shear zone (cross-hole tests and tracer).

- The flow rate through the borehole interval under suitable boundary conditions (outflow from Pinkel surface packer) is consistent with the target range for the in-situ test.

- The location is suitable for post-test over-coring.
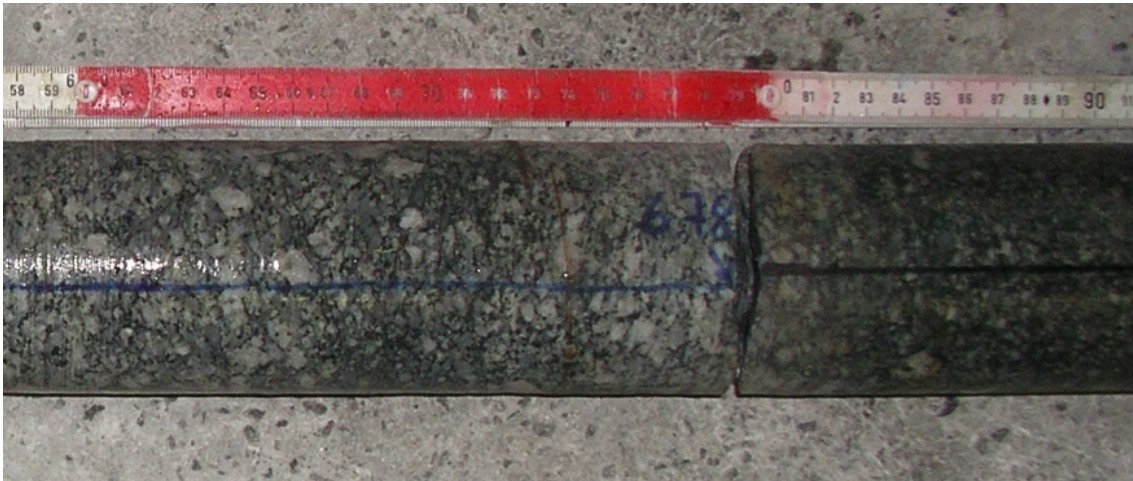
Figure 2-63: Photograph of the core section from borehole CFM 06.002 showing the fracture plane at a depth of 6.78 m. To account for localisation difficulties the key feature is generally considered to be in the depth range of 6.70 – 6.85 m.

While the suitability of the 'single fracture' or 'distinct flow feature' in borehole CFM 06.002 became apparent, there were discrepancies with respect to its exact location in the borehole from the different investigation methods. All conceivable explanations considered, it appeared most sensible at the time to define the position of the key feature in terms of a depth range which accounts for the recognized uncertainty inherent in the depth information. For further planning purposes the depth of the key feature was considered to be 6.70 – 6.85 m from the borehole mouth (Figure 2-63). The third key objective related to the development of instrumentation for monitoring groundwater chemistry and tracer testing. The surface equipment at the CFM site was augmented in November 2009 with two chemistry cabinets. Although their flexible configurations facilitate tracer testing, they are designed also for the long-term sampling and monitoring purposes required for both migration tests and the long-term in-situ test. At the

end of 2009, the field setup at the CFM site included 20 monitoring intervals in twelve bore-holes, seven surface or short borehole packers at the intersection of the MI shear zone and the AU tunnel, and injection and extraction groundwater monitoring systems. Tracer Test Runs 10-01 to 10-04 were performed in 2010 with homologues, colloids and conservative tracers. All were conducted as point dilution tests with recirculation of tracer in interval 2 of borehole CFM 06.002 and extraction from the Pinkel surface packer. The suitability of this dipole for the long-term in-situ test could be confirmed. The tracer tests provided field data on colloid and homologue transport at longer timescales than previously achieved in controlled conditions. Tracer Test run 10-01 was a homologue/colloid tracer test performed at 50 ml min-1 extraction from the Pinkel. Tracer Test Run 10-03 was a homologue/colloid tracer test performed at a low extraction from the Pinkel of 10.3 ml min-1. Although homologues and colloids were identified at the Pinkel an anomalous loss of Uranine was detected. The three monitoring boreholes CFM 11.001, CFM 11.002 and CFM 11.003 were drilled, surveyed, core mapped and equipped with triple packer systems. They are in close proximity (~4 cm) and parallel to borehole CFM 06.002 because of the intention to use them for colloid and radionuclide monitoring at small distances from the source, and for resin injection and stabilization of the key feature in the target shear zone before over-coring will take place. After drilling these monitoring boreholes, Tracer Test Runs 11-01 and 11-02 demonstrated that a low flow velocity zone was present around CFM 06.002-i2 resulting in very little "dilution flow" through the interval necessitating a change to a dipole configuration for future tracer tests from this interval. Only a very small injection rate (0.33 ml min-1) was necessary and this rate was used for Tracer Test Runs 12-01 & 12-02, the confirmation/preparatory conservative tracer test and the Radionuclide/colloid migration test. During Tracer Test Runs 11-01&2 it was also established that at low gradients Uranine showed anomalous losses compared to the tracer Amino-G Acid (AGA). The process causing these losses is not understood although it has been suggested that it is associated with low pH conditions in the injection interval. From Tracer Test Run 11-01 onwards AGA has been used as the primary conservative tracer. Tests with Eosin (from Tracer Test Run 12-04 on) have showed similar behaviour to Uranine. Tracer Test Run 12-01 was a preparatory con-servative tracer test to confirm the setup for the subsequent Radionuclide/colloid test run 12-02. Following Tracer Test Run 12-02 a series of conservative tracer dipole tests (Tracer Test Runs 12-03,4,5,6 and 13-02,3) was performed in the CRR area of the shear zone utilizing boreholes BOMI 87.008, BOMI 87,010, CRR 99002 and CRR0.0.003. The aim was to select a suitable dipole for a 2nd RN test and determine the feasibility of performing tracer migration tests in parallel with the long term in situ test. As part of the preparation for such tests packer systems in these boreholes were replaced with systems suitable for future migration tests in-corporating low-volume PEEK interval completions. Tracer Test Runs 11-03 and 13-01 fo-cused on demonstrating the feasibility of very low flow rate sampling of water from around CFM 06.002-i2 from the near-field monitoring boreholes CFM 11.001,2,3. These tracer tests also provided information on the small-scale heterogeneity around CFM 06.002-i2. Table 2-29 lists the tracer tests performed within the CFM Project from 2007 to 2013.

Table 2-29: Field tracer tests performed within the framework of CFM 2005-2013.

Tracer Test Run	Test Type	Injection BC	Injection	Shear Zone Extraction	SZ flow (ml/min)	Additional Extraction	Comment
05-01	Conservative	Injection	BOMI 87.010i2	Pinkel/fissure	573		Test prior to sealing
06-01	Conservative	Injection	BOCRR00.003i2	Pinkel	602		Test prior to sealing
07-01	Conservative	Injection	CFM06.002i1	Pinkel	164.7		Evaluation of 06.002
07-02	Conservative	Injection	BOMI 87.010i2	Pinkel	119		Repeat 05-01 low outflow
07-03	Conservative	Injection	BOCRR00.003I2	BOMI87.010i2	75	Slight leakage	Dipole selection tests
07-04	Conservative	Injection	BOMI87.010i2	Pinkel	109		Dipole selection tests
07-05	Conservative	Injection	BOMI87.008i2	BOMI87.010i2	110		Dipole selection tests
08-01	Homologue/colloid	Point Dilution	CFM06.002i1	Pinkel	160		Sections 3-5
08-02	Conservative	Point Dilution	CFM06.002i1	Pinkel	160		Sections 3-5
09-01	Conservative	Point Dilution	CFM06.002i2	Pinkel	52		Preparation for 10-01
10-01	Homologue/colloid	Point Dilution	CFM06.002i2	Pinkel	48		Sections 3-5
10-02	Conservative	Point Dilution	CFM06.002i2	Pinkel	10.4		Preparation for 10-03
10-03	Homologue/colloid	Point Dilution	CFM06.002i2	Pinkel	10.1		Sections 3-5
	Homologue/colloid	Point Dilution	CFM06.002i2	BOMI87.010i2	10.3		Additional extraction
10-04	Conservative	Point Dilution	CFM06.002i2	Pinkel	25.15		Higher outflow test
11-01	Homologue/colloid	Point Dilution	CFM06.002i2	Pinkel	10.3		Repeat of 10-03 with AGA

Table 2.21: (continued): Field tracer tests performed within the framework of CFM 2005-20113.

Tracer Test Run	Test Type	Injection BC	Injection	Shear Zone Extraction	SZ flow (ml/min)	Additional Extraction	Comment
11-02	Conservative	Point Dilution	CFM06.002i2	Pinkel	25.15		Repeat with higher outflow
11-02	Conservative	Injection	CFM06.002i2	Pinkel	25.15		Test of injection
11-03	Conservative	Point Dilution	CFM06.002i2	Pinkel	25.15	CFM11.001i2	Sampling feasibility test
	Conservative	Point Dilution	CFM06.002i2	Pinkel	25.15	CFM11.002i2	
	Conservative	Point Dilution	CFM06.002i2	Pinkel	25.15	CFM11.003i2	
	Conservative	Injection	CFM06.002i2	Pinkel	25.15		Test of low rate injection
12-01	Conservative	Injection	CFM06.002i2	Pinkel	25.15		
12-01	Conservative	Injection	CFM06.002i2	Pinkel	25.15		
12-02	RN/Colloid	Injection	CFM06.002i2	Pinkel	25.15		Sections 3-5
12-03	Conservative	Injection	BOCRR00.003i2	Pinkel	25.15		
12-04	Conservative	Injection	BOCRR00.003i2	Pinkel	25.15	BOMI87.010i2	Dipole feasibility tests
12-05	Conservative	Injection	BOCRR00.003i2	Pinkel	25.15	BOMI87.010i2	
12-06	Conservative	Injection	BOMI87.008i2	Pinkel	25.15	BOMI87.010i2	
13-01	Conservative	Point Dilution	CFM06.002i2	Pinkel	25.15	CFM11.002i2	Sampling feasibility test
13-02	Conservative	Injection	BOCRR99.002i2	Pinkel	25.15	BOMI87.010i2	Dipole feasibility tests
13-03	Conservative	Injection	BOCRR99.002i2	Pinkel	25.15	BOMI87.010i2	

2.2.2 New in-situ field experiments at Grimsel Test Site (GTS) within Kollorado-e

T. Schäfer, F. Huber, F. Rinderknecht, S. Heck, F. Quinto, R. Götz, M. Lagos, C. Walschburger, F. Geyer, B. Lanyon, I. Blechschmidt

The influence of colloidal/nano-scale phases on the radionuclide (RNs) solubility and migration behaviour is still one of the uncertainties in repository safety assessment. In this chapter we report on the progress concerning the colloid migration under near natural hydraulic conditions at the Grimsel Test Site. These experiments on the demonstration of colloid mobility under defined hydraulic conditions in the water conducting feature planned for the long-term in situ test (LIT) are of paramount importance to quantify later the potential bentonite erosion and colloid formation.

Site Description. The test shear zone at Nagra's Grimsel Test Site (GTS) is located at about 1730 m above sea level under a ~ 450 m thick overburden of crystalline rock *(Bossart and Mazurek, 1991)*. The thickness of the Migration (MI) shear zone varies between 0.15 and 0.90 m. The fault gouge material (mylonite/ protomylonite) is mainly composed of muscovite, biotite, chlorite, epidote, K-feldspar, plagioclase and quartz. Carbonate minerals are not found. Transmissivities of around 10^{-6} m^2 s^{-1} have been measured. For the tracer tests reported below, a dipole of 6.08 meter was used, which is much longer than the dipole of 2.23 m used in the Colloid Radionuclide Retention (CRR) project *(Geckeis et al., 2004; Möri et al., 2003)*. The relevant geometrical data of the boreholes and dipoles are detailed in *(Nagra, 2016, in press)*. The groundwater at the site is characterized by low ionic strength, low carbonate concentration and high pH *(Geckeis et al., 2004)*. Within the Colloid Formation and Migration (CFM) project at the Grimsel Test Site (GTS Switzerland) a huge geo-technical effort was taken to isolate hydraulically the MI shear-zone from the artificially introduced hydraulic gradient due to the tunnel construction (see Figure 2-64). The construction is based on a polymer resin impregnation of the tunnel surface using three SIKA products (Sika® 4°, SikaDur® Combiflex® Strips and Sikadur®-31) operating as surface sealing. The megapacker essentially consists of a 5 m long steel tube with O-ring type packers at each end. Its purpose is to provide mechanical support to the resin seal when pressure is elevated in the MI shear zone. The segmented steel tube has an outer diameter of 3.03 m while the tunnel diameter is 3.514 m. The steel cylinder with reinforcement rings is sealed on both ends with rubber based hydraulic "donut" packers (Baski Inc., USA) and the annulus between resin and steel ring filled and pressurized with water to counteract the hydrostatic pressure of the water conducting feature giving mechanical support to the resin. The annular space between its outer surface and the tunnel wall is 25 cm wide and has a volume of about 9.3 m^3. Natural outflow points of the MI shear zone were localized prior to the construction and sealed by surface packers. This design gives the opportunity by outflow regulation to adjust the flow velocity in the fracture. The hydraulic heads are well controlled with this "Donut Packer" system essentially stable at level of "natural variations" due to lake level changes of the local hydropower constructions (~tenths of cm over months) and earth tides (~tenths of mm 12/24 cycles). This design gives the opportunity to regulate outflow and thereby adjust the flow velocity and gradient in the fracture. Currently, a very stable

gradient of ~60 mm over a dipole length of 6m resulting (~1%) is established over months. The license was granted in January 2012 by the Swiss regulatory (BAG) to perform the first radio-nuclide tracer test under these low-flow conditions. The radionuclide tracer test Run 12-02 will be presented in detail here, whereas for Run 13-05 a short summary is given. Especially the AMS data is still under evaluation and will be the focus of the KOLLORADO-e^2 final report. For other experiments, see e.g. *(Geckeis et al., 2011)*.
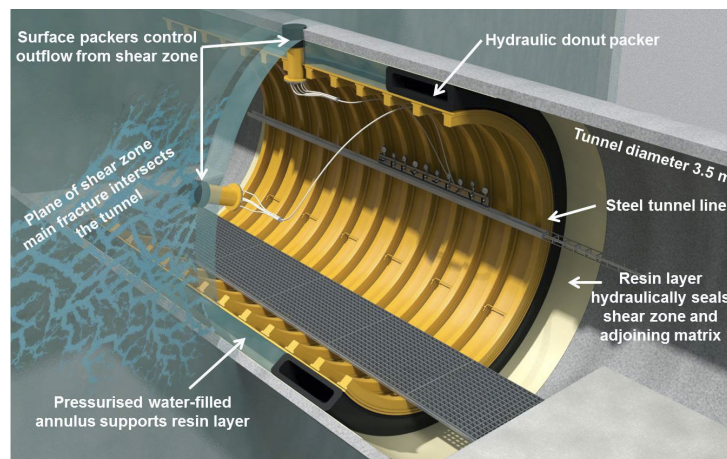
Figure 2-64: Schematic representation of the megapacker setup with the surface packer controls.

Run 12-02: Tidal effects controlling nanoparticle associated radionuclide migration

Introduction

The influence of tidal fluctuations is a phenomenon frequently observed in confined or suffi-ciently deep aquifers. This includes examples from the 4 km deep pilot hole of the Continental Deep Drilling Programme, KTB, Bavaria (peak to peak amplitudes of up to 12 cm) or wells near Dokurçun, North-Anatolia, Turkey *(Wilhelm, 1997)* (peak to peak amplitudes of 0.25 cm). It has been furthermore shown in deep Paleozoic carbonate aquifer (Yucca Mountain, Nevada) by deep borehole testing (UE-25pl) that a good Earth tide water-level fluctuation could be ob-served. Both the large 2-cm amplitude of the tidal signal and the fact that it is in phase with the tidal potential indicate that the deep aquifer is well confined by a layer of low hydraulic conduc-tivity and indicates that the fault zones which cut through the rocks beneath the valley border-ing Yucca Mountain must be relatively tight and of low permeability *(Bredehoeft, 1997)*. The interpretation of natural, deformation induced well level fluctuations presents an easy way to obtain some idea about the values of in situ parameters of mechanical rock-fluid interactions *(Kumpel et al., 1999)*. Tide- induced circulations in shallow coastal subterranean estuary are an important factor controlling chemical fluxes *(Robinson et al., 2007)* and periodic forcing has been implemented rather early in numerical models for aquifer response concerning amplitude and phase *(Townley, 1995)*. Numerical simulations have shown the influence of tidal effects

on contaminant mobility in shallow costal aquifer systems. For a case study consisting of toluene transport and biodegradation, Robinson and coworkers could demonstrate that 79% of toluene initially released in the aquifer was attenuated prior to discharge with tides present, compared to only 1.8% for the non-tidal case *(Robinson et al., 2009)*. Other numerical studies have shown that tidal effects influence the contaminant plume mobility only over a short distance of the tidal-water interface of approx. 40 feet for the parameters used in that study *(Yim and Mohsen, 1992)*. The fate and transport of contaminants including radionuclides depends not only on the initial chemical form (source term) but also on the geochemistry and hydrogeology of the source location and the down-gradient migration pathways. Strongly sorbing tri- and tetravalent actinides were once thought to be immobile having the classical two phase flow concept of transport (stationary phase: sediment; mobile phase: ground water) in mind. Over the last decades this concept had to be extended by a third phase, namely the nanoparticles, which are ubiquitous in aquifer systems *(Kretzschmar and Schäfer, 2005; McCarthy and Zachara, 1989; Schäfer et al., 2012; Wilkinson and Lead, 2006)* and might increase the mobility of strongly sorbing tracers under certain circumstances. Neglecting this nano-particulate phase in groundwater systems can drastically underestimate the mobility of especially strongly sorbing contaminants (e. g. plutonium) *(Kersting, 2013; Kersting et al., 1999; Maher et al., 2013; Novikov et al., 2006; Utsunomiya et al., 2009)*. The discussion of clay colloids mobilized from a compacted bentonite barrier in the context of a deep geological repository for high-level nuclear waste in crystalline formations *(Neretnieks and Liu, 2006; Schäfer et al., 2012; Schwyn et al., 2012)* has focused new attention to this issue. In the course of the safety-assessment period for a nuclear waste repository, low mineralized groundwater *(Bath, 2011)* might intrude down to repository levels forcing an erosion of the geotechnical barrier (bentonite). In general, the importance of colloidal phases or nanoparticles on transport processes depends on (a) the presence, (b) the mobility and stability and (c) the slow reversibility or "irreversibility" of metal/radionuclide interaction with these nanoparticles. Furthermore, it could also be demonstrated that hydraulic fluctuations can have a significantly effect on colloid mobility *(Sirivithayapakorn and Keller, 2003)*. Other work has already shown that flow transients have an important role in colloid mobilization providing a model that accurately reproduces measured pulse-type colloid releases induced by successive step-change increases in flow rate *(Saiers and Lenhart, 2003)*.

In this study, the intention is not to use tidal fluctuations to assess mechanical rock-fluid interaction parameters, but we demonstrate that earth- tide effects can have an important role in the transport of colloidal phases and associated contaminants in deep crystalline environment.

Materials & Methods

For the radionuclide injection cocktail preparation, the Injection cocktail preparation, the on-site and off-site analysis and the experimental procedure for Run 12-02 it is referred to the Kollorado-2 report *(Huber et al., 2014)* and within this report the focus is lead on the interpretation of the tidal influence on colloid and radionuclide transport behaviour and the long-term behaviour of actinides under these low-flow conditions.

Results & Discussion

Conservative tracer behaviour (Amino-G). The results of the conservative tracer breakthrough curve (BTC) are given in Figure 2-65. The conservative tracer Amino-G was injected with a concentration of 1633 ± 21 ppb given a total injected mass of 3675µg. Calculating the recovery for the on- site inline fluorescence detection based on a background signal of 0.3ppb would give a recovery of 3114 ppb or 84.7% recovery, whereas using a baseline of 0 ppb 3700 ppb are calculated resulting in a quantitative recovery. Taking furthermore the off-site data (detection limit of 2-3 ppb) a recovery of 2861 ppb or 77.9%, respectively, could be quantified.
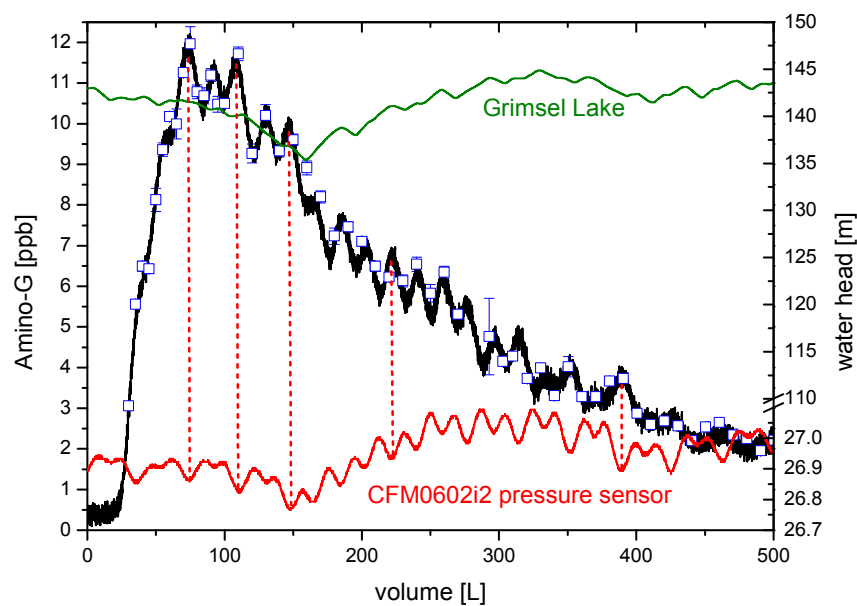
Figure 2-65: Breakthrough curve of Amino-G (black line on-site in- line measurements; open blue squares off-site analysis) used as conservative tracer in Run 12-02 together with the water heads measured on the Grimsel Lake and the CFM0602i2 pressure sensor. (dashed lines for guiding the eye concerning the coincidence of solute transport.

Sinusoidal oscillations observed in the on-site in line fluorimeter measurements could be confirmed by off-site analysis (see Figure 2-65) and clearly shows that this BTC shape is not an effect of electronical noise potentially picked up in the experimental tunnel by the fluorimeter. The BTC could be directly correlated to pressure sensor measurements of the borehole interval and clearly demonstrates that tidal oscillations have a significant influence on the mobility of solutes in deep crystalline rocks of general low permeability. Beside the sinusoidal oscillations with maximum peak to peak ratios of approx. 16 cm the influence of the Grimsel lake could also be observed as shown in Figure 2-65. A similar trend between the Grimsel lake level changes and the hydraulic head above the tunnel axis measured in borehole CFM0602i2 is detected; the head varies by ~1m over the year due to influence of the lake levels.

To our knowledge this direct observation of tidal fluctuations in migration experiments is made for the first time in deep crystalline environments as studied here in the underground research facility of the Grimsel Test Site (GTS). Usually field experiments are performed under rather high gradients to obtain high tracer recoveries in the natural 3D geometry of the flow field. Here, due to the construction of the megapacker system and the unique opportunity to control the hydraulics of shear zone by the outflow of the Pinkel surface packer low gradients (~60mm/6m resulting in ~1%) are established with very stable head differences/gradients < 10mm, which gives the unique opportunity to study flow and transport at near natural or repository relevant conditions in a natural shear zone.
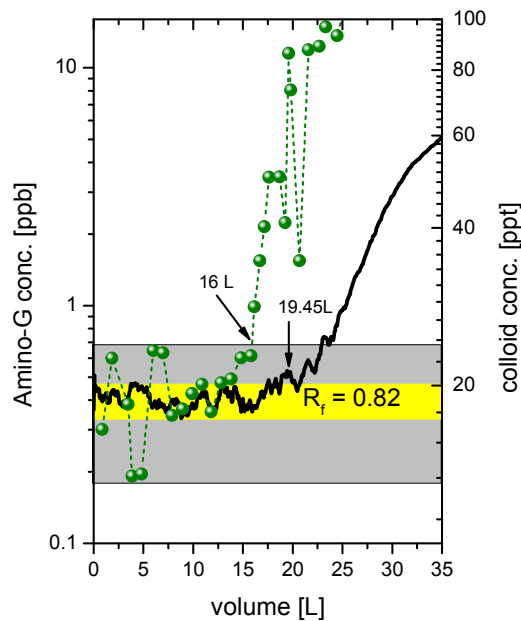
Figure 2-66: Rising edge of the Run 12-02 colloid and Amino-G BTC. The background colloid fluctuations are marked with the grey shaded area and for the fluorescence detection with the yellow shaded area**.**

Colloid/ Nanoparticle transport. Clay colloid breakthrough measurements by LIBD show the colloidal tracer running ahead of the conservative tracer due to size exclusion of the colloidal phase preferentially flowing in the faster streamlines of the fracture flow field compared to the dissolved Amino-G. The retardation factor derived by such a behavior is smaller than 1. However, there is a big uncertainty in such measurements as they are directly dependent on the sensitivity of the method. Former studies at the Grimsel Test Site (GTS) using the CRR dipole in in the same shear zone revealed a colloid retardation factor R_f of 0.9, but for example for Cs a R_f value of 0.81 was found *(Geckeis et al., 2004)*. Here, taking the LIBD detection system with detection levels down to the ppt range we obtain with the onset of the Amino-G breakthrough as indicated in Figure 2-66 a R_f value of 0.82.

Using the first onset of the Al breakthrough the R_f diminishes to a values of ~1 (see Figure 2-67). From Figure 2-67 comparing the rising edge of the Amino-G BTC and the fluctuation

seen in the LIBD signal it seems to be clear, that there is not a continuous release of colloids, but pulse-type events of colloid migration. Going a little bit further in the correlation between the pressure signal and the colloid release events it seems that especially inflection points when the pressure head is starting to rise again are triggering the colloid release and mobility in the migration shear zone (see Figure 2-67).
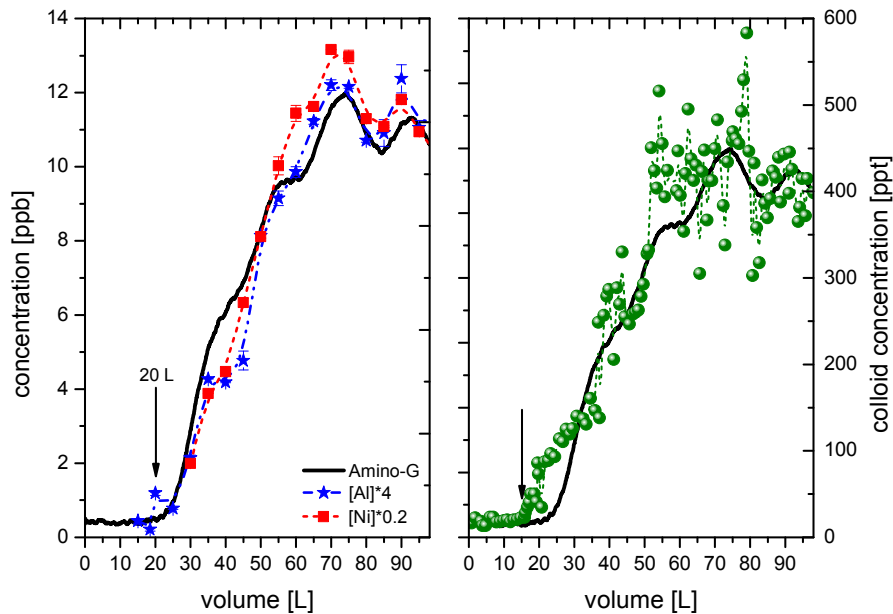
Figure 2-67: Rising edge of the BTC showing the colloid indicative elements [Al] and [Ni] following the Amino-G breakthrough curve. Direct single particle measurements by LIBD are shown for comparison in the right graph. Element analysis due to the sampling intervals feasible show not all the colloid breakthrough features as shown for permanent on-site measurement for LIBD. For further discussions see text.
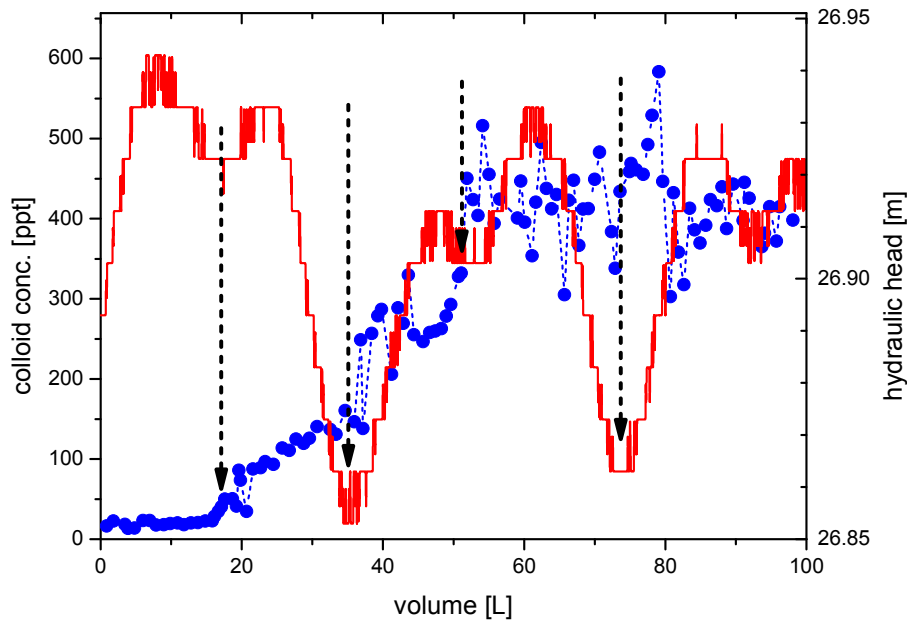
Figure 2-68: Correlation between LIBD measured colloid concentration and the hydraulic head of CFM0602i2. Arrows mark the inflection point with a positive slope of the hydraulic head changes.

The colloid recovery was determined from the [Al] and [Ni] mass spectrometry data (ICP-MS) and by LIBD. Comparing the values of colloid recovery with 48 ± 5% for the LIBD analysis and 51 - 52% recovery based on the [Ni] ICP-MS signal shows very good comparability. However, the Al recovery calculation strongly depends on the background signal chosen. If we use a Grimsel groundwater background concentration value of 28 ppb a recovery of 44 - 49% is calculated, whereas for a [Al] background value of 25 ppb a recovery of 56 - 61% is estimated. Direct linear correlation of all data obtained in the BTC interpolating to the intersection at zero Nickel concentration as observed in the Grimsel groundwater gives also a value of 28 ppb, furthermore co-operating the assumption made for the 28 ppb background signal. The on-site LIBD analysis could also detect the colloid concentration changes due to tidal effects, which was hardly possible to observe in the samples taken by the auto-sampler due to the low sampling frequency. The Al/Ni ratio in the injection cocktail was determined to be 21.6 and an average ratio of 20.4 ± 0.5 was found over the samples analysed given clear evidence that a mobilization of Al containing phases as an additional colloid source from the fracture can be excluded.

Run 12-02: Long-term actinide mobility

The actinide measurements of the BTC by high resolution (HR) ICP-MS could detect the actinides in the tailing down to ~0.01 ppt level. In the course of the Kollorado-*e* project the potential to expand the detection to lower concentrations driving the limits towards fall-out radionuclide detection range. This was evaluated by using resonance ionization mass spectrometry (RIMS) available in the radiochemistry group of Tobias Reich at the Univ. Mainz and accelerator mass

spectrometry (AMS) through collaboration with the Isotope Research and Nuclear Physics group of Robin Golser and Peter Steier using "VERA" (Vienna Environmental Research Accelerator), see Figure 2-69 for Run 12-02 data.
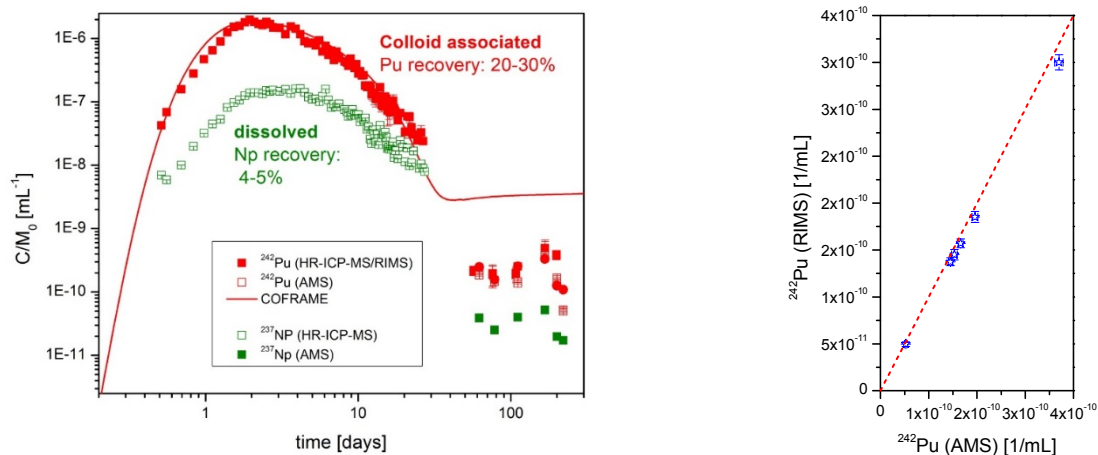
Figure 2-69: (left) [237]Np and [242]Pu BTC measured with HR-ICP-MS and extension to longer monitoring times in the tailing using RIMS and AMS. (right) Comparison between the [242]Pu data measured with RIMS and AMS in comparison to the 1:1 line.

For the RIMS detection and instrumental details can be found elsewhere *(Buerger et al., 2007; Gruning et al., 2004)*. For the AMS measurement technique it is referred to *(Vockenhuber et al., 2003)*. The special treatment for the limited sample volume available in the samples taken of Run 12-02 was already published and is detailed in Section 2.1.3 *(Quinto et al., 2015)*. The RIMS and AMS results for [242]Pu could be directly compared and show a very good agreement between the two detection methods on the ultra-trace level as indicated by the minor deviation to the 1:1 line in Figure 2-69. For the discussion on the fitting procedure using the COFRAME code and the data evaluation concerning desorption kinetics from fracture filling material it is referred to Section 3.1.1

CFM Run 13-05

Identical to the CCR project experiments, Run 13-05 was conducted in the same dipole configuration (injection in CRR 99.002-i2 and extraction in BOMI 87.010-i2) but with much lower flow rates. Based on the current results the following conclusions can be drawn in comparison to the CRR experiments:

➢ The change in the mean residence time of 80 min (CRR run 32) to 2640 min in Run 13-05 had no effect on the conservative tracer recovery (92% for CRR and 92.6% for Run 13-05).

➤ The colloid recovery measured by LIBD was 37 ± 5%, 36 ± 5% for the Al signal and 38 ± 3% for the Ni signal. Compared to the CRR Run 32 a clear decrease in colloid mobility from 85-100% to 36-38% for increasing residence time was observed.

➤ Despite the lower colloid recovery, the quantification of the initially colloid bound RNs [242]Pu and [243]Am (27.6% and 25.4%, respectively) was similar to Run 12-02.

➤ Dissolved concentrations for [233]U(VI) and [237]Np(V) showed recoveries of 15.2% and 4.1% which were clearly lower compared to CRR Run 32 yielding recoveries of 82 ± 4% and 103 ± 5% for [237]Np and [233]U, respectively. The decrease in recoveries can be explained by reduction processes in line with the Eh-pH conditions prevailing (-200 mV and pH of 9.4). Additional AMS measurements will be conducted within KOLLORADO-e2 to further examine the long-term actinide mobility.

Long-term in-situ experiment (LIT)

Installation of the LIT experiments took place in March 2014 at Grimsel Test Site. The bentonite source emplaced in the water conducting migration shear zone consisted of 16 bentonite rings (12 pure FEBEX bentonite rings and 4 FEBEX bentonite rings with an admixture of 10% synthetic Zn-montmorillonite; total mass of 2614g). The 4 Zn-montmorillonite rings contained glass vials filled with a paste of Amino-G (as conservative tracer) and synthetic Ni-montmorillonite with the following RNs: [45]Ca, ^{75}Se, ^{99}Tc, ^{137}Cs, [233]U, [237]Np, [241]Am and [242]Pu. Since the emplacement of the source samples are taken regularly to monitor the geochemical properties like pH, Eh, swelling pressure, turbidity and the chemical composition of the contact water close to the source. Moreover, a complete analysis of the samples is carried out with respect to the conservative tracer concentration, colloid size and colloid concentration. The pH values measured in the close vicinity of the bentonite source are lower (pH = ~9.1) compared to the Grimsel ground water. The conservative tracer Amino-G was first detected after 10d verifying a direct contact of the bentonite source (at least the glass vials containing rings) with the water conducting shear zone. An increase of Amino-G within the first 500d was detected levelling off to a plateau value of 130 ppb subsequently. Colloid concentrations and mean particle colloid sizes measured by LIBD showed a pronounced scattering yielding a maximum value of 75 ppb and a mean value of 29 ppb. The latter is close to the background colloid concentrations in the Grimsel ground water (~10ppb). The elemental composition measured in the initial phase of the experiment showed increased concentrations for Na, Ca, Cl and SO4 indicating dissolution processes of accessory mineral phases of the bentonite. Within the first year of the experiments these concentrations decrease to the natural background level of the Grimsel ground water. The elements Al, Mg and Zn are main components of the bentonite and used as indicators for the quantification of the colloid concentration. Calculated bentonite concentrations based on these elements show a good agreement and yielding a mean colloid concentration between 1.4 mg/L (Al) and 1.7mg/L (Zn) under the assumption that no dissolved Al or Zn species is present. These findings are in disagreement to the LIBD measurements which found

mean colloid concentrations of only 329 µg/L. A discrimination between dissolved and colloidal Al and Zn by e.g. ultracentrifugation was analytically not feasible due to the small sample volume. Increasing the sample volume from 15ml to 40ml ultracentrifugation it is now possible and will be used in the further sample analysis. Regarding the RNs present in the bentonite source, only ^{99}Tc was detectable using the HR-ICP-MS. Therefore, AMS measurements have been conducted additionally which confirm the presence of [99]Tc. Though one has to state that the ^{99}Tc concentrations and mobility are very likely overpredicted due to isobaric interference with [99]Ru in the HR-ICP-MS measurements.

The results of the LIT experiment in the GTS are in good agreement to the results obtained in the laboratory mock-up test. In both experiments, the conservative tracer Amino-G was mobile and the geochemical perturbation by dissolution of accessory mineral phases leading to increased concentrations of Ca, Cl and SO_4 was found.

3   Modelling

The objectives of flow and transport modelling are manifold. Modelling of the flow field and the transport of ideal tracers aims at understanding the flow conditions in the Grimsel shear zone and the impact of the different dipoles on the flow field. Further, predictions about the impact of reduced flow conditions – as planned in future homologue tests – are possible. Flow and transport modelling of a well characterized fracture in a bore core aims in understanding of the effect of heterogeneities on flow field and transport of tracers. Finally, the application of transport models including kinetically-controlled sorption reactions to describe the interaction between radionuclides, colloids and sediment matrix yields – based on the results from the experimental program – in understanding the impact of the different processes on the shape of the break-through curves and on the recovery of the radionuclide tracers. It furthermore contributes to the qualification of the codes and sets the basis for calculations with regard to the long-term safety of deep geological repositories.

3.1   COFRAME and r3t flow and colloid facilitated transport modelling including kinetically controlled sorption processes

U. Noseck, J. Flügge, T. Reiche

Introduction

Up to now altogether five dipole field experiments, where the bentonite colloid facilitated transport of homologues and radionuclides was investigated, have been performed within the CFM project. A description of the newest experiments can be found in Section 2.2.2 and the relevant data with respect to modelling are compiled in this section. The calculations have been performed with the transport codes r³t *(Fein, 2004; Schneider, 2016)* and COFRAME (Reiche et al. 2014). These model simulations are focused on the kinetically controlled interactions between radionuclides/homologues, bentonite colloids and fracture filling material, which is typically fault gouge in the Grimsel shear zone. In addition to previous model simulations the application of AMS spectroscopy allowed detection of sub ppq concentrations of Am-243 and Pu-242 and therewith a long-term analysis of the breakthrough curves (see Section 2.1.3).

Material and Methods

Calculations have been performed with the transport codes r³t and COFRAME. For the calculations with the r³t code the fracture was described as a 2D porous medium. Details about the underlying conceptual model, the basic equations and detailed description of the results can be found in (Schäfer et al., 2013).

In this project phase emphasis was put on the application of the 1D code COFRAME, which has been developed to describe radionuclide transport in the presence of colloids in fractured media (Reiche et al. 2014). A schematic view of the processes considered in this code is shown in Figure 3-1.
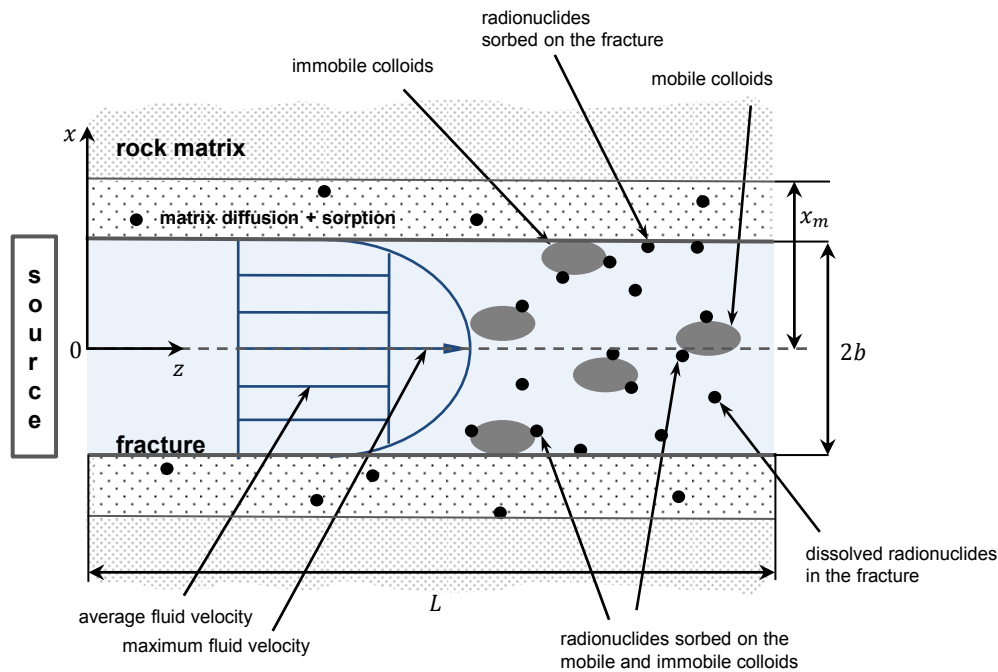
Figure 3-1: Transport code COFRAME for colloid facilitated radionuclide transport in fractured media.

This model represents a double porosity approach for fractured media including the process of matrix diffusion. The formulation of the transport equations is based on mass balance over a representative elementary volume (Bear, 1972), (Helmig, 1997). Transport of colloids and radionuclides is considered in a fracture characterized by its aperture, extension and porosity. Perpendicular to the transport direction in the fracture matrix diffusion into the stagnant matrix porewater with a distinct penetration depth for the contaminants is considered. Sorption on the rock matrix is modelled by K_d-concept. For colloids no matrix diffusion is considered, since it is assumed that colloid size is too large to enter the pore space around the fracture. Colloid transport and interaction processes between colloids, contaminants / radionuclides and fracture surface are considered by kinetically controlled processes. A detailed description of the code can be found in (Reiche et al. 2014).

The following processes are taken into account (see Figure 3-2, exchanging processes between components are labelled Q):

–   contaminant exchange between the fracture and the adjoining rock matrix due to molecular diffusion Q_{fp},

- limited molecular diffusion of contaminants within the rock matrix in the direction perpendicular to the fracture axis,

- sorption of contaminants within the rock matrix Q_{pr},

- sorption of contaminants onto the fracture surface Q_{fr},

- sorption of contaminants on mobile and immobile colloids Q_{frm} and Q_{fri},

- filtration and remobilization of colloids Q_c due to their interaction with the fracture surface as well as thereby induced filtration and remobilisation of contaminants adsorbed on colloids Q_{cr},

- radioactive decay under consideration of nuclide chains.

In the modelling system contaminants and colloids can be present as the following components (Figure 3-2):

- dissolved mobile contaminants in the fracture with concentration C_{fr} [mol/m³],

- dissolved mobile contaminants in the pore water of the rock matrix C_{pr} [mol/m³],

- mobile contaminants adsorbed on mobile colloids C_{cr} [mol/m³],

- immobile contaminants adsorbed on the fracture surface S_{fr} [mol/m²],

- immobile contaminants adsorbed on rock matrix pore surfaces S_{pr} [mol/kg],

- immobile contaminants sorbed on filtered colloids S_{cr} [mol/m²],

- mobile colloids C_c [mol/m³],

- immobile colloids filtered on the fracture surface S_c [mol/m²].

This denotation is used throughout the whole section for description of the respective concentrations and interaction processes.
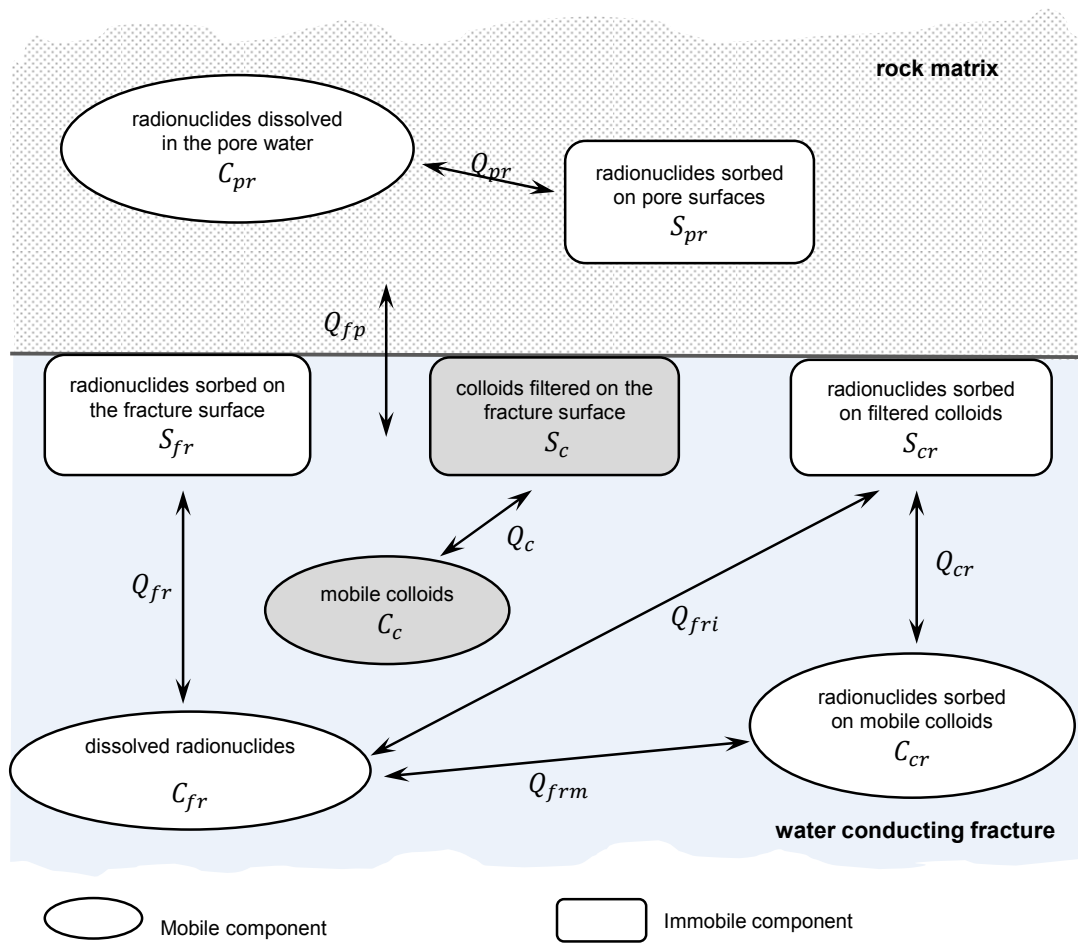
Figure 3-2: Exchange processes between the components that represent radionuclides and colloids in the modelling system.

The interaction terms are formulated as described in the following, for details see (Reiche et al., 2015). Sorption of radionuclides/contaminants on the fracture surface is modelled as a linear kinetic reaction (Equation 30):

$$Q_{fr} = k_{fr}[K_{fr}C_{fr} - S_{fr}] \ ,$$

Equation 30

k_{fr} desorption rate of contaminants from the fracture surface,

K_{fr} distribution coefficient of contaminants on the fracture surface.

Sorption of dissolved contaminants on mobile and immobile colloids is modelled according to (Ibaraki et. al., 1995) (Equation 31 and Equation 32):

$$Q_{frm} = k_{frm}[C_c \cdot K_{frm}C_{fr} - C_{cr}] \; , \qquad \qquad \text{Equation 31}$$

and

$$Q_{fri} = k_{fri}[S_c \cdot K_{fri}C_{fr} - S_{cr}] \; , \qquad \qquad \text{Equation 32}$$

with

K_{frm} distribution coefficient of contaminants sorbed on mobile colloids,

k_{frm} desorption rate of contaminants from mobile colloids,

K_{fri} distribution coefficient of contaminants sorbed on immobile colloids,

k_{fri} desorption rate of contaminants from immobile colloids.

For the filtration and remobilisation process of the colloids the following kinetic linear reactions are realized in COFRAME (Oswald et al. 2001(, (Li et al., 2004) (Equation 33):

$$Q_c = \frac{\partial S_c}{\partial t} = \lambda_f u_c C_c b - R_{mb} S_c \; , \qquad \qquad \text{Equation 33}$$

with

λ_f filtration coefficient,

u_c average colloid velocity,

R_{mb} remobilisation rate.

The filtration rate k_{sc}. can be calculated as the product of λ_f and u_c.

Results and Discussion

CFM field tests. Beside other field experiments up to now five CFM field migration tests have been performed, where, colloid-bound radionuclides or homologues were injected in one bore-hole and the breakthrough curves were detected at the outflow. These field tests are denoted as CFM RUN 08-02, 10-01, 10-03, 12-02 and 13-05. Relevant data used in the model simulations are compiled in Table 3-1. Model calculations with the transport code r³t were already performed for CFM RUN 08-02, 10-01, 10-03 and 12-02 and have been described in (Schäfer et al., 2013). In this project phase emphasis was put on model simulations with the newly developed code COFRAME. Calculations have been performed for the field tests CFM RUN 10-01, 12-02 and 13-05. The results from all the simulations with both codes are compared and discussed in Section 0.

Table 3-1: Outflow, injected mass and measured recoveries of ideal tracers, colloids , homologues and radionuclides in the CFM field tests.

Run*	Outflow [ml/min]	Ideal Tracer		Colloids		Homologues / RN	
		Mass [mg]	Recovery [%]	Mass [mg]	Recovery [%]	Mass [µg]	Recovery [%]
08-02	165	15.4	99	15	99	19.8 (^{232}Th)	93
						23.4 (^{178}Hf)	78
						14.3 (^{159}Tb)	56
10-01	48	5	84	30 / 144	47-65	14.9 (^{232}Th)	32
						12.8 (^{178}Hf)	30
						10.2 (^{159}Tb)	7
						12 (^{152}Eu)	14
12-02	25	4.5	80	330	>33-38 66	1.4 (^{232}Pu)	38
						0.049 (^{232}Am)	20
10-03	10	9	60	240	41	49.8 (^{232}Th)	43
						51.6 (^{178}Hf)	46
						45.4 (^{159}Tb)	6
						45.5 (^{152}Eu)	14
13-05	5 (BO) 25 (P)	4.5	88	225	37-39	4.73 (^{232}Pu)	28
						0.969 (^{232}Am)	24

*CFM RUN 08-02, 10-01, 10-03 and 12-02 were performed at dipole 1 and CFM RUN 13-05 at dipole 2.

Except CFM RUN 13-05 all of these field migration tests have been performed at the same dipole (injection in CFM 06.002 and extraction at Pinkel), denoted here as dipole 1, see Figure 3-3Figure 3-3:. CFM-RUN 13-05 was carried out at a tripole with injection in BOCR 99.002 and outflow at BOMI 87.010 and the Pinkel, with pumping rates of 5 and 25 ml/minute, respectively. However, no tracer signal was detected at Pinkel, therefore, this migration test was also simulated as a dipole, denoted here as dipole 2. This dipole was already used in the CRR project for field migration tests.
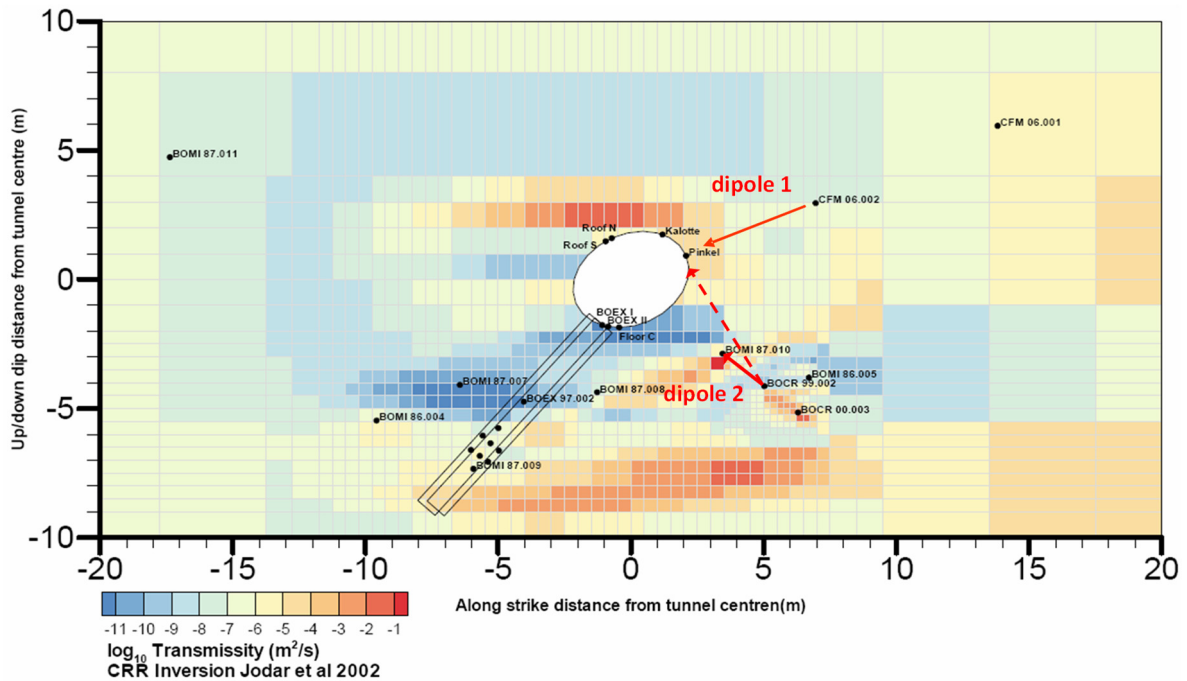
Figure 3-3: Cross section of the shear zone with transmissivities and location of boreholes. The red arrows indicate the dipoles used for the homologue / radionuclide migration tests in the CFM project: dipole 1 with injection borehole CFM06-02 and outflow at tunnel surface Pinkel and dipole 2 located between BOCR 99.002 and BOMI 87.010. See text for more explanation.

Model simulations of CFM RUN 10-01 and 12-02 with COFRAME. The calculations followed three objectives, (i) to test the newly developed transport code COFRAME using real field data, (ii) to use a second conceptually different model compared to the r^3t calculations for simulation of the tracer tests and (iii) to create a basis and derive interaction rates for predictive calculations of CFM RUN 13-05 (see Section 2.2).

In contrast to the r^3t calculations (Schäfer et al. 2013) the shear zone of the CFM experiment is considered in these calculations as an open fracture with an aperture of 2.5 mm. All information about the field experiments can be derived from (Rösli et al. 2010; Kontar et al. 2012) and are not described here. The transport parameters are taken from these descriptions and the cross sections (total trace length) are fitted to match the breakthrough curve of the conservative tracer uranine and AGA, respectively. The injection flow rate has been adapted to the injected mass of the conservative tracer, M_0. All parameters are listed in Table 3-2.

Table 3-2: Transport parameters used in the simulations for CFM-RUN 10-01 and CFM-RUN 12-02.

	CFM RUN 10-01	CFM RUN 12-02
Transport pathway length [m]	6.2	
cross section [m²]	0.485	0.132
Fracture aperture [m]	0.0025	0.0025
Fracture porosity	1	
Total trace length [m⁻¹]	9.64	23.53
Volume flow [ml/min]	48.4	25

3. Modelling

Injection flow rate [ml/min]	0.55	0.47
Penetration depth [m]	0.02	
Rock porosity [-]	0.05	
Rock density [kg/m^3]	2670	
Diffusion coefficient in rock matrix [m^2/a]	0.008	
Diffusion coefficient in fracture [m^2/a]	0.03 (RN) / 0.003 (colloids)	
Dispersion length [m]	0.6	

The applied injection functions for both field tests can be found in (Schäfer et al., 2013). The injected masses are according to Table 3-1 assumed as follows:

(i) 10-01: Uranine: 5 mg, colloids: 144 mg, Eu: 0.012 mg, Tb: 0.0102 mg, Hf: 0.128 mg, Th: 0.144 mg;

(ii) 12-02: AGA: 4.45 mg, Pu-242: $1.37 \cdot 10^{-3}$ mg, Am-243: $4.87 \cdot 10^{-5}$ mg

After fixation of transport parameters, the breakthrough curves of the colloids have been simulated. In case of CFM-RUN 10-01 the colloid curve appears slightly retarded compared to uranine, which was modelled by a reversible interaction of colloids with the fracture surface. A reduction of the recovery was simulated by a reduction factor of 0.8 which corresponds to an irreversible filtration rate of 0.01 h^{-1}. For CFM RUN 12-02 no retardation of the colloid curve was observed. A decrease of the colloid recovery was calculated by an irreversible filtration coefficient of 0.09 m^{-1} corresponding to filtration rate of 0.0174 h^{-1}). All interaction parameter are listed in Table 3-3. The resulting breakthrough curves of the experiments and simulations are shown in Figure 3-4 and Figure 3-5.

Table 3-3: Interaction parameters used in the simulations for CFM-RUN 10-01 and CFM-RUN 12-02.

	CFM RUN 10-01	CFM RUN 12-02
Interaction of colloids with fracture		
Colloid filtration coefficient [m^{-1}]	0.041	0.092
Reversible interaction		
Filtration coefficient [m^{-1}]	0.333	-
Remobilisation rate [h^{-1}]	0.1095	-
Interaction of homologues / radionuclides with colloids		
Kd (trivalent) [m^3/kg]	1500	
Kd (tetravalent) [m^3/kg]	1600	
Sorption rate (trivalent) [h^{-1}]	0.051 (Tb)	0.0228 (Am)
	0.068 (Eu)	
Sorption rate ([tetravalent) [h^{-1}]	0.023 (Th)	0.0017 (Pu)
	0.029 (Hf)	
Interaction of radionuclides with fracture		
Kd (trivalent) [m^3/kg]	1.56	
Kd (tetravalent) [m^3/kg]	1.56	
Sorption rate (trivalent) [h^{-1}]	1.14×10^2 (1×10^6 a^{-1})	
Sorption rate (tetravalent) [h^{-1}]	1.14×10^2 (1×10^6 a^{-1})	

[1] irreversible filtration coefficient of 0.04 (filtration rate of 0.01 h^{-1}) is considered by a reduction factor 0.8 for colloids and colloid-bound homologues in CFM RUN10-01

[2] corresponding to a filtration rate k_{sc} of 0.0174 [h^{-1}]

[3] corresponding to a filtration rate k_{sc} of 0.082 [h^{-1}]
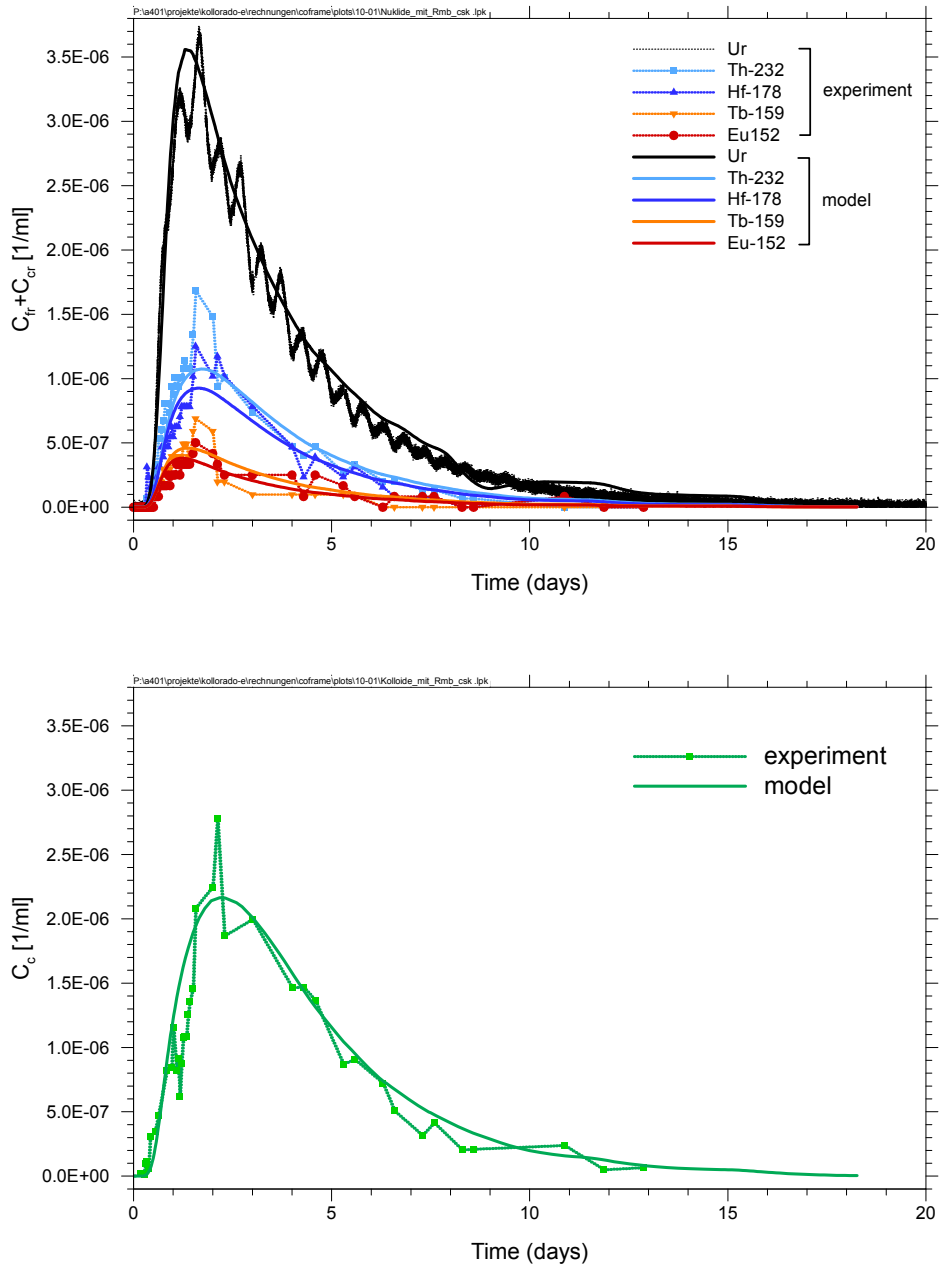
Figure 3-4: Simulation results for CFM RUN 10-01: Breakthrough curves for uranine and homologues (top) and for colloids (bottom) from experiment and modelling. Curves scaled by a factor of 0.84 in order to account for an uranine recovery of 84 %.
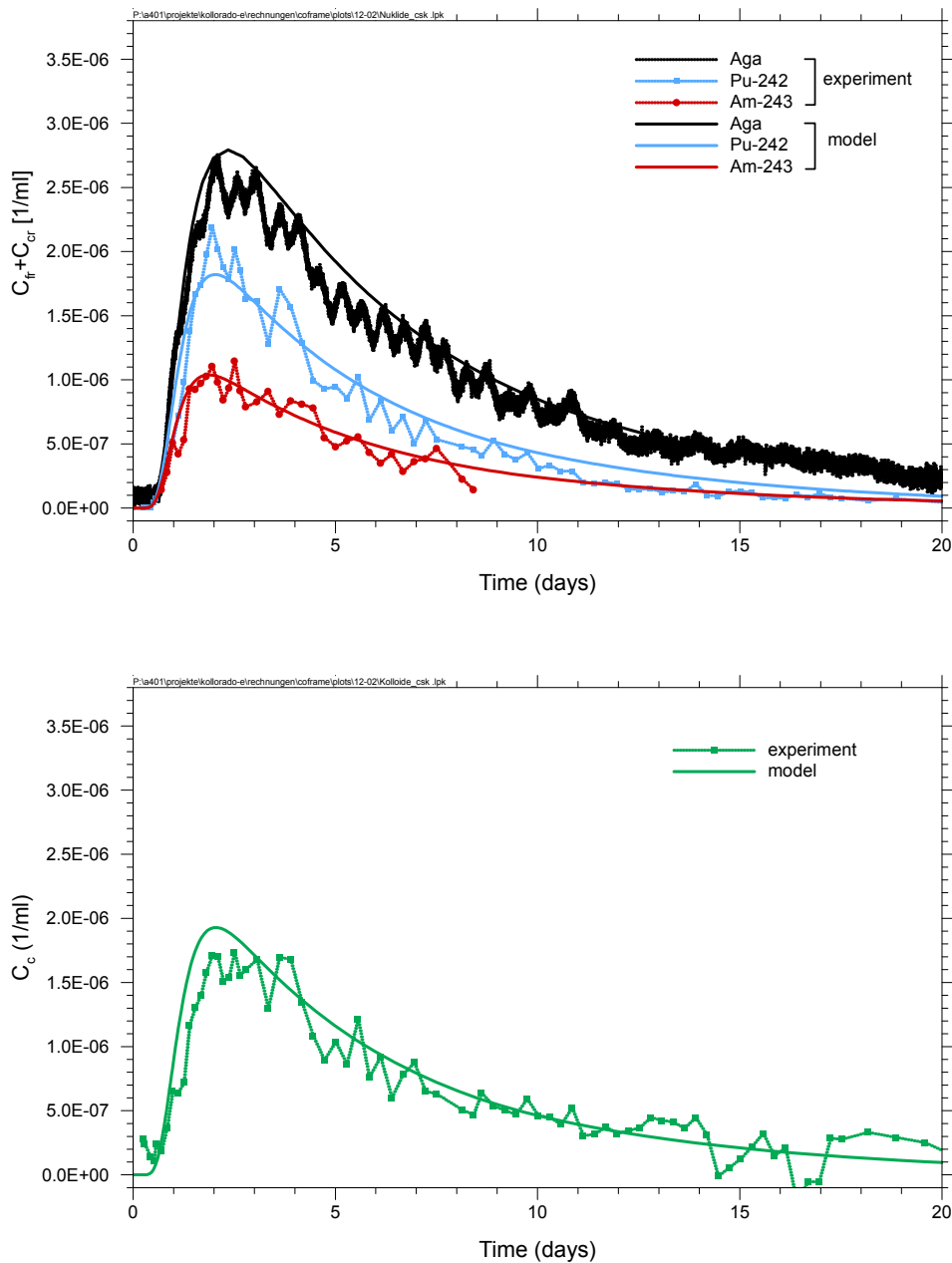
Figure 3-5: Simulation results for CFM RUN 12-02: Breakthrough curves for uranine and homologues (top) and for colloids (bottom) from experiment and modelling. For colloids the experimental breakthrough curve of Al is applied, reduced by an offset of $8.5 \cdot 10^{-7}$ [ml^{-1}] for naturally occurring Al and normalized by an initial Al mass of 30 mg. Curves scaled by a factor of 0.8 in order to account for AGA recovery of 80 %.

The results show that the experimental breakthrough curves can well be simulated with the transport code COFRAME. The most sensitive interaction parameters, namely the filtration rates k_{sc} and the desorption rates of the homologues or radionuclides from the colloids $k_{frm, fri}$, which have been derived by these simulations are generally in good agreement with results obtained with the transport code r^{3}t (Schäfer et al., 2013), Table 3-4.

Table 3-4: Interaction rates for CFM RUN 10-01 and 12-02 derived by calculations with r^3t and COFRAME, respectively**.**

	Interaction parameter	r3t	COFRAME
CFM RUN 10-01	Irrevers. filtration rate, ksc [h⁻¹]	0.01	0.01
	Desorption rate for tetravalent elements kfrm, fri [h⁻¹]	0.03	0.026 (Th) 0.029 (Hf)
	Desorption rate for trivalent elements kfrm, fri [h⁻¹]	0.075	0.068 (Eu) 0.074 (Tb)
CFM RUN 12-02	Irrevers. filtration rate, ksc [h⁻¹]	0.01	0.0174
	Desorption rate for tetravalent elements kfrm, fri [h⁻¹]	0.0025	0.0017 (Pu)
	Desorption rate for trivalent elements kfrm, fri [h⁻¹]	0.02	0.016 (Am)

Dipole test CFM RUN 13-05 and modelling. One objective of the project work was to perform predictive calculations with the transport code COFRAME for the field experiment CFM-RUN 13-05 in order to test the assumptions about the interaction rates and their transferability to other experiments. In particular, it is of interest, whether the parameter derived for one dipole can be applied to a different dipole in the shear zone. In a first step the newly developed program was tested and transport calculations for the homologue field experiment CFM-RUN 10-01 and the radionuclide field experiment CFM-RUN 12-02 have been performed (see above).

Predictive calculations for CFM RUN 13-05. The field test CFM RUN 13-05 was performed on a different multipole system compared to the other four dipole tests. The tracer cocktail was injected in CRR 99.002-i2 and extraction occurred at borehole BOMI 87.010 (5 ml/min) and Pinkel surface packer (25 ml/min). Details are described in (Kontar et al., 2013). Since the experimental results show that more than 90 % of the conservative tracer AGA are obtained at BOMI 87.010 and no signal could be detected at Pinkel surface packer, this experiment is simulated here as a dipole between CRR 99.002-i2 and BOMI 87.010, see Figure 3-3. All transport parameters assumed for this dipole are listed in Table 3-5. The injection flow rate was adapted to 0.77 ml/min to match the injected mass M_0 of the AGA tracer. The injected mass M_0 are as follows: AGA: 4.5 mg, bentonite colloids: 225 mg, Pu-242: $4.73 \cdot 10^{-3}$ mg, Am-243: $9.69 \cdot 10^{-4}$ mg.

Table 3-5: Transport parameters for simulation of CFM-RUN 13-05.

Parameter	CFM RUN 13-05
Transport pathway length [m]	2.23
cross section [m²]	0.0829
Fracture aperture [m]	0.0025
Fracture porosity	1
Total trace length [m⁻¹]	23.53
Volume flow [ml/min]	5
Injection flow rate [ml/min]	0.77
Penetration depth [m]	0.02
Rock porosity [-]	0.05
Rock density [kg/m³]	2670
Diffusion coefficient in rock matrix [m²/a]	0.008
Diffusion coefficient in fracture [m²/a]	0.03 (RN) / 0.003 (colloids)

Dispersion length [m]	0.3

The dispersion length for conservative tracer, radionuclides and colloids was reduced to 0.3 m, because of a reduced transport pathway length. The same fracture aperture compared to the other dipole experiments was selected and the cross section and total tracer length was adapted to adjust the pore velocity.

With respect to the interaction parameters three calculation cases were considered. In case A, which is the best-estimate prediction case, a filtration rate of 0.01 h^{-1} in good agreement with the rates observed in the other dipole experiments was assumed. For the sorption rates of radionuclides to/from the colloids the values derived from CFM Run 12-02 were selected, since so far a decrease of desorption rates with transport time was observed and transport times of CFM RUN 13-05 and CFM RUN 12-02 are similar. In case B the same sorption rates are applied but an increased colloid filtration coefficient is applied, which more reflects the colloid – fracture interaction observed in CFM-RUN 12-02. In case C the same colloid–fracture inter-action as in case A is assume but the sorption rates of radionuclides on/from colloids are in-creased, reflecting the data obtained from CFM-RUN 10-01. All interaction parameters are compiled in Table 3-6. The calculated recoveries for colloids, Pu-242 and Am-243 are shown in Table 3-7 and the breakthrough curves for all three cases are illustrated in Figure 3-6 to Figure 3-8.

Table 3-6: Interaction parameters for predictive calculations of CFM RUN 13-05.

	Case A	Case B	Case C
Interaction of colloids with fracture			
Colloid filtration coefficient [m^{-1}]	0.162	0.325	0.162
corresponding to coll. filtration rate [h^{-1}]	0.01	0.02	0.01
Interaction of homologues / radionuclides with colloids			
Kd (trivalent) [m^3/kg]		1500	
Kd (tetravalent) [m^3/kg]		1600	
Sorption rate [trivalent] [h^{-1}]		0.0228	0.0684
Sorption rate [tetravalent] [h^{-1}]		0.0017	0.0285
Interaction of radionuclides with fracture			
Kd (trivalent) [m^3/kg]		1.56	
Kd (tetravalent) [m^3/kg]		1.56	
Sorption rate [trivalent] [h^{-1}]		1.14x102 (1x10^6 a^{-1})	
Sorption rate [tetravalent] [h^{-1}]		1.14x102 (1x10^6 a^{-1})	

Table 3-7: Calculated recoveries for colloids, Pu-242 and Am-243 after 30 days.

Recoveries[1]	Case A	Case B	Case C
Colloids	0.62	0.48	0.62
Pu-242	0.58	0.43	0.27
Am-243	0.31	0.27	0.1

[1] Recoveries include a decreased recovery of the Aga-tracer of 90 %.
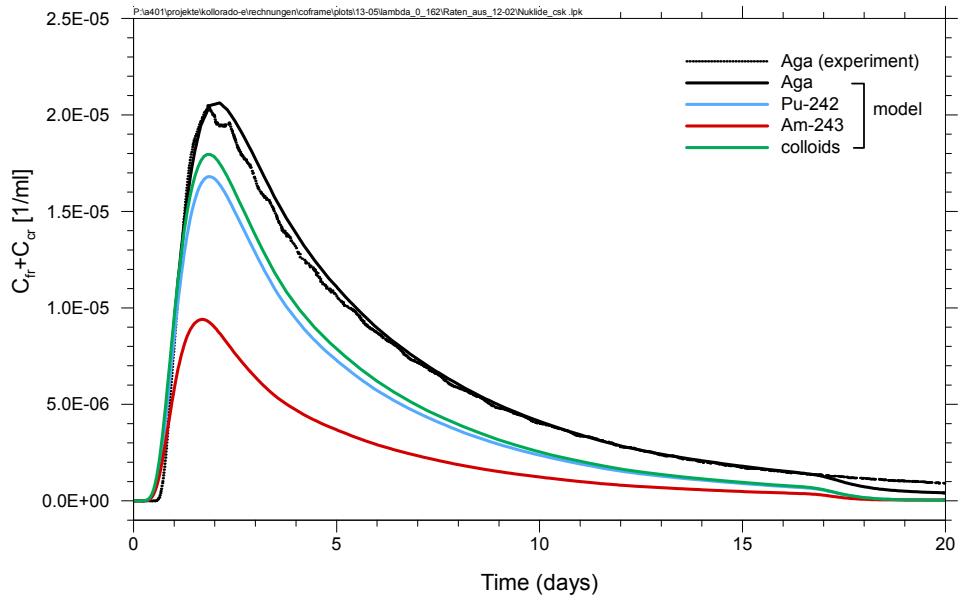
Figure 3-6: Predictive calculation case A. All curves are scaled with a factor of 0.89 due to a recovery of AGA of app. 0.9 observed in the experiment.
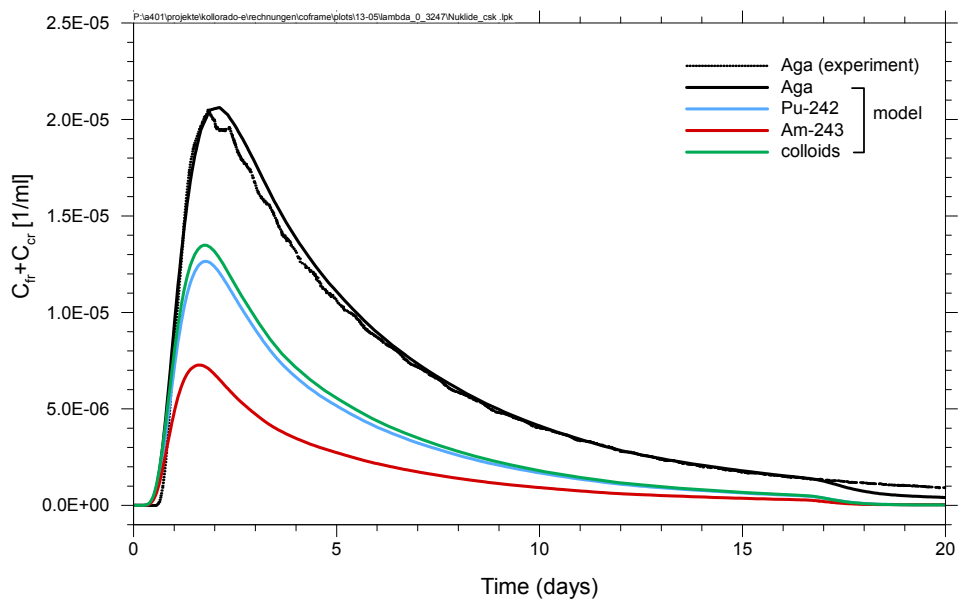
Figure 3-7: Predictive calculation case B. All curves are scaled with a factor of 0.89 due to a recovery of AGA of app. 0.9 observed in the experiment.
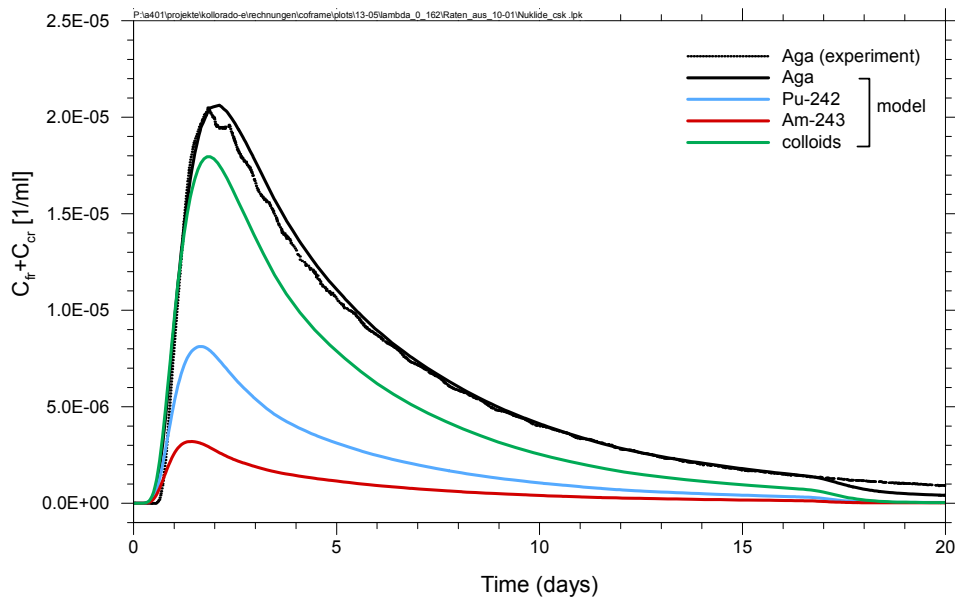
Figure 3-8: Predictive calculation case C. All curves are scaled with a factor of 0.89 due to a recovery of AGA of app. 0.9 observed in the experiment.

Final adjustment to the experimental data. The detailed comparison with the experimental results, which became available within the project, is shown in Figure 3-9 and Figure 3-10. A first observation of the experimental breakthrough curves for the colloids and radionuclides showed a less pronounced tailing as expected. Therefore, the dispersion length and the aperture have been slightly decreased. As a consequence, the maximum of the AGA curve is a bit overestimated by the model curve but the tailing is very well represented. The colloid breakthrough curve shows a lower recovery as predicted in all calculation cases A – C. The bentonite colloid filtration in dipole 2 seems to be slightly higher compared to dipole 1. Therefore, a higher filtration rate of 0.024 h^{-1} (see also Table 3-8) was applied to fit the experimental breakthrough curve as shown in Figure 3-9:
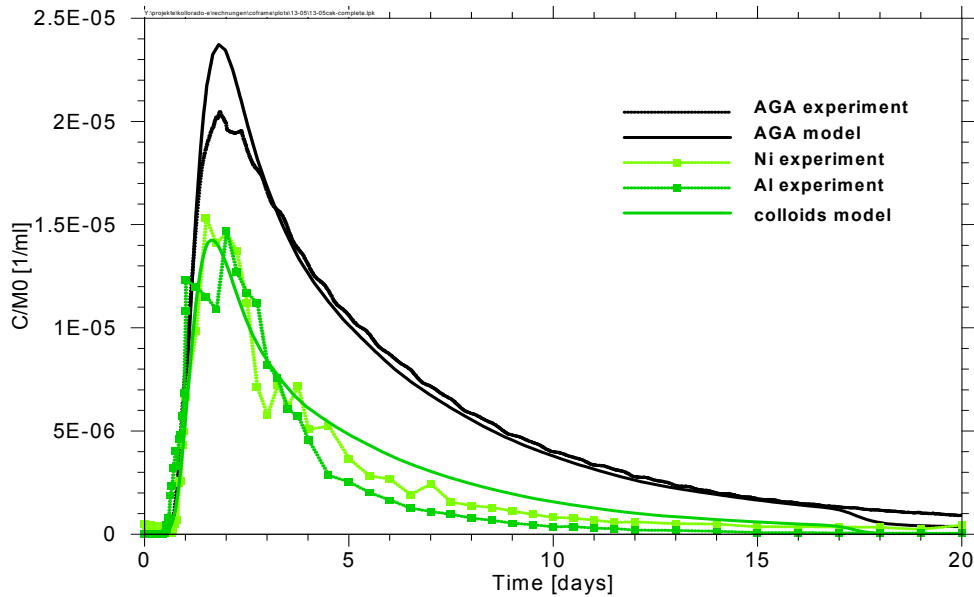
Figure 3-9: Normalized breakthrough curves of AGA tracer and colloids for CFM RUN 13-05, experimental data and model calculations. All curves are scaled with a factor of 0.89 due to a recovery of AGA of app. 0.9 observed in the experiment .

An observation regarding the breakthrough curves of Am-243 and Pu-242 is that the difference between the breakthrough curves of the trivalent and tetravalent actinides is less than assumed in the predictive calculations. This is mainly due to a comparably high recovery and therewith a comparably low desorption rate of Am-242 from the colloids. For the tetravalent Pu-242 the desorption rate from the colloids applied in case A and B of the predictive calculations could very well describe the experimental curve, whereas the rate for the trivalent Am-242 needed to be decreased by a factor of 3.5. Experimental and fitted breakthrough curves are shown in Figure 3-10. All interaction parameter used for the predictive calculations and for the re-calculation are listed in Table 3-8.
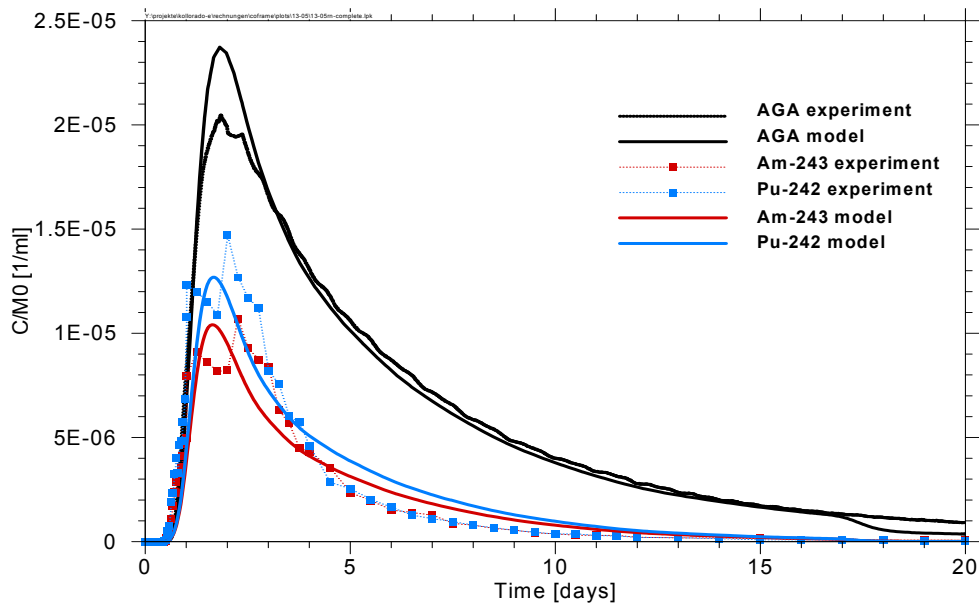
Figure 3-10: Normalized breakthrough curves of AGA tracer, Am-243 and Pu-242 for CFM RUN 13-05, experimental data and model calculations. All curves are scaled with a factor of 0.89 due to a recovery of AGA of app. 0.9 observed in the experiment.

Table 3-8: Interaction parameters used in predictive calculations and re-calculation.

	Case A	Case B	Case C	Re-calculation
Interaction of colloids with fracture (filling material)				
Colloid filtration coefficient [m^{-1}]	0.162	0.325	0.162	0.343
Corresponding filtration rate [h^{-1}]	0.01	0.02	0.01	0.024
Interaction of radionuclides with colloids				
Kfrm,fri (trivalent) [m^3/kg]		1500		
Kfrm,fri (tetravalent) [m^3/kg]		1600		
Sorption rate (trivalent) [h^{-1}]	0.0228		0.0684	0.0086
Sorption rate (tetravalent) [h^{-1}]	0.0017		0.0285	0.0017
Interaction of radionuclides with fracture				
Kfr* (trivalent) [m^3/kg]		1.56		
Kfr* (tetravalent) [m^3/kg]		1.56		
Sorption rate (trivalent) [h^{-1}]		1.14×10^2 (10x6 a^{-1})		
Sorption rate (tetravalent) [h^{-1}]		1.14×10^2 (10x6 a^{-1})		

The recoveries for colloids, Pu-242 and Am-243 derived from the predictive calculations, the experiment and the re-calculation are compiled in Table 3-9. It illustrates both issues, which have been discussed above, that (i) the filtration rate, which reduces the colloid recovery, was lower than expected in the predictive calculations and (ii) the difference in recoveries for Pu-242 and Am-243 was less than assumed in the predictions. For a further detailed discussion of the interaction parameter see Section 0.

Table 3-9: Recoveries of colloids, Am-243 and Pu-242 for predictive calculations, experiment and re-calculation.

Recoveries[1]	Colloids	Pu-242	Am-243
Case A	0.62	0.58	0.31
Case B	0.48	0.43	0.27
Case C	0.62	0.27	0.1
Experiment	0.38	0.32	0.26
Re-calculation	0.4	0.32	0.26

[1]After 30 days

Investigation of long-term behaviour in CFM field test 12-02. Analysis of Pu and Am concentrations in the sub ppq range by accelerator mass spectroscopy (AMS) opens a new aspect for the investigation of the CFM field experiments. Such analyses have been performed by (Quinto et al., 2015) for Pu-242 and Am-243 in samples from the field experiment CFM RUN 12-02 obtained at times > 50 days, as described in Section 2.1.3. This offers the opportunity to investigate the long-term tailing of the breakthrough curves, which might contain further information about long-term interaction processes. The observed concentrations of Am-243 and Pu-242 in the long-term tailing are in the range between 10^{-10} and 10^{-9} mol/l. In order to understand these experimentally observed long-term tailing transport calculations have been performed with the code COFRAME. First a reference case has been defined, with parameter values obtained from the simulation of the main breakthrough curve and from accompanying batch experiments. The selected parameters are based upon the values described in Section 0. In the next step parameter variations were performed, where one key interaction parameter, either a rate or a distribution coefficient (K_d value), was varied and all other parameters were kept constant. Thereby the impact of each parameter on the long-term tailing of the breakthrough curve can be estimated. The applied values are compiled in Table 3-10.

Table 3-10: Interaction data used in the model calculations.

Parameter	Unit	Reference	Variation (lower value)	Variation (higher value)
Kfr	[m]	12.5	1.25	125
Kfr*	[m³/kg]	1	0.1	10
kfr	[1/a]	106	103	
Kfrm,fri	[m³/kg]	1 600	160	16 000
kfrm,fri	[1/a]	Am: 220	0 - 100	Am: 660
		Pu: 35	-	Pu: 105
Remobilisation rate Rmb	[1/a]	0	-	100 - 1000
Colloid-bound RN fraction	[%]	99	90	99.9

In the model calculation with COFRAME an open fracture is considered. In order to describe sorption on fracture filling material, which partly fills the fractures, the following approach for calculation of the appropriate distribution coefficient K_{fr} is applied: Sorption on fracture filling material is described in our model as sorption on the fracture surface. In case that the filling material in the fracture can be described as a porous medium (with porosity n_f^* and density ρ_f^*) with known distribution coefficients K_{fr}^* [m³/kg], appropriate surface distribution coefficients can

165

be estimated via formulas for the retardation coefficients. It can be assumed that (Equation 34):

$$R_{fr} = 1 + \frac{1 - n_f^*}{n_f^*} \rho_f^* K_{fr}^* = 1 + \frac{K_{fr}}{b} \quad .$$

Equation 34

Distribution coefficients for the fracture surface can then be calculated as (Equation 35):

$$K_{fr} = b \frac{1 - n_f^*}{n_f^*} \rho_f^* K_{fr}^*$$

Equation 35

For estimation of K_{fr} we used a fracture aperture $2b$ = 2.5 µm, porosity in the filled fracture n_f^* = 20 % and ρ_f^* = 2500 kg/m³. The resulting breakthrough curves for the reference case are illustrated in Figure 3-11.

The presentation in logarithmic scale (bottom) shows that the long-term tailing is dominated by the fraction of free dissolved radionuclides. The curves show a plateau in the range between 0.2 and 20 years and decrease after a small peak beyond 50 years. For the reference case the concentration of Am-243 in the plateau is slightly higher than that for Pu-242, which is in agreement with the by AMS analysis observed concentrations. The plateau shows normalized concentrations in the range between $6 \cdot 10^{-10}$ to $9 \cdot 10^{-10}$ mol/l, whereas the experimental values are spreading over the whole range between 10^{-9} and 10^{-10} mol/l.

Parameter variations. In order to investigate the influence of the interaction parameter on the long-term behaviour of the radionuclides parameter variations have been performed. For most of the parameters a higher and a lower value (cf. Table 3-2) has been applied, respectively. For the parameters, which are not varied in the calculation the values for the reference case were used. First, parameters for the interaction of radionuclides with fracture filling material are varied. The results of the variation of the parameter K_{fr}, describing the distribution coefficient of radionuclides on the fracture filling material, show that it has a strong impact on the absolute concentration and the temporal extension of the tailing (see Figure 3-12). A by a factor of ten increased K_{fr}-value lowers the concentration and increases the occurrence time by a factor of ten whereas a decreased K_{fr}-value affects the curve in the opposite direction. On the other hand, this parameter does not affect the breakthrough curves at early times at all. A variation of the interaction rate k_{fr} for this process (in the range between 10^3 and 10^6 a⁻¹) has no influence on the shape of the curve (not shown).
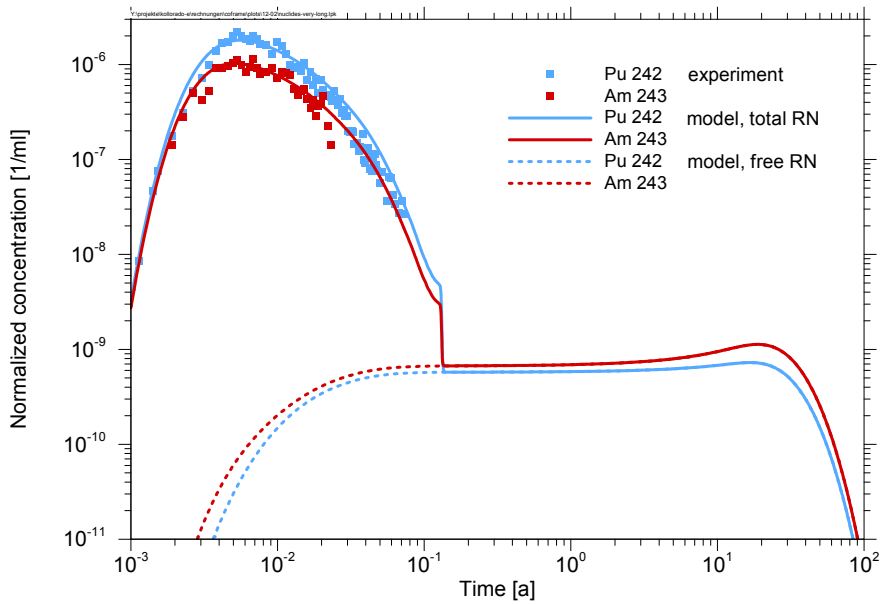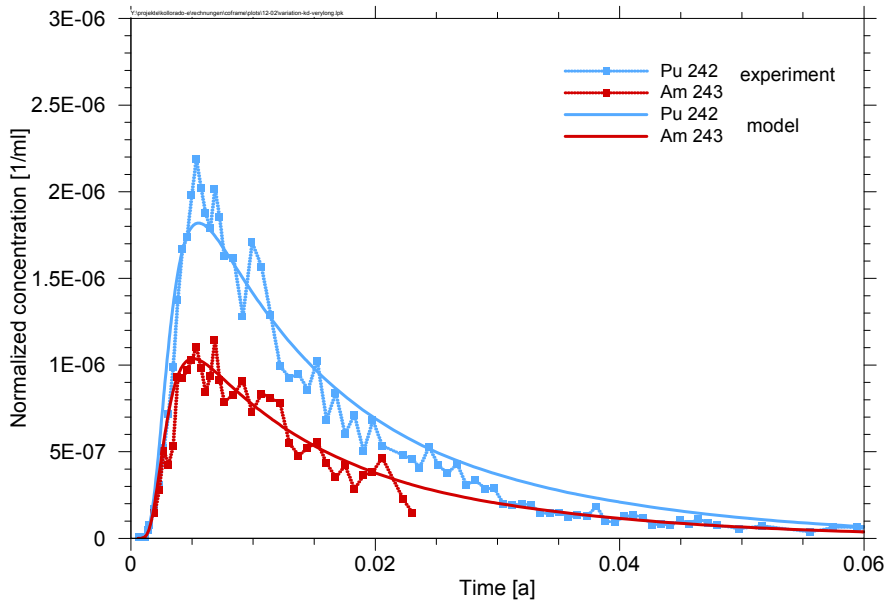
Figure 3-11: Normalized concentrations of Pu-242 and Am-243. Calculation with reference values for CFM-RUN 12-02. Linear scale (top) and logarithmic scale (bottom).
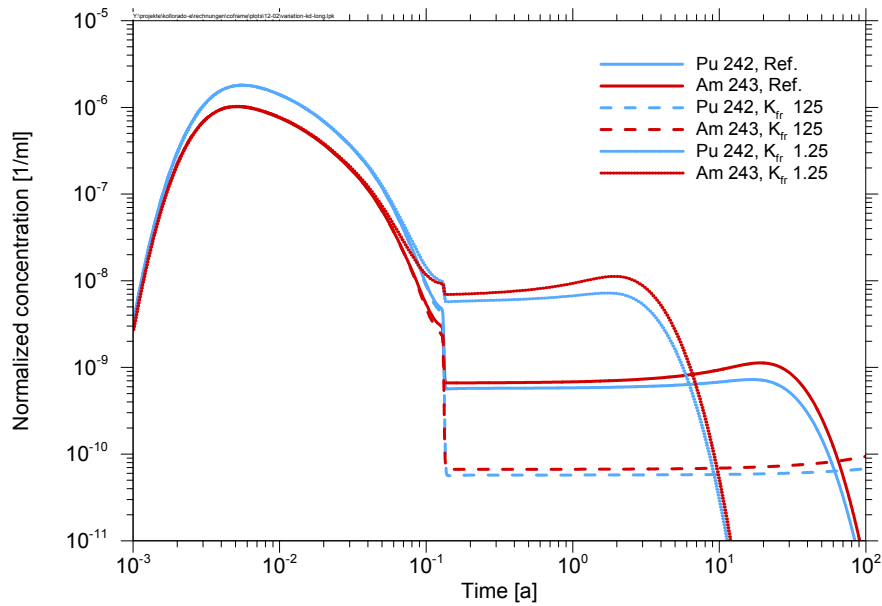
Figure 3-12: Normalized concentrations of Pu-242 and Am-243 calculated for the reference case and for parameter variations of Kfr.

Second, parameter for the interaction processes between radionuclides and colloids are investigated. The variation of the distribution coefficient $K_{frm,fri}$ for the sorption of radionuclides on colloids do not have any influence on the curves (not shown). Contrariwise the variation of the respective desorption rates $k_{frm,fri}$ does impact the curves. The results for a reduced rate $k_{frm,fri}$ compared to the reference case are shown exemplarily for Am-243 in Figure 3-13. A decrease of the rate $k_{frm,fri}$ leads to a decrease of the plateau concentration. At rates lower than 10 a^{-1} the shape of the long term tailing change from a plateau to a linearly increasing concentration profile. If the desorption rate is reduced to 0 y^{-1}, in the long term only a peak at 30 years is visible resulting from the fraction of 1 % Am-243, which was initially injected as free dissolved radionuclides (not colloid-bound). This fraction is retarded by a factor of app. 5000, cf. equation (1.5). However, it has to be mentioned that the radionuclide desorption rate from the colloids also impacts the shape of the early breakthrough curve, and a value of 100 a^{-1} already leads to a curve with a significantly increased maximum concentration compared to the experimental values.
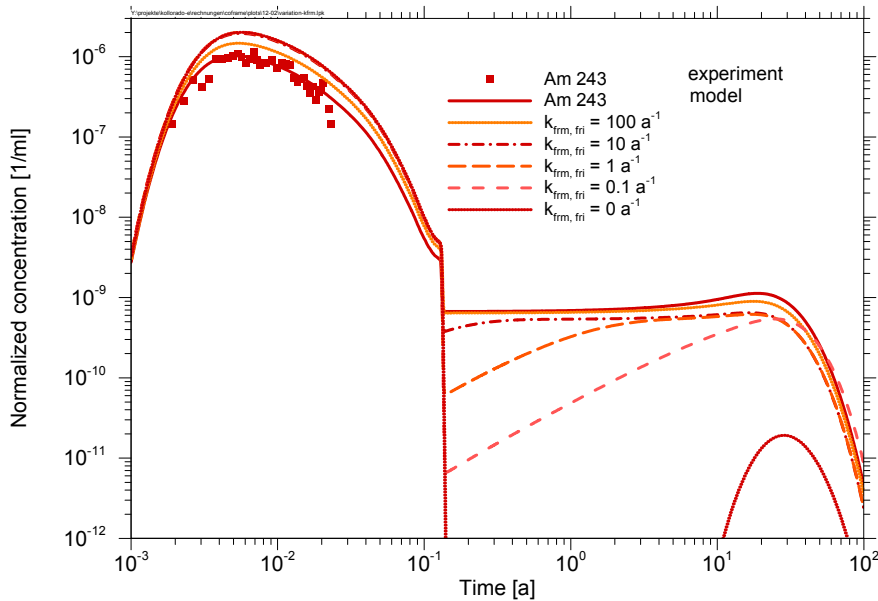
Figure 3-13: Normalized concentrations of Am-243 calculated for the reference case and for parameter variations for sorption/desorption rates of Am on/from colloids kfrm,fri.

For the interaction of colloids with the fracture filling material an irreversible filtration rate has been assumed for the reference case. This rate is directly derived from a fit of the colloid breakthrough curve to the experimental data. Here it was tested, how much the assumption of an increased reversibility of the filtration reaction does affect the long-term tailing. This was realized by variation of the remobilisation rate R_{mb} in a range between 0 a^{-1} (irreversible filtration) and 10 000 a^{-1}, shown in Figure 3-14. The impact of the remobilisation rate is different for both radionuclides. Whereas a remobilisation rate of 100 a^{-1} already reduces the plateau concentration in the long-term and the breakthrough curve at early times for Pu-242 it has nearly no effect on the curve of Am-243. A further increase of the remobilisation rate increases the curve at early times and reduces the plateau concentration further. Finally, a variation of the colloid bound fraction between 99 % and 90 % directly impacts the whole curve in the long term but less significant compared to K_{fr}, $k_{frm,fri}$ and R_{mb}, see Figure 3-15.
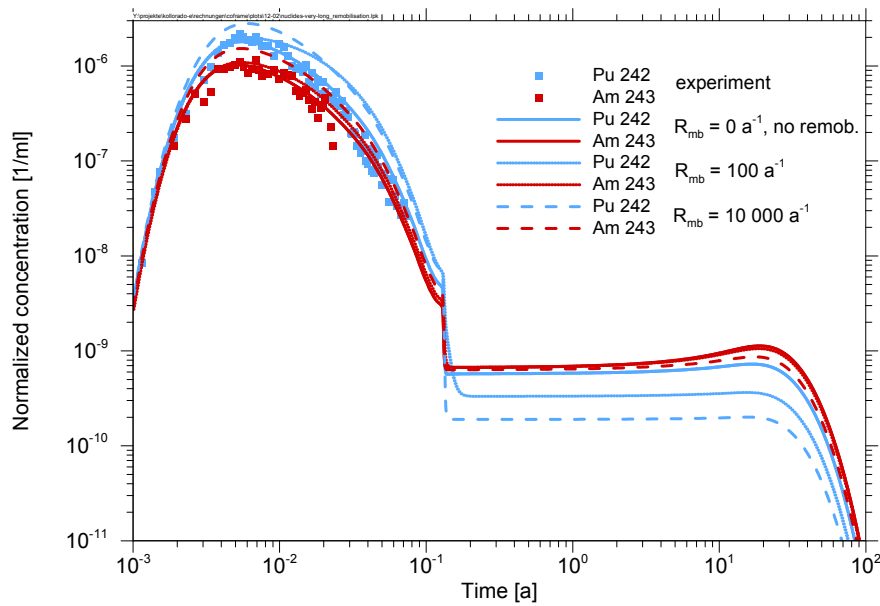
Figure 3-14: Normalized concentrations of Pu-242 and Am-243 calculated for the reference case and for parameter variations for colloid remobilisation rates Rmb.
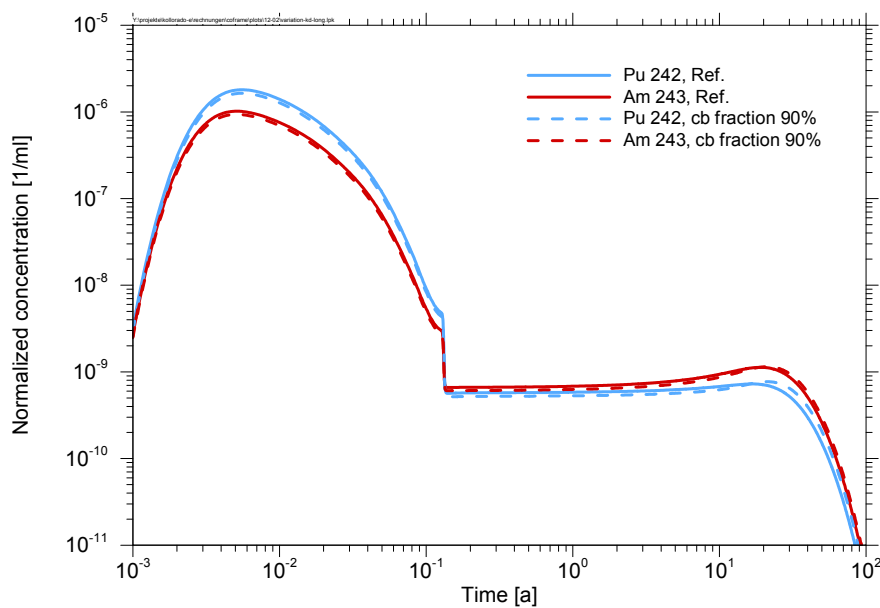
Figure 3-15: Normalized concentrations of Pu-242 and Am-243 calculated for the reference case and for parameter variation of the colloid-bound (cb) fraction.

Concluding so far, under the conditions of CFM RUN 12-02, the model calculations support a plateau of the long-term tailing, which was observed in the experiments. The simulation results indicate that the radionuclides in the plateau are freely dissolved. The parameters with highest influence on the absolute concentration and the form of the plateau in the long-term tailing of the breakthrough curve are K_{fr}, $k_{frm,fri}$ and R_{mb}. The latter two parameters also impact the major breakthrough curve at early times, i.e. at values, which markedly change the concentration or form of the plateau, the major breakthrough curve is already described unsatisfactory. This

indicates that these parameters might not be as important as the distribution coefficient K_{fr} of radionuclides on the fracture filling material with respect to the long-term tailing. Due to this fact additional sorption experiments in binary systems with radionuclides and fracture filling material have been performed (cf. Section 2.1.2.1) to closer determine distribution coefficients (and sorption/desorption rates) of radionuclides on the fracture filling material. From these experiments K_{fr} values of 2.85 m ($K_{fr}^* = 0.23$ m³/kg) and 7.5 m ($K_{fr}^* = 0.6$ m³/kg) were derived for Am and Pu, respectively. Further, sorption/desorption rates k_{fr} were determined to 71 a⁻¹ and 45 a⁻¹ for Am and Pu, respectively, considering a one site sorption/desorption reaction. At least the data for Pu suggest a two site desorption process, with a fast and a slow desorption reaction, which is not yet implemented in the code COFRAME. In addition, the finalized AMS and RIMS data for AM-243 and Pu-242 became available at the project end. Figure 3-16 shows these data covering a time frame of 57 to 200 days of the breakthrough curve together with COFRAME simulations using the new K_{fr} values and k_{fr} data implemented in a one site sorption/desorption model. In agreement with the experimental data the long-term tailings of the simulated breakthrough curves show a plateau after app. 50 days with three to four times higher normalized concentrations of Am compared to Pu. However, the simulated concentrations are about one order of magnitude higher than the measured concentrations. A better simulation of the result might be achieved with a modelling approach accounting for a two site desorption process with two different rates, which is planned in the future.

As discussed in Section 2.1.2.1 ^{242}Pu(IV) and ^{243}Am(III) show a fast sorption kinetic with more than 90% sorbed after 7d. After 228d contact time, the sorption reaches values around 98 to 99%. At these high amounts of sorption the analytical uncertainty is rather pronounced. Furthermore, at such high sorption values slight changes in the sorbed amount can significantly change the K_{fr} values mentioned above, e.g under the applied experimental conditions values of 98% and 99.9% result in K_{fr} values of 0.28 m³/kg and 5.69 m³/kg, respectively. Therefore, the K_{fr} values are covered by a high uncertainty.

A more thorough investigation of the processes affecting the long-term behaviour of the system will be performed in the follow-on project. This includes new experimental and model evaluations of CFM RUN 13-05 and, if possible, laboratory and field experiments yielding information on the status of the radionuclides in the long-term tailing, namely, whether they are free dissolved or colloid-bound.

Discussion of CFM field migration test results. Up to now, five field experiments have been evaluated by model simulations. The results highlight different aspects. The model simulations by r³t and COFRAME show that the breakthrough curve of the ideal tracer in the different field experiments can adequately well be described by very similar values for the most relevant flow parameters as porosity in case of r³t and flow aperture in case of COFRAME for each field test. With respect to the interaction parameters two processes turned out to be most relevant for the description of the breakthrough curves. The trivalent and tetravalent homologues and radionuclides were pre-equilibrated with Grimsel groundwater and bentonite colloids and then injected into the dipole. The colloid-bound fraction before injection was typically between 98 and 100 %. During transport through the fracture colloids became filtrated and homologues or radionuclides desorbed from the colloids subsequently sorbing to the fracture filling material.

Both processes cause a decrease in the recovery of the homologues or radionuclides, respectively. Therefore, the colloid filtration rates and the desorption rates of homologues and radionuclides from the colloids were identified as the most relevant interaction parameters with respect to the form of the breakthrough curve and the recovery under the boundary conditions of the CFM field tests. Although different conceptual models have been used to describe the flow and transport in the fracture, the values for the interaction parameters are in good agreement for the calculations with r^3t, COFRAME and the model RELAP, which was applied by LANL as a partner of the CFM modeller group (Reimus et al., 2014) and is also shown for comparison. The data for the colloid filtration rates are shown in Figure 3-17 and the values derived for the desorption rates of radionuclides and homologues from the bentonite colloids are shown in Figure 3-18 and Figure 3-19 for the tetravalent and trivalent elements, respectively. The colloid filtration rates are in a range between 0.005 and 0.025 h^{-1} indicating a weak, not pronounced trend of decrease with increasing travel time. The value derived for the dipole 2 (used for CFM RUN 13-05 and marked by the open triangle) show a slightly higher filtration rate compared to the values determined for the four other CFM field migration experiments performed at dipole 1.

Figure 3-18 and Figure 3-19 show that the desorption rates for the trivalent elements are higher than for the tetravalent elements as also observed in batch experiments (Huber et al., 2011) and in other lab investigations, e.g. (Bryan et al., 2014).

The desorption rates of the radionuclides / homologues show a significant decrease of the desorption rate with increasing travel time. This is true for both, the tetravalent and trivalent elements. Both curves significantly decrease with increasing travel time for travel times up to 40 hours and reach a plateau for travel times >50 hours. The values observed at the plateau are very similar to desorption values derived from batch experiments in ternary systems (Huber et al. 2011) indicated in Figure 3-18 and Figure 3-19 as black dotted horizontal lines. It can also be seen that the desorption rates derived by the different transport codes RELAP, r^3t and COFRAME are in good agreement.
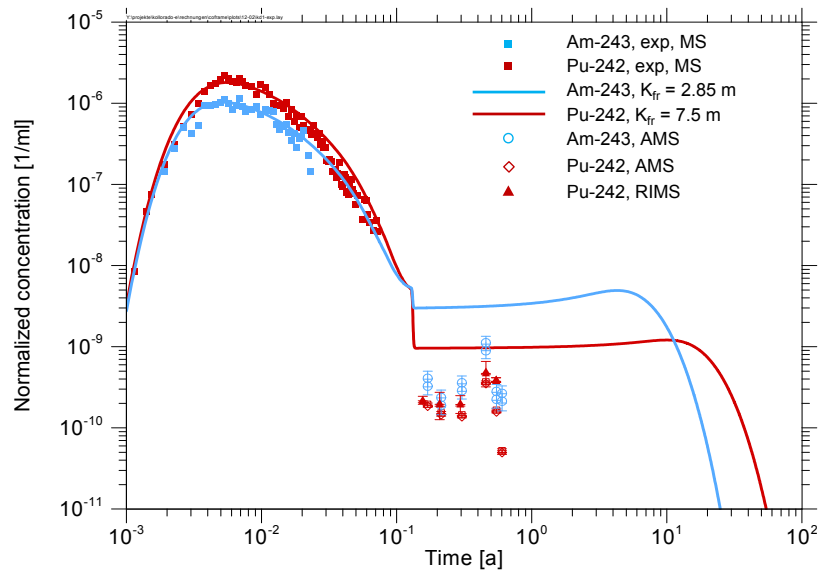
Figure 3-16: Normalized concentrations of Pu-242 and Am-243 calculated with distribution coefficients Kfr and sorption rates kfr derived from new experimental data (see text for explanation).
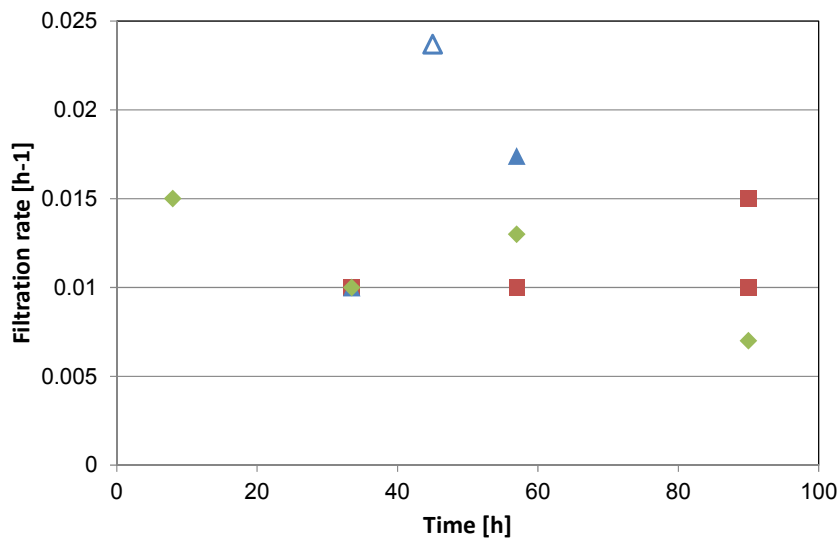
Figure 3-17: Filtration rates ksc as a function of travel time derived from model simulations with the codes RELAP (green rhomb), r3t (red square) and COFRAME (blue triangle). Data for dipole 1 are marked by filled symbols data for dipole 2 by open symbol.
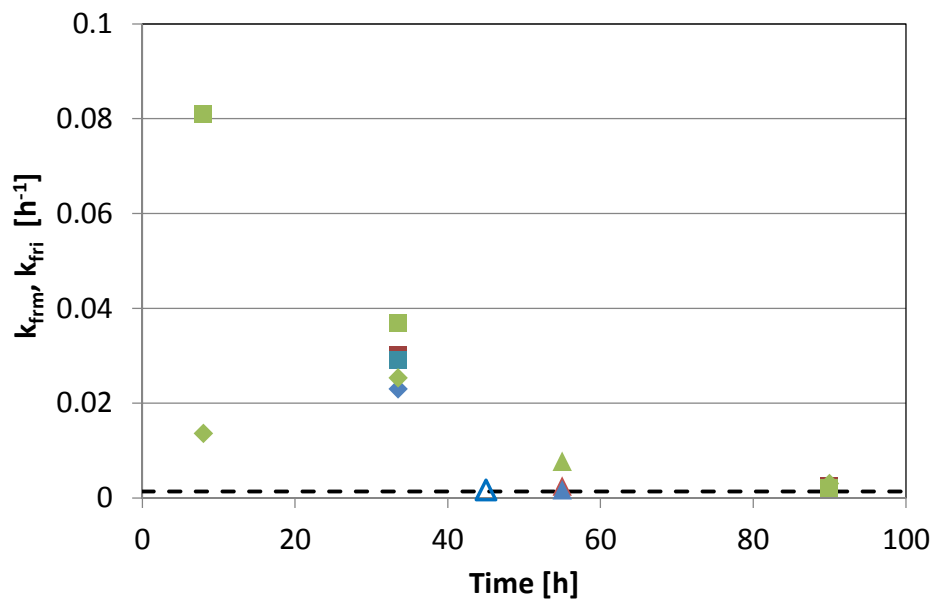
Figure 3-18: Desorption rates of tetravalent Th (squares), Hf (rhomb) and Pu (triangles) from colloids as a function of travel time derived from model simulations with the codes RELAP (green), r3t (red) and COFRAME (blue). The dotted black line indicates values determined in batch experiments.
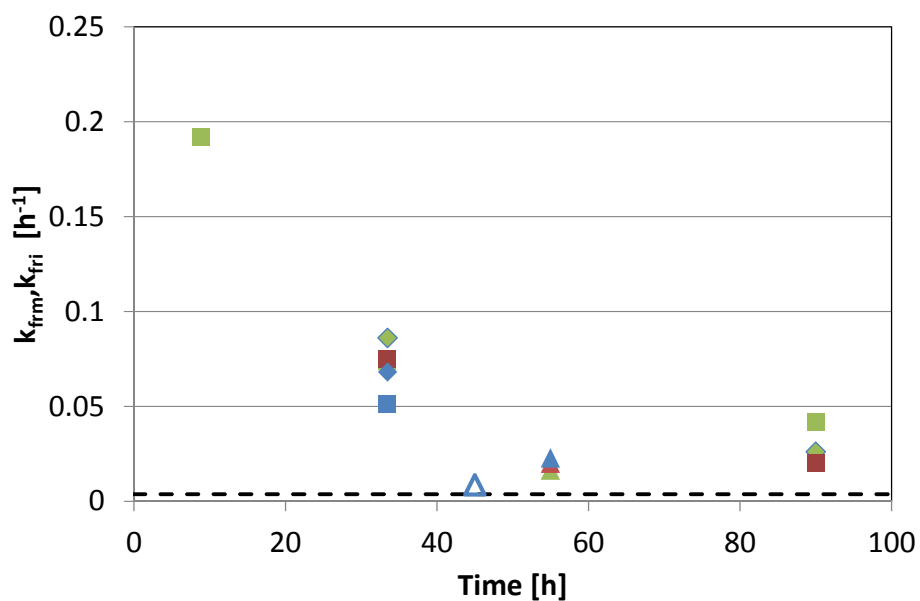
Figure 3-19: Desorption rates of trivalent Eu (squares), Tb (rhomb) and Am (triangles) from colloids as a function of travel time as derived from model simulations with the codes RELAP (green), r3t (red) and COFRAME (blue). The dotted black line indicates values determined in batch experiments.

One explanation for the observed decrease of the desorption rates might be the existence of two different sorption sites on the bentonite colloids causing a two stage desorption kinetics, which was for example observed by (Sheriff et al., 2015). *Sheriff et al.* investigated Eu interactions with bentonite colloids and measured desorption rate constants by a resin competition

method. They found, independent of equilibration time, a fast desorbing fraction of about 30 to 40 % of Eu and a slow desorbing fraction of 60 to 70 % Eu with a desorption rate for the slow desorbing fraction of 0.0032 h^{-1}. This value corresponds well with the lowest value derived in ternary batch experiments by (Huber et al., 2011) of 0.0037 h^{-1} for trivalent Am and is by a factor of 2.3 lower compared to the lowest value derived from the field migration tests for the trivalent elements of 0.008 h^{-1} (see Figure 3-19). In the following the discussion is focussed on the recoveries derived from the field migration tests. During Tracer Test Runs 11-01 and 11-02 it was established that at low gradients uranine showed anomalous losses compared with the tracer Amino-G Acid (AGA). The process causing these losses is not understood although it has been suggested that it is associated with low pH conditions in the injection interval. Therefore, it is not clear, whether a recovery of the uranine tracer below 100 % is caused by some flow of uranine out of the dipole field or by degradation of the uranine tracer. For all simulation results shown it was assumed that part of the tracers did flow out of the dipole field and do not reach the outflow, i.e. all breakthrough curves were scaled by the recovery of the ideal tracer to account for this mass loss (cf. Table 3-11). Another aspect is some uncertainty in the injected mass M_0 of the conservative tracer, which also causes uncertainties in the re-covery of the ideal tracer. In the following discussion it is assumed that a reduced recovery (<100%) of the ideal tracer was either caused by a degradation of the tracer and/or by some uncertainty in the injected mass M_0, i.e. it is considered that in all cases 100 % of the ideal tracer reached the outflow. Therefore, the experimentally observed recoveries for colloids, homologues and radionuclides are not scaled, see Table 3-11.

Table 3-11: Travel times and recoveries (not scaled) of colloids, tetravalent and trivalent elements observed in the CFM field migration experiments.

CFM RUN	Travel time* [h]	Recoveries [%]		
		colloids	tetravalent	trivalent
08-02	8	99	93 (Th)	56 (Tb)
			78 (Hf)	
10-01	33.5	55	28 (Th)	11 (Eu)
			24 (Hf)	8 (Tb)
10-03	110	55	45 (Th)	14 (Eu)
			47 (Hf)	6 (Tb)
12-02	55	45	38 (Pu)	20 (Am)
13-05	40	38	28 (Pu)	24 (Am)
CRR#32	1.5	98	97 (Th)	89 (Tb)
			98 (Hf)	

* Time of maximum of ideal tracer breakthrough curve.

The respective recoveries for the colloids are shown in Figure 3-20. For travel times up to 10 hours the recoveries are near 100 % and for higher values decrease down to values of 45-55 %. After about 40 hours travel time the recoveries tend to be constant. The recoveries obtained at dipole 2 (for illustration the results from CRR experiment #32 are also shown) tend to be slightly lower compared to dipole 1, which was already indicated by slightly higher filtration rates for colloids in CFM RUN 13-05, cf. Figure 3-17. Two simulation curves, assuming a linear first order filtration reaction with filtration rates k_{sc} = 0.01 h^{-1} and 0.025 h^{-1}, respectively are shown here for comparison. However, particularly the shape of the curve for the recoveries of

dipole 1 covering travel times up to 110 hours are not sufficiently well described. The experimental data suggest a plateau at 50 ± 5 % recovery for travel times >40 h, which cannot be described with a constant filtration rate. This observation is reflected in the weak trend of decreasing filtration rates with increasing travel time as shown in Figure 3-17.
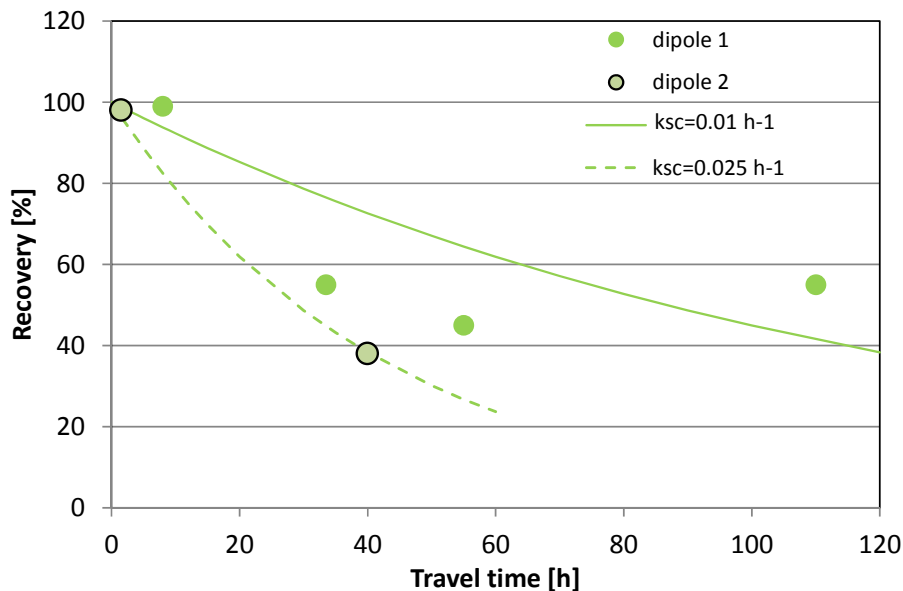
Figure 3-20: Recoveries for colloids and simulation withfor two different filtration rates.

In order to better illustrate the effect of the desorption rates of homologues / radionuclides from the colloids their recoveries have been normalized by the recovery of the colloids, i.e. the homologue / radionuclide recoveries of each field test have been divided by the recovery of the colloids. This is a simplified procedure, but, therewith the impact of the desorption process on the element recovery is separated from the impact of the colloid filtration process. The corresponding normalized recoveries for the tetravalent elements are shown in Figure 3-21 and illustrate a slow decrease with increasing travel time The recovery derived from field experiment CFM RUN 10-01 (travel time 33 years) is remarkably low compared to those of the other field tests. One reason for that might be significantly lower colloid concentration of 30 mg/l, in this run compared to colloid concentrations of about 100 mg/l in CFM RUNs 10-03, 12-02 and 13-05. The normalized recoveries are >70 % even for longest travel times realized in CFM of 110 hours, except for CFM RUN 10-01 where the values are between 40 and 50 %. In order to check the assumption of two different sorption sites being responsible for a decrease of desorption rates with travel time (see above) simulation curves assuming an element desorption from two different sorption sites on the colloids with two different linear first order desorption kinetics are included in Figure 3-21. For desorption of the fast desorbing fraction, denoted as site 1, a desorption rate of 0.1 h^{-1} is applied and for desorption of the slow desorbing fraction, denoted as site 2, a desorption rate of 0.0002 h^{-1} is used. Five different distributions of the tetravalent elements on site 1 and site 2 were assumed: (i) an initial coverage of 50 % of both sites, (ii) a coverage of 60 % and 40 %, (iii) a coverage of 40 % and 60 % (iv) a coverage of 30 % and 70 %, and (v) a coverage of 20 % and 80 % on site 1 and 2, respectively. The shape

of the curves reflects the trend of the normalized recoveries, however, the strong discrepancy between the recoveries of CFM RUN 10-01 and the recoveries of the other field tests cannot be satisfactorily described. Neglecting the low recoveries of CFM RUN 10-01 a relatively high initial coverage of sites 2 (70 to 80 %) with slow desorption kinetics as observed for the trivalent Eu would better describe the curves.
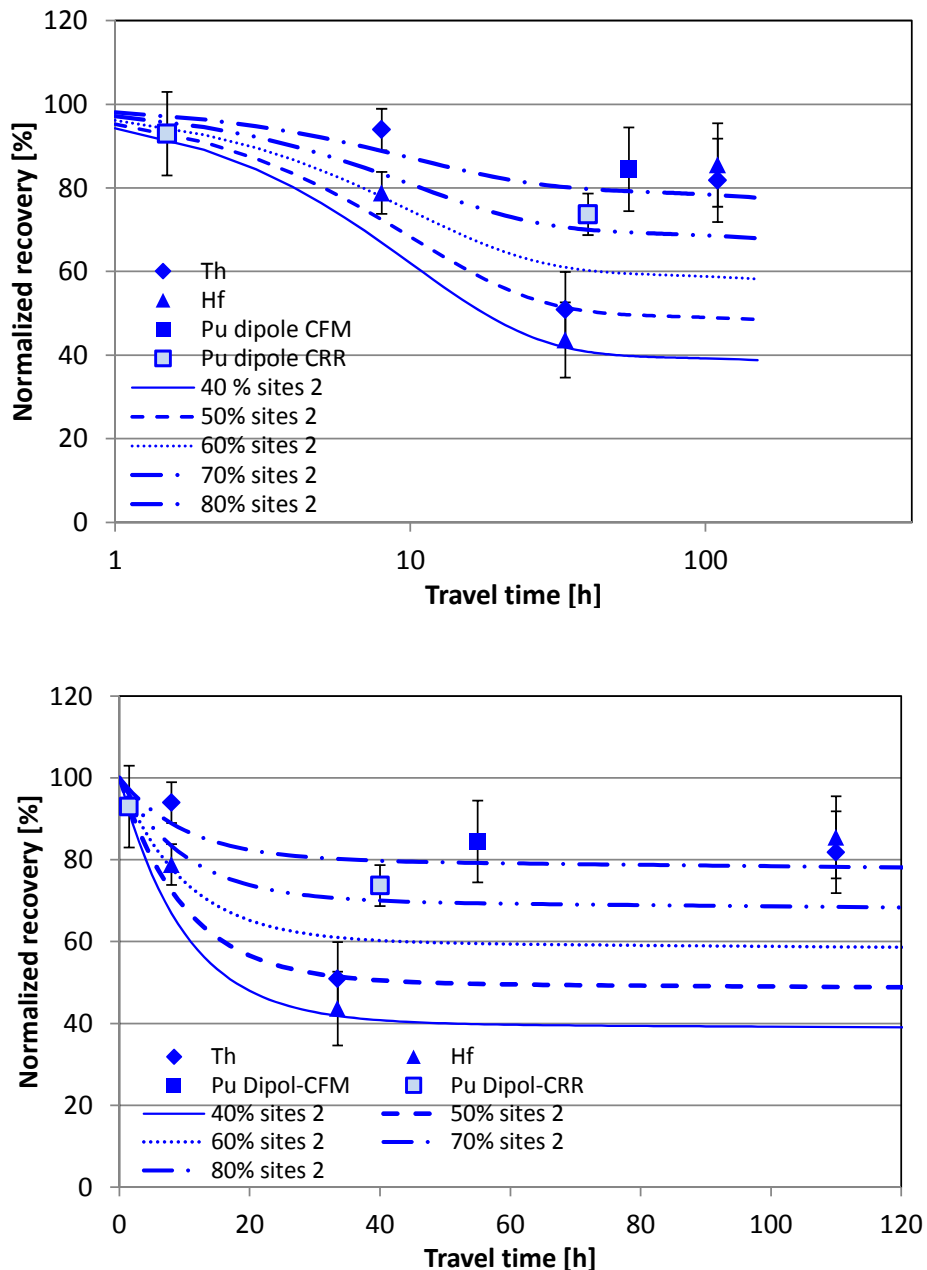
Figure 3-21: Normalized recoveries for tetravalent actinides as function of travel time and simulation curves using a two site model for desorption logarithmic time scale (top), linear time scale (bottom). See text for more information.

The situation for the trivalent elements is shown in Figure 3-22. The first obvious difference compared to the tetravalent elements is the stronger decrease of the normalized recoveries with increasing travel time, due to higher desorption rates of the trivalent elements, see Figure

177

3-19. As observed for the trivalent homologues, the normalized recoveries for Eu and Tb in CFM RUN 10-01 are comparably low, here in the same order of magnitude as observed for travel times of 110 years in CFM RUN 10-01. On the other hand, the values observed for Am are comparably higher as those for the lanthanides Eu and Tb, indicating a slightly different (slower) desorption behaviour of Am.
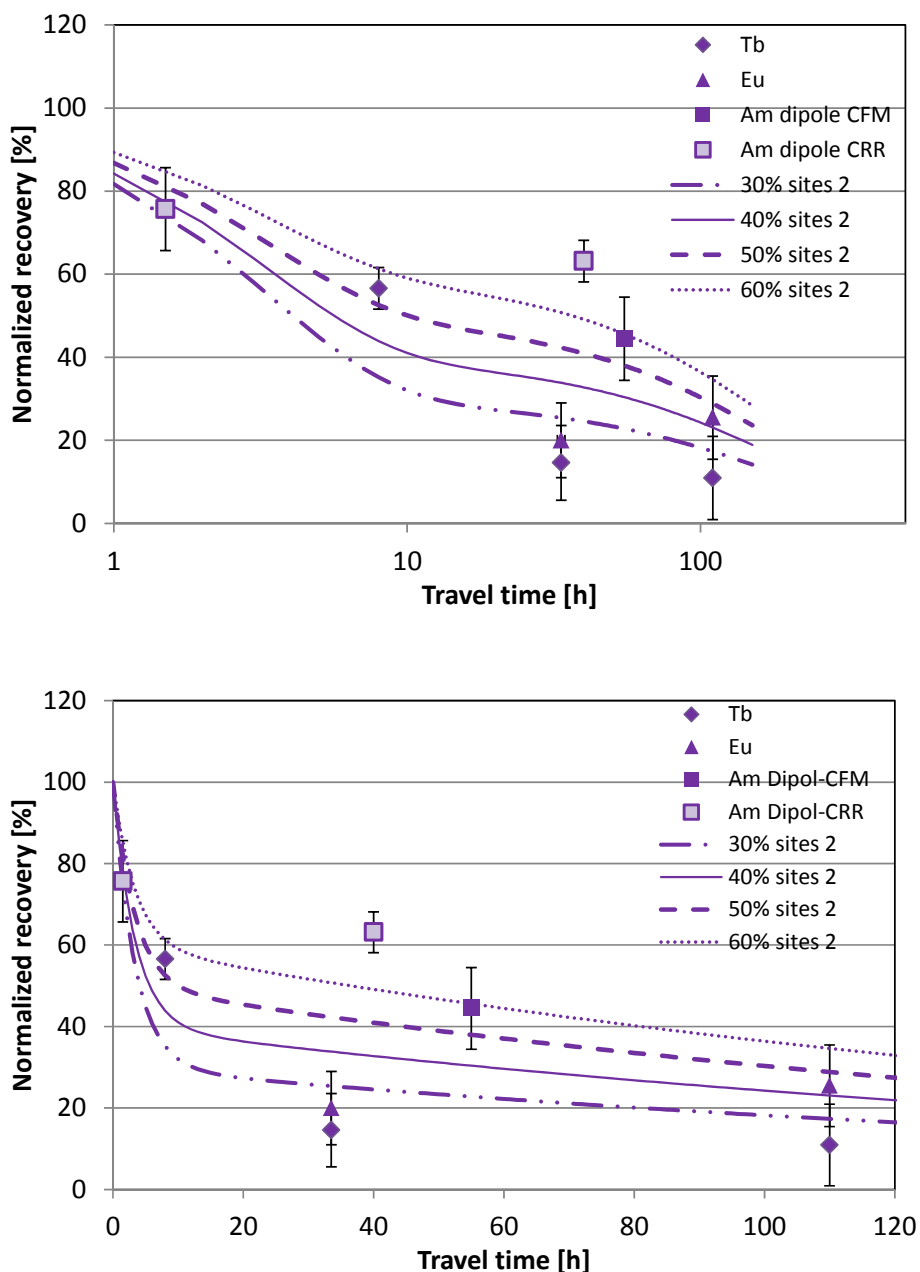
Figure 3-22: Normalized recoveries for trivalent actinides as function of travel time and simulation curves using a two site model for desorption; logarithmic time scale (top), linear time scale (bottom). See text for more information.

As for the tetravalent elements simulation curves assuming an element desorption from two different sorption sites on the colloids with two different linear first order desorption kinetics are included in Figure 3-22. As initial distributions, (i) an initial coverage of 50 % of both sites, (ii)

a coverage of 70 % and 30 %, (iii) a coverage of 60 % and 40 %, and (iv) a coverage of 40 % and 60 % on site 1 and 2, respectively, were assumed. As desorption rates a value of 0.3 h^{-1} is applied for the sites with the fast desorbing fraction and 0.005 h^{-1} for the sites with the slow desorbing fraction. The graph shows the difficulty to describe the relatively low recoveries in CFM RUN 10-01 on the one hand and the comparably high recoveries of Am on the other hand. The latter indicates a slightly different behaviour of Am compared the lanthanides Eu and Tb. All data are covered by uncertainties, which have not been completely analysed within this project phase. This will be a task of the following work. In order to further investigate the existence of two different sorption sites an additional field migration experiment is planned in the CFM project, where the radionuclides should be equilibrated with bentonite colloids and Grimsel water in the usual way. Before injection into the field dipole, large-scale desorption experiments should be carried out using shear zone material in the presence of the equilibrated cocktail to remove homologues or radionuclides that are adsorbed to weaker colloid sorption sites. The remaining colloids and associated homologues could be used as injection cocktail in the field migration test. The maximum effective desorption rate constants associated with homologues or radionuclides that remain adsorbed to the colloids after a certain amount of desorption time could then be derived.

3.2   Impact of fracture heterogeneity on bentonite erosion

F. Huber, D. Leone, M. Trumm, L. Moreno, I. Neretnieks, A. Wenka, T. Schäfer

Introduction

Moreno et al. presented model calculations on bentonite erosion in a parallel plate fracture (Moreno et al., 2011) with a constant aperture of 1 mm and spatial fracture dimensions of at least 10m x 5m (depending on the imposed flow velocity). The simulations covered a range of mean velocities in the fracture of 1×10^{-5} m/s (315 m/a) down to 1×10^{-8} m/s (0.315 m/a). To achieve these velocities, they selected arbitrarily chosen constant hydraulic conductivities (1×10^{-4} m/s to 1×10^{-7} m/s) to be used in the Darcy law. Natural fractures are characterized by complex heterogeneous aperture distributions and complex overall geometries (Adler and Thovert, 1999) in contrast to the parallel plate type fracture assumed in the model by Moreno et al. Numerous laboratory and numerical studies carried out in the last decades have shown the effect and importance of fracture geometry and aperture distributions on the fracture flow field (Detwiler et al., 2000; Moreno and Neretnieks, 1993; Moreno et al., 1990; Tsang and Neretnieks, 1998; Tsang, 1984). One of the most pronounced features is flow channelling arising from geometrical heterogeneity and thus variability in fracture hydraulic conductivities as function of the fracture apertures. That is, areas of high flow velocities are localized next to low flow areas within the fracture. These flow gradients lead to complex patterns of e.g. fluid shear forces or hydrodynamic dispersion of e.g. solute and particle/colloids present in the seeping water. Thus, the focus of this study investigates the potential impact of fracture geometry (equivalent to flow field and mass transport heterogeneity) on the bentonite erosion behaviour and rate.

Material and Methods

General approach/concept. The most sophisticated model available on bentonite erosion presented by Neretnieks et al. (Neretnieks et al., 2009) was implemented in the software COM-SOL Multiphysics (Multiphysics, 2015) and used by Moreno et al. in their simulations. In the present study the identical model was applied implementing heterogeneous fracture aperture fields instead of the previously used homogeneous aperture field. The governing set of equations for the description of the fluid flow (Darcy Law), bentonite expansion and erosion processes were left untouched. The reader is referred to the papers by Moreno et al. and Liu et al. for details on the bentonite erosion model (Liu et al., 2009a; Moreno et al., 2011; Neretnieks et al., 2009). In the following an overview on the model setup used in this study is presented.

Model implementation. In Figure 3-23 the model geometry in conjunction with details on the boundary conditions for flow and mass transport for the case of 1×10^{-5} m/s mean velocity over the whole fracture model domain are depicted. Water enters from the left side and is allowed to leave the domain only through the right border. On the top and on the bottom of the model no flow and no flux conditions are applied, respectively except around the bentonite source,

which is allowed to swell and expand. The model spatial dimension changes as a function of the water velocity imposed. The slower the water flux, the bentonite swelling and expansion increases. In order to contain the fully expanded bentonite in the model domain, the model dimensions are changed according to the mean water velocity (see Table 3-12). The diameter of the bentonite source is kept constant at 1.75 m independent on the overall spatial model dimensions.
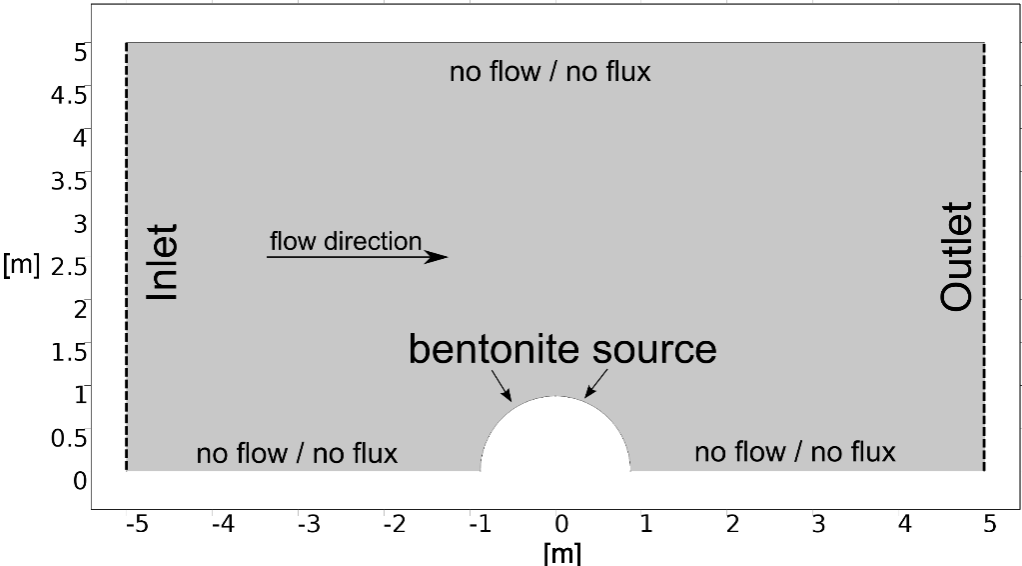
Figure 3-23: Model geometry, spatial dimensions and boundary conditions for the case of a mean fracture flow velocity of $1x10^{-5}$m/s.

For lower flow velocities, bigger spatial dimensions were used (see Table 3-12 for more details) as mentioned in Moreno et al. (2011). The diameter of the bentonite source is kept constant at 1.75 m independent on the overall spatial model dimensions. On the left and right of the model domain pressure boundary conditions are applied to create a pressure gradient driving the water flow across the model domain

Table 3-12: Overview of model spatial dimensions and number of elements and nodes.

Velocity	Model dimensions Length and Height	Number of elements
[m/s]	[m]	[-]
1e-5	10 x 5	13362
1e-6	10 x 5	13362
1e-7	20 x 10	56763
1e-8	30 x 15	65267

Generation of the fracture aperture fields. Since data on detailed natural aperture and/or hydraulic conductivity distributions of field scale fractures are not available, synthetic randomized fracture aperture distributions were generated and used in the model. From µ-computed x-ray tomography (µCT) characterizations (resolution of 80 µm and 32 µm, respectively) of cm scale drill cores from Äspö, Sweden by e.g. *(Huber et al., 2012)* information on natural fracture aperture distributions are known. These measured aperture distributions follow normal or log-normal distributions (both distributions give equally good fits, so the simpler normal distributions have been chosen). Calculated mean apertures of these two cores are 0.192 mm with a standard deviation (STD) of 0.064 mm and 0.451 mm with a standard deviation of 0.14 mm, respectively. These two measurements display STDs in the range of ~30% of the mean aperture. Based on literature results, standard deviations of fracture apertures show a rather broad range from ~30% STD *(Hakami and Larsson, 1996)* up to more than 100% STD *(Keller, 1998)*. In the present study the fracture heterogeneity is produced by letting the aperture vary in a range of STDs from 10% up to 50%. That is, given a 1 mm mean aperture, STDs of 0.1 mm (10%), 0.3 mm (30%) and 0.5 mm (50%) are obtained in case of normal distributions. The random aperture distributions were generated using the random number function (function "*randn*") of the software Matlab R2015a *(The MathWorks, 2015)*. A regular distribution of apertures across the model domain was achieved by producing a quadratic mesh of the model domain within COMSOL (Figure 3-24). The distribution (or resolution) of the mesh is not fully regular due to the model geometry with elements being smaller close to the cylindrical bentonite source. As an order of magnitude a resolution of 20 cm on the borders was achieved. The aperture distributions with STD 0.5 mm have some negative values. Having no physical meaning, these apertures were replaced by positive values randomly selected of a distribution with the same mean and sigma values. Thus we ignore the possibility of having asperities in our fractures which can be found in natural fractures *(Huber et al., 2012)*. The next step involved the assignment of a random aperture value of the normal distribution mentioned above on each node of the quadratic mesh. This aperture field was then used in COMSOL as input in an interpolation function (build-in capability of COMSOL). A simple linear interpolation function from the quadratic mesh to the numerical triangular mesh was chosen between the aperture values.

For computing the flow and bentonite erosion a triangular mesh is defined in COMSOL (Figure 3-24). This triangular mesh has a finer resolution than the quadratic one, especially around the bentonite source, where the largest gradients are present. The triangular mesh resolution on the border is roughly 10 cm, i.e. a factor of 2 higher as for the aperture field. Because of the difference between the two meshes, there are less aperture values than mesh nodes. A sketch is given in Figure 3-24 where the blue points represent the triangular mesh and the red ones the aperture field. This approach results in having an aperture value in each triangular mesh point. The choice of the triangular mesh size was driven by a finding a compromise between simulation run time and stability of the model. Following this approach, a correlation length between the apertures of ~20cm is obtained representing in a way a fracture roughness on the same spatial resolution. Further work will investigate also correlation lengths in the scale of the bentonite source (1.75 diameter; macro-scale roughness). In Figure 3-25 two aperture fields are shown exemplarily for STDs of 0.1mm and 0.5mm, respectively in conjunction with their

corresponding (interpolated) aperture distribution histograms. The increasing degree of heterogeneity with increasing STD is obvious.
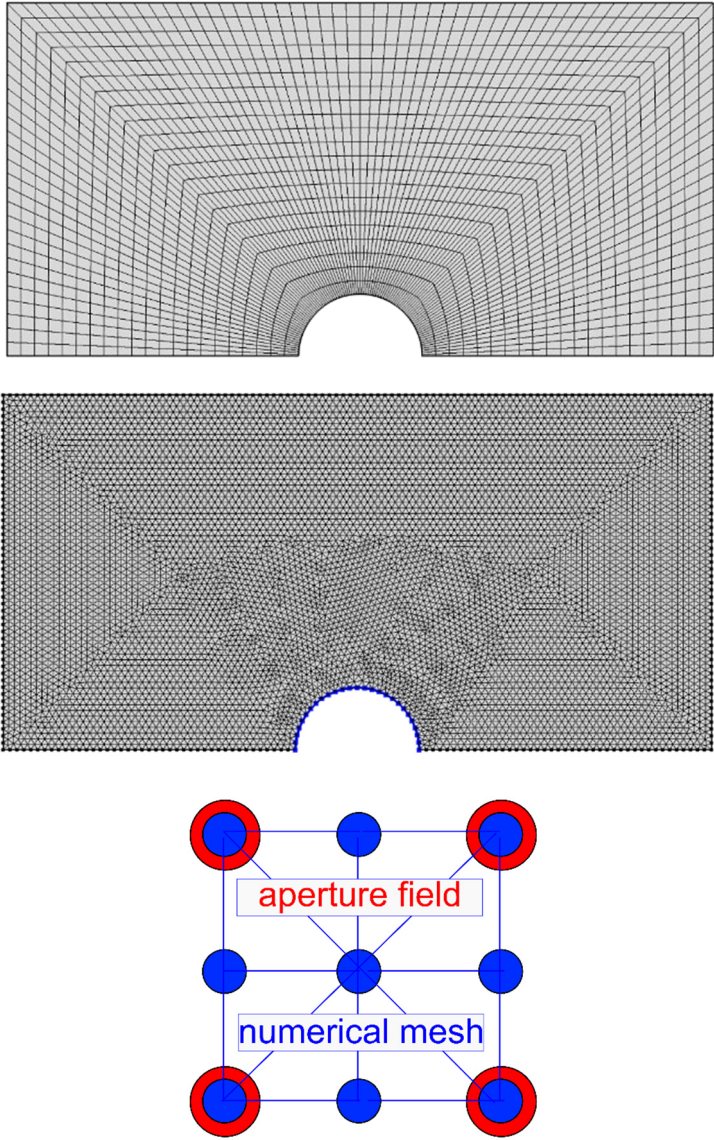
Figure 3-24: (top) Spatial aperture distribution on the nodes of the quadratic mesh (middle) numerical trinagular mesh used in the simulaitons (bottom) sketch to visualize the interpolation between the aperture field and the triangular mesh.
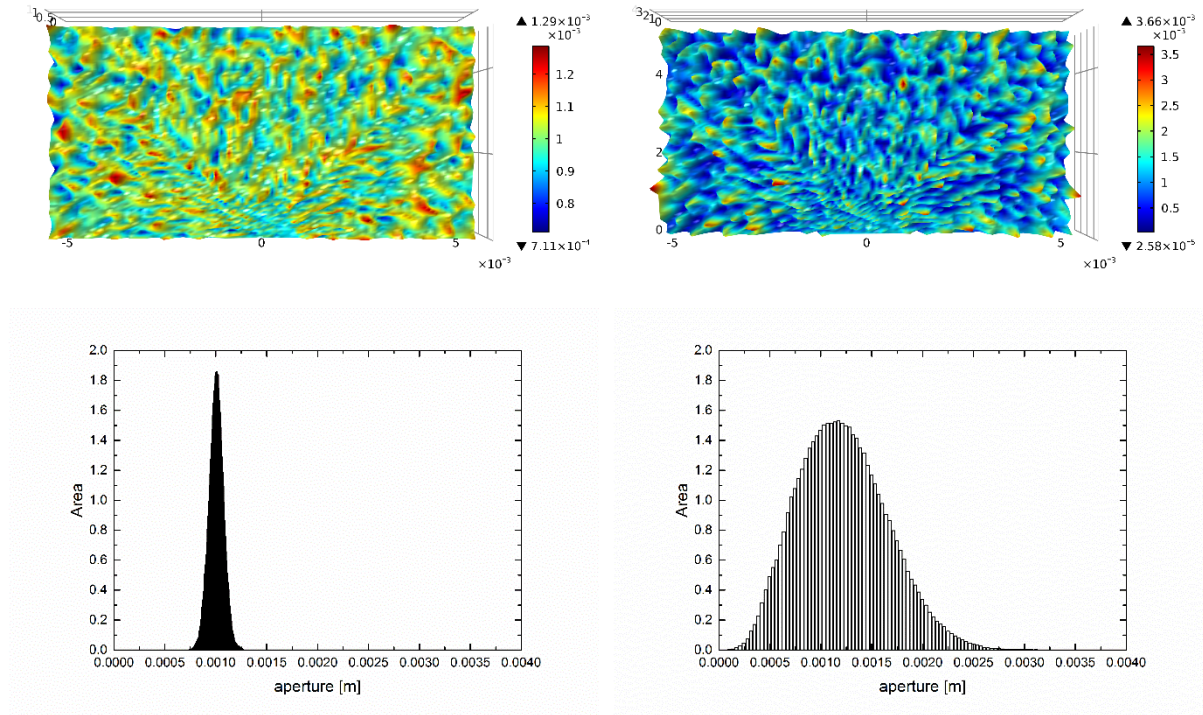
Figure 3-25: (top left and right) Example of two aperture distributions (STD 0.1 mm and 0.5 mm) with their corresponding histograms (bottom left and right).

Governing equations and model setup. Based on the aperture distributions hydraulic conductivity fields were calculated using the C*ubic Law (Witherspoon et al., 1980)* (Equation 36):

$$K = \frac{\rho g}{12\mu} a^2$$

Equation 36

Where K is the hydraulic conductivity [m/s], ρ is the density of water [kg/m³], g is the gravitational constant [m/s²], μ is the dynamic viscosity [Pa ·s] and a is the aperture [m]. The flow is solved subsequently by application of the Darcy equation within COMSOL (Equation 37):

$$\vec{u} = \frac{T \cdot \vec{\imath}}{\delta}$$

Equation 37

where u is the Darcy velocity [m/s], T is the transmissivity [m²/s], i is the hydraulic gradient over the domain [m/m] and δ is the aperture [m]. Since the transmissivity depends on the water viscosity which simultaneously depends on the bentonite volume fraction, it is corrected as function of the bentonite volume fraction and viscosity. With this step, the model flow field is coupled to the bentonite erosion. The equations governing the bentonite expansion and erosion implemented in the COMSOL model used in this study are not given here since they are untouched in the model used in this study. The reader is referred to the works of *(Liu et al., 2009a; Liu et al., 2009b; Moreno et al., 2011; Neretnieks et al., 2009)* for a thorough overview of the theoretical and scientific basis leading to the development of the bentonite expansion and erosion model. The bentonite erosion simulations conducted within this study were performed with the identical settings as in Moreno et al. except the use of the variable aperture

fields instead of the constant 1mm aperture. That is, the background sodium concentration in the seepage water is 10mM and the initial volume fraction at the bentonite source is 0.4.

Results

Hydraulic conductivity and velocity fields. Figure 3-26 presents the hydraulic conductivity fields and flow velocity distributions (flow field) for the 1×10^{-5} m/s mean velocity for all cases investigated (STD 0mm (top), 0.1 mm (middle top) and 0.3 mm (middle bottom) and 0.5 mm (bottom), i.e. constant aperture, 10%, 30% and 50% variation of the mean aperture, respectively.
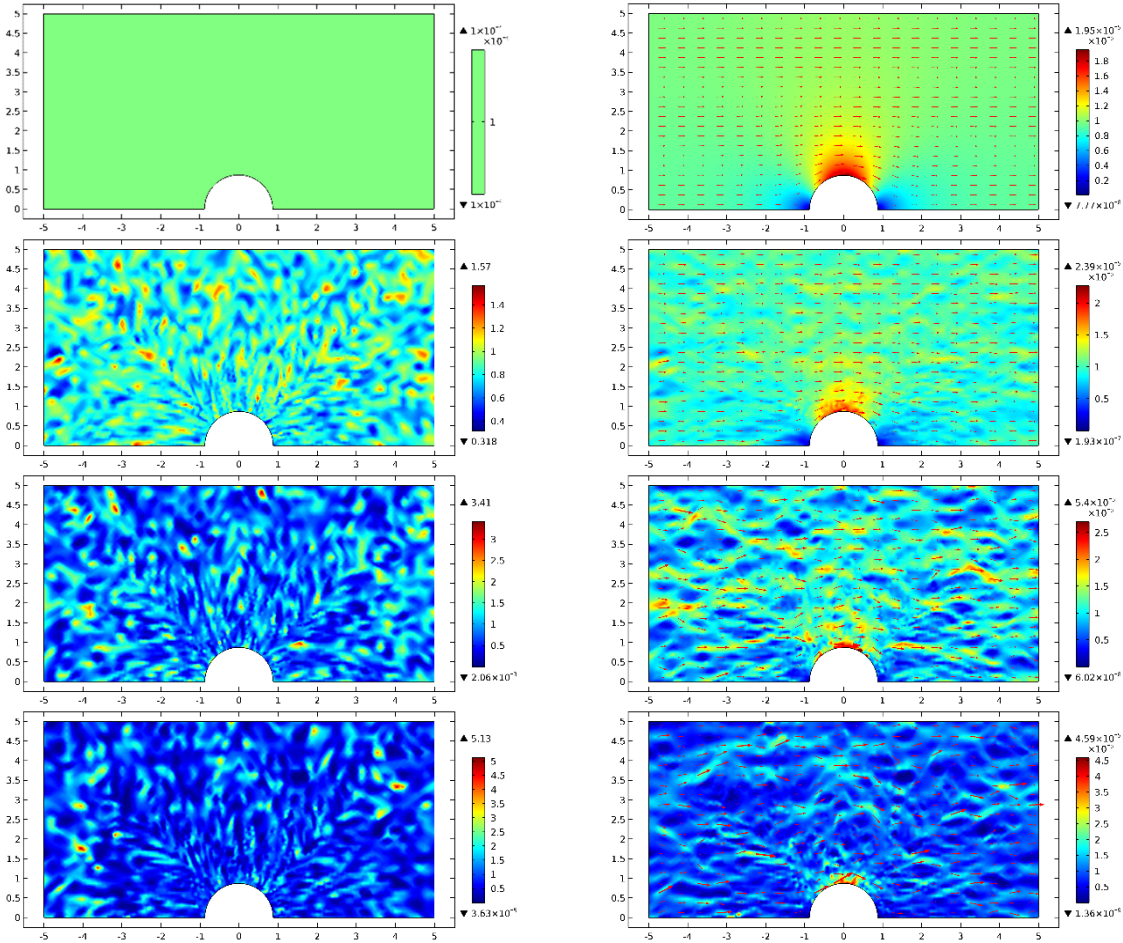
Figure 3-26: (left column) hydraulic conductivity fields [m/s] (right column) corresponding velocity fields (Darcy velocity magnitude [m/s]) for a mean velocity of 1×10^{-5} m/s . Note that the color bars are different for visualization purposes.

The flow field for the homogeneous case (Figure 3-26 (right top)) shows two stagnation points with minimum flow velocities in front and after the bentonite source. The highest flow velocities are found at the top of the bentonite source where the 2D model cross section is the narrowest. Further away from the bentonite source the flow velocities are quite homogeneously distributed. The maximum velocity is 1.95×10^{-5} m/s and the minimum velocity is 7.77×10^{-8} m/s, respectively. With increasing STD of the aperture distribution, both the fields for the hydraulic conductivity and the flow velocities become more heterogeneous. Consequently, the maximum

velocity increases with increasing STD from 2.06×10^{-5} m/s for STD 0.1mm to 4.59×10^{-5} m/s for STD 0.5 mm (always given the same mean velocity within the whole domain). The opposite trend is visible for the minimum velocity magnitude which decreases for increasing STDs from 1.71×10^{-7} m/s (STD 0.1mm) to 1.36×10^{-9} m/s (STD 0.5mm). To further visualize the heterogeneity, arrows for the flow velocities are shown in Figure 3-26. The arrow size is proportional to the flow velocity. For the homogeneous case, the flow arrows are mostly parallel to each other with the same size (= velocity). With increasing heterogeneity, both the size and direction of the arrows are changing significantly. In case of STD 0.5, the arrows highlight the heterogeneity and a flow channelling within the fracture as induced by the heterogeneous aperture distribution can be detected.
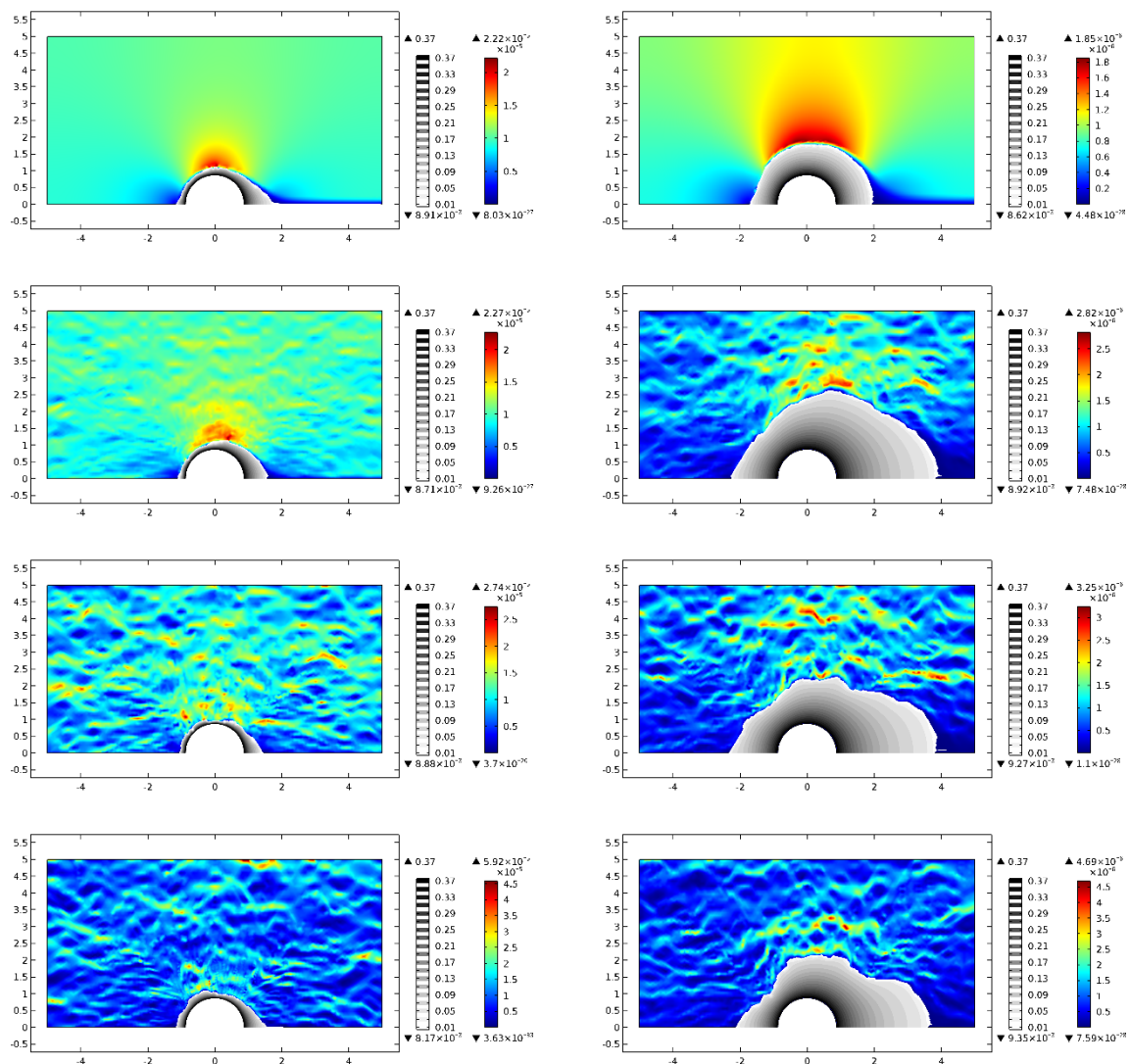
Figure 3-27: Bentonite erosion patterns (greyish areas) for STDs of 0mm (top), 0.1 mm (middle top), 0.3 mm (middle bottom) and 0.5 mm (bottom) for 1×10^{-5} m/s (left column) and 1×10^{-6} m/s (right column). The colors represent the same flow field distribution as in Figure 3-26 (right column).

Bentonite expansion and erosion rates. The flow field heterogeneity has a qualitative effect on the bentonite erosion behaviour as shown in in Figure 3-27. Here, plots for both 1×10^{-5} m/s

and 1x10^{-6} m/s mean velocity with STDs of 0mm, 0.1mm, 0.3mm and 0.5 mm are depicted. In these plots the bentonite volume fraction is shown (in greyish filled contour lines around the bentonite source) on top of the Darcy velocity fields. The results are presented for a simulation time of 10 a where the erosion and flow have reached an equilibrium state (that is, the erosion rate is also at equilibrium). Regarding 1x10^{-5} m/s mean velocity, only slight differences in the erosion patterns are observed. Generally speaking, there is only little bentonite swelling and extrusion into the fracture. The expansion is more pronounced on the lee side of the flow behind the bentonite source where a kind of flow shadow exists. In this area the lowest erosion of the flow occurs, allowing the maximum bentonite expansion. The opposite is true for areas with highest flow velocities e.g. at the top of the bentonite source. Here, the bentonite cannot swell and expand freely due to the shear forces of the flow acting on the bentonite carrying away the bentonite by advection. As mentioned and discussed by (Moreno et al., 2011), the bentonite volume fraction must be below ~0.001 to possess a viscosity low enough to be transported away by the flow. The effect of the fracture heterogeneity on the bentonite erosion behaviour is best observed in the case of 1x10^{-6} m/s mean velocity shown in Figure 3-27 (right column). Under these conditions the bentonite is able to swell and expand more into the fracture as it could for 1x10^{-5} m/s. For the homogeneous aperture field, the expansion is only slightly skewed to the lee side of the bentonite source. By increasing the flow heterogeneity, the expanded bentonite area is growing irregularly. This deformation can again be correlated to local flow gradients induced by the aperture distribution. By decreasing the mean flow velocity to 1x10^{-7} m/s the effect of the fracture heterogeneity is decreasing steadily. As shown in Figure 3-28 the bentonite expansion and erosion patterns for the homogeneous case (left column) and for STD 0.5 mm as the most heterogeneous case (right column) is very similar. In both cases the bentonite expands completely into the fracture urging the flow velocities to become very low due to the high viscosity of the bentonite. In consequence, the flow shear forces are not high enough to excerpt a pronounced effect on the bentonite swelling and expansion. For the heterogeneous case the expanded area is flattened slightly at the top where the highest flow velocities are located verifying small erosion heterogeneity effects. The results are shown for 1000 a simulation time and indicating no equilibrium state has been reached in terms of erosion rates. Longer simulation times and bigger spatial model dimensions need to be considered to resolve this issue.
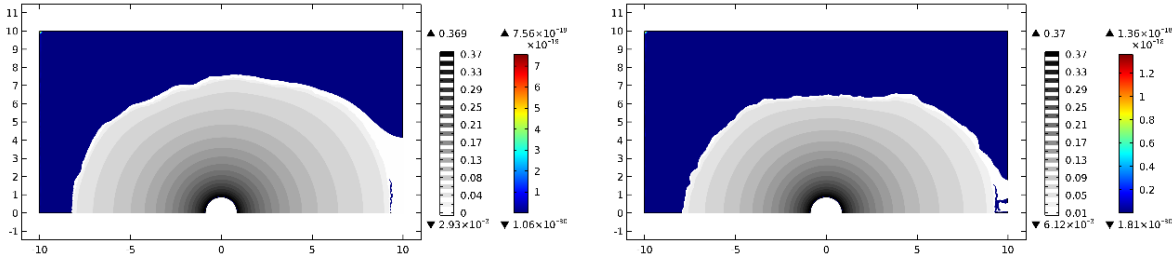
Figure 3-28: Bentonite erosion patterns (greyish areas) for STDs of 0mm (left) and 0.5 mm (right) for 1x10^{-7}m/s.

In conjunction to the qualitatively results presented so far, erosion rates have been calculated for all the different flow conditions and STDs mentioned above. The erosion rates are calculated as line integration of the smectite volume fraction at the bentonite source, corrected by

the smectite density and by a time factor in order to return the flux of bentonite (kg/a) over the outlet. The results are presented in Figure 3-29 a-d. The erosions rates are shown for STDs of 0mm (constant aperture), 0.1 mm, 0.3 mm and 0.5 mm and for mean velocities of $1x10^{-5}$ m/s, $1x10^{-6}$ m/s and $1x10^{-7}$ m/s.
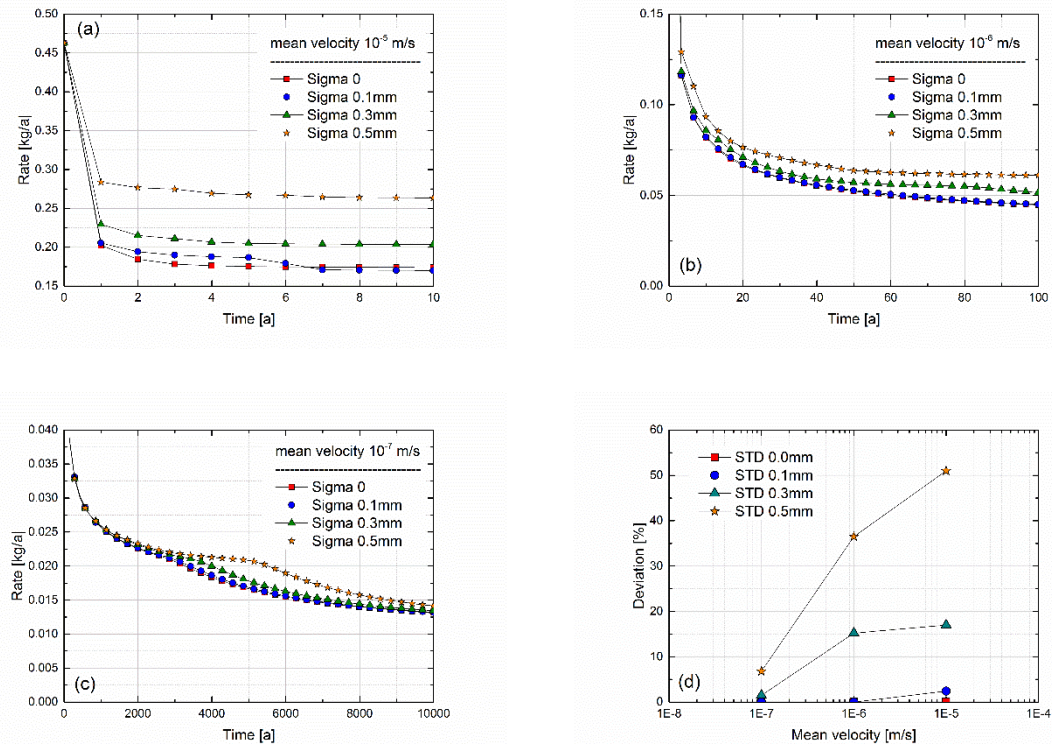
Figure 3-29: Calculated bentonite erosion rates for all three mean velocities studied. (Bottom right) Deviations in percentage of erosion rates from the homogeneous case (STD 0.0mm).

In case of $1x10^{-5}$ m/s mean velocity, an erosion rate of 0.174 kg/a is obtained at the equilibrium state reached after 10 a of simulation time for the homogeneous aperture field. No noticeable effect is visible for a STD of 0.1 mm compared to the homogeneous case. For a STD of 0.3 mm with an increase in the erosion rate to 0.204 kg/a (equivalent to 17 % increase in erosion rate) was obtained. For the highest STD examined (0.5 mm), the erosion rate is further increased to a value of 0.263 (equivalent to 51 % increase in erosion rate). With decreasing flow velocity, the difference in erosion rates is decreasing. For $1x10^{-6}$ m/s mean velocity, no difference is detectable for STD of 0.1 mm and the differences for STD of 0.3 mm and 0.5 mm decrease to 15 % and 36 %, respectively. Even lower differences to the homogeneous case are observed for the case of $1x10^{-7}$ m/s mean velocity. Here, the STDs 0.1 mm and 0.3 mm are very similar (max. 1.5 % for STD 0.3 mm) and the most heterogeneous case (STD 0.5 mm) yields an increase in erosion rate of only 6.8 %. It was therefore decided at the moment to skip the simulation of $1x10^{-8}$ m/s mean velocity since the difference will likely diminish completely.

Conclusions

The effect of flow field heterogeneity on the bentonite erosion has been studied by means of numerical simulations. For this, normal distributed aperture distributions with a mean aperture of 1mm have been generated for different standard deviations (STD 0.1 mm, 0.3 mm and 0.5 mm). So far, aperture correlation lengths of ~20 cm have been considered. Based on these aperture fields hydraulic conductivity fields were calculated applying the Cubic Law and in turn used in the Darcy equation to calculate the fracture flow fields. The flow is then coupled in the bentonite erosion model to the bentonite expansion and swelling processes rendering both physical processes to be transient. A range of mean fracture flow velocities was covered in the study (1×10^{-5} m/s, 1×10^{-6} m/s and 1×10^{-7} m/s, respectively). The results obtained so far clearly verify the importance of fracture heterogeneity on the bentonite erosion for mean velocities higher than ~1×10^{-7} m/s. Generally speaking, the heterogeneous aperture fields induced flow field gradients and features like flow channelling and therefore locally varying shear forces lead to irregular bentonite swelling and erosion patterns. With increasing flow velocity and standard deviation, the effect on the bentonite erosion increases causing higher bentonite erosion rates. A maximum deviation (that is, an increase) of erosion rates of up to 50 % has been observed compared to the homogeneous constant aperture results in case of the 1×10^{-5} m/s and STD of 0.5 mm representing the most extreme conditions investigated. For a mean flow velocity of 1×10^{-7} m/s the effect is mostly diminished with an increase in bentonite erosion rates of ~ 7 % only for a STD of 0.5 mm. Under these conditions, the shear forces are too weak to impact the bentonite swelling and expansion into the fracture and thus, only little effect of flow field heterogeneities are observed at all. Future work will focus on (i) the statistical nature of the aperture field and (ii) on an aperture correlation length in the scale of ~2 m (the scale of the bentonite source). Regarding the former, one needs to evaluate quantitatively the effect of several aperture distributions on the erosion rates having the same statistically parameters (mean aperture and STD). This will generate completely different flow fields within the model domain leading to different erosion patterns and ultimately to different erosion rates. This is also true when looking at different aperture correlation lengths (ii). Up to now, a correlation length of 20 cm was examined. By increasing the aperture correlation length to ~2 m one increases the scale of heterogeneous geometrical features from the meso-scale (~20 cm) to the macro-scale.

4   Conclusions and Outlook

Within the Kollorado-e project the state of the art with respect to colloid formation, migration and interaction with radionuclides has been improved. Important experimental activities have been performed in the laboratory and the field accompanied by process modelling, which have increased the process understanding and substantiated the basis for modelling calculations in performance assessment. Moreover, the application and further development of analytical methods (AMS and RIMS) enabled the radionuclide detection in a sub ppq concentration range. This allows for the first time the study of the long-term tailing of the breakthrough curves of the field dipole tests at Grimsel test site giving insight in timescales of several months of the interaction processes in the field.

The results of the project can be used in different ways in safety assessment and in a safety case: (i) as direct input parameters for the performance assessment codes, (ii) by improvement of the assessment basis due to increase of the process understanding, which is necessary for predictive calculations and up-scaling, and (iii) for demonstration issues as corrosion behaviour of a bentonite source and radionuclide mobility under near natural hydraulic conditions. The results of all three aspects are summarized in the following sections.

4.1   Understanding of colloidal/nanoparticle processes

A number of different issues concerning the colloid/nanoparticle formation and fate have been tackled within the KOLLORADO-1 and KOLLORADO-2 project and the investigation has been continued within the follow-on project KOLLORADO-e.

Radionuclide speciation and interaction with fracture filling material. For the interpretation of the long-term migration data of the trivalent and tetravalent actinides, namely ^{243}Am and ^{242}Pu the sorption/desorption process of radionuclides on the fracture filling material turned out to be of relevance. Model simulations show that the concentration plateaus observed in the long-term tailing of the breakthrough curves is particularly influenced by the distribution coefficient and the desorption kinetics on the fault gauge material in the fracture. From experiments in binary systems distribution coefficients for ^{99}Tc, ^{233}U, ^{237}Np, ^{242}Pu and ^{243}Am on fault gouge material under Grimsel groundwater conditions were determined, which could be directly used in the PA transport codes. It became also obvious that the distribution coefficients of the strong sorbing Am and Pu are covered with high uncertainties. In addition, sorption and desorption rates were derived. The study also revealed information about redox processes, which are relevant for ^{99}Tc, and ^{237}Np under the conditions at Grimsel site. ^{233}U seems to remain stable in the hexavalent state. With respect to a possible sorption competition effect no clear trends are visible for all radionuclides within the analytical uncertainty. It seems that there is an excess of sorption sites on the FG material for all radionuclides available.

Colloid - radionuclide interaction

In colloid size dependent radionuclide sorption studies RN uptake onto size separated mont-morillonite colloids Np(V), Tc(VII) and U(VI) were not found to adsorb under the respective experimental conditions, while Th(IV) and Pu(IV) strongly adsorbed onto montmorillonite. No significant changes in adsorption behaviour of Th and Pu onto different sized clay colloids, expressed as mass-normalized K_d values, were found. Between the clay dispersions with smallest and the largest mean sizes, an estimated difference by a factor of six in the amounts of edge sites was calculated. This was too small to be detected given the experimental uncer-tainties. Therefore, based on our experimental results for MX-80, it seems appropriate to im-plement an "average log K_d" for all colloidal sizes in reactive transport modelling codes. While a variation in the montmorillonite colloidal size does not seem to influence the adsorption be-haviour of strongly adsorbing radionuclides.

Colloid generation at the compacted bentonite fracture interface. The experimental pro-gram focused on a further increase of understanding of the erosion processes. The results of erosion experiments in a custom-made flow through cell showed that the hydration of the ben-tonite sample leads to a strong pressure increase within the compacted sample. This forces the movement of large amounts of mainly small clay particles into the aperture forming the gel layer. Due to the high swelling pressure also traces of other minerals like feldspars, micas or carbonates are carried along into the gel layer. To some extend these mineral grains have sizes of more than 100 µm. Furthermore, as could be expected the size of the aperture plays an important role in the formation and size of the gel layer around a compacted bentonite.

Bentonite erosion experiments, with raw or cation exchanged compacted and confined ben-tonite under dynamic conditions simulating the presence of a hydraulically active fracture showed erosion (clay colloid detachment) even for a Ca-MX80 bentonite, although to a much lower extent than for raw-MX80, Na-Ca-MX80 or Na-MX80 bentonite. The results confirm that, at fixed flow rate, the amount of exchangeable Na^+ and the presence of Ca^{2+} are the most important parameters with respect to clay colloidal particle detachment. The Ca-homoioniza-tion process was shown to drastically decrease the Cs retention capacity of the Ca-exchanged clay and that might have strong consequence on the sink properties of the backfill material.

Long-term bentonite erosion experiments in an artificial fracture showed that bentonite erosion of an untreated Febex sample using natural GGW can be divided into a washing phase of the sample that only lasts for the very first days and in which colloid concentrations are increased due to the removal of loosely bound particles followed by an up to 150 days lasting dissolution of accessory mineral phase. Thereby, bentonite erosion is limited due to increased ionic strength. Divalent ions like Ca^{2+} and Mg^{2+} in particular have an impact on the colloid stability. Once the accessory minerals are fully depleted and the elemental concentrations level off to-wards the background values, colloid stability increases and higher colloid concentrations are detected. An additional cationic exchange of sodium and small amounts of the interlayer mag-nesium by Ca takes place during the whole experiment. It is remarkable that the exchange of sodium is faster compared to magnesium as the binding strength increases with the valence. Furthermore, it has been shown that bentonite erosion scatters quite varying in the size of one

order of magnitude concerning colloid concentrations. Erosion rates were calculated from the mean colloid concentration normalized to the contact area between the swelling zone and the surrounding groundwater.

Colloid – mineral surface interactions and colloid mobility. Results of the Kollorado-2 project emphasized the importance of surface heterogeneity and its role to retain colloidal particles onto surfaces even under unfavourable conditions (surfaces with same charge). Therefore, in the Kollorado-e project colloid size dependent transport and deposition on rough granodiorite surfaces and more smooth acrylic glass was investigated both experimentally and numerically. The microscopic investigations performed with 1000 nm and 25 nm colloids (monodisperse fluorescent carboxylated polystyrene spheres) show a positive correlation between residence time and colloid retention on both collector surfaces. Due to the geometry of the fracture set-up it was possible to see a dependence of fracture orientation, more precisely the effect of gravity over Brownian motion on the retention of the large 1000 nm size colloids. This was not found for the small-size 25 nm colloids, where the deposition is controlled by Brownian motion. On the other hand, it was found that the colloid retention of the 25 nm colloids is much stronger influenced by the collector surface material with a higher retention on granodiorite. Compared to 1000 nm colloids, 25 nm colloids are exposed to a higher surface roughness on granodiorite, whereas the "felt" roughness for the smoother acrylic glass is comparable. These findings led to the conclusion that 1000 nm colloids undergo sedimentation due to a higher influence of gravity over Brownian motion. 25 nm colloids are retained by surface roughness due to their small colloid size and higher diffusivity into cracks and scratches of the material. This study gives mechanistic details on the retention processes expected in fractures under unfavourable conditions as a function of the fracture orientation and shows the size dependent retention. Although obtained in simplified geometries and under low ionic strength groundwater conditions the investigations show the significant effect of fracture orientation on colloid deposition.

4.2 Improvement and optimization of in-situ experiments

The long-term stable very low hydraulic gradients enabled the observation of tidal fluctuations, for the first time in deep crystalline environments as studied here in the underground research facility of the Grimsel Test Site (GTS). Due to the construction of the megapacker system and the unique opportunity to control the hydraulics of shear zone by the outflow of the Pinkel surface packer low gradients are established with very stable head differences/gradients < 10mm, which gives the unique opportunity to study flow and transport at near natural or repository relevant conditions in a natural shear zone.

The proof of the long-term stable hydraulic conditions in the shear zone and particularly in the CFM dipole was the basis for installation of the long-term in-situ experiment (LIT), which was started in 2014. After successful mock-up tests the radionuclide source a radionuclide-labelled bentonite plug was emplaced in the shear zone in the well-established borehole CFM 06.002-i2. This experiment is still running and geochemical parameters are continuously followed by in-situ analyses and sampling from an observation borehole in the direct vicinity of the source.

This experiment will be investigated in detail in the follow-on project Kollorado-e[2] and documented there.

So far, the actinide measurements of the breakthrough curves by high resolution (HR) ICP-MS could detect the actinides in the tailing down to ~0.01 ppt level. During this project phase major improvement of the analytical techniques allowed analyses of radionuclide concentrations in the sub ppq range. This became possible by using resonance ionization mass spectrometry (RIMS) and accelerator mass spectrometry (AMS). Therefore, the long-term tailing of the breakthrough curves, where concentrations decreased by orders of magnitude, could be analysed and, accompanied by transport modelling, gave insight into long-term acting processes.

Up to now altogether five dipole field experiments, where the bentonite colloid facilitated transport of homologues and radionuclides was investigated, have been performed within the CFM project. The general findings have already been reported in the final report of the Kollorado-2 project and are confirmed with the additional field experiment. The simulation and interpretation of all these experiments clearly show the decrease of desorption rates of the tri- and tetravalent homologues/actinides from the bentonite colloids with increasing travel time, indicating a two site desorption process with a fast and slow kinetic, respectively.

4.3 Impact on long-term safety assessment

U. Noseck

4.3.1 Conceptual model

In order to estimate the impact of colloid-facilitated transport for the long-term safety of a repository under more realistic conditions, calculations with the code COFRAME have been carried out for the conditions of the Finnish repository site considered in *(POSIVA, 2012)*. Therefore, a conceptual model based on the information from *(POSIVA, 2012)* was developed and data for colloid-facilitated radionuclide transport are derived from the current results from CFM dipole tests and accompanying modelling approaches. In the following, firstly a brief introduction to the most relevant features of the Finnish scenario addressing bentonite erosion and formation of colloids during glacial cycles including radionuclide release is given. All assumptions and parameters used in our calculations are compiled. Afterwards simulation results are presented. Within the POSIVA safety case 2012 *(POSIVA, 2012)* in Variant Scenario 2 (VS2) chemical erosion of the buffer and backfill is assumed to take place due to low ionic strength water penetrating to repository depth, e.g. in association with glacial retreat. POSIVA considered four calculation cases for this scenario: VS2-H1, VS2-H2, VS2-H3 and VS2-H4, one for each of the four canisters that are calculated to fail within the million-year assessment time frame in the erosion/corrosion case. Here only calculation case VS2-H1 is considered, which causes the highest consequences within the time frame of one million years. For Variant Scenario 2, after an initial temperate 50´000 a period, the pattern of flow and composition variations in the following 120´000 a period is assumed to be repeated throughout the one-million-year assessment time frame. Depending on the climate state the water type and the groundwater velocity (described by a velocity factor) in the granite is assumed to change. This is briefly summarized in Table 4-1.

Table 4-1: Temporal change of water type and velocity factor for Variant VS2 *(POSIVA, 2012)*.

Time window in years (starting from present)	Water type	Velocity factor, f_v	Comments
0 to 50 000	Brackish	1	Initial temperate Period
50 000 to 105 000	Brackish	1	120 000 year cycle, subsequently repeated up to one million years
105 000 to 105 333	Glacial	10	
105 333 to 120 000	Brackish	1	
120 000 to 120 333	Glacial	10	
120 333 to 155 000	Brackish	1	
155 000 to 155 333	Glacial	10	
155 333 to 170 000	Brackish	1	

Radionuclide release from the bentonite

The main features of the radionuclide release, retention and transport model used to analyse the calculation cases are described in *(POSIVA, 2012)*.

For the calculations performed here the radionuclide fluxes [Bq/y] from the near field (bentonite barrier) into the far field – as calculated for scenario VS2 H1 *(POSIVA, 2012)* – are directly used as source term, see Figure 4-1 for selected radionuclides. The distinct peaks in the release rates are caused by increased radionuclide releases during inflow of low mineralised glacial water into the repository. The container failure occurs 575´000 a after repository closure, which is reflected by the first appearance of radionuclide releases after that time.

Colloidal facilitated transport in the geosphere

Because advective conditions are assumed to exist between the failed canister and the fracture, the so-called F-path as described in *(POSIVA, 2012)* is the dominant transport path and is the only path considered in the calculations.

In the calculations for the POSIVA safety case calculated releases are directly transferred from the near-field code to the far-field code. A very important parameter is the so called transport resistance *WL/Q*. It´s value for the F-path (f_v = 1) in the VS2 H1 scenario is given as (Equation 38):

$$WL/Q = 1.2 \cdot 10^5 \text{ [a/m]}, \qquad \textbf{Equation 38}$$

with the width *W* of the transport path along which advection occurs, the length *L* of the transport pathway and volume flow through the path *Q*.

For each deposition hole, a particle tracking approach was performed by POSIVA to identify areas of release to near-surface water *(POSIVA, 2012)*. Thus a number of different transport pathways exist and an individual transport length is not given. For our model a transport length is set to 3570 m.
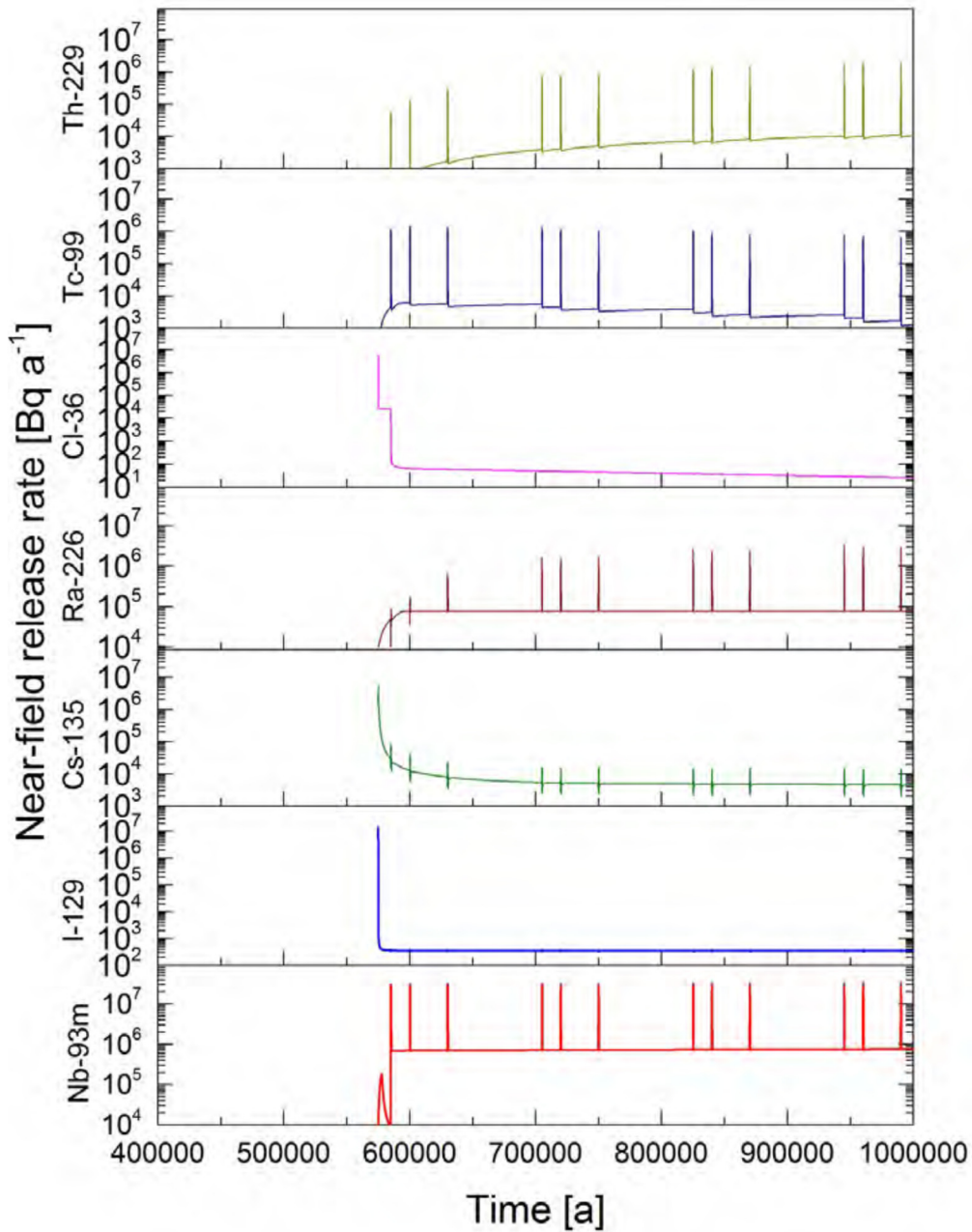
Figure 4-1: Evolution of radionuclide release rates from the repository near field to the geosphere, considering the main contributing radionuclides in case VS2-H1 *(POSIVA, 2012)*.

For the far-field calculations here the value 0.169 m³/y is applied. For the width of the transport path *W* a value of 5 m is used. For the aperture of the fracture *2b* a value of $1.47 \cdot 10^{-3}$ m is given in *(POSIVA, 2012)* and applied here. With these parameters the value for the flow resistance of $1.2 \cdot 10^5$ a/m (see above) is sufficiently well met. The transport parameters are summarized in Table 4-2.

Table 4-2: Transport parameters.

Parameter	Unit	Value
Transport pathway length	m	3570
Fracture aperture	m	1.47×10^{-3}
Width of transport path	m	5
Volume flow	m^3/a	0.169
Transport resistance	a/m	1.1×10^5
Pore velocity	m/a	23
Travel time	a	155

In each case, transport is modelled through a representative flow channel, with up to three consecutive layers of diffusion-accessible rock adjacent to each of the channel walls. For our calculations the geometry of the so-called *other fractures transport class* is applied, shown in Figure 4-2. A planar fracture is assumed. The thickness of the unaltered host rock adjacent to the fracture is 3 m in each direction. This value is used as parameter for the penetration depth.
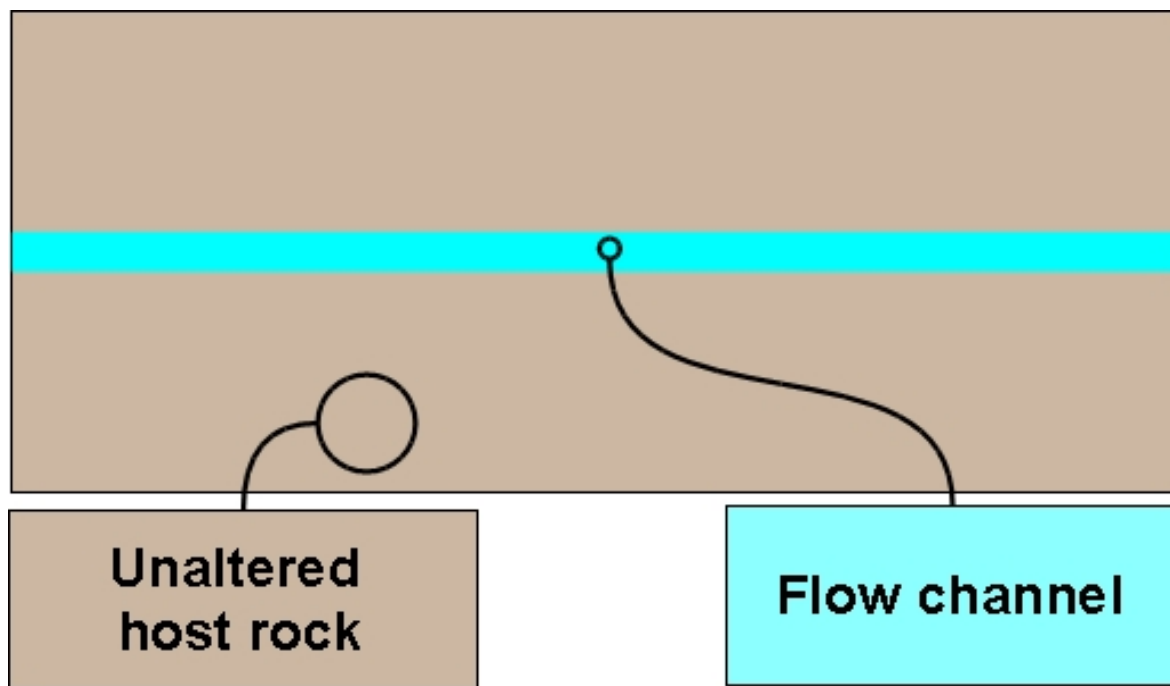
Figure 4-2: Geometry of the fracture and unaltered host rock (Other fractures transport class in *(POSIVA, 2012)*).

According to the applied model the pore velocity u in the fracture is calculated to (Equation 39):

$$u = \frac{q}{2bgn_f} = \frac{Q}{2bgn_f A} \quad . \qquad \textbf{Equation 39}$$

with the flow porosity in the fracture n_f and the length per unit area g, which is the trace length of open fractures per unit area in a plane normal to the flow direction. The aperture $2b$ is given above and the cross section A is the product of W and the penetration depths. In this case the

total trace length is 0.167 m/m^2 and the flow porosity is 1 for an open fracture. This results in a pore velocity u = 23 m/a, i.e. a transport time of 155 years. In *(POSIVA, 2012)* a time-dependent velocity factor, f_v, is used to scale the steady-state groundwater flow rates to account for the periodically increased flow rates. At the same time chemistry-related retention and transport parameters are assumed to switch periodically between those for brackish water and those for glacial water. However, in this modelling approach the increased flow is considered (in the discrete colloid source case) but constant conditions are assumed for the chemistry-related retention parameters.

Interaction RN – colloids –rock matrix

As oxidation state for the actinides it is assumed that Am and Cm occur as trivalent cations and Np, Pu, Tc, Th, U and Zr as tetravalent radionuclides. This agrees with the conditions applied for the reference case brackish water *(POSIVA, 2012)*. For the bentonite source two cases are distinguished: In a first set of calculations a continuous bentonite source is assumed. The bentonite erosion rate is set to 0.0395 kg/a resulting in an initial colloid concentration at the inflow of 0.234 kg/m^3, which is the same concentration as in the case with a discrete colloid source. This case is not realistic but applied for system understanding. In a second set of calculations a discrete colloid source, which is active only in the time period of glacial retreat, where glacial water might enter the repository depth (cf. Table 4-1 water type glacial). During this time frame a water flow increased by a factor of 10 at time periods of glacial retreat is assumed. For this case the colloid source is set to an erosion rate of 0.395 kg/a resulting in the same initial inflow concentration of colloids of 0.234 kg/m^3. The respective loss of bentonite from the deposition hole is listed in Table 4-3. It shows that the calculation with continuous bentonite release is not a realistic case, since the released mass of bentonite exceeds the available mass.

Table 4-3: Bentonite loss for the different calculation cases. Percentage of bentonite loss is related to an initial bentonite mass of 23 800 kilogrammes per borehole *(POSIVA, 2012)*

	Continuous release	Discrete release, increased flow
Release rate [kg/a]	0.0395	0.395
Bentonite loss1 [kg]	39500	3157
Bentonite loss1 [%]	>100 %	13 %

[1] after 1 Mio years

All other transport parameters are summarised in Table 4-4 These data refer to the so called transport class "other fractures" defined in *(POSIVA, 2012)*.

Table 4-4: Transport-relevant parameters for granite matrix (other fractures).

Parameter	Unit	Values for "Unaltered rock"
Layer thickness	m	3
Grain density	kg/m^3	2700
Porosity	-	5×10^{-3}
Effective diffusion coefficient	m^2/s	6×10^{-14}

The sorption processes for contaminants dissolved in fracture water with colloids (both mobile and filtered) are treated as reversible linear kinetic reactions, according to the following equations, cf. Section 3.1 (Equation 40 and Equation 41)

$$Q_{frm} = k_{frm}\left[C_c \cdot K_{frm}C_{fr} - C_{cr}\right]$$ **Equation 40**

$$Q_{fri} = k_{fri}\left[S_c \cdot K_{fri}C_{fr} - S_{cr}\right]$$ **Equation 41**

The sorption/desorption rates for the trivalent and tetravalent cations are derived from the CFM dipole tests CFM-RUN 10-01, CFM-RUN 10-02, CFM-RUN 10-03, CFM-RUN 12-02 and CFM-RUN 13-05, which cover peak arrival times of 10 to about 90 hours. The results from simulations of the breakthrough curves with the three transport codes RELAP (LANL), r^{3}t and COFRAME (both GRS) are shown in Figure 4-3 for the tetravalent homologues/actinides. A detailed description of these modelling studies can be found in *(Noseck et al., 2016)*. In general, a decrease of desorption rates with increasing transport time is observed. The lowest values derived from the simulations derived with the GRS model 0.0017 h^{-1} agree well with the lowest value derived from independent batch experiments of 0.0014 h^{-1} *(Huber et al., 2011)*. The former value corresponds to a rate of 15 a^{-1}, which was chosen here as a reference value for modelling the tetravalent actinides. In all experiments for the trivalent actinides a higher rate (elevated by a factor between 1.5 and 10) was observed. In order to keep the system simple a rate increased by a factor of 5 compared to the tetravalent actinides is applied, namely a reference rate of 75 a^{-1}. These data are based on the time scales of the experiments. However, a decreasing desorption rate with increasing travel time is observed and particularly for the tetravalent actinides it is not clear, whether the process is fully reversible in the long-term. To account for this uncertainty, beside the reference radionuclide sorption/desorption rates derived from the field tests values of two orders and four orders of magnitude lower have been applied, respectively.
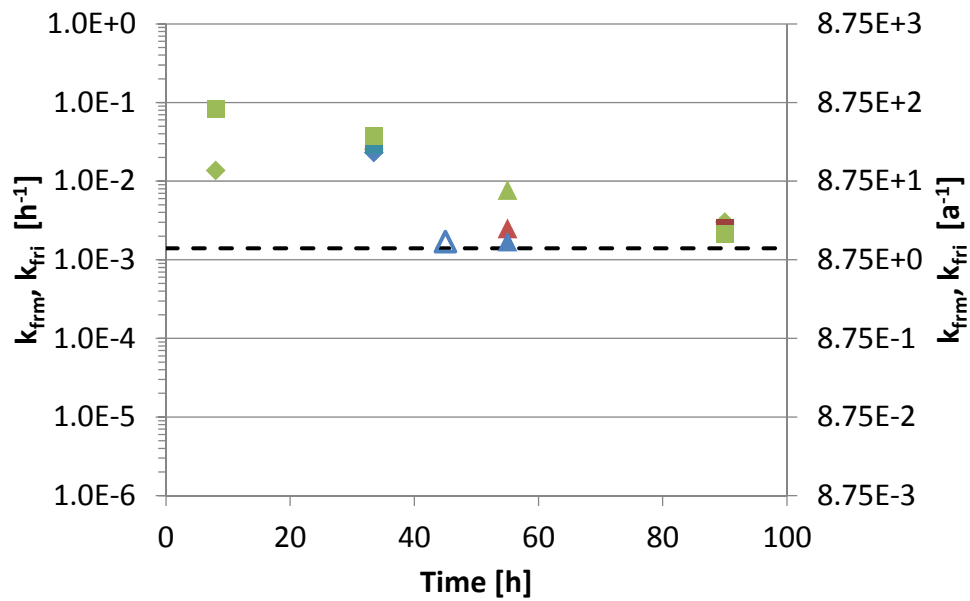
Figure 4-3: Desorption rates of tetravalent homologues/actinides from bentonite colloids derived from field experiments in dependence of fluid transport time (square =Th, rhomb = Hf, triangular = Pu; results from calculations with transport codes RELAP (green), COFRAME (blue) and r3t (red)).
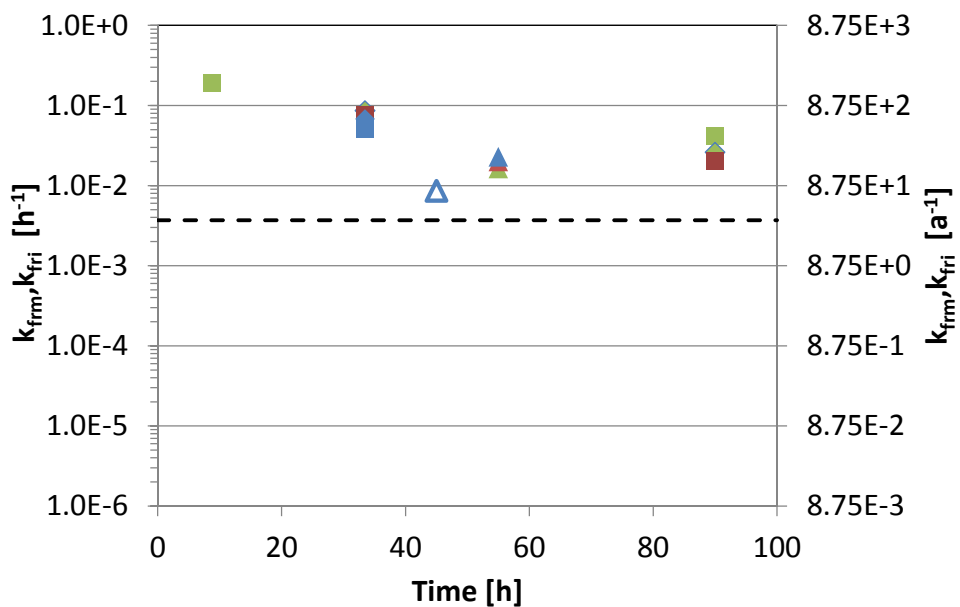
Figure 4-4: Desorption rates of triavalent homologues/actinides from bentonite colloids derived from field experiments in dependence of fluid transport time (square =Th, rhomb = Hf, triangular = Pu; results from calculations with transport codes RELAP (green), COFRAME (blue) and r3t (red)).

The major fraction of the radionuclides ($\geq$ 98 %) is initially – before release from the bentonite buffer – bound to the bentonite colloids. Such values have been observed in injection solutions equilibrated with Grimsel groundwater, colloids and homologues/radionuclides. For solutions with a bentonite colloid concentration of 256 mg/l a distribution coefficient of 1500 m³/kg was calculated for sorption of Am on bentonite colloids using the following equation (Equation 42)

$$K_{frm} = \frac{C_{cr}}{C_c C_{fr}}$$

Equation 42

Distribution coefficients for the radionuclides on the granite matrix are listed in Table 4-5 distribution coefficients as well as sorption/desorption rates for the interaction of radionuclides with colloids are listed in Table 4-6. Sorption of radionuclides to the granite is assumed to occur very fast, i.e. a rate of 1000 a⁻¹ is applied.

Table 4-5: Element distribution coefficients in granite matrix.

Element	Distribution coefficient [m³/kg]	Element	Distribution coefficient [m³/kg]
Am	1.5×10^{-1}	Pd	5.5×10^{-3}
C	0	Pu	1.5×10^{-1}
Cl	0	Ra	3.0×10^{-3}
Cm	1.5×10^{-1}	Sm	1.5×10^{-1}
Cs	5.4×10^{-2}	Tc	4.0×10^{-1}
I	0	Th	4.0×10^{-1}
Ni	5.5×10^{-3}	U	1.6×10^{-2}
Np	4.0×10^{-1}	Zr	4.0×10^{-1}
Pa	2.2×10^{-2}		

Table 4-6: Radionuclide – colloid interaction data.

Oxidation state	K_{fri} , K_{frm} [m³/kg]	contaminant-colloid interaction rates k_{fri}, k_{frm} [a⁻¹]		
		high	medium	low
trivalent	1500	75	0.75	0.0075
tetravalent	1600	15	0.15	0.0015

For the interaction of colloids with the granite parameter variations have been performed. This interaction process is described by the filtration coefficient and the remobilisation coefficient. In these first calculations no remobilisation is considered. From the tests CFM-RUN 10-01, CFM-RUN 10-02, CFM-RUN 10-03 and CFM-RUN 12-02 a typical value for the filtration rate of 0.01 h⁻¹ was derived. This corresponds to a filtration coefficient of 4.38 m⁻¹ for the conditions considered here. Since the filtration rate and the interaction rates of radionuclides with colloids are of highest relevance for the radionuclide transport, both are varied in the calculations. Figure 4-5 illustrates the ranges of experimentally derived colloid filtration and radionuclide desorption rates and the ranges applied in the parameter variations for the Finnish long-term safety assessment. It shows that the experimentally derived values correspond to the upper values of the applied in the parameter variation calculations.
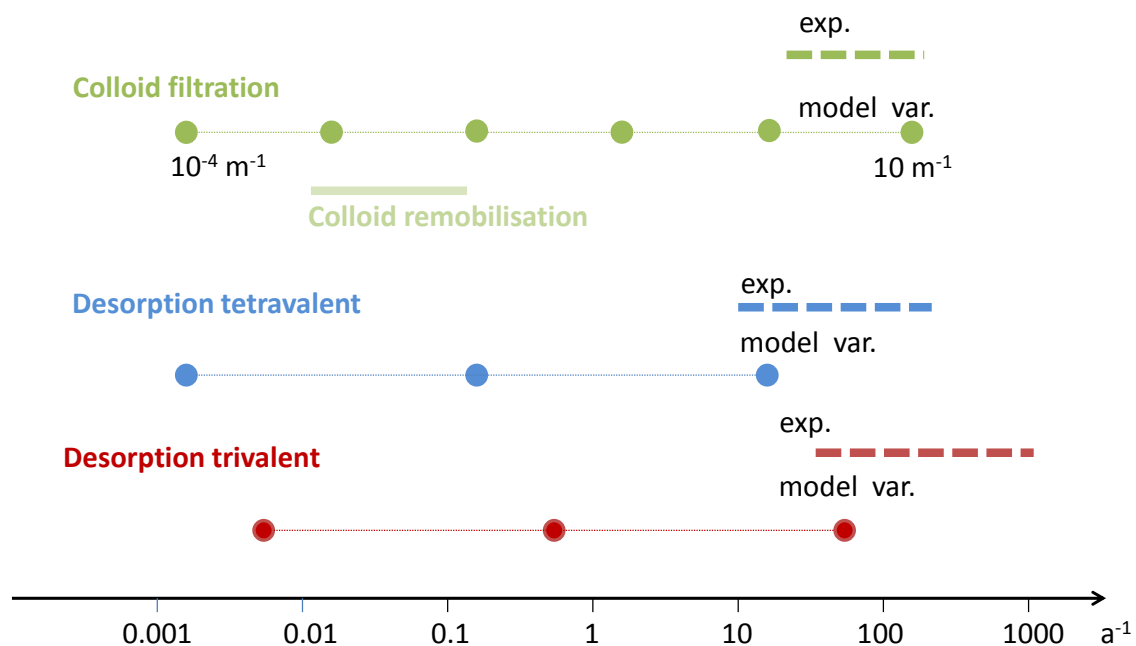
Figure 4-5: Illustration of ranges for the interaction rates observed in the experiment (dotted lines) and applied in the calculations for long-term safety assessment (lines and dots).

4.3.2 Calculation results

The concentration for selected radionuclides directly at the inflow into the granitic fracture system is shown in Figure 4-6. As visible from the graph the near-field calculations for the Posiva safety case have been performed for a time frame of 1.2 Mio years. As a reference for the calculation with colloids Figure 4-7 shows the concentration of these radionuclides after transport through the granite, without considering colloids, i.e. the colloid concentration was set to zero. For better illustration all far-field calculations with COFRAME have been performed over a time frame of 2 Mio years. The fact that there are no periods of glaciation (and associated spikes) after 1 M years simply reflects that the near-field release calculation results were obtained courtesy of Posiva, and Posiva's safety case focussed on a 1 Mio year time frame. The concentration curves appear after 575 000, the time point, when the container failed. For the calculations here only transport along the fractures is regarded, no further dilution in the granite or an upper aquifer is assumed. With these assumptions the granitic system seems to be only a weak barrier for the radionuclides. A comparison of both figures shows that the radionuclide concentrations are typically decreased by only one to two orders of magnitude for most of the radionuclides due to matrix diffusion and sorption on the fracture surface. And there is no significant delay of the curves, since the fluid transport is relatively fast with travel times of 155 years.
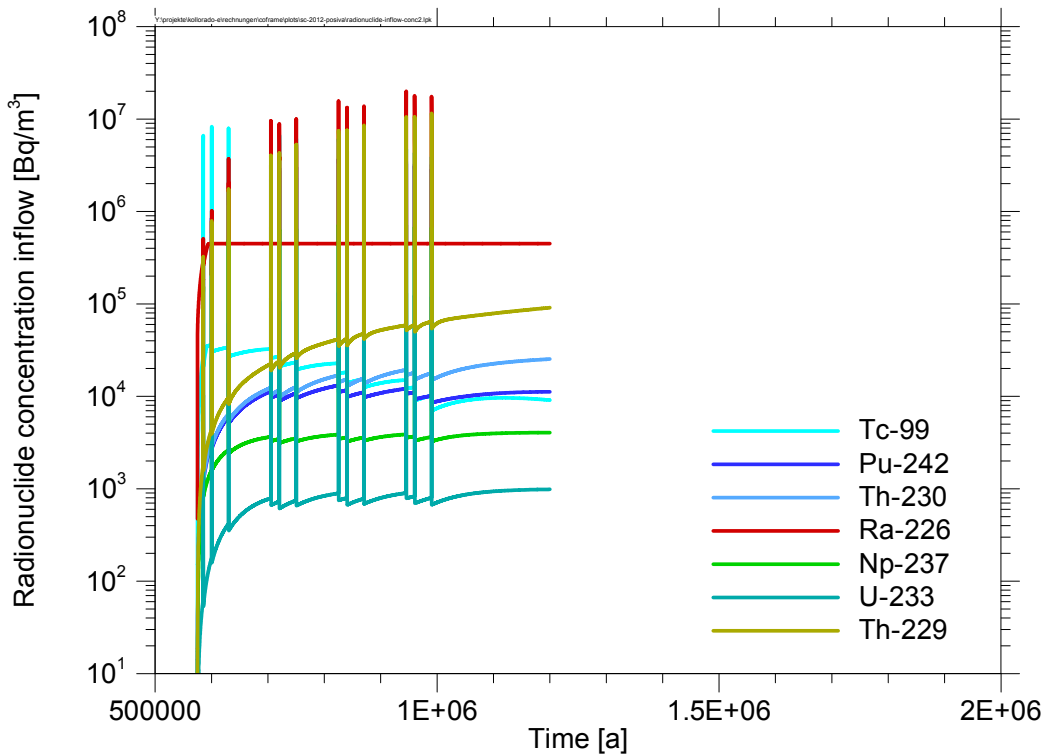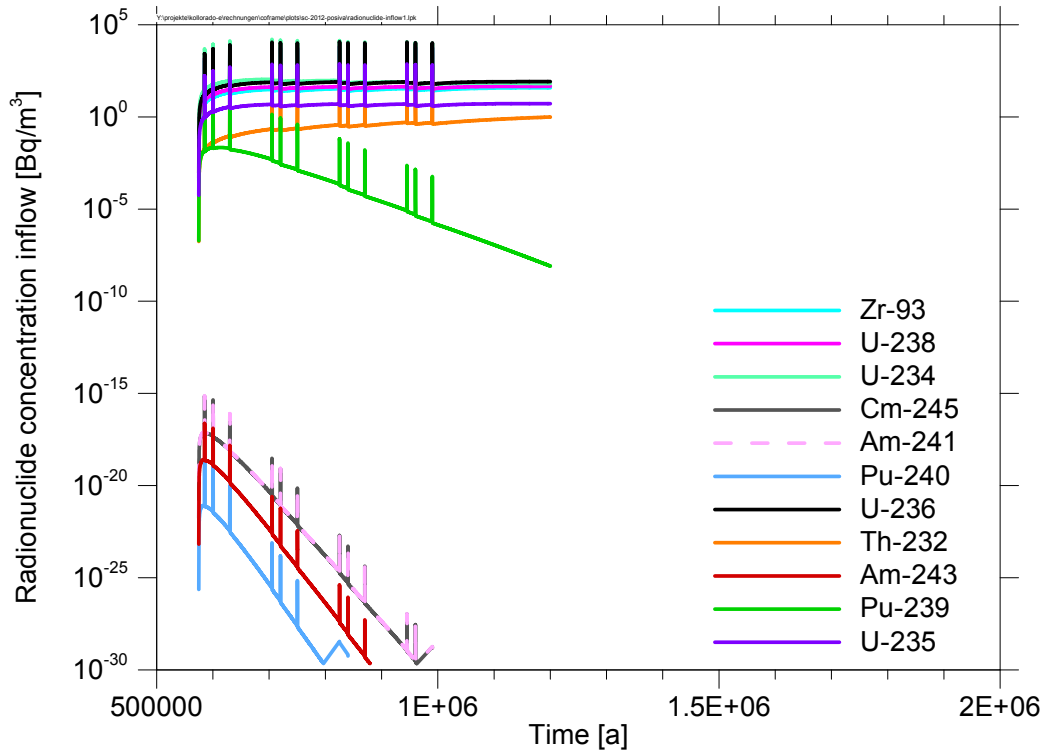
Figure 4-6: Radionuclide concentrations at the interface between bentonite and granite fractures.
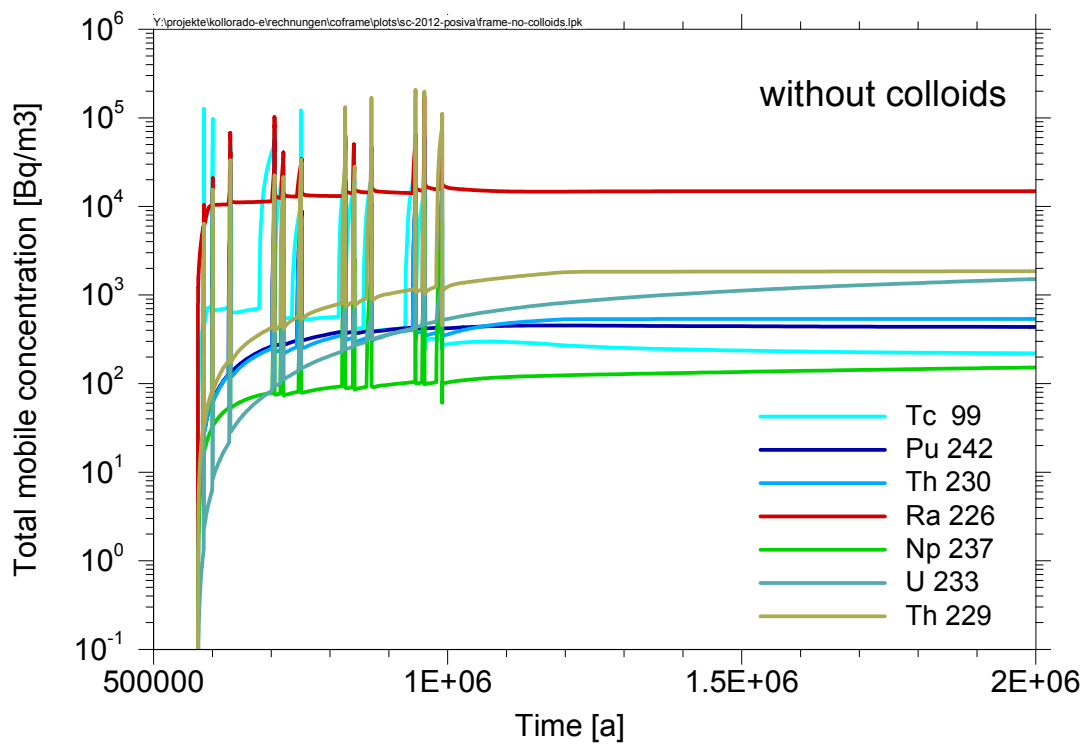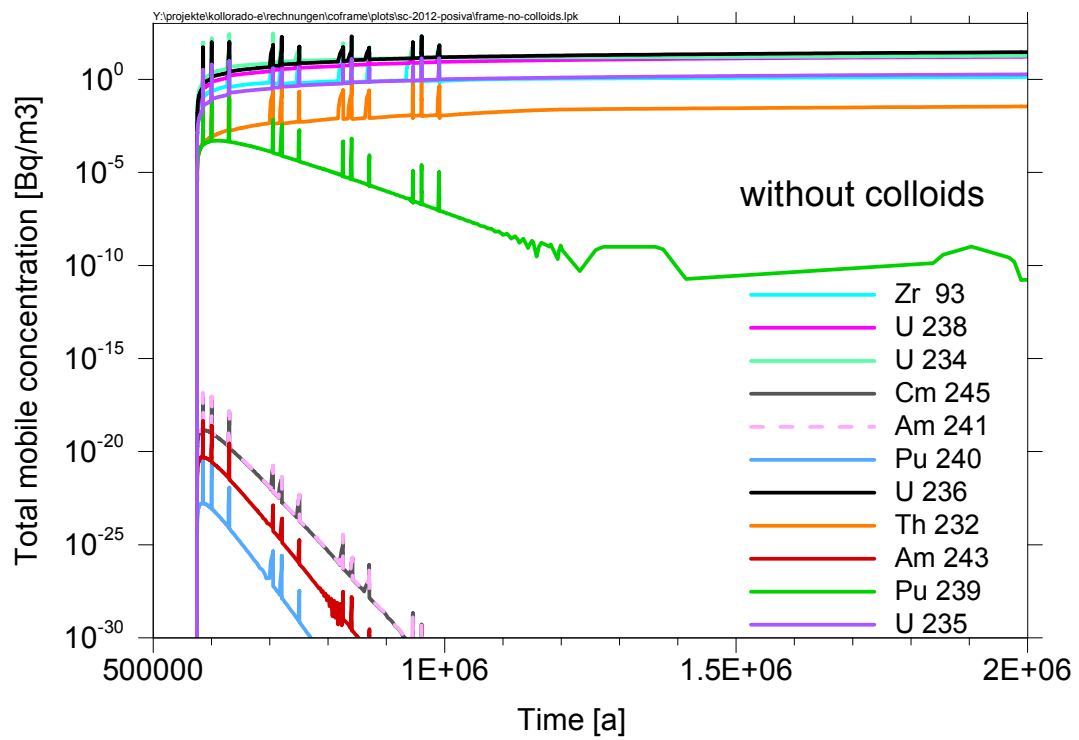
Figure 4-7: Concentrations of selected radionuclides at the end of the transport pathway calculated with COFRAME considering no impact of colloids (logarithmic scale).

Figure 4-8 is a presentation on the linear scale for the most relevant radionuclides with respect to their concentrations. The evaluation of all calculation results is restricted to these radionuclides to not overload the information in this section. In comparison Figure 4-9 shows the results of a calculation without radionuclide sorption in the rock matrix. In this case the radionuclide concentrations of the considered radionuclides are about one order of magnitude higher.
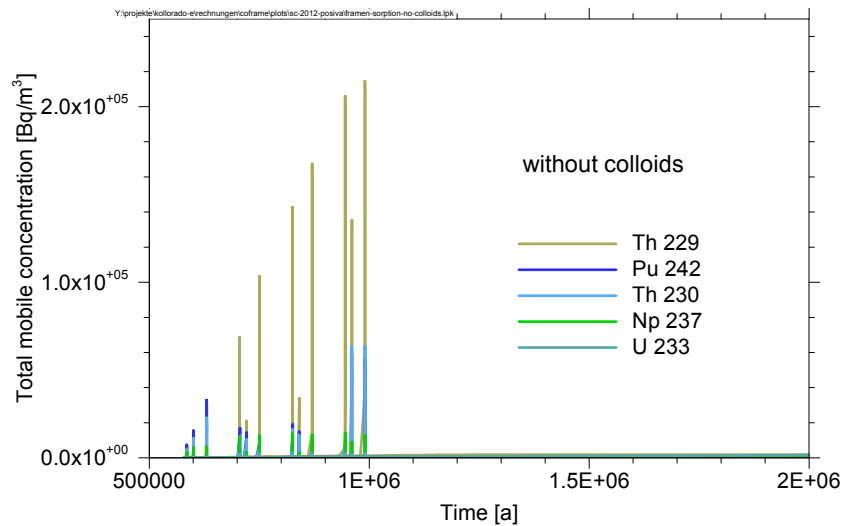
Figure 4-8: Concentrations of selected radionuclides (with highest concentration) at the end of the transport pathway calculated with COFRAME considering no impact of colloids (linear scale).
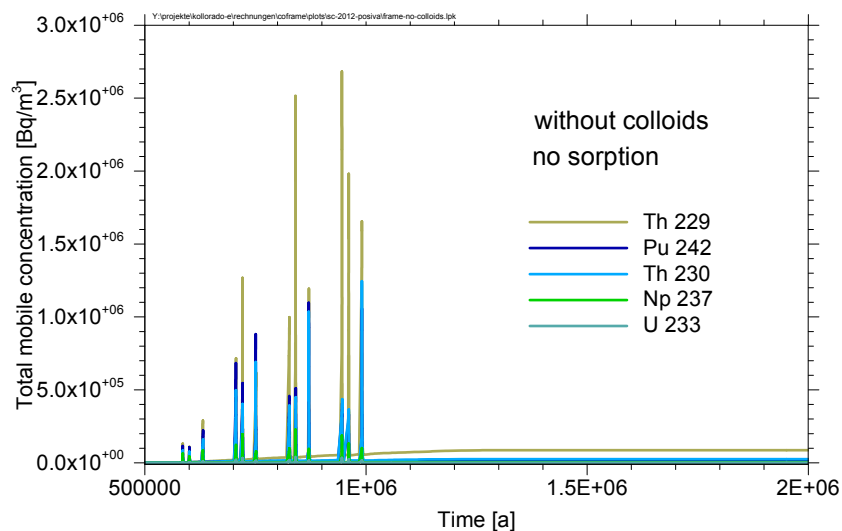
Figure 4-9: Concentrations of selected radionuclides (with highest concentration) at the end of the transport pathway calculated with COFRAME considering no impact of colloids and no sorption in the rock matrix (linear scale).

205

Results for constant colloid source and constant flow conditions

In this section results for a constant colloid source are presented. Figure 4-10 shows the normalised concentration of mobile colloids along the transport pathway for different filtration coefficients. The remobilisation coefficient is set to 0, which corresponds to an irreversible filtration of colloids. The figure shows that in case of a filtration coefficient of 10^{-4} m^{-1} nearly all colloids arrive at the end of the pathway, i.e. nearly no filtration occurs. With increasing filtration rate an increased amount of colloids is filtered and for a rate of 10^{-1} m^{-1}, which is still one order of magnitude lower than the lowest coefficient observed in the CFM field tests, the colloids are effectively filtered and the colloid concentration is decreased to zero after 100 m of the transport pathway.
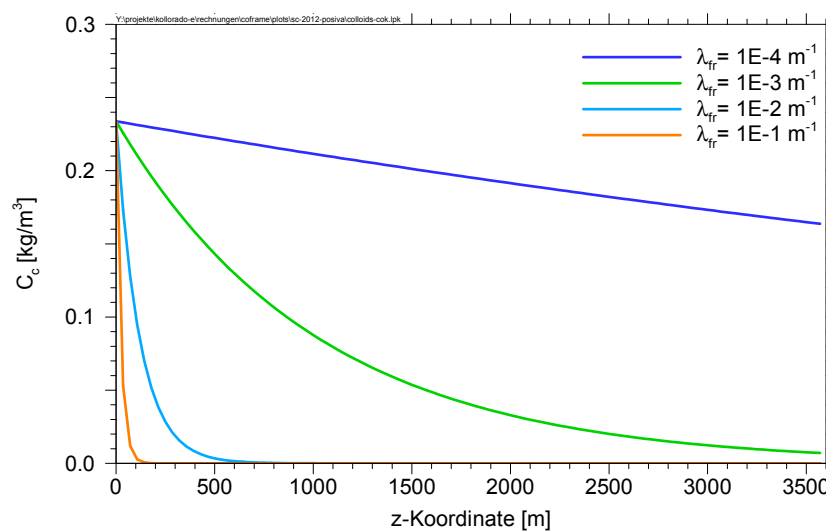
Figure 4-10: Normalised distribution of colloid concentration along the transport pathway at 1 Million years for different filtration coefficients.

Calculation case: high desorption rates k_{fri}, k_{frm}

In Figure 4-11 the breakthrough curves of selected actinides are shown with colloids present, but assuming a low filtration rate of 10^{-5} per meter. The curve reflects for all actinides the peaks of four glacial cycles, each with three phases of glacial water inflow (cf. Figure 4-1). However, compared to the release curves from the near field the curves are broader and shifted to longer times. Firstly, high interaction rates with the colloids of 15 and 75 a^{-1} for the tri- and tetravalent actinides are chosen, respectively (see Table 4-6). These rates are high compared to the fluid transport time of 155 years. Therefore, the curves reflect equilibrium between free dissolved actinides and actinides sorbed on mobile colloids and on the surface of the granite matrix. Due to a high concentration of mobile colloids the concentration of mobile (colloid-bound) actinides is quite high, but the retardation on the granite matrix causes a shift to higher arrival times. If the filtration coefficient λ_{fr} is increased, as shown in Figure 4-12 and Figure 4-14 this results in a reduction of mobile colloids as well as a reduced actinide mobility. Thus, the breakthrough concentrations of the colloid-bound radionuclides become strongly reduced within one million

years and for a filtration coefficient of 10^{-2} m^{-1} are app. nine orders of magnitude lower than in the case of no filtration.
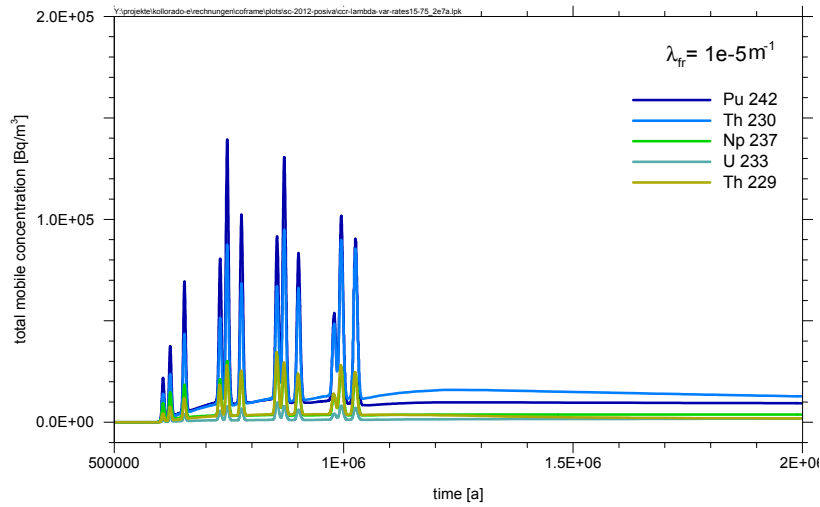
Figure 4-11: Concentration of radionuclides (colloid-bound fraction) at the end of the transport pathway; λfr = 10^{-5} m^{-1}, k_{fri}, k_{frm} = 1.5 / 7.5 a^{-1}.
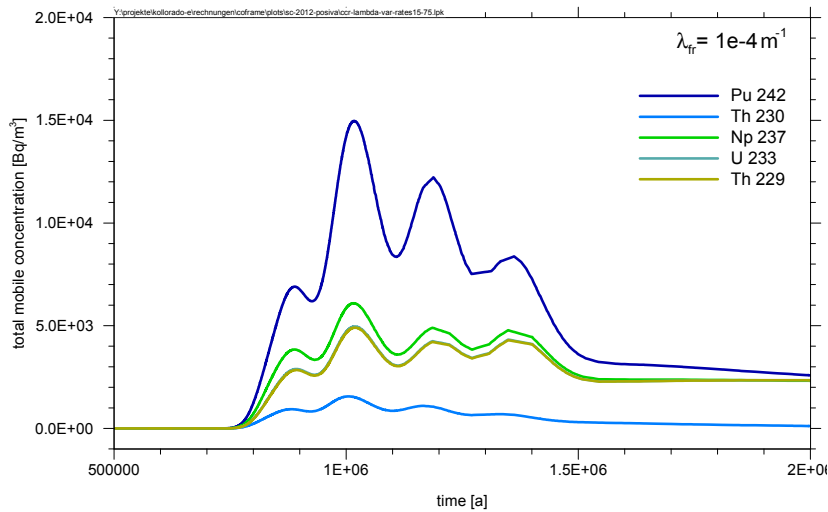
Figure 4-12: Concentration of radionuclides (colloid-bound fraction) at the end of the transport pathway; λfr = 10^{-4} m^{-1}, k_{fri}, k_{frm} = 1.5 / 7.5 a^{-1}.
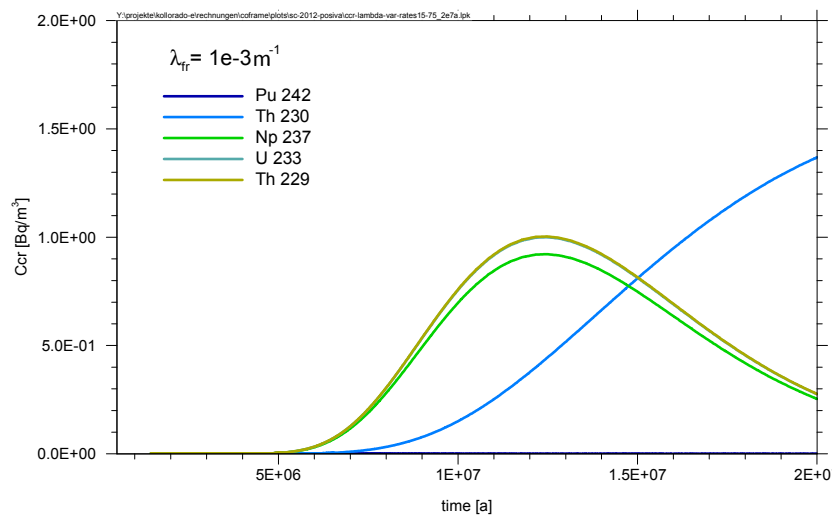
Figure 4-13: Concentration of radionuclides (colloid-bound fraction) at the end of the transport pathway; λfr = 10^{-3} m^{-1}, k_{fri}, k_{frm} = 1.5 / 7.5 a^{-1}.
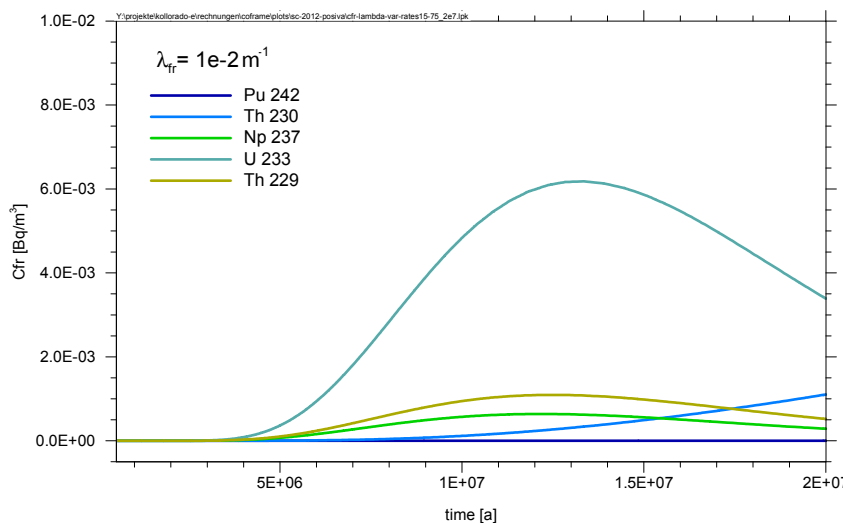
Figure 4-14: Concentration of radionuclides (colloid-bound fraction) at the end of the transport pathway; λ_{fr} = 10^{-2} m^{-1}, k_{fri}, k_{frm} = 1.5 / 7.5 a^{-1}.

For a further increase of the colloid filtration coefficient, the free dissolved fraction of the actinides in the breakthrough curve increases, since more radionuclides desorb from filtrated colloids quite early (colloids are filtrated on the first few meters and do not reach the end of the transport pathway which is then also true for colloid-bound radionuclides). Then the transport is more and more determined by the radionuclide transport of the actinides in dissolved form. However, due to a still strong interaction with filtrated colloids in the first part of the transport pathway the curves are very broad and concentration decreased by more than five orders of magnitude compared to the case without colloid impact.
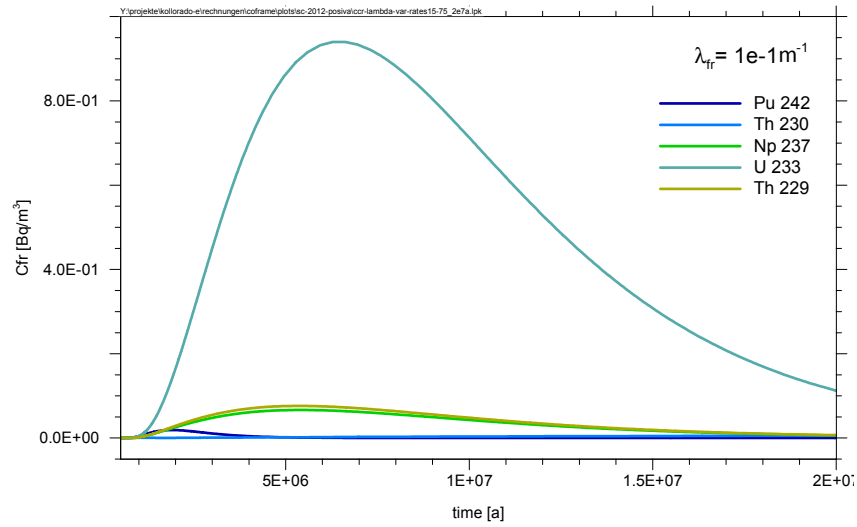
Figure 4-15: Concentration of radionuclides (dissolved fraction) at the end of the transport pathway; λ_{fr} = 10^{-1} m^{-1}, $\boldsymbol{k_{fri}}$, $\boldsymbol{k_{frm}}$ = 1.5 / 7.5 a^{-1}.
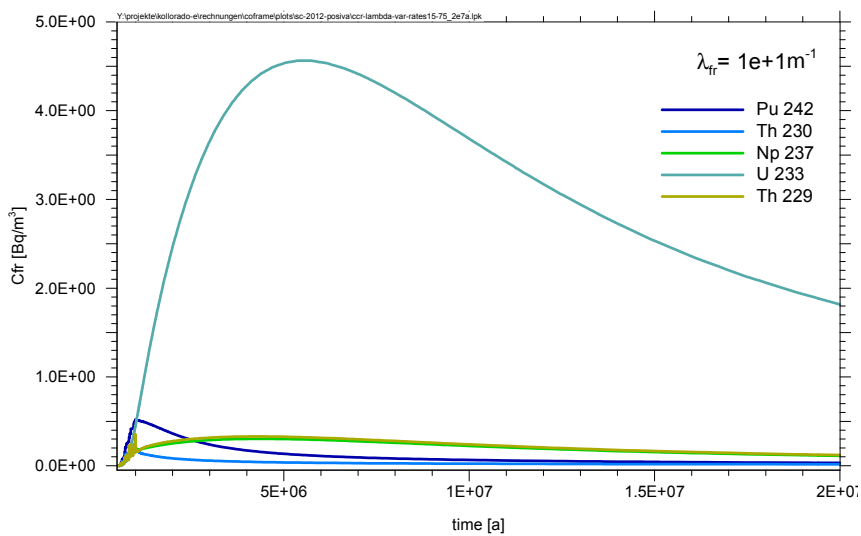
Figure 4-16: Concentration of radionuclides (dissolved fraction) at the end of the transport pathway; λ_{fr} = 10 m^{-1}, $\boldsymbol{k_{fri}}$, $\boldsymbol{k_{frm}}$ = 1.5 / 7.5 a^{-1}.

Calculation case: medium desorption rates k_{fri}, k_{frm}

Further insight into the system can be derived, when radionuclide interaction rates with the colloids are varied. Therefore, interaction rates have been reduced by a factor of 100 to 0.15 a^{-1} for tetravalent and 0.75 a^{-1} for trivalent radionuclides (the "medium" case described in Table 3.6). Figure 4-17 and Figure 4-18 show the resulting radionuclide concentration curves for the colloid-bound fraction using very low filtration coefficients of 10^{-5} and 10^{-4} m^1. Desorption from colloids is slow and the major fraction of radionuclides is transported on mobile colloids with the same velocity as the groundwater. Figure 4-18 illustrates that this leads to high concentrations of the colloid-bound radionuclides in the breakthrough curve and narrow peak shapes similar to the release from the near field (cf. Figure 4-1). There is no significant shift in time, since transport through the fracture only needs 155 years. An increase of the desorption rate of radionuclides to colloids results in a stronger interaction of radionuclides with colloids causing an increase in the dissolved radionuclide fraction and a broadening of the breakthrough curve of colloid-bound radionuclide fraction, see Figure 4-18 and Figure 4-19. For filtration rates >10-2 m-1 the transport is dominated by the free dissolved radionuclide fraction, which shows broad curves with concentration maxima, which are decreased by more than five orders of magnitude compared to the inflow concentration (Figure 4-20, Figure 4-21). This is due to a slow desorption from and interaction with the relatively immobile colloids.
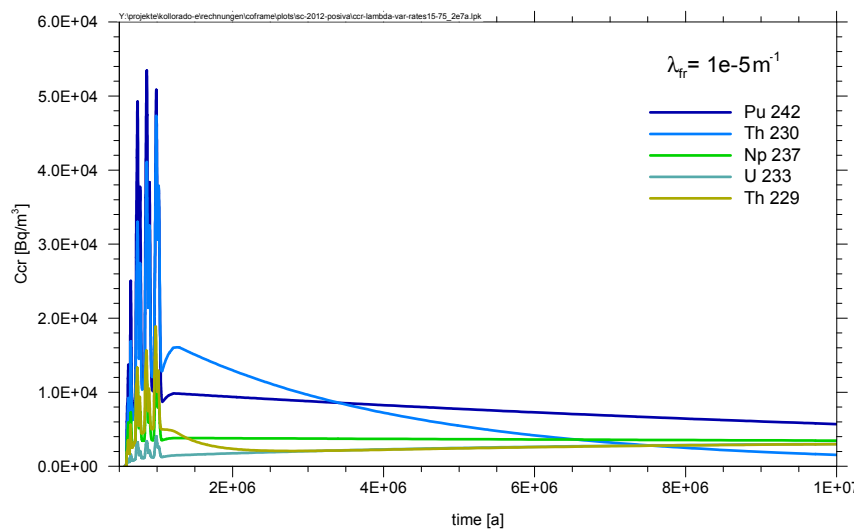
Figure 4-17: Concentration of radionuclides (colloid-bound fraction) at the end of the transport pathway; λ_{fr} = 10^{-5} m^{-1}, k_{fri}, k_{frm} = 0.15 / 0.75 a^{-1}.
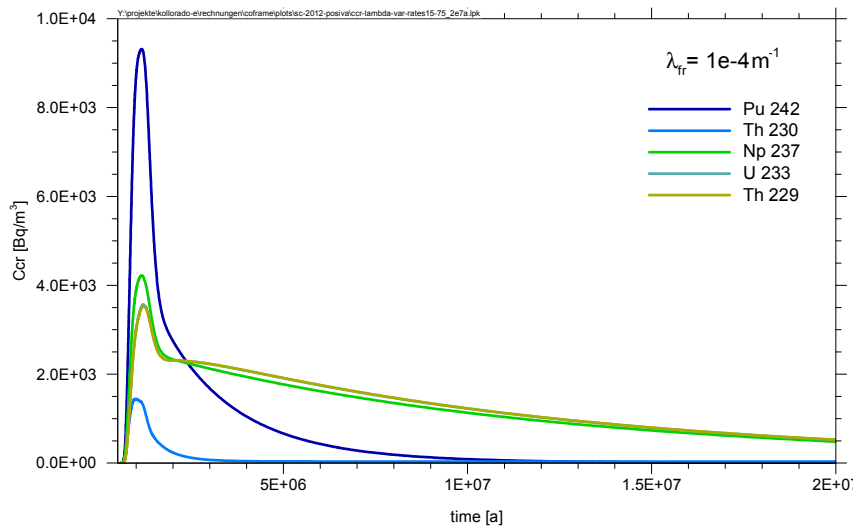
Figure 4-18: Concentration of radionuclides (colloid-bound fraction) at the end of the transport pathway; $\lambda_{fr} = 10^{-4}$ m^{-1}, $\boldsymbol{k_{fri}}$, $\boldsymbol{k_{frm}}$ = 0.15 / 0.75 a^{-1}.
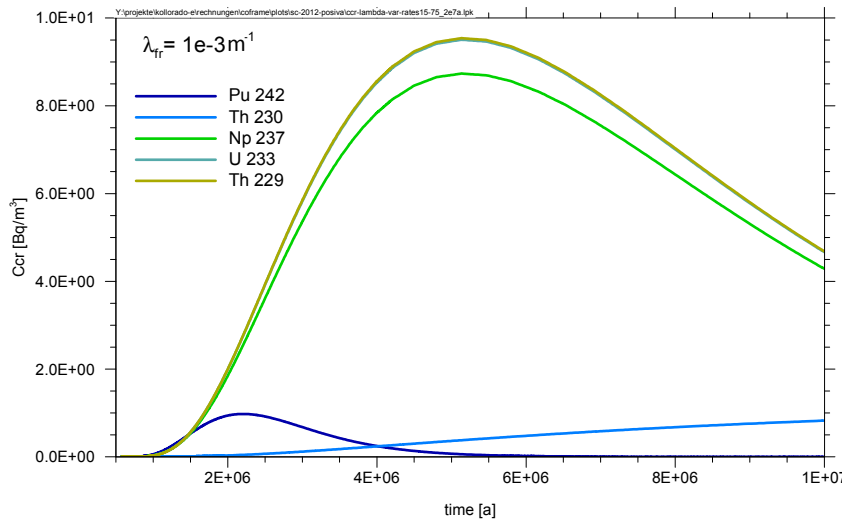
Figure 4-19: Concentration of radionuclides (colloid-bound fraction) at the end of the transport pathway; $\lambda_{fr} = 10^{-3}$ m^{-1}, $\boldsymbol{k_{fri}}$, $\boldsymbol{k_{frm}}$ = 0.15 / 0.75 a^{-1}.

211
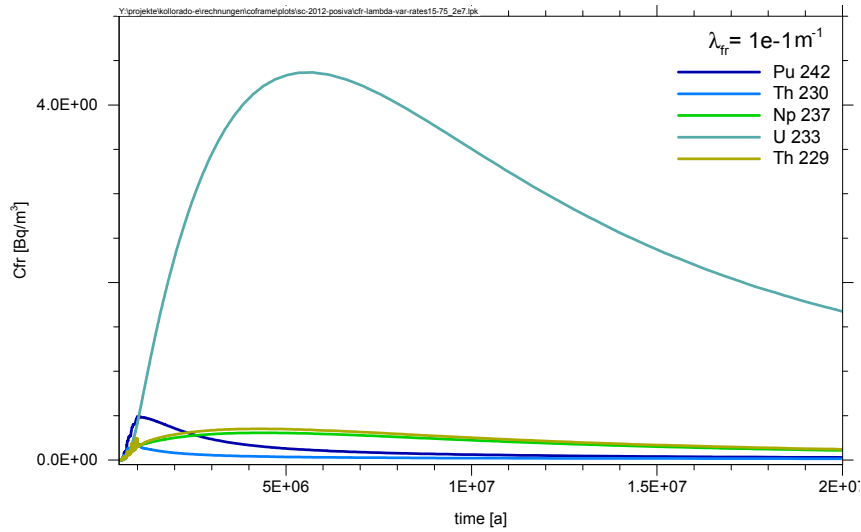
Figure 4-20: Concentration of radionuclides (dissolved fraction) at the end of the transport pathway; λ_{fr} = 10^{-1} m^{-1}, k_{fri}, k_{frm} = 0.15 / 0.75 a^{-1}.
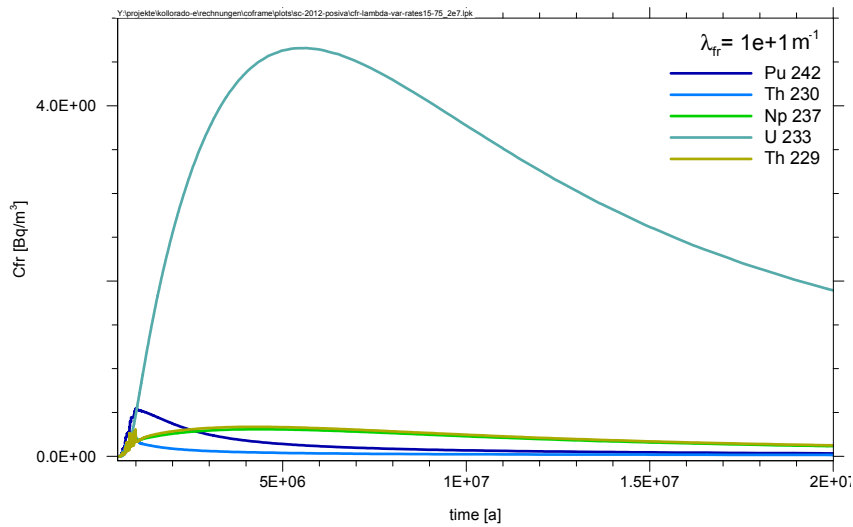
Figure 4-21: Concentration of radionuclides (dissolved fraction) at the end of the transport pathway; λ_{fr} = 10 m^{-1}, k_{fri}, k_{frm} = 0.15 / 0.75 a^{-1}.

Calculation case: low desorption rates k_{fri}, k_{frm}

For a further decrease of the desorption rates , k_{fri}, k_{frm} to values of $1.5 \cdot 10^{-3}$ a^{-1} for tetravalent and $7.5 \cdot 10^{-3}$ a^{-1} for trivalent radionuclides (the "slow" case described in Table 3.6) the results are shown in the following. Under these conditions the radionuclides are strongly fixed to the colloids within the transport time of 155 years resulting in very sharp peaks of the colloid-bound radionuclide fractions and high radionuclide concentrations one order of magnitude higher than in the case without colloids for low filtration rate of 10^{-4} m^{-1}, see Figure 4-22. With increasing filtration rate more colloids are filtrated and the radionuclide concentrations decrease but the peaks are still very sharp, cf. Figure 4-23. For high colloid filtration rates, the curves are dominated by the free dissolved radionuclides, which are broad and have by orders of magnitude decreased concentrations (Figure 4-24 and Figure 4-25) due to the slow desorption and interaction with the immobile colloids, similar as in the case with medium desorption rates.
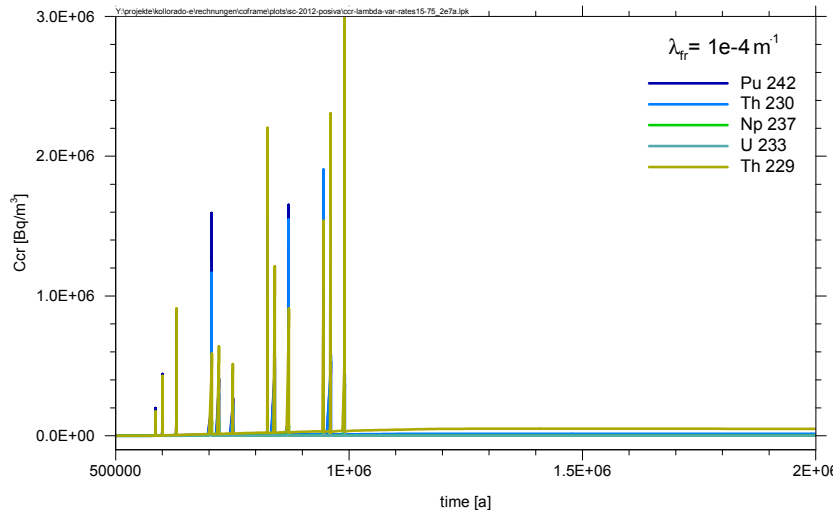
Figure 4-22: Concentration of radionuclides (dissolved fraction) at the end of the transport pathway; $\lambda_{fr} = 10^{-4}$ m^{-1}, k_{fri}, k_{frm} = $1.5 \cdot 10^{-3}$ / $7.5 \cdot 10^{-3}$ a^{-1}.
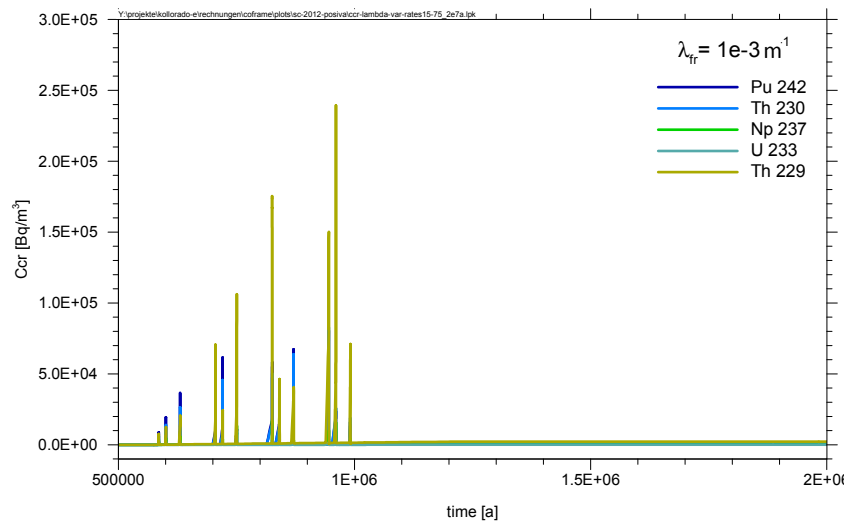
Figure 4-23: Concentration of radionuclides (dissolved fraction) at the end of the transport pathway; $\lambda_{fr} = 10^{-3}$ m^{-1}, k_{fri}, k_{frm} = 1.5·10^{-3} / 7.5·10^{-3} a^{-1}.
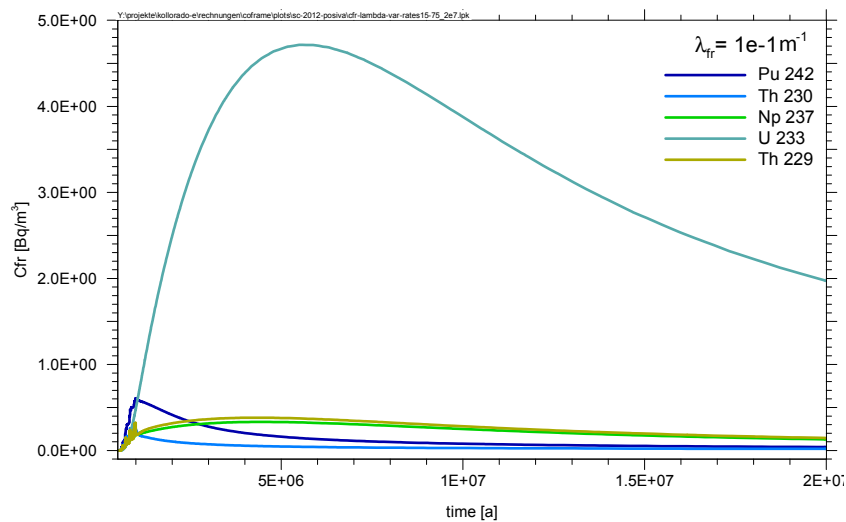
Figure 4-24: Concentration of radionuclides (dissolved fraction) at the end of the transport pathway; $\lambda_{fr} = 10^{-1}$ m^{-1}, k_{fri}, k_{frm} = 1.5·10^{-3} / 7.5·10^{-3} a^{-1}.
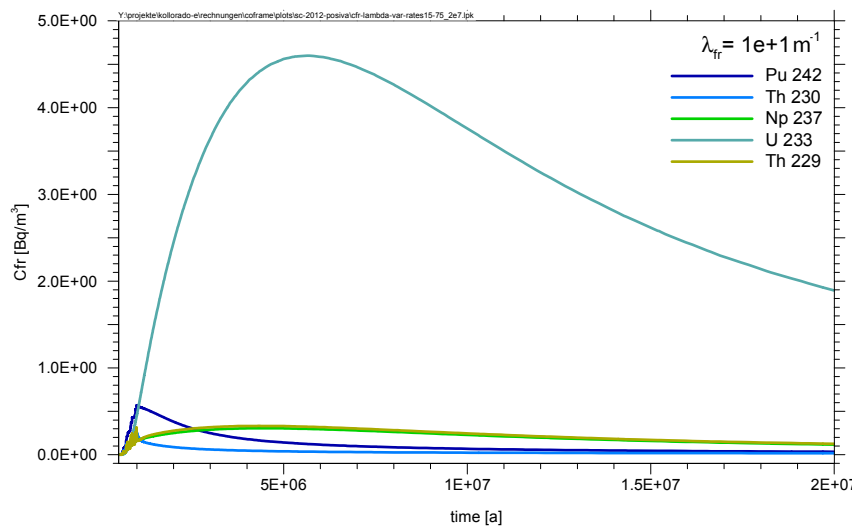
Figure 4-25: Concentration of radionuclides (dissolved fraction) at the end of the transport pathway; λ_{fr} = 10 m^{-1}, k_{fri}, k_{frm} = 1.5·10^{-3} / 7.5·10^{-3} a^{-1}.

Results for increased flow and discrete colloid source during glacial melt

The results shown so far illustrated the impact of colloids on the radionuclide transport under varying filtration and desorption rates and served for understanding of the interacting processes. These calculations, however, presented an unrealistic case, since colloids are not expected to be eroded from the buffer under brackish conditions. In the following the calculations are repeated assuming the more realistic case of a discrete colloid mobilisation from the bentonite buffer only occurring during inflow of melt water with an accompanying increased flow velocity during this time. The results are compiled in the same way as for the constant colloid source.

Calculation case: high desorption rates k_{fri}, k_{frm}

The calculations with high desorption rates of k_{fri}, k_{frm} = 15 a^{-1} for tetravalent and 75 a^{-1} for trivalent radionuclides show for a filtration rate of 10^{-4} m^{-1} (Figure 4-26) distinct peaks, which are reflect the characteristics of discrete increased flow during glacial melt and are therefore sharper than in the case with constant colloid source and constant flow (cf. Figure 4-12). With an increased filtration rate of 10^{-3} m^{-1} nearly no colloid-bound radionuclides arrive at the end of the transport pathway and the amount of free radionuclides is also extremely low in the time frame of 2 Mio years (Figure 4-27 and Figure 4-28). With further increase of the filtration rate the free dissolved radionuclide fraction arrives earlier with higher concentrations, since the radionuclides desorb at the beginning of the transport pathway from the immobile colloids and interacts less during the following transport, since the content of immobile colloids along the residual pathway is much lower. The maximum concentrations are about four orders of magnitude lower compared to the case without colloids.
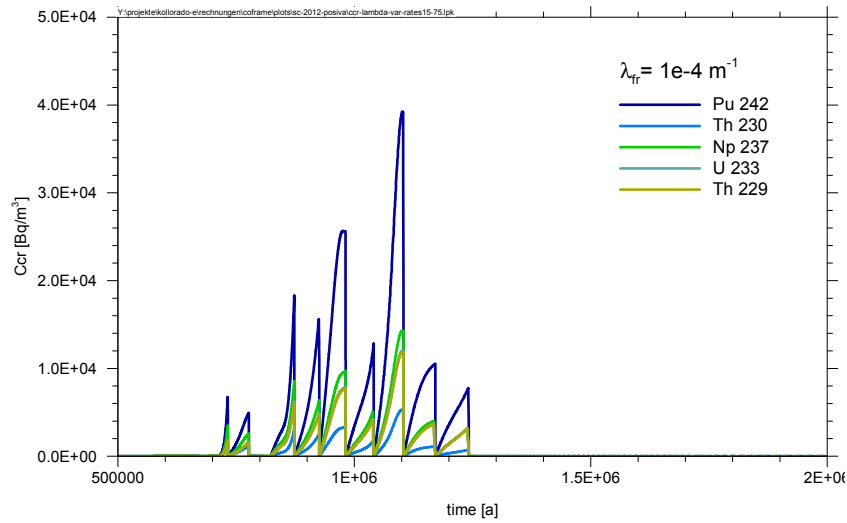
Figure 4-26: Concentration of radionuclides (colloid-bound fraction) at the end of the transport pathway; $\lambda_{fr} = 10^{-4}$ m^{-1}, $\boldsymbol{k_{fri}}$, $\boldsymbol{k_{frm}}$ = 15 / 75 a^{-1}.
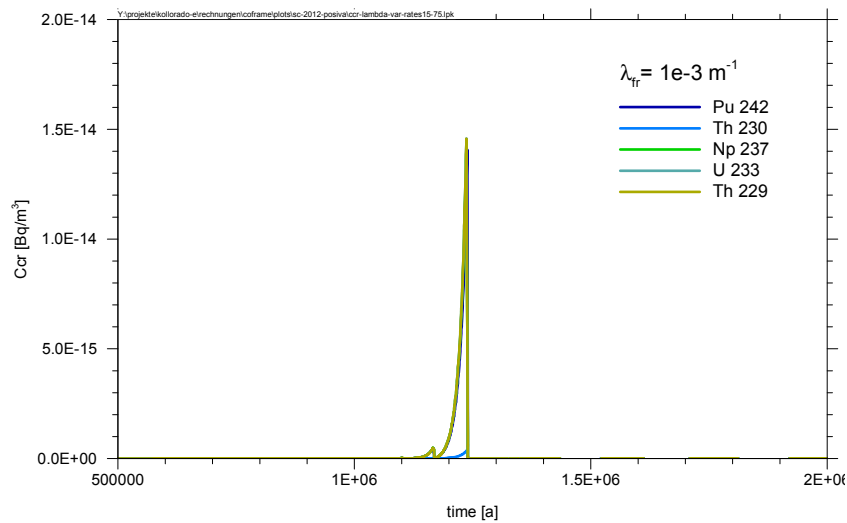
Figure 4-27: Concentration of radionuclides (colloid-bound fraction) at the end of the transport pathway; $\lambda_{fr} = 10^{-3}$ m^{-1}, $\boldsymbol{k_{fri}}$, $\boldsymbol{k_{frm}}$ = 15 / 75 a^{-1}.
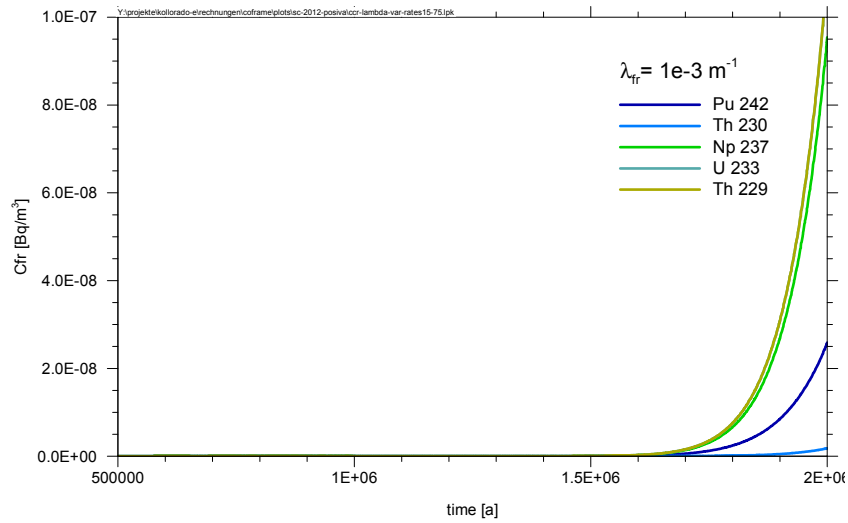
Figure 4-28: Concentration of radionuclides (dissolved fraction) at the end of the transport pathway; λ_{fr} = 10^{-3} m^{-1}, $\boldsymbol{k_{fri}}$, $\boldsymbol{k_{frm}}$ = 15 / 75 a^{-1}.
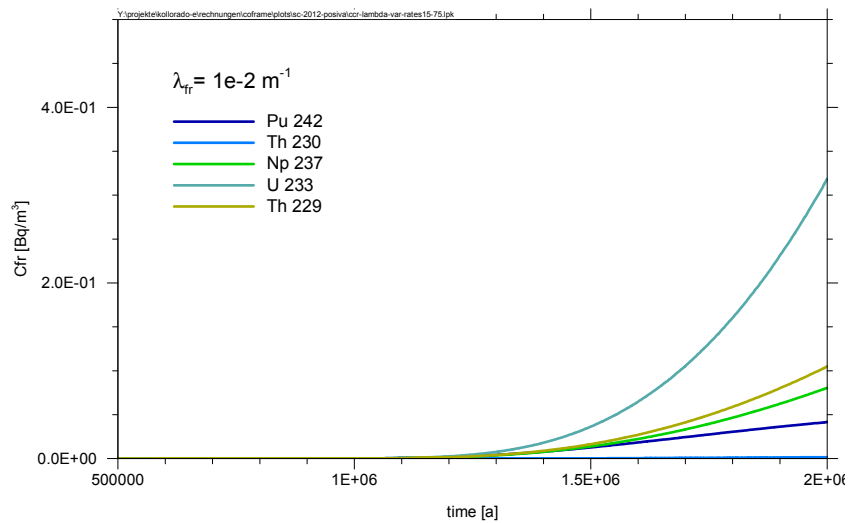
Figure 4-29: Concentration of radionuclides (dissolved fraction) at the end of the transport pathway; λ_{fr} = 10^{-2} m^{-1}, $\boldsymbol{k_{fri}}$, $\boldsymbol{k_{frm}}$ = 15 / 75 a^{-1}.
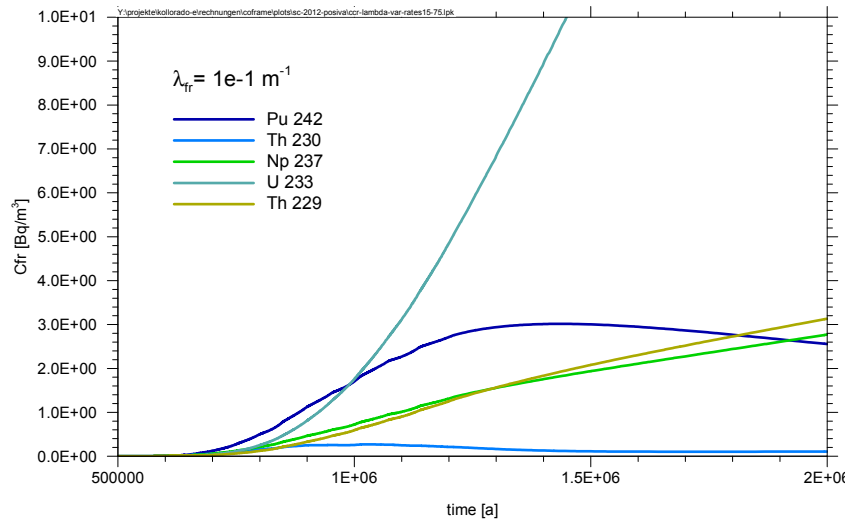
Figure 4-30: Concentration of radionuclides (dissolved fraction) at the end of the transport pathway; λ_{fr} = 10^{-1} m^{-1}, $\boldsymbol{k_{fri}}$, $\boldsymbol{k_{frm}}$ = 15 / 75 a^{-1}.
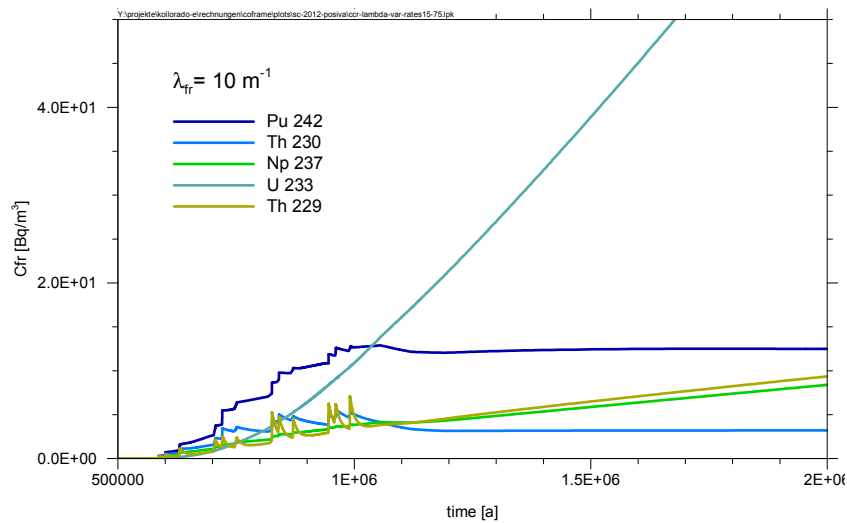
Figure 4-31: Concentration of radionuclides (dissolved fraction) at the end of the transport pathway; λ_{fr} = 10 m^{-1}, $\boldsymbol{k_{fri}}$, $\boldsymbol{k_{frm}}$ = 15 / 75 a^{-1}.

Calculation case: medium desorption rates k_{fri}, k_{frm}

The calculations with medium desorption rates show for a very low filtration coefficient of 10^{-4} m^{-1} (Figure 4-32) similar pattern as for the case with high desorption rates. Distinct peaks occur triggered by high flow at times of glacial melt. Due to interaction of radionuclides with colloids and granite matrix during transport the curves are broader than in the case of low desorption rates, where this interaction is much lower, because the radionuclides are strongly fixed on the mobile colloids, see below in Figure 4-37.

With increasing filtration rate the colloid-bound fraction strongly decreases (Figure 4-33), but radionuclide concentrations are higher compared to Figure 4-27 since radionuclide desorption from the colloids is much lower. At high filtration rates radionuclide transport is dominated by the free dissolved fraction with a broad curve with maximum concentrations of about four orders of magnitude lower compared to the case without colloids.
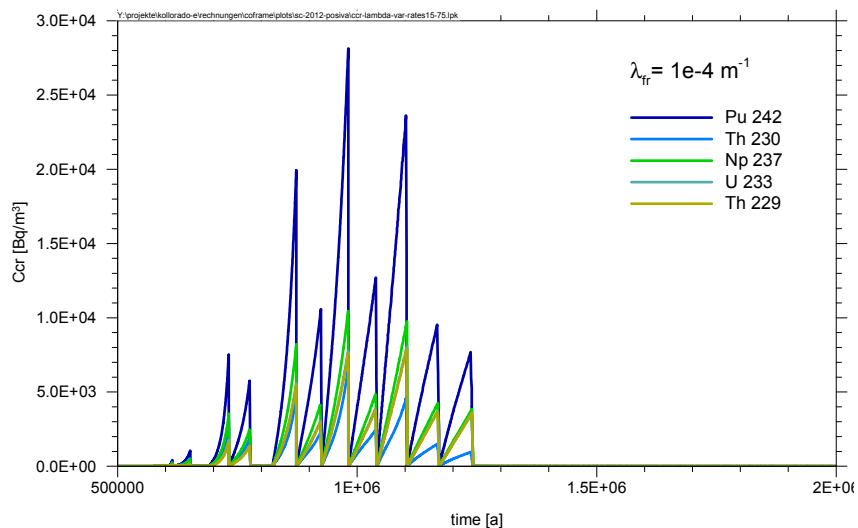
Figure 4-32: Concentration of radionuclides (colloid-bound fraction) at the end of the transport pathway; λ_{fr} = 10^{-4} m^{-1}, k_{fri}, k_{frm} = 0.15 / 0.75 a^{-1}.
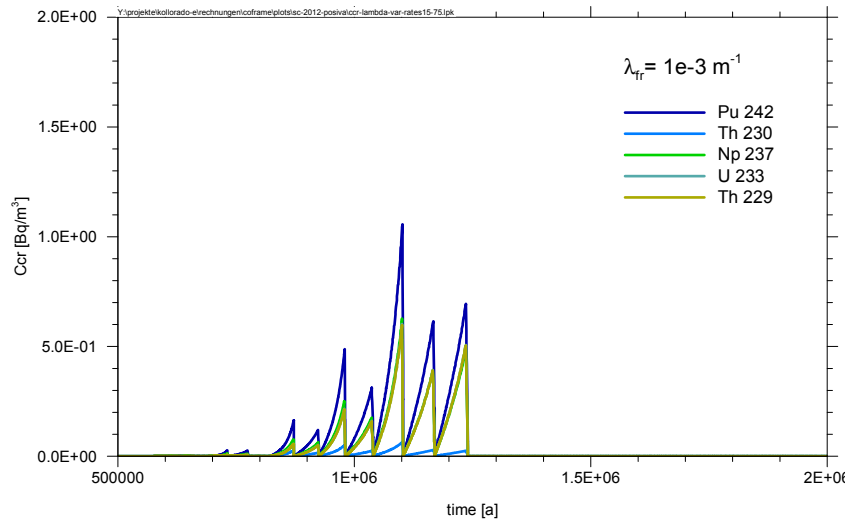
Figure 4-33: Concentration of radionuclides (colloid-bound fraction) at the end of the transport pathway; λ_{fr} = 10^{-3} m^{-1}, k_{fri}, k_{frm} = 0.15 / 0.75 a^{-1}.
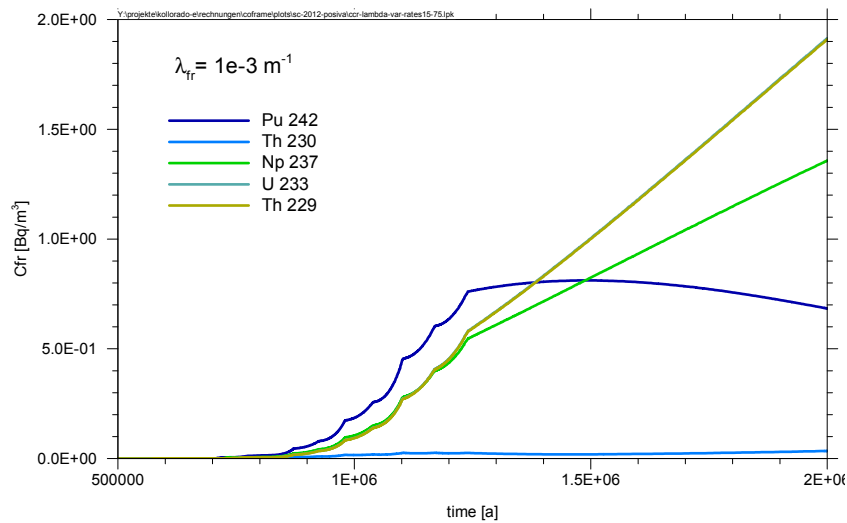
Figure 4-34: Concentration of radionuclides (dissolved fraction) at the end of the transport pathway; λ_{fr} = 10^{-3} m^{-1}, k_{fri}, k_{frm} = 0.15 / 0.75 a^{-1}.
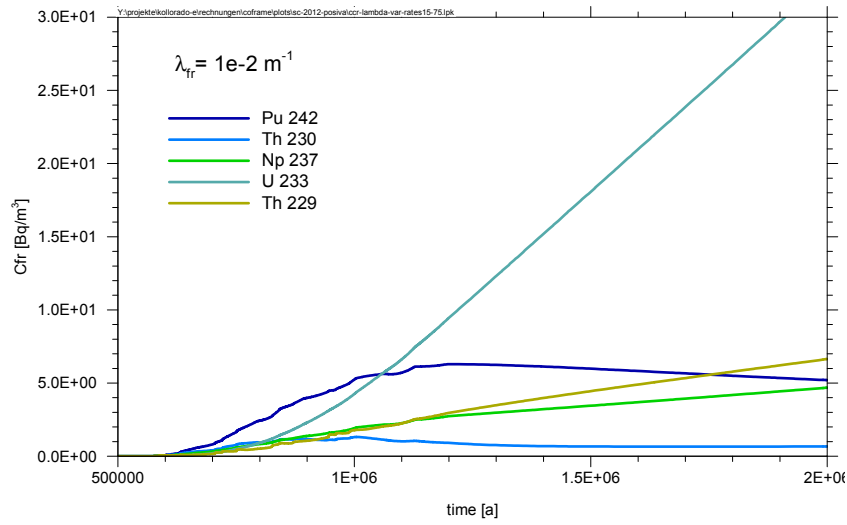
Figure 4-35: Concentration of radionuclides (dissolved fraction) at the end of the transport pathway; λ_{fr} = 10^{-2} m^{-1}, $\boldsymbol{k_{fri}}$, $\boldsymbol{k_{frm}}$ = 0.15 / 0.75 a^{-1}.
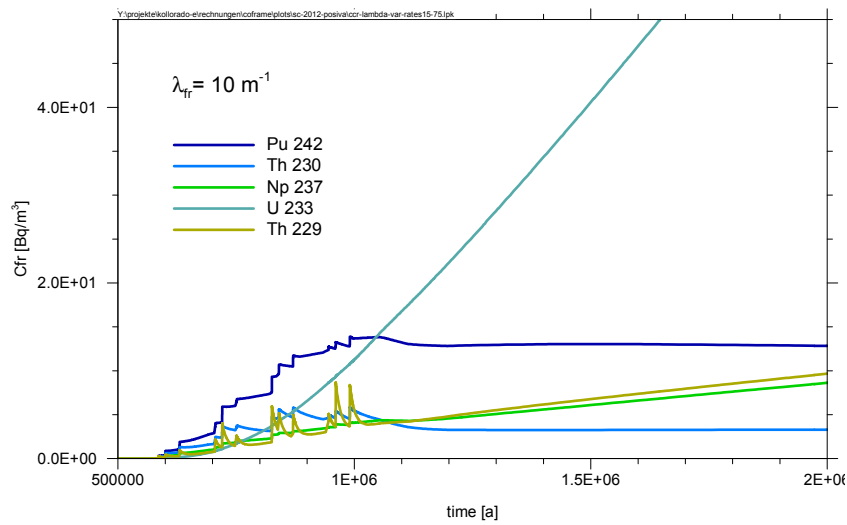
Figure 4-36: Concentration of radionuclides (dissolved fraction) at the end of the transport pathway; λ_{fr} = 10 m^{-1}, $\boldsymbol{k_{fri}}$, $\boldsymbol{k_{frm}}$ = 0.15 / 0.75 a^{-1}.

Calculation case: slow desorption rates k_{fri}, k_{frm}

In the calculation case with slow desorption rates the colloid-bound radionuclides show very sharp peaks and highest concentrations for a very low filtration rate. These concentrations are only slightly decreased compared to the concentrations at the inflow. Due to the high flow rates and the slow desorption rates there is nearly now desorption of radionuclides from the colloids. Further, the colloids are assumed to be too large for matrix diffusion. Therefore, the barrier function of the granitic fracture for the colloid-bound radionuclides is very low. With increasing filtration coefficient the concentration of the colloid-bound radionuclide fraction is reduced but the curves are still very sharp (Figure 4-38 and Figure 4-39). For high filtration coefficients the transport is dominated by free radionuclides which show a broad curve at low concentrations due to slow desorption from the immobile colloids in the first part of the transport pathway and impact of matrix diffusion, see Figure 4-40 and Figure 4-41. The maximum concentrations are again about four orders of magnitude lower compared to the case without colloids.
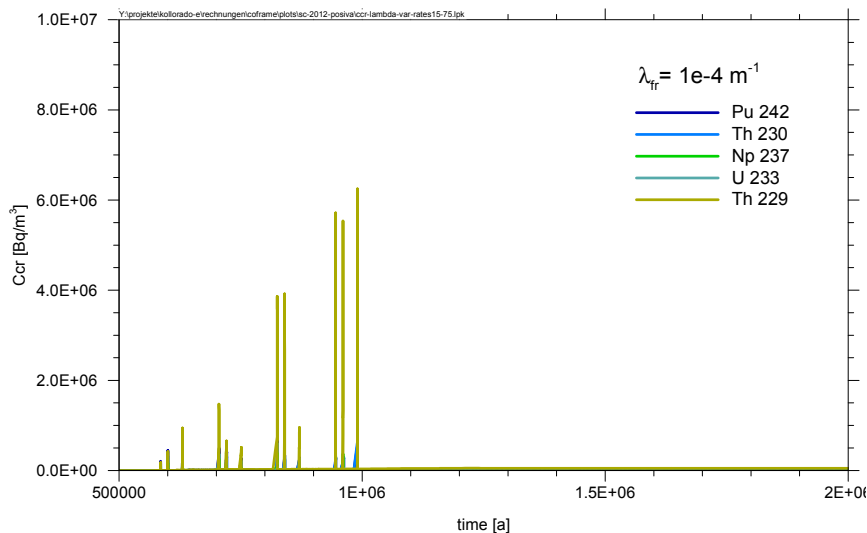
Figure 4-37: Concentration of radionuclides (colloid-bound fraction) at the end of the transport pathway; λ_{fr} = 10^{-4} m^{-1}, k_{fri}, k_{frm} = $1.5 \cdot 10^{-3}$ / $7.5 \cdot 10^{-3}$ a^{-1}.

222
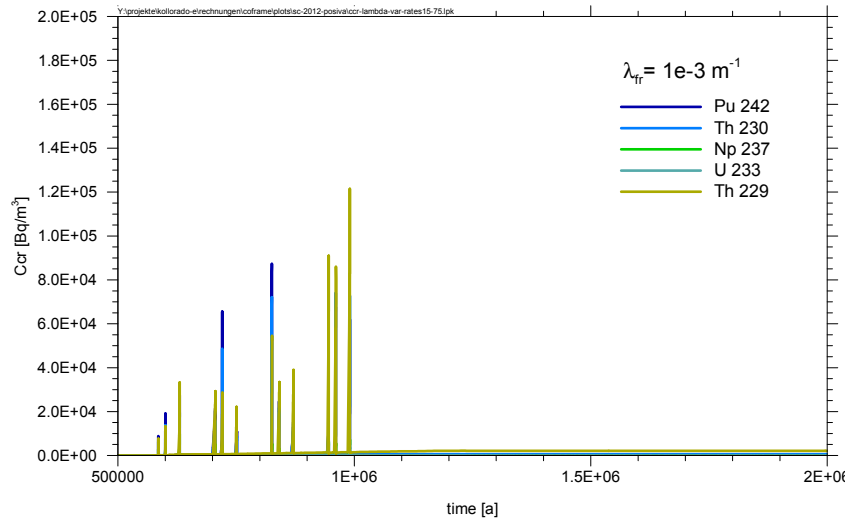
Figure 4-38: Concentration of radionuclides (colloid-bound fraction) at the end of the transport pathway; λ_{fr} = 10^{-3} m^{-1}, $\boldsymbol{k_{fri}}$, $\boldsymbol{k_{frm}}$ = $1.5 \cdot 10^{-3}$ / $7.5 \cdot 10^{-3}$ a^{-1}.
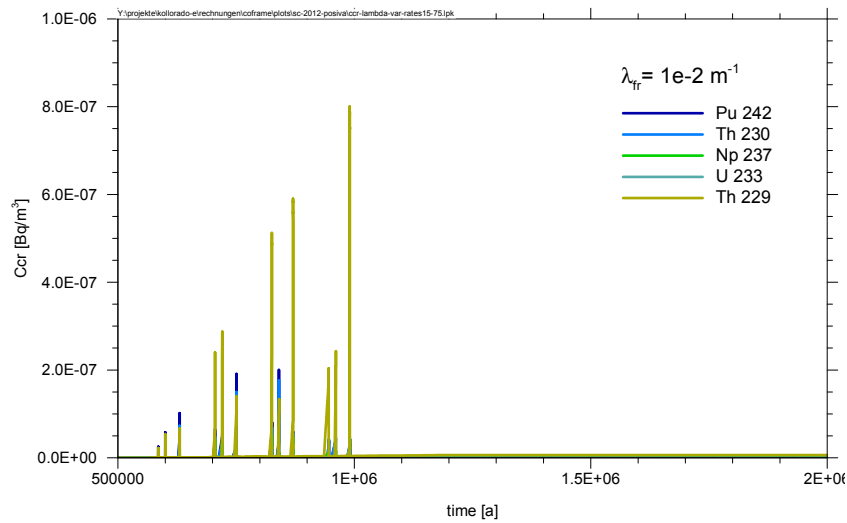
Figure 4-39: Concentration of radionuclides (colloid-bound fraction) at the end of the transport pathway; λ_{fr} = 10^{-2} m^{-1}, $\boldsymbol{k_{fri}}$, $\boldsymbol{k_{frm}}$ = $1.5 \cdot 10^{-3}$ / $7.5 \cdot 10^{-3}$ a^{-1}.

223
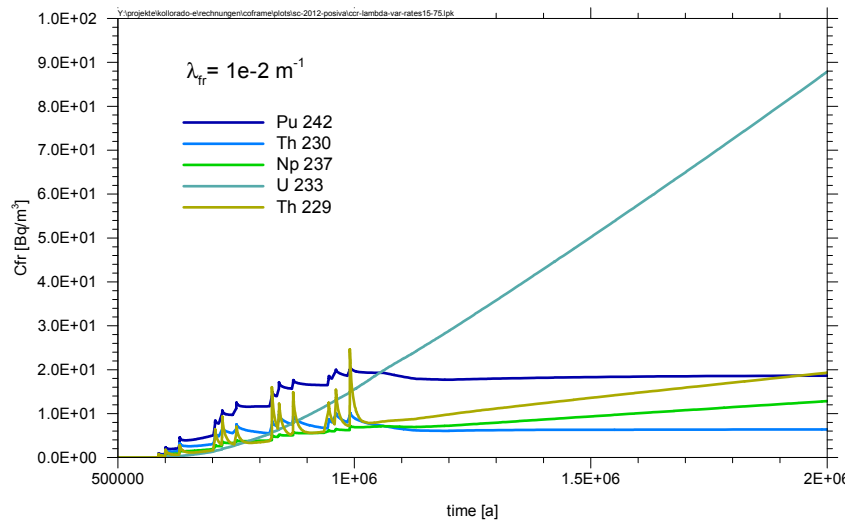
Figure 4-40: Concentration of radionuclides (dissolved fraction) at the end of the transport pathway; λ_{fr} = 10^{-2} m^{-1}, k_{fri}, k_{frm} = $1.5 \cdot 10^{-3}$ / $7.5 \cdot 10^{-3}$ a^{-1}.
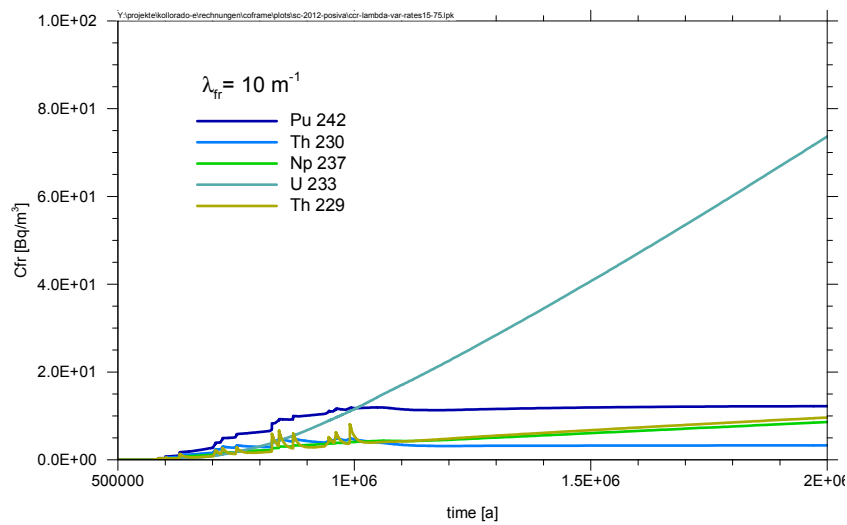
Figure 4-41: Concentration of radionuclides (dissolved fraction) at the end of the transport pathway; λ_{fr} = 10 m^{-1}, k_{fri}, k_{frm} = $1.5 \cdot 10^{-3}$ / $7.5 \cdot 10^{-3}$ a^{-1}.

Impact of colloid remobilisation

For all calculations described in the preceding sections it was assumed that colloid filtration is always irreversible. However, this would cause an extremely high amount of colloids deposited in the fractures of the granite. Figure 4-42 shows a spatial distribution of the colloid concentration. For a filtration rate of 10^{-4} m^{-1} the colloids are relatively mobile, and most colloids migrate to the end of the pathway. For filtration rates of 0.1 m^{-1}, which are still higher than the lowest rates derived from the CFM field tests, nearly all colloids are filtered within the first 100 meters.
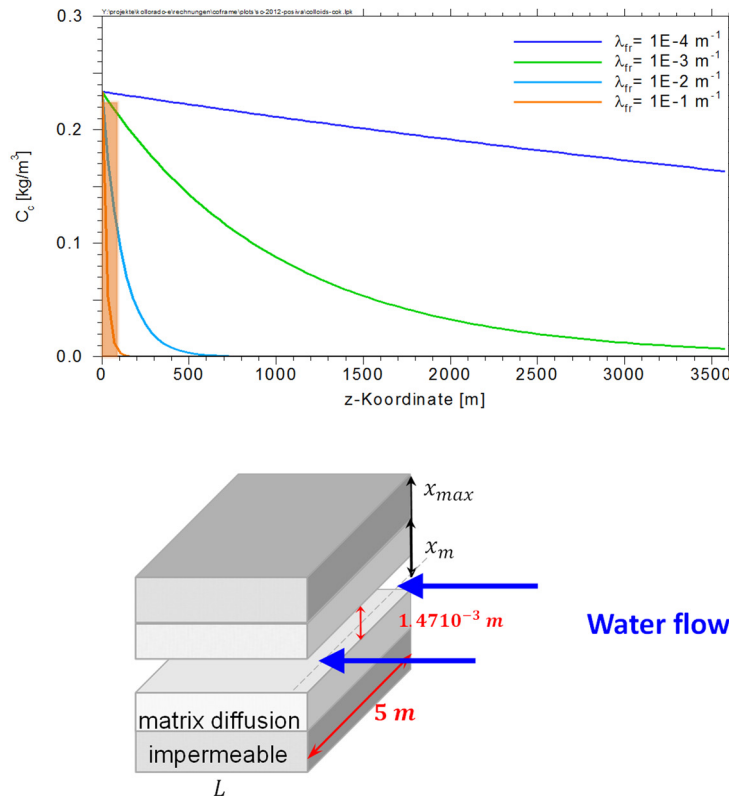
Figure 4-42: Spatial distribution of colloid concentration along the transport pathway (top) and geometry of the conceptual model assumed for the transport (bottom).

In the geometrical model assumed for the Finish safety case, which is shown in Figure 4-42 (bottom), the first 100 m of the fracture provides a volume of 0.735 m^3. For a calculation time of 1 Mio years, where 8 glacial cycles occur and colloids become released at the three times of each cycle, where the inland ice sheets are retreated for periods of 333 years (see *(POSIVA, 2012)*). The amount of filtered bentonite colloids then sums up to about 3157 kg. This amount of filtered bentonite colloids would completely fill this volume with a hypothetical density of 4330 kg/m^3, which would be about double the density of natural bentonite. This shows that the model is oversimplified in this respect. However, in a natural granitic fracture system the colloids are expected to disperse much more than 5 m in lateral direction, which would reduce the filtered amount of bentonite per pore volume. Nevertheless, the question remains, how much of the pore volume is expected to be filled up by bentonite filtration. Two processes will

act against this clogging effect, (i) a remobilization of the colloids which cannot be observed on the scale of the field experiments and (ii) a strong decrease of the filtration rate below the values observed in the field experiments. An indication for the latter effect is the observed plateau of the colloid recovery in CFM field migration experiments with long travel times, cf. Section 2.1.3. With respect to the first process, some screening calculations on the repository scale have been performed. The results for the spatial distribution of the colloids are shown in Figure 4-43. If no remobilization occurs (Figure 4-43, top), more than 90% of the colloids are filtered along the first 100 m of the transport pathway with a filtration rate of 0.1 m^{-1} (see discussion above). With remobilization the colloid concentration along the transport pathway increases showing a similar profile as for lower irreversible filtration rates, i.e. the colloid transport occurs over a much longer distance compared to the irreversible filtration. A further increase of the filtration rate to 1 a^{-1} further enhances the colloid transport showing a profile, which is similar to a very low filtration rate in the range between 10^{-3} and 10^{-4} m^{-1}. The corresponding breakthrough curves of the colloids are shown in Figure 4-44. In case of high remobilization rates of 1 a^{-1} the colloids are transported nearly without retardation, in good agreement to the high mobility observed in the spatial distribution profile. As a consequence, the distinct, sharp peaks representing the colloid release over time frames of glacial melt (333 years) are visible at the end of the transport pathway. With increasing remobilization rates these peaks become broader and retarded. For a remobilization rate of 0.01 a^{-1} the first two peaks of each glaciation are merged into one peak. A further increase further broadens the curve and shifts it to later times. For a remobilization rate of $3 \cdot 10^{-4}$ a^{-1} the maximum of the colloid concentration does not occur before 1.5 Mio years with a long-term plateau and strongly reduced maximum concentration. The curve for Pu-242 corresponds well with the calculated colloid curves. For high remobilisation rates of 1 a^{-1} some numerical problems occurred, i.e. the distinct concentration peaks are still visible but show oscillations to lower concentration values. For lower remobilisation rates the peak becomes broadened and is shifted towards later times.
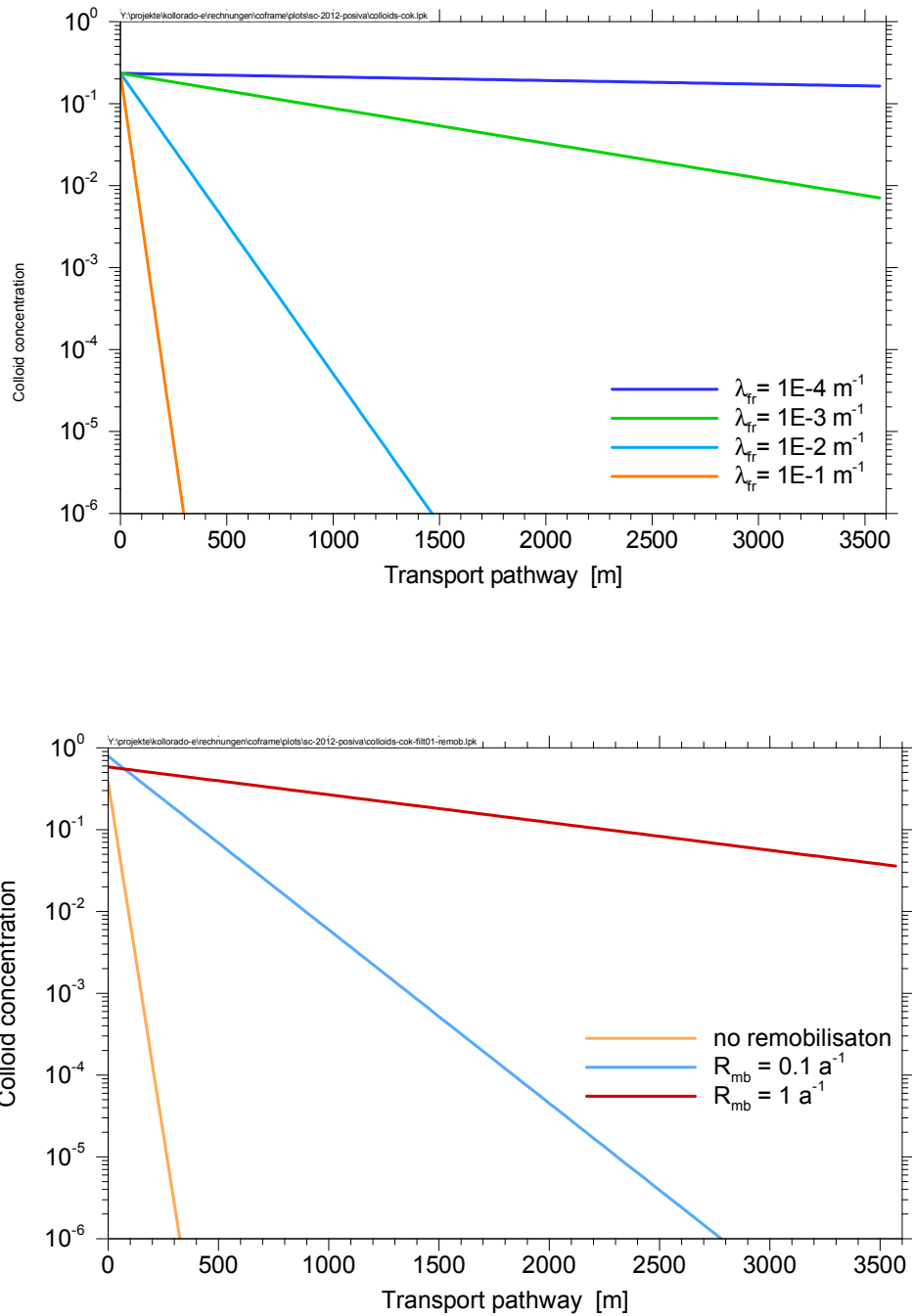
Figure 4-43: Spatial distribution of colloid concentration along the transport pathway for different irreversible filtration rates (top) and for a filtration rate of 10^{-1} m^{-1} and varying remobilisation rates (bottom) after 650 000 years.
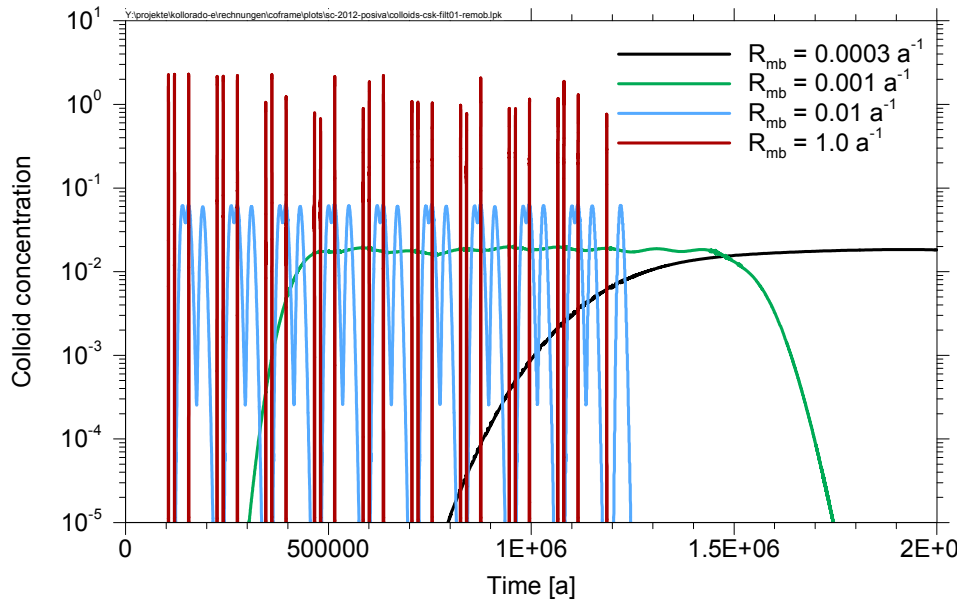
Figure 4-44: Breakthrough curves of the colloids at the end of the transport pathway of 3500 m for a filtration rate of 0.1 m^{-1} and different remobilisation rates.
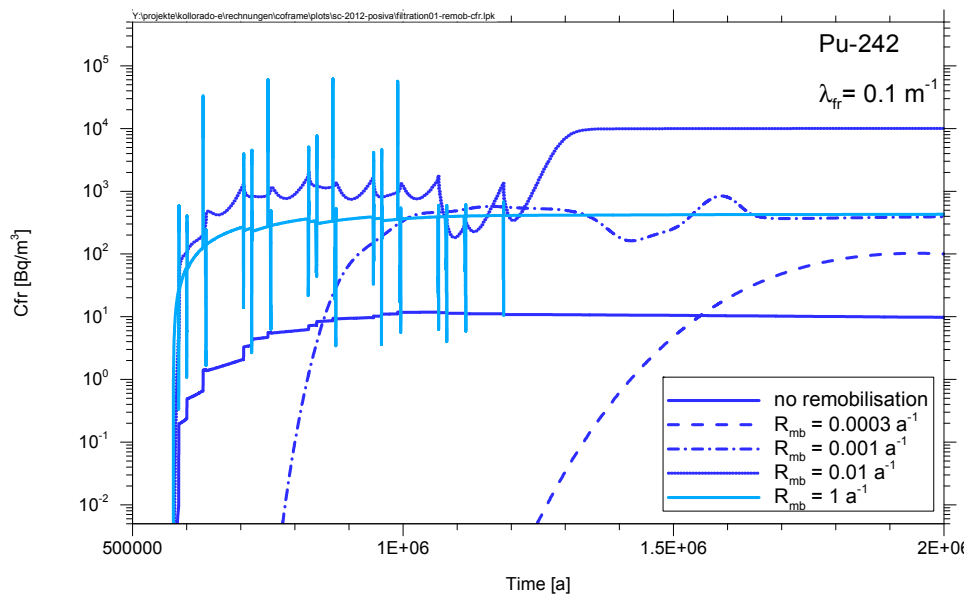
Figure 4-45: Breakthrough curves of Pu-242 at the end of the transport pathway of 3500 m for a filtration rate of 0.1 m^{-1} and different remobilisation rates.

4.3.3 Impact on long-term safety assessment - conclusions

The transport calculations with the new code COFRAME shows interesting results for colloid-facilitated radionuclide transport through a repository system in granite. The source term from the near-field calculations was provided by POSIVA *(POSIVA, 2012)*. The presentation of the calculation results was focussed on the actinides Pu-242, Th-230, Np-237, U-233 and Th-229, which showed highest activity concentrations and which are assumed here to have a strong interaction with colloids. For comparison a reference calculation without colloids was also performed. The quantitative comparison is mainly based on results for Th-229. In dependence of the colloid filtration rate the following conclusions can be made:

For low values of λ (λ <10^{-4} m^{-1}) the filtration of colloids is low and a major fraction of colloids is transported without retardation along the transport pathway. In this case the transport strongly depends on the interaction rates of radionuclides with colloids. For (i) low radionuclide desorption rates (in the range of $10^{-3}/10^{-2}$ a^{-1}) from the colloids high and narrow radionuclide peaks occur, since radionuclides are strongly fixed to the colloids and are transported with nearly no retardation along the migration pathway. Radionuclide concentrations at the end of the transport pathway through the granite are still high, about one order of magnitude higher compared to a calculation without colloids. In case of (ii) increasing radionuclide desorption rates from the colloids the peaks are broadened and retarded accompanied by a decrease in concentration of more than two orders of magnitude (λ=10^{-4} m^{-1}).

For high values of λ (λ >10^{-1} m^{-1}) the filtration of colloids is very high and consequently the radionuclide transport is determined by free radionuclides. Colloid-bound radionuclides are not of relevance since the colloids become completely filtrated on the first part of the transport pathway. However, the colloids act as an important barrier since radionuclides interact with them in the first part of the transport pathway. Thus their transport is retarded to a significant extent. The radionuclide peaks at the end of the transport pathway are rather broad and the concentration is decreased by more than four orders of magnitude compared to the calculation without colloids. However, as discussed in the preceding section this is a simplified case, which would – under the boundary conditions used in the model – lead to a complete clogging of the fractures with unrealistically high amounts of bentonite. Processes acting against this are an expected much wider dispersion of the colloids as assumed in the model and colloid remobilisation processes, which have not been observed on the scale of the CFM field migration experiments so far. Screening calculations for colloid remobilization show, that increasing remobilization rates lead to spatial concentration distributions, which are similar to those of low filtration rates. Accordingly, the colloid-bound radionuclide transport increases with increasing remobilization rates, being comparable to transport at low filtration rates. The highest retardation of the radionuclide peaks is observed for colloid filtration rates in the range of λ = 10^{-2} to 10^{-3} m^{-1}. At those rates colloids travel a longer distance but are still filtrated to a large extent. Under such conditions the interaction of radionuclides with immobile colloids occur over a much longer part of the transport pathway compared to conditions where λ >10^{-1} m^{-1}. This causes a much longer travel time of the radionuclides.

These calculations show in general that under the far-field conditions considered in the Finnish safety case relatively short travel time and low retardation for the radionuclide peaks occur. Under such conditions the impact of colloids is more retarding than facilitating as long as a significant amount of colloids become filtrated. Only in case of very low filtration rates (far below those observed in CFM field experiments) and very low desorption rates of radionuclides from the colloids an increase of radionuclide concentration compared to a calculation without colloids is observed.

5 References

Abbas, Z., Labbez, C., Nordholm, S., Ahlberg, E., 2008. Size-Dependent Surface Charging of Nanoparticles. The Journal of Physical Chemistry C, 112(15): 5715-5723.

Abdul Aziz, H. et al., 2010. Integrated stratigraphy and Ar-40/Ar-39 chronology of the early to middle Miocene Upper Freshwater Molasse in western Bavaria (Germany). International Journal of Earth Sciences, 99(8): 1859-1886.

Adler, P.M., Thovert, J.-F., 1999. Fractures and fracture networks. Theory and applications of transport in porous media ; 15. Kluwer, Dordrecht [u.a.], XII, 429 S. pp.

Albarran, N., Missana, T., Alonso, U., García-Gutiérrez, M., López, T., 2013. Analysis of latex, gold and smectite colloid transport and retention in artificial fractures in crystalline rock. Colloids and Surfaces A: Physicochemical and Engineering Aspects, 435: 115-126.

Alexander, W.R., Ota, K., Frieg, B., 2001. The NAGRA-JNC in situ study of safety relevant radionuclide retardation in fractured crystalline rock II: the RRP project methodology development, field and laboratory tests,. NAGRA Technical Report Series NTB 00-06, NAGRA, Wettingen, Switzerland

Ali, S., Bandyopadhyay, R., 2013. Use of Ultrasound Attenuation Spectroscopy to Determine the Size Distribution of Clay Tactoids in Aqueous Suspensions. Langmuir, 29(41): 12663-12669.

Alliot, I., Alliot, C., Vitorge, P., Fattahi, M., 2009. Speciation of Technetium(IV) in Bicarbonate Media. Environmental Science & Technology, 43(24): 9174-9182.

Alonso, U. et al., 2006a. Grimsel Test Site - Investigation Phase V "The CRR final project report series II: Supporting Laboratory Experiments with Radionuclides and Bentonite Colloids". 03-02, Nagra, Wettingen, Switzerland.

Alonso, U., Missana, T., García-Gutiérrez, M., 2007a. Experimental approach to study the bentonite colloid generation source term in different geochemical conditions. In: Buckau, G., Kienzler, B., Duro, L., Montoya, V. (Eds.), 2nd Annual Workshop Proceedings of the Integrated Project "Fundamental Processes of Radionuclide Migration" - 6th EC FP IP FUNMIG. SKB, Stockholm, pp. 329-335.

Alonso, U. et al., 2006b. Role of inorganic colloids generated in a high-level deep geological repository in the migration of radionuclides: open questions. Journal of Iberian Geology, 32(1): 79.

Alonso, U., Missana, T., Patelli, A., Rigato, V., 2007b. Bentonite colloid diffusion through the host rock of a deep geological repository. Physics and Chemistry of the Earth, Parts A/B/C, 32(1-7): 469-476.

Alonso, U., Missana, T., Patelli, A., Rigato, V., Ravagnan, J., 2004. μPIXE study on colloid heterogeneous retention due to colloid/rock electrostatic interactions.

Alonso, U., Missana, T., Patelli, A., Rigato, V., Ravagnan, J., 2007c. Colloid diffusion in crystalline rock: An experimental methodology to measure diffusion coefficients and evaluate colloid size dependence. Earth and Planetary Science Letters, 259(3-4): 372-383.

Altmaier, M., Gaona, X., Fellhauer, D., Buckau, G., 2010. Intercomparison of redox determination methods on designed and near-neutral aqueous systems; KIT-SR 7572. Karlsruhe Institute of Technology, Karlsruhe, 34.

Altmaier, M., Neck, V., Fanghänel, T., 2004. Solubility and colloid formation of Th(IV) in concentrated NaCl and $MgCl_2$ solution, Radiochimica Acta/International journal for chemical aspects of nuclear science and technology, pp. 537.

Ammann, L., Bergaya, F., Lagaly, G., 2005. Determination of the cation exchange capacity of clays with copper complexes revisited. Clay Minerals, 40(4): 441-453.

Amram, K., Ganor, J., 2005. The combined effect of pH and temperature on smectite dissolution rate under acidic conditions. Geochimica et Cosmochimica Acta, 69(10): 2535-2546.

Apted, M.J. et al., 2010. Buffer erosion: An overview of concepts and potential safety consequences. SSM Research Report: 2010:31.

Baalousha, M., Kammer, F.D., Motelica-Heino, M., Le Coustumer, P., 2005. 3D characterization of natural colloids by FlFFF-MALLS-TEM. Analytical and Bioanalytical Chemistry, 383(4): 549-556.

Baalousha, M., Kammer, F.V.D., Motelica-Heino, M., Hilal, H.S., Le Coustumer, P., 2006. Size fractionation and characterization of natural colloids by flow-field flow fractionation coupled to multi-angle laser light scattering. Journal of Chromatography A, 1104(1-2): 272-281.

Baeyens, B., Bradbury, M.H., 1997. A mechanistic description of Ni and Zn sorption on Na-montmorillonite .1. Titration and sorption measurements. Journal of Contaminant Hydrology, 27(3-4): 199-222.

Baik, M.H., Cho, W.J., Hahn, P.S., 2007. Erosion of bentonite particles at the in-terface of a compacted bentonite and a fractured granite. Engineering Geology, 91(2-4): 229-239.

5. References

Bailey, S.W., 1982. Nomenclature for regular interstratifications. American Mineralogist, 67: 394-398.

Baker, J.C., Grabowska-Olszewska, B., Uwins, P.J.R., 1995. ESEM study of osmotic swelling of bentonite from Radzionkow (Poland). Applied Clay Science, 9(6): 465-469.

Bath, A., 2011. Infiltration of dilute groundwaters and resulting groundwater compositions at repository depth., SSM Report 2011:22, Stockholm.

Becker, M.W., Reimus, P.W., Vilks, P., 1999. Transport and Attenuation of Carboxylate-Modified Latex Microspheres in Fractured Rock Laboratory and Field Tracer Tests. Ground Water, 37(3): 387-395.

Beckett, R., Murphy, D., Tadjiki, S., Chittleborough, D.J., Calvin Giddings, J., 1997. Determination of thickness, aspect ratio and size distributions for platey particles using sedimentation field-flow fractionation and electron microscopy. Colloids and Surfaces A: Physicochemical and Engineering Aspects, 120(1–3): 17-26.

Behrens, S.H., Christl, D.I., Emmerzael, R., Schurtenberger, P., Borkovec, M., 2000. Charging and Aggregation Properties of Carboxyl Latex Particles: Experiments versus DLVO Theory. Langmuir, 16(6): 2566-2575.

Bergaya, F., Lagaly, G., 2006. Chapter 1 General Introduction: Clays, Clay Minerals, and Clay Science. In: Bergaya, F., Theng, B.K.G., Lagaly, G. (Eds.), Developments in Clay Science. Elsevier, pp. 1-18.

Bergaya, F., Theng, B.K.G., Lagaly, G., 2006. Handbook of Clay Science, 1.

Bernhard, G. et al., 2001. Uranyl(VI) carbonate complex formation: Validation of the Ca2UO2(CO3)3(aq.) species. Radiochimica Acta, 89(8): 511-518.

Bessho, K., Degueldre, C., 2009. Generation and sedimentation of colloidal bentonite particles in water. Applied Clay Science, 43(2): 253-259.

Bhatia, M.P., Das, S.B., Longnecker, K., Charette, M.A., Kujawinski, E.B., 2010. Molecular characterization of dissolved organic matter associated with the Greenland ice sheet. Geochimica et Cosmochimica Acta, 74(13): 3768-3784.

Bickmore, B.R., Nagy, K.L., Sandlin, P.E., Crater, T.S., 2002. Quantifying surface areas of clays by atomic force microscopy. American Mineralogist, 87(5-6): 780-783.

Birgersson, M., Börgesson, L., Hedström, M., Karnland, O., Nilsson, U., 2009. Bentonite erosion (Final report), SKB Technical Report TR-09-34, Clay Technology, AB.

Blechschmidt, I. et al., 2006. GTS Phase VI: CFM Status Report on Field Work 2004 – 2005. Arbeitsbericht NAB 06-06. Natonale Genossenschaft für die Lagerung radioaktiver Abfälle (NAGRA). Wettingen.

Boggs, M.A., Dai, Z., Kersting, A.B., Zavarin, M., 2015. Plutonium(IV) sorption to montmorillonite in the presence of organic matter. Journal of Environmental Radioactivity, 141(0): 90-96.

Boily, J.-F., Kozin, P.A., 2014. Particle morphological and roughness controls on mineral surface charge development. Geochimica Et Cosmochimica Acta, 141: 567-578.

Bol, W., Gerrits, G.J.A., van Panthaleon Eck, C.L., 1970. The hydration of divalent cations in aqueous solution. An X-ray investigation with isomorphous replacement. Journal of Applied Crystallography, 3(6): 486-492.

Bondietti, E.A., Francis, C.W., 1979. Geologic Migration Potentials of Technetium-99 and Neptunium-237. Science, 203(4387): 1337-1340.

Bossart, P., Mazurek, M., 1991. Grimsel Test Site: Structural geology and water flow-paths in the migration shear zone. Nagra Technical Report 91-12, Nagra, Wettingen, Switzerland.

Bouby, M., Finck, N., Geckeis, H., 2012. Flow field-flow fractionation (FlFFF) coupled to sensitive detection techniques: A way to examine radionuclide interactions with nanoparticles. Mineralogical Magazine, 76(7): 2709-2721.

Bouby, M., Geckeis, H., Geyer, F.W., 2008. Application of asymmetric flow field-flow fractionation (AsFlFFF) coupled to inductively coupled plasma mass spectrometry (ICPMS) to the quantitative characterization of natural colloids and synthetic nanoparticles. Analytical and Bioanalytical Chemistry, 392(7-8): 1447-1457.

Bouby, M., Geckeis, H., Luetzenkirchen, J., Mihai, S., Schaefer, T., 2011. Interaction of bentonite colloids with Cs, Eu, Th and U in presence of humic acid: A flow field-flow fractionation study. Geochimica et Cosmochimica Acta, 75(13): 3866-3880.

Bouby, M. et al., 2004. Laser-induced breakdown detection combined with asymmetrical flow field-flow fractionation: application to iron oxi/hydroxide colloid characterization. Journal of Chromatography A, 1040(1): 97-104.

Bourg, I.C., Sposito, G., Bourg, A.C.M., 2007. Modeling the acid–base surface chemistry of montmorillonite. Journal of Colloid and Interface Science, 312(2): 297-310.

Bowen, P., 2002. Particle Size Distribution Measurement from Millimeters to Nanometers and from Rods to Platelets. Journal of Dispersion Science and Technology, 23(5): 631-662.

Bowen, P., Sheng, J., Jongen, N., 2002. Particle size distribution measurement of anisotropic—particles cylinders and platelets—practical examples. Powder Technology, 128(2–3): 256-261.

232

Bowen, W.R., Doneva, T.A., 2000. Atomic force microscopy studies of membranes: Effect of surface roughness on double-layer interactions and particle adhesion. Journal of Colloid and Interface Science, 229(2): 544-549.

Bradbury, M.H., Baeyens, B., 1999. Modelling the sorption of Zn and Ni on Ca-montmorillonite. Geochimica et Cosmochimica Acta, 63(3-4): 325-336.

Bradbury, M.H., Baeyens, B., 2002. Porewater chemistry in compacted re-saturated MX-80 bentonite: Physico-chemical characterisation and geochemical modelling PSI Bericht Nr. 02-10: 28.

Bradbury, M.H., Baeyens, B., 2005. Modelling the sorption of Mn(II), Co(II), Ni(II), Zn(II), Cd(II), Eu(III), Am(III), Sn(IV), Th(IV), Np(V) and U(VI) on montmorillonite: Linear free energy relationships and estimates of surface binding constants for some selected heavy metals and actinides. Geochimica Et Cosmochimica Acta, 69(4): 875-892.

Bradbury, M.H., Baeyens, B., 2006. Modelling sorption data for the actinides Am(III), Np(V) and Pa(V) on montmorillonite. Radiochimica Acta, 94(9-11): 619-625.

Bradbury, M.H., Baeyens, B., 2009. Sorption modelling on illite. Part II: Actinide sorption and linear free energy relationships. Geochimica Et Cosmochimica Acta, 73(4): 1004-1013.

Bradbury, M.H., Baeyens, B., 2011. Predictive sorption modelling of Ni(II), Co(II), Eu(IIII), Th(IV) and U(VI) on MX-80 bentonite and Opalinus Clay: A "bottom-up" approach. Applied Clay Science, 52(1–2): 27-33.

Bradford, S.A., Torkzaban, S., 2013. Colloid Interaction Energies for Physically and Chemically Heterogeneous Porous Media. Langmuir, 29(11): 3668-3676.

Bredehoeft, J.D., 1997. Fault permeability near Yucca Mountain. Water Resources Research, 33(11): 2459-2463.

Brigatti, M.F., Galan, E., Theng, B.K.G., 2006. Chapter 2 Structures and Mineralogy of Clay Minerals. In: Bergaya, F., Theng, B.K.G., Lagaly, G. (Eds.), Developments in Clay Science. Elsevier, pp. 19-86.

Bro, R., De Jong, S., 1997. A fast non-negativity-constrained least squares algorithm. Journal of chemometrics, 11(5): 393-401.

Brown, G.H., 2002. Glacier meltwater hydrochemistry. Applied Geochemistry, 17(7): 855-883.

Brunauer, S., Emmett, P.H., Teller, E., 1938. Adsorption of Gases in Multimolecular Layers. Journal of the American Chemical Society, 60(2): 309-319.

Buddemeier, R.W., Hunt, J.R., 1988. Transport of colloidal contaminants in groundwater: radionuclid migration at the Nevada test site. Appl. Geochem., 3: 535-548.

Buerger, S. et al., 2007. Speciation of the oxidation states of plutonium in aqueous solutions by UV/Vis spectroscopy, CE-ICP-MS and CE-RIMS. Radiochimica Acta, 95(8): 433-438.

Caballero, E. et al., 2005. Bentonites from Cabo de Gata, Almeria, Spain: a mineralogical and geochemical overview. Clay Minerals, 40(4): 463-480.

Caballero, E., Reyes, E., Yusta, A., Huertas, F., Linares, J., 1985. Las bentonitas de la zona sur de Cabo de Gata (Almería). Geoquímica y Mineralogía. Acta Geològica Hispànica, 20(3-4): 267-287.

Cadene, A., Durand-Vidal, S., Turq, P., Brendle, J., 2005. Study of individual Na-montmorillonite particles size, morphology, and apparent charge. Journal of Colloid and Interface Science, 285(2): 719-730.

Carrado, K.A., Decarreau, A., Petit, S., Bergaya, F., Lagaly, G., 2006. Chapter 4 Synthetic Clay Minerals and Purification of Natural Clays. In: Bergaya, F., Theng, B.K.G., Lagaly, G. (Eds.), Developments in Clay Science. Elsevier, pp. 115-139.

Carrier, B. et al., 2013. ESEM Study of the Humidity-Induced Swelling of Clay Film. Langmuir, 29(41): 12823-12833.

Cases, J.M. et al., 1992. Mechanism of adsorption and desorption of water vapor by homoionic montmorillonite. 1. The sodium-exchanged form. Langmuir, 8(11): 2730-2739.

Champ, D.R., Schroeter, J., 1988. Bacterial Transport in Fractured Rock — A Field-Scale Tracer Test at the Chalk River Nuclear Laboratories. Water Science & Technology, 20(11): 81–87.

Chang, Y.-I., Wang, M.-C., 2004. Heteroflocculation of equal numbers of different sized colloidal particles in binary dispersions under enhanced gravity forces. Colloids and Surfaces A: Physicochemical and Engineering Aspects, 251(1–3): 75-86.

Chinju, H., Kuno, Y., Nagasaki, S., Tanaka, S., 2001. Deposition Behavior of Polystyrene Latex Particles on Solid Surfaces during Migration through an Artificial Fracture in a Granite Rock Sample. Journal of Nuclear Science and Technology, 38(6): 439-443.

Chrysikopoulos, C.V., 1999. Transport of colloids in saturated fractures. Fracture of Rock: 297-331.

Civan, F., 2011. Reservoir formation damage. Gulf Professional Publishing.

Cuadros, J., Linares, J., 1996. Experimental kinetic study of the smectite-to-illite transformation. Geochimica et Cosmochimica Acta, 60(3): 439-453.

Cumbie, D.H., McKay, L.D., 1999. Influence of diameter on particle transport in a fractured shale saprolite. Journal of Contaminant Hydrology, 37(1-2): 139-157.

5. References

Czigány, S., Flury, M., Harsh, J.B., 2005. Colloid Stability in Vadose Zone Hanford Sediments. Environmental Science & Technology, 39(6): 1506-1512.

Darbha, G.K., Fischer, C., Lützenkirchen, J., Schäfer, T., 2012a. Site-specific retention of colloids at rough rock surfaces. Environ Sci Technol, 46(17): 9378-87.

Darbha, G.K. et al., 2012b. Deposition of latex colloids at rough mineral surfaces: an analogue study using nanopatterned surfaces. Langmuir, 28(16): 6606-17.

Darbha, G.K., Schäfer, T., Heberling, F., Lüttge, A., Fischer, C., 2010. Retention of Latex Colloids on Calcite as a Function of Surface Roughness and Topography. Langmuir, 26(7): 4743-4752.

Degueldre, C., Grauer, R., Laube, A., Oess, A., Silby, H., 1996. Colloid properties in granitic groundwater systems .2. Stability and transport study. Applied Geochemistry, 11(5): 697-&.

Delhorme, M., Labbez, C., Caillet, C., Thomas, F., 2010. Acid-Base Properties of 2:1 Clays. I. Modeling the Role of Electrostatics. Langmuir, 26(12): 9240-9249.

Delon, J.F., Lietard, O., Cases, J.M., Yvon, J., 1986. Determination of porosity of platy materials using slit-shaped and bevelled pores. Clay Minerals, 21(3): 361-375.

Derjaguin, B.V., Landau, L., 1941. Theory of the stability of strongly charged lyophobicsols and the adhesion of strongly charged particles in solutions of electrolytes. Acta Physicochim. URSS, 14.

Detwiler, R.L., Rajaram, H., Glass, R.J., 2000. Solute transport in variable-aperture fractures: An investigation of the relative importance of Taylor dispersion and macrodispersion. Water Resources Research, 36(7): 1611-1625.

Dokou, E., Barteau, M.A., Wagner, N.J., Lenhoff, A.M., 2001. Effect of Gravity on Colloidal Deposition Studied by Atomic Force Microscopy. J Colloid Interface Sci, 240(1): 9-16.

Donald, A.M., 1998. Environmental scanning electron microscopy for the study of 'wet' systems. Current Opinion in Colloid & Interface Science, 3(2): 143-147.

Drits, V.A., Besson, G., Muller, F., 1995. An improved model for structural transformations of heat-treated aluminous dioctahedral 2:1 layer silicates. Clays and Clay Minerals, 43(6): 718-731.

Duc, M., Thomas, F., Gaboriaud, F., 2006. Coupled chemical processes at clay/electrolyte interface: A batch titration study of Na-montmorillonites. Journal of Colloid and Interface Science, 300(2): 616-625.

Einstein, A., 1905. Über die von der molekularkinetischen Theorie der Wärme geforderte Bewegung von in ruhenden Flüssigkeiten suspendierten Teilchen. Annalen der Physik, 322(8): 549-560.

Elimelech, M., O'Melia, C.R., 1990. Effect of particle size on collision efficiency in the deposition of Brownian particles with electrostatic energy barriers. Langmuir, 6(6): 1153-1163.

Emmerich, K., Koeniger, F., Kaden, H., Thissen, P., 2015. Microscopic structure and properties of discrete water layer in Na-exchanged montmorillonite. Journal of Colloid and Interface Science, 448: 24-31.

Emmerich, K., Wolters, F., Kahr, G., Lagaly, G., 2009. Clay Profiling: The Classification of Montmorillonites. Clays and Clay Minerals, 57(1): 104-114.

Evans, K.F., Genter, A., Sausse, J., 2005. Permeability creation and damage due to massive fluid injections into granite at 3.5 km at Soultz: 1. Borehole observations. Journal of Geophysical Research-Solid Earth, 110(B4).

Fein, E., 2004. Software Package r³t. Model for Transport and Retention in Porous Media. Final Report., Gesellschaft für Anlagen- und Reaktorsicherheit (mbH), Braunschweig.

Fernández, A.M., Baeyens, B., Bradbury, M., Rivas, P., 2004. Analysis of the porewater chemical composition of a Spanish compacted bentonite used in an engineered barrier. Physics and Chemistry of the Earth, Parts A/B/C, 29(1): 105-118.

Fernandez, A.M.R., P., 2005. Analysis and distribution of waters in the compacted FEBEX bentonite: pore water chemistry and adsorbed water properties. In: Alonso, E.E., Ledesma, A. (Eds.), Advances in Understanding Engineered Clay Barriers, Advances in understanding engineered clay barriers. Taylor and Francis Group, London, pp. 257-275.

Ferrage, E., Lanson, B., Sakharov, B.A., Drits, V.A., 2005. Investigation of smectite hydration properties by modeling experimental X-ray diffraction patterns: Part I. Montmorillonite hydration properties American Mineralogist, 90: 1359-1374.

Ferrage, E. et al., 2007. Investigation of dioctahedral smectite hydration properties by modeling of X-ray diffraction profiles: Influence of layer charge and charge location American Mineralogist, 92: 1731-1743.

Filby, A., Plaschke, M., Geckeis, H., Fanghänel, T., 2008. Interaction of latex colloids with mineral surfaces and Grimsel granodiorite. Journal of Contaminant Hydrology, 102(3-4): 273-284.

Finck, N., Bouby, M., Dardenne, K., Geckeis, H., 2012. Characterization of Eu(III) co-precipitated with and adsorbed on hectorite: From macroscopic crystallites to nanoparticles. Mineralogical Magazine, 76(7): 2723-2740.

Fischer, C., Michler, A., Darbha, G.K., Kanbach, M., Schäfer, T., 2012. Deposition of mineral colloids on rough rock surfaces. American Journal of Science, 312(8): 885-906.

French, R.A. et al., 2009. Influence of Ionic Strength, pH, and Cation Valence on Aggregation Kinetics of Titanium Dioxide Nanoparticles. Environmental Science & Technology, 43(5): 1354-1359.

Fu, M.H., Zhang, Z.Z., Low, P.F., 1990. Changes in the properties of a montmorillonite-water system during the adsorption and desorption of water: hysteresis. Clays and Clay Minerals, 38: 485-492.

Furukawa, Y., Watkins, J.L., 2012. Effect of Organic Matter on the Flocculation of Colloidal Montmorillonite: A Modeling Approach. Journal of Coastal Research, 28(3): 726-737.

Gallé, C., 2000. Gas breakthrough pressure in compacted Fo-Ca clay and interfacial gas overpressure in waste disposal context. Applied Clay Science, 17(85-97).

Gallego-Urrea, J., Hammes, J., Cornelis, G., Hassellöv, M., 2014. Multimethod 3D characterization of natural plate-like nanoparticles: shape effects on equivalent size measurements. Journal of Nanoparticle Research, 16(5): 1-17.

Gantenbein, D., Schoelkopf, J., Matthews, G.P., Gane, P.A.C., 2011. Determining the size distribution-defined aspect ratio of platy particles. Applied Clay Science, 53(4): 544-552.

Gaucher, E.C. et al., 2009. A robust model for pore-water chemistry of clayrock. Geochimica Et Cosmochimica Acta, 73(21): 6470-6487.

Geckeis, H., Lützenkirchen, J., Polly, R., Rabung, T., Schmidt, M., 2013. Mineral–Water Interface Reactions of Actinides. Chemical Reviews, 113(2): 1016-1062.

Geckeis, H., Rabung, T., Schäfer, T., 2011. Actinide - Nanoparticle interaction: generation, stability and mobility. In: Kalmykov, S.N., Denecke, M.A. (Eds.), Actinide Nanoparticle Research. Springer-Verlag, Berlin, Heidelberg. p1-33.

Geckeis, H. et al., 2004. Results of the Colloid and Radionuclide Retention experiment (CRR) at the Grimsel Test Site (GTS), Switzerland -Impact of reaction kinetics and speciation on radionuclide migration-. Radiochimica Acta, 92(9-11): 765-774.

Geiermann, J., Schill, E., 2010. 2-D Magnetotellurics at the geothermal site at Soultz-sous-Forêts: Resistivity distribution to about 3000 m depth. Comptes Rendus Geoscience, 342(7–8): 587-599.

Gélinas, V., Vidal, D., 2010. Determination of particle shape distribution of clay using an automated AFM image analysis method. Powder Technology, 203(2): 254-264.

Glaus, M.A. et al., 2007. Diffusion of 22Na and 85Sr in Montmorillonite: Evidence of Interlayer Diffusion Being the Dominant Pathway at High Compaction. Environmental Science & Technology, 41(2): 478-485.

Golub, G. et al., 1995. Use of hydrophobic ligands for the stabilization of low-valent transition-metal complexes. 1. The effect of N-methylation of linear tetraazaalkane ligands on the properties of their copper-complexes. Journal of the American Chemical Society, 117(32): 8353-8361.

Greene-Kelly, R., 1953. The identification of montmorillonoids in clays. Journal of soil Science, 4: 233-237.

Grenthe, I., Stumm, W., Laaksuharju, M., Nilsson, A.C., Wikberg, P., 1992. Redox potentials and redox reactions in deep groundwater systems. Chemical Geology, 98(1-2): 131-150.

Gruning, C. et al., 2004. Resonance ionization mass spectrometry for ultratrace analysis of plutonium with a new solid state laser system. International Journal of Mass Spectrometry, 235(2): 171-178.

Guggenheim, S. et al., 2006. Summary of recommendations of nomenclature committees relevant to clay mineralogy: Report of the Association Internationale pour l'Etude des Argiles (AIPEA) Nomenclature. Clays and Clay Minerals, 54(6): 761-772.

Guillaumont, R., Mompean, F.J. (Eds.), 2003. Update on the chemical thermodynamics of uranium, neptunium, plutonium, americium and technetium. OECD Nuclear Energy Agency, Data Bank, Issy-les-Moulineaux, France.

Hakami, E., Larsson, E., 1996. Aperture measurements and flow experiments on a single natural fracture. International Journal of Rock Mechanics and Mining Sciences & Geomechanics Abstracts, 33(4): 395-404.

Hartmann, E., Geckeis, H., Rabung, T., Lützenkirchen, J., Fanghänel, T., 2008. Sorption of radionuclides onto natural clay rocks, Radiochimica Acta International journal for chemical aspects of nuclear science and technology, pp. 699.

Harvey, C.C., Lagaly, G., 2006. Chapter 10.1 Conventional Applications. In: Bergaya, F., Theng, B.K.G., Lagaly, G. (Eds.), Developments in Clay Science. Elsevier, pp. 501-540.

Hauser, W., Geckeis, H., Kim, J.I., Fierz, T., 2002. A mobile laser-induced breakdown detection system and its application for the in situ-monitoring of colloid migration. Colloids and Surfaces A: Physicochemical and Engineering Aspects, 203(1–3): 37-45.

Heathman, J.H., 1939. Bentonite in Wyoming, University of Wyoming, Laramie, Wyoming.

5. References

Henry, C. et al., 2015. A refined algorithm to simulate latex colloid agglomeration at high ionic strength. Adsorption: 1-13.

Hiemstra, T., Van Riemsdijk, W.H., 1991. Physical chemical interpretation of primary charging behaviour of metal (hydr) oxides. Colloids and Surfaces, 59: 7-25.

Hiemstra, T., Venema, P., Riemsdijk, W.H.V., 1996. Intrinsic Proton Affinity of Reactive Surface Groups of Metal (Hydr)oxides: The Bond Valence Principle. Journal of Colloid and Interface Science, 184(2): 680-692.

Hinsby, K., McKay, L.D., Jorgensen, P., Lenczewski, M., Gerba, C.P., 1996. Fracture aperture measurements and migration of solutes, viruses, and immiscible creosote in a column of clay-rich till. Ground Water, 34(6): 1065-1075.

Hixon, A.E., Arai, Y., Powell, B.A., 2013. Examination of the effect of alpha radiolysis on plutonium(V) sorption to quartz using multiple plutonium isotopes. Journal of Colloid and Interface Science, 403(0): 105-112.

Hofmann, U., Klemen, R., 1950. Verlust der Austauschfähigkeit von Lithiumionen aus Bentonit durch Erhitzung. Zeitschrift für Anorganische und Allgemeine Chemie(262): 95-99.

Holthoff, H., Egelhaaf, S.U., Borkovec, M., Schurtenberger, P., Sticher, H., 1996. Coagulation Rate Measurements of Colloidal Particles by Simultaneous Static and Dynamic Light Scattering. Langmuir, 12(23): 5541-5549.

Hu, J., Xu, D., Chen, L., Wang, X.K., 2009. Characterization of MX-80 bentonite and its sorption of radionickel in the presence of humic and fulvic acids. Journal of Radioanalytical and Nuclear Chemistry, 279(3): 701-708.

Huber, F. et al., 2012. Natural micro-scale heterogeneity induced solute and nanoparticle retardation in fractured crystalline rock. Journal of Contaminant Hydrology, 133(0): 40-52.

Huber, F., Kunze, P., Geckeis, H., Schafer, T., 2011. Sorption reversibility kinetics in the ternary system radionuclide-bentonite colloids/nanoparticles-granite fracture filling material. Applied Geochemistry, 26(12): 2226-2237.

Huber, F.H. et al., 2014. "Colloid/nanoparticle formation and mobility in the context of deep geological nuclear waste disposal (Project KOLLORADO-2) ; final report", Karlsruhe Institute of Technology (KIT), Karlsruhe.

Huber, F.M. et al., 2015. Radionuclide desorption kinetics on synthetic Zn/Ni-labeled montmorillonite nanoparticles. Geochimica et Cosmochimica Acta, 148(0): 426-441.

Huertas, F. et al., 2000. Full scale engineered barriers experiment for a deep geological repository for high-level radioactive waste in crystalline host rock (FEBEX project), Brussels.

James, S.C., Chrysikopoulos, C.V., 2003. Effective velocity and effective dispersion coefficient for finite-sized particles flowing in a uniform fracture. Journal of Colloid and Interface Science, 263(1): 288-295.

James, S.C., Chrysikopoulos, C.V., 2011. Monodisperse and polydisperse colloid transport in water-saturated fractures with various orientations: Gravity effects. Advances in Water Resources, 34(10): 1249-1255.

Jansson, M., 2009. Bentonite erosion (Laboratory studies) SKB Technical Report TR-09-33. SKB Technical Report TR-09-33.

Jasmund, K., Lagaly, G. (Eds.), 1993. Tonminerale und Tone: Struktur, Eigenschaften, Anwendungen und Einsatz in Industrie und Umwelt. Steinkopf, Darmstadt, 490 pp.

Jennings, B.R., 1993. Size and thickness measurement of polydisperse clay samples. Clay Minerals, 28(4): 485-494.

Jennings, B.R., Parslow, K., 1988. Particle Size Measurement: The Equivalent Spherical Diameter. Proceedings of the Royal Society of London. A. Mathematical and Physical Sciences, 419(1856): 137-149.

Jia, J., Iwata, S., 2010. Nonequilibrium structure of primary particles in colloidal bidispersion. Colloid and Polymer Science, 288(14-15): 1485-1493.

Johnson, P.R., Sun, N., Elimelech, M., 1996. Colloid transport in geochemically heterogeneous porous media: Modeling and measurements. Environmental Science & Technology, 30(11): 3284-3293.

Jokelainen, L. et al., 2013. The determination of 134Cs and 22Na diffusion profiles in granodiorite using gamma spectroscopy. Journal of Radioanalytical and Nuclear Chemistry, 295(3): 2153-2161.

Kaden, H., Königer, F., Stromme, M., Niklasson, G.A., Emmerich, K., 2013. Low-frequency dielectric properties of three bentonites at different adsorbed water states. Journal of Colloid and Interface Science, 411: 16-26.

Kalmykov Stepan, N. et al., 2015. Partitioning and speciation of Pu in the sedimentary rocks aquifer from the deep liquid nuclear waste disposal, Radiochimica Acta, pp. 175.

Kammer, F.v.d., Baborowski, M., Friese, K., 2005. Field-flow fractionation coupled to multi-angle laser light scattering detectors: Applicability and analytical benefits for the analysis of environmental colloids. Analytica Chimica Acta, 552(1–2): 166-174.

Karnland, O., Olsson, S., Nilsson, U., 2006. Mineralogy and sealing properties of various bentonites and smectite-rich clay materials. SKB internal report TR-06-30.

Kaufhold, S., Dohrmann, R., 2013. The variable charge of dioctahedral smectites. Journal of Colloid and Interface Science, 390: 225-233.

Kaufhold, S., Dohrmann, R., Klinkenberg, M., Siegesmund, S., Ufer, K., 2010. N-2-BET specific surface area of bentonites. Journal of Colloid and Interface Science, 349(1): 275-282.

Keiding, K., Nielsen, P.H., 1997. Desorption of organic macromolecules from activated sludge: Effect of ionic composition. Water Research, 31(7): 1665-1672.

Keller, A., 1998. High resolution, non-destructive measurement and characterization of fracture apertures. International Journal of Rock Mechanics and Mining Sciences, 35(8): 1037-1050.

Keren, R., Shainberg, I., 1975. Water vapor isotherms and heat of immersion of Na/Ca-montmorillonite systems I: homoionic clay. Clays and Clay Minerals, 23: 193-200.

Kersting, A.B., 2013. Plutonium transport in the environment. Inorganic Chemistry, 52(7): 3533-46.

Kersting, A.B. et al., 1999. Migration of plutonium in ground water at the Nevada Test Site. Nature, 397: 56-59.

Kim, J.I., Buckau, G., Baumgärtner, F., Moon, H.C., Lux, D., 1983. Colloid Generation and the Actinide Migration in Gorleben Groundwaters. MRS Online Proceedings Library Archive, 26: 31-40.

Kim, M.A., Panak, P.J., Yun, J.I., Priemyshev, A., Kim, J.I., 2005. Interaction of actinides(III) with aluminosilicate colloids in "statu nascendi" Part III. Colloid formation from monosilanol and polysilanol. Colloids and Surfaces a-Physicochemical and Engineering Aspects, 254(1-3): 137-145.

Kinniburgh, D.G., Cooper, D.M., 2009. PhreePlot: Creating graphical output with PHRREQC.

Kirsch, R. et al., 2011. Oxidation State and Local Structure of Plutonium Reacted with Magnetite, Mackinawite, and Chukanovite. Environmental Science & Technology, 45(17): 7267-7274.

Kloprogge, J.T., Duong, L.V., Frost, R.L., Boström, T.E., 2013. Use of Environmental Scanning Electron Microscopy to Study Uncoated Minerals. Microscopy and Analysis, 19: 17-19.

Knapp, R.B., Chiarappa, M.L., Durham, W.B., 2000. An experimental exploration of the transport and capture of abiotic colloids in a single fracture. Water Resources Research, 36(11): 3139-3149.

Köster, H.M., 1977. Die Berechnung kristallchemischer Strukturformeln von 2:1-Schichtsilikaten unter Beruecksichtigung der gemessenen Zwischenschichtladungen und Kationenumtauschkapazitaeten, sowie die Darstellung der Ladungsverteilung in der Struktur mittels Dreieckskoordinaten. Clay Minerals, 12(1): 45-54.

Kretzschmar, R., Holthoff, H., Sticher, H., 1998. Influence of pH and humic acid on coagulation kinetics of kaolinite: a dynamic light scattering study. J. Colloid and Interface Science, 202: 95-103.

Kretzschmar, R., Schäfer, T., 2005. Metal retention and transport on colloidal particles in the environment. Elements, 1(4): 205-210.

Kumpel, H.J., Grecksch, G., Lehmann, K., Rebscher, D., Schulze, K.C., 1999. Studies of in situ pore pressure fluctuations at various scales. Oil & Gas Science and Technology-Revue D Ifp Energies Nouvelles, 54(6): 679-688.

Kunkel, W.B., 1948. Magnitude and Character of Errors Produced by Shape Factors in Stokes' Law Estimates of Particle Radius. Journal of Applied Physics, 19(11): 1056-1058.

Kunze, P. et al., 2008. The influence of colloid formation in a granite groundwater bentonite pore water mixing zone on radionuclide speciation. Journal of Contaminant Hydrology, 102: 263-272.

Lagaly, G., 1981. Characterization of clays by organic-compounds. Clay Minerals, 16(1): 1-21.

Lagaly, G., 1994. Layer charge determination by alkylammonium ions. In: Mermut, A.R. (Ed.), Layer charge characteristics of clays. The Clay Minerals Society, Boulder, Colorado, pp. 1-46.

Lagaly, G., 2006. Chapter 5 Colloid Clay Science. In: Bergaya, F., Theng, B.K.G., Lagaly, G. (Eds.), Developments in Clay Science. Elsevier, pp. 141-245.

Lagaly, G., Weiss, A., 1969. Determination of the layer charge mica-type layer silicates. In: Heller, L. (Editor), International Clay Conference. Israel University Press, Jerusalem, Tokyo, pp. 61-80.

Lagaly, G., Weiss, A., 1971. Anordnung und Orientierung kationischer Tenside auf ebenen Silicatoberflächen. IV. Anordnung von n-Alkylammoniumionen bei niedrig geladenen Schichtsilicaten. Kolloid-Zeitschrift und Zeitschrift für Polymere, 243(1): 48-55.

Lanyon, B., Blechschmidt, I., 2008. Hydraulic interference between CFM and LTD experiments. Arbeitsbericht NAB 08-11. Natonale Genossenschaft für die Lagerung radioaktiver Abfälle (NAGRA). Wettingen.

Latrille, C., Ly, J., Herbette, M., 2006. Retention of Sn(IV) and Pu(IV) onto four argillites from the Callovo–Oxfordian level at Bure (France) from eight equilibrated sedimentary waters, Radiochimica Acta, pp. 421.

Le Forestier, L., Muller, F., Villieras, F., Pelletier, M., 2010. Textural and hydration properties of a synthetic montmorillonite compared with a natural Na-exchanged clay analogue. Applied Clay Science, 48(1–2): 18-25.

5. References

Leone, G., Reyes, E., Cortecci, G., Pochini, A., Linares, J., 1983. Genesis of bentonites from Cabo de Gata, Almeria, Spain- A stable isotope study. Clay Minerals, 18(3): 227-238.

Li, Y., Wang, X., Wang, J., 2012. Cation exchange, interlayer spacing, and thermal analysis of Na/Ca-montmorillonite modified with alkaline and alkaline earth metal ions. Journal of Thermal Analysis and Calorimetry, 110(3): 1199-1206.

Liu, J., Neretnieks, I., 2006. Physical and chemical stability of the bentonite buffer. SKB Rapport R-06-103, Svensk Kärnbränslehantering AB.

Liu, L., Moreno, L., Neretnieks, I., 2009a. A Dynamic Force Balance Model for Colloidal Expansion and Its DLVO-Based Application. Langmuir, 25(2): 679-687.

Liu, L., Moreno, L., Neretnieks, I., 2009b. A Novel Approach to Determine the Critical Coagulation Concentration of a Colloidal Dispersion with Plate-like Particles. Langmuir, 25(2): 688-697.

Lujanienė, G., Motiejūnas, S., Šapolaitė, J., 2007. Sorption of Cs, Pu and Am on clay minerals. Journal of Radioanalytical and Nuclear Chemistry, 274(2): 345-353.

Lützenkirchen, J., Boily, J.-F., Lövgren, L., Sjöberg, S., 2002. Limitations of the potentiometric titration technique in determining the proton active site density of goethite surfaces. Geochimica Et Cosmochimica Acta, 66(19): 3389-3396.

Lützenkirchen, J., Richter, C., 2013. Zeta-potential measurements of OTS-covered silica samples. Adsorption, 19(2-4): 217-224.

Macdonald, D.D., Sharifi-Asl, S., 2011. Is Copper Immune to Corrosion When in Contact With Water and Aqueous Solutions? Swedish Radiation Safety Authourity, SSM, Report 2011:09.

Madden, A.S., Hochella, M.F., Luxton, T.P., 2006. Insights for size-dependent reactivity of hematite nanomineral surfaces through Cu^{2+} sorption. Geochim. Cosmochim. Acta, 70(Copyright (C) 2012 American Chemical Society (ACS). All Rights Reserved.): 4095-4104.

Maher, K., Bargar, J.R., Brown, G.E., Jr., 2013. Environmental speciation of actinides. Inorganic Chemistry, 52(7): 3510-32.

Mahmood, A., Amirtharajah, T., Sturm, W., Denett, K.E., 2001. A micromechanics approach for attachment and detachment of asymmetric colloidal particles. Colloids and Surfaces A: Physicochemical and Engeneering Aspects, 177: 99-110.

Marques Fernandes, M., Baeyens, B., Dähn, R., Scheinost, A.C., Bradbury, M.H., 2012. U(VI) sorption on montmorillonite in the absence and presence of carbonate: A macroscopic and microscopic study. Geochimica Et Cosmochimica Acta, 93(0): 262-277.

Marsac, R. et al., 2015a. Modeling plutonium sorption to kaolinite: Accounting for redox equilibria and the stability of surface species. Chemical Geology, 400: 1-10.

Marsac, R. et al., 2015b. Neptunium redox speciation at the illite surface. Geochimica et Cosmochimica Acta, 152: 39-51.

McCarthy, J.F., McKay, L.D., 2004. Colloid Transport in the Subsurface. Vadose Zone Journal, 3(2): 326.

McCarthy, J.F., McKay, L.D., Bruner, D.D., 2002. Influence of Ionic Strength and Cation Charge on Transport of Colloidal Particles in Fractured Shale Saprolite. Environmental Science & Technology, 36(17): 3735-3743.

McCarthy, J.F., Zachara, J.M., 1989. Subsurface transport of contaminants: Mobile colloids in the subsurface environment may alter the transport of contaminants. Environ. Sci. Technol., 23(5): 497-502.

McKay, L.D., Harton, A.D., Wilson, G.V., 2002. Influence of Flow Rate on Transport of Bacteriophage in Shale Saprolite. Journal of Environment Quality, 31(4): 1095.

Mehra, O.P., Jackson, M.L., 1960. Iron oxide removal from soils and clays by a dithionite-citrate system duffered with sodium bicarbonate. In: Ingerson, E. (Ed.), Clays and Clay Minerals. Pergamon, pp. 317-327.

Meier, L.P., Kahr, G., 1999. Determination of the cation exchange capacity (CEC) of clay minerals using the complexes of copper(II) ion with triethylenetetramine and tetraethylenepentamine. Clays and Clay Minerals, 47(3): 386-388.

Metz, V., Raanan, H., Pieper, H., Bosbach, D., Ganor, J., 2005. Towards the establishment of a reliable proxy for the reactive surface area of smectite. Geochimica et Cosmochimica Acta, 69(10): 2581-2591.

Meunier, A., 2005. Clays. Springer, Berlin, Heidelberg, 472 pp.

Michot, L.J., Villiéras, F., 2006. Chapter 12.9 Surface Area and Porosity. In: Bergaya, F., Theng, B.K.G., Lagaly, G. (Eds.), Developments in Clay Science. Elsevier, pp. 965-978.

Missana, T., Adell, A., 2000. On the applicability of DLVO theory to the prediction of clay colloids stability. J. Colloid Interface Sci., 230: 150-156.

Missana, T., Alonso, T., Turrero, M.J.S., 2003. Generation and stability of bentonite colloids at the bentonite/granite interface of a deep geological radioactive waste repository. Journal of Contaminant Hydrology, 61(1-4): 17-31.

Missana, T., Alonso, U., Albarran, N., Garcia-Gutierrez, M., Cormenzana, J.-L., 2011. Analysis of colloids erosion from the bentonite barrier of a high level radioactive waste repository and implications in safety assessment. Physics and Chemistry of the Earth, 36(17-18): 1607-1615.

Missana, T., Alonso, U., Garcia-Gutierrez, M., Mingarro, M., 2008. Role of bentonite colloids on europium and plutonium migration in a granite fracture. Applied Geochemistry, 23(6): 1484-1497.

Missana, T., Geckeis, H., 2006. Grimsel Test Site – Investigation Phase V. The CRR Final Project Report Series II: Supporting Laboratory Experiments with Radionuclides and Bentonite Colloids NAGRA Technical Report Series NTB 03-02.

Moll, W.F., 2001. Baseline studies of The Clay Minerals Society Source Clays: Geological origin. Clays and Clay Minerals, 49(5): 374-380.

Montes-H, G., 2005. Swelling–shrinkage measurements of bentonite using coupled environmental scanning electron microscopy and digital image analysis. Journal of Colloid and Interface Science, 284(1): 271-277.

Montes-H, G., Duplay, J., Martinez, L., Geraud, Y., Rousset-Tournier, B., 2003a. Influence of interlayer cations on the water sorption and swelling–shrinkage of MX80 bentonite. Applied Clay Science, 23(5–6): 309-321.

Montes-H, G., Duplay, J., Martinez, L., Mendoza, C., 2003b. Swelling–shrinkage kinetics of MX80 bentonite. Applied Clay Science, 22(6): 279-293.

Moore, D.M., Reynolds, R.C., Jr., 1997. X-Ray Diffraction and the Identifiaction and analysis of Clay Minerals Oxford University Press, Oxford.

Moreno, L., Liu, L., Neretnieks, I., 2011. Erosion of sodium bentonite by flow and colloid diffusion. Physics and Chemistry of the Earth, Parts A/B/C, 36(17–18): 1600-1606.

Moreno, L., Neretnieks, I., 1993. Flow and nuclide transport in fractured media - the importance of the flow-wetted surface for radionuclide migration. Journal of Contaminant Hydrology, 13(1-4): 49-71.

Moreno, L., Neretnieks, I., Liu, L., 2010. Modelling of erosion of bentonite gel by gel/sol flow. SKB Technical Report 06-103, SKB Technical Report 10-64, Svensk Kärnbränslehantering AG, Stockholm, Sweden, .

Moreno, L., Tsang, C.-F., Tsang, Y., Neretnieks, I., 1990. Some anomalous features of flow and solute transport arising from fracture aperture variability. Water Resources Research, 26(10): 2377-2391.

Möri, A. et al., 2003. The colloid and radionuclide retardation experiment at the Grimsel Test Site: influence of bentonite colloids on radionuclide migration in a fractured rock. Colloids and Surfaces A: Physicochemical and Engineering Aspects, 217(1–3): 33-47.

Möri, A., Blechschmidt, I., 2006. GTS Phase VI: CFM Experiment – Structural geological model. Arbeitsbericht NAB 06-18. Natonale Genossenschaft für die Lagerung radioaktiver Abfälle (NAGRA). Wettingen.

Müller-Vonmoos, M., Kahr, G., 1982. Bereitstellung von Bentoniten für Laboruntersuchungen.

Multiphysics, C., 2015. COMSOL Reference Guide.

Nagra, 2006. Grimsel Test Site Investigation Phase V, The CRR Final Report Series II: Supporting laboratory experiments with radionuclides and bentonite colloids. Nagra Technical Report NTB 03-02, Nagra, Wettingen, Switzerland.

NAGRA, 2016. Grimsel Test Site Investigation Phase VI: Colloid Formation and Migration Project: Site instrumentation and initiation of the long-term in-situ test. Nagra Technical Report NTB 15-03, Nagra, Wettingen, Switzerland.

Nagra, 2016, in press. CFM site instrumentation and initiation of the long-term in-situ test. NTB 15-03, Wettingen.

Neck, V., Kim, J.I., Kanellakopulos, B., 1992. Solubility and Hydrolysis Behaviour of Neptunium(V). Radiochimca Acta, 56(1): 25–30.

Neretnieks, I., Liu, J., 2006. Physical and chemical stability of the bentonite buffer. SKB Technical Report 06-103, SKB Technical Report 06-103, Svensk Kärnbränslehantering AG, Stockholm, Sweden.

Neretnieks, I., Liu, L., Moreno, L., 2009. Mechanisms and models for bentonite erosion. SKB Technical report TR-09-35, Svensk Kärnbränslehantering AB, Stockholm, Sweden.

Norrfors, K.K., 2015. Stability and sorption capacity of montmorillonite colloids: Investigation of size fractional differences and effects of γ-irradiation, KTH Royal Institute of Technology, Stockholm, Sweden.

Norrfors, K.K. et al., 2015. Montmorillonite colloids: I. Characterization and stability of dispersions with different size fractions. Applied Clay Science, 114: 179-189.

Norrfors, K.K. et al., 2016a. Montmorillonite colloids: II. Colloidal size dependency on radionuclide adsorption. Applied Clay Science.

Norrfors, K.K. et al., 2016b. Montmorillonite colloids: II. Colloidal size dependency on radionuclide adsorption. Applied Clay Science, 123: 292-303.

Noseck, U. et al., 2016. Modelling of Tracer, Colloid and Radionuclide/Homologue Transport for Dipole CFM 06.002 – Pinkel surface packer. NTB 16-06 (to be published).

5. References

Novich, B.E., Ring, T.A., 1984. Colloid stability of clays using photon correlation spectroscopy. Clays and Clay Minerals, 32(5): 400-406.

Novikov, A.P. et al., 2006. Colloid Transport of Plutonium in the Far-Field of the Mayak Production Association, Russia. Science, 314(5799): 638-641.

Nurchi, V.M. et al., 2013. Complex formation equilibria of Cu-II and Zn-II with triethylenetetramine and its mono- and di-acetyl metabolites. Dalton Transactions, 42(17): 6161-6170.

Ohshima, H., 2001. Approximate Analytic Expression for the Electrophoretic Mobility of a Spherical Colloidal Particle. Journal of Colloid and Interface Science, 239(2): 587-590.

Oncsik, T., Trefalt, G., Csendes, Z., Szilagyi, I., Borkovec, M., 2014. Aggregation of Negatively Charged Colloidal Particles in the Presence of Multivalent Cations. Langmuir, 30(3): 733-741.

Östhols, E., Bruno, J., Grenthe, I., 1994. On the influence of carbonate on mineral dissolution: III. The solubility of microcrystalline ThO_2 in CO_2-H_2O media. Geochimica Et Cosmochimica Acta, 58(2): 613-623.

Ottewill, R.H., Shaw, J.N., 1966. Stability of monodisperse polystyrene latex dispersions of various sizes. Discussions of the Faraday Society, 42(0): 154-163.

Overbeek, J.T.G., 1980. The Rule of Schulze and Hardy. Pure Appl. Chem., 52, No. 5: 1151-1161.

Pabst, W., Berthold, C., 2007. A Simple Approximate Formula for the Aspect Ratio of Oblate Particles. Particle & Particle Systems Characterization, 24(6): 458-463.

Pálková, H., Madejová, J., Righi, D., 2003. Acid dissolution of reduced-charge Li- and Ni-montmorillonites. Clays and Clay Minerals, 51(2): 133-142.

Pan, D.-Q., Fan, Q.-H., Li, P., Liu, S.-P., Wu, W.-S., 2011. Sorption of Th(IV) on Na-bentonite: Effects of pH, ionic strength, humic substances and temperature. Chemical Engineering Journal, 172(2–3): 898-905.

Pantina, J.P., Furst, E.M., 2006. Colloidal Aggregate Micromechanics in the Presence of Divalent Ions. Langmuir, 22(12): 5282-5288.

Parkhurst, D.L., Appelo, C.A.J., 1999. User's guide to PHREEQC (version 2). US Geol. Surv. Water Resour. Inv. Rep. 99-4259, 312p. .

Patelli, A., Alonso, U., Rigato, V., Missana, T., Restello, S., 2006. Validation of the RBS analysis for colloid migration through a rough granite surface. Nuclear Instruments & Methods in Physics Research Section B-Beam Interactions with Materials and Atoms, 249: 575-578.

Perret, D., Newman, M.E., Nègre, J.-C., Chen, Y., Buffle, J., 1994. Submicron particles in the rhine river—I. Physico-chemical characterization. Water Research, 28(1): 91-106.

Plaschke, M. et al., 2001. Size characterization of bentonite colloids by different methods. Analytical Chemistry, 73(17): 4338-4347.

POSIVA, 2012. Safety case for the disposal of spent nuclear fuel at Olkilouto - Synthesis 2012, POSIVA Oy, Eurajoki, Finland.

Powell, B.A., Fjeld, R.A., Kaplan, D.I., Coates, J.T., Serkiz, S.M., 2005. Pu(V)$O2+$ Adsorption and Reduction by Synthetic Hematite and Goethite. Environmental Science & Technology, 39(7): 2107-2114.

Pusch, R., 1983. Stability of bentonite gels in crystalline rock - physical aspects, SKBF/KBS report TR 83-04. TR-report 83-04, University of Luleå, SKB was formerly: SKBF/KBS; SKBF - Svensk Kärnbränsleförsörjning AB.

Pusch, R., 2006. Chapter 11.4 Clays and Nuclear Waste Management. In: Bergaya, F., Theng, B.K.G., Lagaly, G. (Eds.), Developments in Clay Science. Elsevier, pp. 703-716.

Push, R., 1983. Stability of bentonite gels in crystalline rock - Physical aspects. TR 83-04, SKB, Stockholm.

Quinto, F. et al., 2015. Accelerator Mass Spectrometry of Actinides in Ground- and Seawater: An Innovative Method Allowing for the Simultaneous Analysis of U, Np, Pu, Am, and Cm Isotopes below ppq Levels. Analytical Chemistry, 87(11): 5766-5773.

Rand, R., Fuger, J., Neck, V., Grenthe, I., Rai, D., 2009. Chemical Thermodynamics of Thorium, Chemical Thermodynamics, vol. 11. OECD Publishing

Rard, J.A., 1999. Chemical thermodynamics of technetium. North Holland.

Rasband, W., 2015. ImageJ 1.48v.

Reerink, H., Overbeek, J.T.G., 1954. The rate of coagulation as a measure of the stability of silver iodide sols. Discussions of the Faraday Society.

Regenspurg, S., Schild, D., Schäfer, T., Huber, F., Malmström, M.E., 2009. Removal of uranium(VI) from the aqueous phase by iron(II) minerals in presence of bicarbonate. Applied Geochemistry, 24(9): 1617-1625.

Reiche, T., Noseck, U., Schäfer, T., 2016. Migration of Contaminants in Fractured-Porous Media in the Presence of Colloids: Effects of Kinetic Interactions. Transport in Porous Media, 111(1): 143-170.

Reid, C., Lunn, R., El Mountassir, G., Tarantino, A., 2015. A mechanism for bentonite buffer erosion in a fracture with a naturally varying aperture. Mineralogical Magazine, 79(6): 1485-1494.

Reimus, P.W., 1995. The Use of Synthetic Colloids in Tracer Transport Experiments in Saturated Rock Fractures, University of New Mexico, Albuquerque.

Reinholdt, M., Brendlé, J., Tuilier, M.-H., Kaliaguine, S., Ambroise, E., 2013. Hydrothermal Synthesis and Characterization of Ni-Al Montmorillonite-Like Phyllosilicates. Nanomaterials, 3(1): 48-69.

Robinson, C., Brovelli, A., Barry, D.A., Li, L., 2009. Tidal influence on BTEX biodegradation in sandy coastal aquifers. Advances in Water Resources, 32(1): 16-28.

Robinson, C., Li, L., Barry, D.A., 2007. Effect of tidal forcing on a subterranean estuary. Advances in Water Resources, 30(4): 851-865.

Robinson, P., Bath, A., 2011. Workshop on copper corrosion and buffer erosion. Stockholm 15-17. September 2010. SSM Research Report: 2011:8.

Romero, E., Simms, P.H., 2008. Microstructure Investigation in Unsaturated Soils: A Review with Special Attention to Contribution of Mercury Intrusion Porosimetry and Environmental Scanning Electron Microscopy. Geotechnical and Geological Engineering, 26(6): 705-727.

Rosenbrand, E., Haugwitz, C., Jacobsen, P.S.M., Kjøller, C., Fabricius, I.L., 2014. The effect of hot water injection on sandstone permeability. Geothermics, 50: 155-166.

Rozalén, M., Brady, P.V., Huertas, F.J., 2009. Surface chemistry of K-montmorillonite: Ionic strength, temperature dependence and dissolution kinetics. Journal of Colloid and Interface Science, 333(2): 474-484.

Rozalen, M.L., Huertas, F.J., Linares, J., 2004. Experimental study of the effect of pH on the montmorillonite dissolution kinetics at 25 degrees C. Geochimica et Cosmochimica Acta, 68(11): A144-A144.

Runde, W. et al., 2002. Solubility and sorption of redox-sensitive radionuclides (Np, Pu) in J-13 water from the Yucca Mountain site: comparison between experiment and theory. Applied Geochemistry, 17(6): 837-853.

Rutherford, D.W., Chiou, C.T., Eberl, D.D., 1997. Effects of exchanged cation on the microporosity of montmorillonite. Clays and Clay Minerals, 45(4): 534-543.

Saiers, J.E., Lenhart, J.J., 2003. Colloid mobilization and transport within unsaturated porous media under transient-flow conditions. Water Resources Research, 39(1).

Salles, F. et al., 2008. A calorimetric study of mesoscopic swelling and hydration sequence in solid Na-montmorillonite. Applied Clay Science, 39(3–4): 186-201.

Schäfer, T., 2010. Colloid/ Nanoparticle formation and mobility in the context of deep geological nuclear waste disposal (Project KOLLORADO-1; Final report). Forschungszentrum Karlsruhe in der Helmholtz-Gemeinschaft FZKA, Karlsruhe.

Schäfer, T., Geckeis, H., Bouby, M., Fanghänel, T., 2004. U, Th, Eu and colloid mobility in a granite fracture under near-natural flow conditions. Radiochimica Acta, 92: 731-737.

Schäfer, T. et al., 2012. Nanoparticles and their influence on radionuclide mobility in deep geological formations. Applied Geochemistry, 27(2): 390-403.

Schatz, T., Kanerva,N., Martikainen, J., Sane, P., Olin, M., Seppälä, A., Koskinen, K., 2013. Buffer Erosion in Dilute Groundwater.

Schimpf, M., Caldwell, K., Giddings, J.C., 2000. Field flow fractionation handbook.

Schneider, A.e., 2016. Modeling of data uncertainties on hybrid computers. GRS-392, GRS Braunschweig, June 2016.

Schneider, C.A., Rasband, W.S., Eliceiri, K.W., 2012. NIH Image to ImageJ: 25 years of image analysis. Nat Meth, 9(7): 671-675.

Schramm, L.L., Kwak, J.C.T., 1982. Interactions in clay suspensions: The distribution of ions in suspension and the influence of tactoid formation. Colloids and Surfaces, 4(1): 43-60.

Schudel, M., Behrens, S.H., Holthoff, H., Kretzschmar, R., Borkovec, M., 1997. Absolute aggregation rate constants of hematite particles in aqueous suspensions: A comparison of two different surface morphologies. Journal of Colloid and Interface Science, 196(2): 241-253.

Schultz, L.G., 1969. Lithium and potassium absorption, dehydroxylation temperature, and structural water content of aluminous smectites Clays and Clay Minerals, 17(3): 115-149.

Schwyn, B. et al., 2012. FUNMIG Integrated Project results and conclusions from a safety case perspective. Applied Geochemistry, 27(2): 501-515.

Sellin, P., Leupin, O.X., 2013. THE USE OF CLAY AS AN ENGINEERED BARRIER IN RADIOACTIVE-WASTE MANAGEMENT – A REVIEW. Clays and Clay Minerals, 61(6): 477-498.

Shah, P.S., Holmes, J.D., Johnston, K.P., Korgel, B.A., 2002. Size-selective dispersion of dodecanethiol-coated nanocrystals in liquid and supercritical ethane by density tuning. Journal of Physical Chemistry B, 106(10): 2545-2551.

Shen, C., Huang, Y., Li, B., Jin, Y., 2010. Predicting attachment efficiency of colloid deposition under unfavorable attachment conditions. Water Resources Research, 46(11): n/a-n/a.

Simpkins, L., 2011. Influence of natural organic matter on plutonium sorption to gibbsite.

5. References

Sing, K.S.W. et al., 1985. Reporting Physisorption Data for Gas/Solid Systems with Special Reference to the Determination of Surface Area and Porosity. Pure & Applied Chemistry, 57(4): 603-619.

Sirivithayapakorn, S., Keller, A., 2003. Transport of colloids in saturated porous media: A pore-scale observation of the size exclusion effect and colloid acceleration. Water Resources Research, 39(4).

SKB, 2006a. Buffer and backfill process report for the safety assessment SR-Can. Technical report TR-06-18, Svensk Kärnbränslehantering AB, Stockholm, Sweden.

SKB, 2006b. Long-term safety for KBS-3 repositories at Forsmark and Laxemar - a first evaluation; Main report of the SR-Can project. SKB Technical report TR-06-09. Technical report TR-06-09, Svensk Kärnbränslehantering AB, Stockholm, Sweden.

SKB, 2010. Design and production of the KBS-3 repository. SKB internal report TR-10-12.

SKB, 2011. Long-Term Safety for the Final Repository for Spent Nuclear Fuel at Forsmark. Main Report of the SR-Site Project. SKB Technical report TR-11-01, Svensk Kärnbränslehantering AB.

Smith, P.A. et al., 2008. CFM Phase I Modeling Report NAB 08-31. NAB 08-31, Nagra, Wettingen (Switzerland).

Sposito, G., 1981. THE OPERATIONAL DEFINITION OF THE ZERO-POINT OF CHARGE IN SOILS. Soil Science Society of America Journal, 45(2): 292-297.

Sposito, G., 1989. The Chemistry of Soils. Oxford Univ. Press, New York.

Sposito, G., 1992. The diffuse-ion swarm near smectite particles suspended in 1:1 electrolyte solutions: modified Gouy-Chapman theory and quasicrystal formation. In: Güven, N., Pollastro, R.M. (Editors), CMS Workshop Lectures 4, Clay water interface and its rheological implications. Clay minerals society, pp. 127-156.

Srodon, J., Morgan, D.J., Eslinger, E.V., Eberl, D.D., Karlinger, M.R., 1986. Chemistry of illite smectite and end-member illite. Clays and Clay Minerals, 34(4): 368-378.

Steudel, A., Emmerich, K., 2013. Strategies for the successful preparation of homoionic smectites. Applied Clay Science, 75–76(0): 13-21.

Stokes, D., 2008. Principles and Practice of Variable Pressure: Environmental Scanning Electron Microscopy (VP-ESEM). Wiley.

Stumm, W., 1993. Aquatic colloids as chemical reactants: surface structure and reactivity. Colloids and Surfaces A: Physicochemical and Engineering Aspects, 73(0): 1-18.

Stumpf, S., Stumpf, T., Lutzenkirchen, J., Walther, C., Fanghänel, T., 2008. Immobilization of trivalent actinides by sorption onto quartz and incorporation into siliceous bulk: Investigations by TRLFS. Journal of Colloid and Interface Science, 318(1): 5-14.

Svensson, D., Dueck, A., Lydmark, S., Hansen, S., 2011. Alternative buffer material - Status of the ongoing laboratory investigation of reference materials and test package 1.

Taboada-Serrano, P., Vithayaveroj, V., Yiacoumi, S., Tsouris, C., 2005. Surface charge heterogeneities measured by atomic force microscopy. Environmental Science & Technology, 39(17): 6352-6360.

Tang, X.Y., Weisbrod, N., 2009. Colloid-facilitated transport of lead in natural discrete fractures. Environ Pollut, 157(8-9): 2266-74.

Tarazona, P., Marconi, U.M.B., Evans, R., 1987. Phase equilibria of fluid interfaces and confined fluids Non-local versus local density functionals. Molecular Physics, 60(3): 573-595.

Teuten, E.L. et al., 2009. Transport and release of chemicals from plastics to the environment and to wildlife. Philosophical Transactions of the Royal Society of London B: Biological Sciences, 364(1526): 2027-2045.

The MathWorks, I., 2015. MATLAB and Statistics Toolbox Release 2015a, The MathWorks, Inc., Natick, Massachusetts, United States.

Ticknor, K.V., Vilks, P., Vandergraaf, T.T., 1996. The effect of fulvic acid on the sorption of actinides and fission products on granite and selected minerals. Applied Geochemistry, 11(4): 555-565.

Tombacz, E., Szekeres, M., 2004. Colloidal behavior of aqueous montmorillonite suspensions: the specific role of pH in the presence of indifferent electrolytes. Applied Clay Science, 27(1-2): 75-94.

Tompsett, G.A., Krogh, L., Griffin, D.W., Conner, W.C., 2005. Hysteresis and Scanning Behavior of Mesoporous Molecular Sieves. Langmuir, 21(18): 8214-8225.

Tournassat, C., Bizi, M., Braibant, G., Crouzet, C., 2011. Influence of montmorillonite tactoid size on Na–Ca cation exchange reactions. Journal of Colloid and Interface Science, 364(2): 443-454.

Tournassat, C., Ferrage, E., Poinsignon, C., Charlet, L., 2004a. The titration of clay minerals II. Structure-based model and implications for clay reactivity. Journal of Colloid and Interface Science, 273(1): 234-246.

Tournassat, C., Greneche, J.-M., Tisserand, D., Charlet, L., 2004b. The titration of clay minerals: I. Discontinuous backtitration technique combined with CEC measurements. Journal of Colloid and Interface Science, 273(1): 224-233.

Tournassat, C., Neaman, A., Villieras, F., Bosbach, D., Charlet, L., 2003. Nanomorphology of montmorillonite particles: Estimation of the clay edge sorption site density by low-pressure gas adsorption and AFM observations. American Mineralogist, 88(11-12): 1989-1995.

Townley, L.R., 1995. The response of aquifers to periodic forcing. Advances in Water Resources, 18(3): 125-146.

Tributh, H., G., L., 1986. Aufbereitung und Identifizierung von Boden und Lagerstättentonen. I. Aufbereitung der Proben im Labor. GIT Fachzeitschrift für das Laboratorium, 30: 524-529.

Tributh, H., Lagaly, G., 1986. Aufbereitung und identifizierung von Bden- und Lagerstättentonen. I. Aufbereitung des Proben im Labor. GIT-Fachzeitschrift für das Laboratorium, 30: 524-529.

Tsang, C.F., Neretnieks, I., 1998. Flow channeling in heterogeneous fractured rocks. Reviews of Geophysics, 36(2): 275-298.

Tsang, Y.W., 1984. The effect of tortuosity on fluid-flow through a single fracture. Water Resources Research, 20(9): 1209-1215.

Tufenkji, N., Elimelech, M., 2004. Correlation equation for predicting single-collector efficiency in physicochemical filtration in saturated porous media. Environ Sci Technol, 38(2): 529-36.

Turner, D.R., Pabalan, R.T., Bertetti, F.P., 1998. Neptunium(V) sorption on montmorillonite; an experimental and surface complexation modeling study. Clays and Clay Minerals, 46(3): 256-269.

Ulbig, A., 1994. Vergleichende Untersuchungen an Bentoniten, Tuffen und sandig-tonigen Einschaltungen in den Bentonitlagerstätten der Oberen Süßwassermolasse Bayerns, TU München, München, 245 pp.

Utsunomiya, S., Kersting, A.B., Ewing, R.C., 2009. Groundwater Nanoparticles in the Far-Field at the Nevada Test Site: Mechanism for Radionuclide Transport. Environmental Science & Technology, 43(5): 1293-1298.

Vahlund, F., Hermansson, H., 2006. A direct numerical approach to solving the transport equations for radionuclide transport in fractured rock. SKB internal report R-04-50.

Vakarelski, I.U., Ishimura, K., Higashitani, K., 2000. Adhesion between silica particle and mica surfaces in water and electrolyte solutions. Journal of Colloid and Interface Science, 227(1): 111-118.

van Oss, C.J., Giese, R.F., Costanzo, P.M., 1990. DLVO and non-DLVO interactions in hectorite. Clays and Clay Minerals, 38(2): 151-159.

Vayssieres, L., 2009. On the Effect of Nanoparticle Size on Water-Oxide Interfacial Chemistry. The Journal of Physical Chemistry C, 113(12): 4733-4736.

Veghte, D.P., Freedman, M.A., 2014. Facile Method for Determining the Aspect Ratios of Mineral Dust Aerosol by Electron Microscopy. Aerosol Science and Technology, 48(7): 715-724.

Velegol, D., Thwar, P.K., 2001. Analytical model for the effect of surface charge nonuniformity on colloidal interactions. Langmuir, 17(24): 7687-7693.

Verwey, E.J.W., Overbeek, J.T.G., 1948. Theory of the stability of lyophobic colloids. Elsevier, Amsterdam.

Vieno, T., Ikonen, A.T.K., 2005. Plan for Safety Case of Spent Fuel Repository at Olkiluoto, POSIVA Report 2005-1. POSIVA.

Vilks, P., Bachinski, D.B., 1996. Colloid and suspended particle migration experiments in a granite fracture. Journal of Contaminant Hydrology, 21(1-4): 269-279.

Vilks, P., Miller, H.G., Doern, D.C., 1991. Natural Colloids and Suspended Particles in the Whiteshell Research Area, Manitoba, Canada, and Their Potential Effect on Radiocolloid Formation. Applied Geochemistry, 6(5): 565-574.

Vockenhuber, C. et al., 2003. Accelerator mass spectrometry of heavy long-lived radionuclides. International Journal of Mass Spectrometry, 223(1-3): 713-732.

Vogt, K., Köster, H.M., 1978. Zur Mineralogie, Kristallchemie und Geochemie einiger Montmorillonite aus Bentoniten. Clay Minerals, 13(1): 25-43.

Vuorinen, U., Snellman, M., 1998. Finnish reference waters for solubility, sorption and diffusion studies Posiva Working Report 98-61 17-19.

Walther, C., Cho, H.R., Fanghanel, T., 2004. Measuring multimodal size distributions of aquatic colloids at trace concentrations. Applied Physics Letters, 85(26): 6329-6331.

Wan, J. et al., 2004. Colloid formation at waste plume fronts. Environmental Science & Technology, 38: 6066-6073.

Wanner, H. et al., 1994. THE ACID-BASE CHEMISTRY OF MONTMORILLONITE. Radiochimica Acta, 66-7: 157-162.

Weber, C., Heuser, M., Stanjek, H., 2014. A collection of aspect ratios of common clay minerals determined from conductometric titrations. Clay Minerals, 49(3): 495-498.

Weisbrod, N., Dahan, O., Adar, E.M., 2002. Particle transport in unsaturated fractured chalk under arid conditions. Journal of Contaminant Hydrology, 56(1-2): 117-136.

White, G.N., Zelazny, L.W., 1988. Analysis and implications of the edge structure of dioctahedral phyllosilicates. Clays and Clay Minerals, 36(2): 141-146.

5. References

Wiberg, N., Wiberg, E., Holleman, A., 2007. Hollemann und Wiberg – Lehrbuch der Anorganischen Chemie, 102. De Gruyter, Berlin, Germany.

Wilhelm, H., 1997. Tidal phenomena : with 30 tables, Lecture notes in earth sciences ; 66. Springer, Berlin, pp. 398 S.

Wilkinson, K.J., Lead, J.R. (Eds.), 2006. Environmental Colloids and Particles Behaviour, Separation and Characterisation. IUPAC Series on Analytical and Physical Chemistry of Environmental Systems, 10. John Wiley & Sons, New York, 702 pp.

Witherspoon, P.A., Wang, J.S.Y., Iwai, K., Gale, J.E., 1980. VALIDITY OF CUBIC LAW FOR FLUID-FLOW IN A DEFORMABLE ROCK FRACTURE. Water Resources Research, 16(6): 1016-1024.

Wold, S., 2010. Sorption of prioritized elements on montmorillonite colloids and their potential to transport radionuclides. SKB internal report TR-10-20.

Wolf, M., Buckau, G., Geyer, S., 2004. Isolation and characterisation of new batches of GoHy-573 humic and fulvic acids. In: ed., G.B. (Ed.), Humic substances in performance assessment of nuclear waste disposal: Actinide and iodine migration in the far-field. Wissenschaftliche Berichte FZKA 6969, Forschungszentrum Karlsruhe, pp. 111–124.

Wolters, F., Emmerich, K., 2007. Thermal reactions of smectites - Relation of dehydroxylation temperature to octahedral structure. Thermochimica Acta, 462(1–2): 80-88.

Wolters, F., Lagaly, G., Kahr, G., Nueesch, R., Emmerich, K., 2009. A Comprehensive Characterization of Dioctahedral Smectites. Clays and Clay Minerals, 57(1): 115-133.

Wu, T., Amayri, S., Drebert, J., Loon, L.R.V., Reich, T., 2009. Neptunium(V) Sorption and Diffusion in Opalinus Clay. Environmental Science & Technology, 43(17): 6567-6571.

Yao, K.-M., Habibian, M.T., O'Melia, C.R., 1971. Water and waste water filtration. Concepts and applications. Environmental Science & Technology, 5(11): 1105-1112.

Yim, C.S., Mohsen, M.F.N., 1992. Simulation of tidal effects on contaminant transport in porous-media. Ground Water, 30(1): 78-86.

Yoshida, H., Takeuchi, M., Metcalfe, R., 2005. Long-term stability of flow-path structure in crystalline rocks distributed in an orogenic belt, Japan. Engineering Geology, 78: 275.

Yu, S.M. et al., 2008. Adsorption of Th(IV) onto Al-pillared rectorite: Effect of pH, ionic strength, temperature, soil humic acid and fulvic acid. Applied Clay Science, 38(3–4): 219-226.

Zänker, H. et al., 2002. The colloid chemistry of acid rock drainage solution from an abandoned Zn-Pb-Ag mine. Applied Geochemistry, 17(5): 633-648.

Zänker, H., Richter, W., Hüttig, G., 2003. Scavenging and immobilization of trace contaminants by colloids in the waters of abandoned ore mines. Colloids and Surfaces a-Physicochemical and Engineering Aspects, 217(1-3): 21-31.

Zarzycki, P., Thomas, F., 2006. Theoretical study of the acid–base properties of the montmorillonite/electrolyte interface: Influence of the surface heterogeneity and ionic strength on the potentiometric titration curves. Journal of Colloid and Interface Science, 302(2): 547-559.

Zavarin, M., Powell, B.A., Bourbin, M., Zhao, P., Kersting, A.B., 2012. Np(V) and Pu(V) Ion Exchange and Surface-Mediated Reduction Mechanisms on Montmorillonite. Environmental Science & Technology, 46(5): 2692-2698.

Zhang, W., Tang, X., Weisbrod, N., Guan, Z., 2012. A review of colloid transport in fractured rocks. Journal of Mountain Science, 9(6): 770-787.

Zhao, P., Zavarin, M., Kersting, A., Carroll, S., 2011. Sorption and Precipitation of Plutonium in the Presence of Goethite at Elevated Temperatures, Lawrence Livermore National Laboratory (LLNL), Livermore, CA.

Zvikelsky, O., Weisbrod, N., 2006. Impact of particle size on colloid transport in discrete fractures. Water Resources Research, 42(12): n/a-n/a.

Zvikelsky, O., Weisbrod, N., Dody, A., 2008. A comparison of clay colloid and artificial microsphere transport in natural discrete fractures. J Colloid Interface Sci, 323(2): 286-92.